frontiers | Research Topics

Advances in distributed energy resources aggregation for the low carbon future

Edited by
Qinran Hu, Qiuwei Wu, Tao Chen, Qingxin Shi and Hantao Cui

Published in
Frontiers in Energy Research

ISSN 1664-8714
ISBN 978-2-83251-454-2
DOI 10.3389/978-2-83251-454-2

About Frontiers

Frontiers is more than just an open access publisher of scholarly articles: it is a pioneering approach to the world of academia, radically improving the way scholarly research is managed. The grand vision of Frontiers is a world where all people have an equal opportunity to seek, share and generate knowledge. Frontiers provides immediate and permanent online open access to all its publications, but this alone is not enough to realize our grand goals.

Frontiers journal series

The Frontiers journal series is a multi-tier and interdisciplinary set of open-access, online journals, promising a paradigm shift from the current review, selection and dissemination processes in academic publishing. All Frontiers journals are driven by researchers for researchers; therefore, they constitute a service to the scholarly community. At the same time, the *Frontiers journal series* operates on a revolutionary invention, the tiered publishing system, initially addressing specific communities of scholars, and gradually climbing up to broader public understanding, thus serving the interests of the lay society, too.

Dedication to quality

Each Frontiers article is a landmark of the highest quality, thanks to genuinely collaborative interactions between authors and review editors, who include some of the world's best academicians. Research must be certified by peers before entering a stream of knowledge that may eventually reach the public - and shape society; therefore, Frontiers only applies the most rigorous and unbiased reviews. Frontiers revolutionizes research publishing by freely delivering the most outstanding research, evaluated with no bias from both the academic and social point of view. By applying the most advanced information technologies, Frontiers is catapulting scholarly publishing into a new generation.

What are Frontiers Research Topics?

Frontiers Research Topics are very popular trademarks of the *Frontiers journals series*: they are collections of at least ten articles, all centered on a particular subject. With their unique mix of varied contributions from Original Research to Review Articles, Frontiers Research Topics unify the most influential researchers, the latest key findings and historical advances in a hot research area.

Find out more on how to host your own Frontiers Research Topic or contribute to one as an author by contacting the Frontiers editorial office: frontiersin.org/about/contact

Advances in distributed energy resources aggregation for the low carbon future

Topic editors

Qinran Hu — Southeast University, China
Qiuwei Wu — Technical University of Denmark, Denmark
Tao Chen — Southeast University, China
Qingxin Shi — North China Electric Power University, China
Hantao Cui — Oklahoma State University, United States

Citation

Hu, Q., Wu, Q., Chen, T., Shi, Q., Cui, H., eds. (2023). *Advances in distributed energy resources aggregation for the low carbon future*. Lausanne: Frontiers Media SA. doi: 10.3389/978-2-83251-454-2

Table of contents

frontiers | Frontiers in Energy Research

TYPE Editorial
PUBLISHED 12 January 2023
DOI 10.3389/fenrg.2022.1029751

OPEN ACCESS

EDITED AND REVIEWED BY
Yogendra Arya,
YMCA University of Science and Technology, India

*CORRESPONDENCE
Qinran Hu,
qhu@seu.edu.cn

SPECIALTY SECTION
This article was submitted to Smart Grids, a section of the journal Frontiers in Energy Research

RECEIVED 27 August 2022
ACCEPTED 24 October 2022
PUBLISHED 12 January 2023

CITATION
Hu Q, Cui H, Wu Q, Chen T and Shi Q (2023), Editorial: Advances in distributed energy resources aggregation for the low carbon future.
Front. Energy Res. 10:1029751.
doi: 10.3389/fenrg.2022.1029751

Editorial: Advances in distributed energy resources aggregation for the low carbon future

Qinran Hu[1]*, Hantao Cui[2], Qiuwei Wu[3], Tao Chen[1] and Qingxin Shi[4]

[1]School of Electrical Engieering, Southeast University, Nanjing, China, [2]School of Electrical and Computer Engineering, Oklahoma State University, Stillwater, OK, United States, [3]Department of Electrical Engineering, Technical University of Denmark, Kongens Lyngby, Denmark, [4]School of Electrical Engieering, North China Electric Power University, Beijing, China

KEYWORDS

DER-distributed energy resources, low carbon, energy systems, DER aggregation, renewable energy

Editorial on the Research Topic
Advances in distributed energy resources aggregation for the low carbon future

To realize low carbon energy systems, a large number of Distributed Energy Resources (DERs), including energy storage systems, electric vehicles, and flexible loads have been integrated into power grids, from transmission systems to distribution networks. However, system reliability is facing severe challenges due to the intermittency of distributed energy resources. In recent years, with the digitalization of power systems, Advanced Metering Infrastructure (AMI) and Internet of things (IoT) devices have been widely deployed. Meanwhile, as a huge amount of real-time information about the system and end-user status become available, distributed energy resources aggregation draws increasing attention from both academia and industry. It is expected to facilitate the operation of low-carbon energy systems. Therefore, research on the enhancement of distributed resource aggregation capability has been continuously funded by various national research projects. New principles, technologies, and methods to help enhance distributed resource aggregation capability have emerged, especially positive progress has been made in the following aspects: 1) renewables and distributed energy, 2) low-carbon and energy efficiency, 3) scheduling strategy and optimization.

To present the latest progress and future development trend of distributed energy resources aggregation capacity enhancement and share academic and technical achievements, we organized “Advances in Distributed Energy Resources” to address this hot issue. The call for articles received a great response from scholars in related fields, and many submissions were received. After the editorial team organized an expert review, 13 articles were finally selected for inclusion in this issue. Through this issue, we hope to discuss the latest advances, theoretical results, and future directions of advances in distributed energy resources aggregation for the low carbon future and jointly promote

the research of new principles, new technologies, and new methods of distributed energy resources aggregation, low-carbon and energy efficiency, scheduling strategy and optimization. Brief information on the 13 accpted papers as follows.

1 Renewable and distributed energy

Improving power grid resilience under extreme weather conditions with proper regulation and management on DERs—Experiences learned from Texas power crisis in 2021 by Pan and Li.

Small-Signal Distributed Frequency Modeling and Analysis for Grid-Forming Inverter Based Power System by Qi et al.

Robust Bi-Level Planning Method for Multi-Source System Integrated with Offshore Wind Farms Considering Prediction Error by Jian et al.

Control strategy of distributed energy micro-grid involving distribution system resilience by Wu et al.

2 Low-carbon and energy efficiency

Optimization For Transformer District Operation Considering Carbon Emission And Differentiated Demand Response by Jia et al.

A Low-carbon Dispatch Strategy for Power Systems Considering Flexible Demand Response and Energy Storage by Han et al.

Multi-objective Optimization of Multi-energy Flow Coupling System with Carbon Emission Target Oriented by Zong et al.

Fast and Accurate Traction Induction Machine Performance Calculation Method for Integrated On-board Charging in Vehicle to Grid Application by Cai et al.

3 Scheduling strategy and optimization

An optimal scheduling strategy for integrated energy systems using demand response by Lin et al.

Multi-agent schedule optimization method for regional energy internet considering the improved tiered reward and punishment carbon trading model by Li et al.

Day-ahead operation of an urban energy system considering traffic flows and peak shaving by Peng et al.

Optimal capacity allocation model for integrated energy microgrid considered aggregation of prosumers under multi-market mechanisms by Wang et al.

Unified Active and Reactive Power Coordinated Optimization for Unbalanced Distribution Network in Radial and Looped Topology by Zeng et al.

Author contributions

All authors listed have made a substantial, direct, and intellectual contribution to the work and approved it for publication.

Acknowledgments

We sincerely thank the authors and readers for their great support of this topic, and especially the editorial board of Frontiers in Energy Research and the reviewers for their efforts to make this topic published successfully. We hope this topic can provide a reference for experts and scholars interested in and engaged in related research to promote the development of original innovation and key technology practice of distributed resource aggregation.

Conflict of interest

The authors declare that the research was conducted in the absence of any commercial or financial relationships that could be construed as a potential conflict of interest.

Publisher's note

frontiers in Energy Research

METHODS
published: 04 February 2022
doi: 10.3389/fenrg.2021.840014

Unified Active and Reactive Power Coordinated Optimization for Unbalanced Distribution Networks in Radial and Looped Topology

Yuanjing Zeng[1]*, *Yang Wang*[2] *and Peishuai Li*[3]

[1]Industrial Center, Nanjing Institute of Technology, Nanjign, China, [2]Economic Research Institution, State Grid Jiangsu Electric Power Co., Ltd., Nanjign, China, [3]School of Automation, Nanjing University of Science and Technology, Nanjing, China

Facing the high proportion of distributed generations incorporating in a single phase, the active distribution network has become more unbalanced with flexible topology. In this paper, a unified active and reactive power coordinated optimization (ARPCO) method, which is applicable in both radial and looped unbalanced distribution networks, is proposed. Aiming to reduce power losses and restrain undervoltage and overvoltage problems, the ARPCO model which regulates the active and reactive power output of distributed generations coordinately and optimally is constructed. A novel trust region sequential linear programming (SLP) method, which is effective in nonlinear and nonconvex model solving, is developed and employed in APRCO model solution. A multi-scenario case study based on the modified IEEE 123 node distribution system shows that the proposed method is able to reduce the system active power loss and solve undervoltage and overvoltage problems efficiently, at the same time maximizing the utilization of distributed generations.

Keywords: distributed energy resources, active and reactive power coordinated optimization, unbalanced distribution network, radial and looped topology, trust region SLP

OPEN ACCESS

Edited by:
Qinran Hu,
Southeast University, China

Reviewed by:
Ke Meng,
University of New South Wales, Australia
Siqi Bu,
Hong Kong Polytechnic University, Hong Kong SAR, China
Sheng Chen,
Hohai University, China

***Correspondence:**
Yuanjing Zeng
yjzeng@njit.edu.cn

Specialty section:
This article was submitted to Smart Grids, a section of the journal Frontiers in Energy Research

Received: *20 December 2021*
Accepted: *27 December 2021*
Published: *04 February 2022*

Citation:
Zeng Y, Wang Y and Li P (2022) Unified Active and Reactive Power Coordinated Optimization for Unbalanced Distribution Networks in Radial and Looped Topology. Front. Energy Res. 9:840014. doi: 10.3389/fenrg.2021.840014

1 INTRODUCTION

With construction of low-carbon energy systems, the penetration of distributed generations (DGs) in distribution networks (DNs) has been growing rapidly (D'Adamo et al., 2009). The large amounts of grid-connected DGs have been changing the voltage level and power flow distribution of the DN (Wu et al., 2017) evidently; especially, the frequent power variation of DGs may cause voltage fluctuation and overvoltage and undervoltage problems, even sacrificing power quality. Under the worst conditions, it may lead up to the DGs out of service and destruction of electric equipment, which is a severe waste of renewable energy and power grid assets (Tonkoski et al., 2012; Eftekharnejad et al., 2013; Gao et al., 2018; Zhang et al., 2019). On the other hand, the integrated inverter-based DGs are excellent active and reactive power supply resources with a fast response speed; thus, it promotes the controllability and optimal operation potential of DN significantly (Li et al., 2018).

Generally, the reasonable reactive power optimization can restrain supply voltage fluctuation introduced by DGs and reduce active power loss of DN. In Chen et al. (2015), a centralized reactive power optimization method designed for low-voltage DN is proposed to reduce power losses. In Daratha et al. (2014) and Wang et al. (2014), volt/var optimization of DN is implemented by

comprehensive regulation of on-load tap changers (OLTCs), static var compensators (SVCs), and CBs. In Tonkoski et al. (2011) and Lemkens et al. (2013), the photovoltaic (PV) active power curtailment strategy based on voltage droop is proposed to restrain the overvoltage problem. Although the DN safe operation is ensured, the renewable energy power is wasted. Actually, the typical DGs, for example, PVs, are installed in DN with inverters, of which the active and reactive power can be controlled separately. In addition, in Barr and Majumder (2014), grid voltage feedback is introduced into the reactive power control loop of the DG inverter to limit the voltage rise of point of common coupling (PCC) by real-time adjustment of DG reactive power output. However, voltage is regulated locally by this method and voltage qualification of the whole network cannot be guaranteed. Calderaro et al. (2014) proposes a DN voltage control method with the objective of minimizing the reactive power output of DGs, and the DN voltage is regulated with relatively small occupation of DG capacity. Li et al. (2020) further considers the coordination of PV reactive power output and OLTC. It has been widely known that the remaining capacity of DGs can be high-quality reactive power sources to provide auxiliary services as voltage regulation, power losses, and so forth. In Farivar et al. (2012), a second-order cone programming (SOCP)-based inverter varoptimization model is established to reduce DN active power losses within the bus voltage limitations, and Zheng et al. (2016) develop an alternating direction method of multipliers based on the full distributed algorithm to solve the proposed SOC model.

The above research studies are all based on balanced network assumption; however, the low-voltage DN is always unbalanced due to the fact that the load unbalance, line parameter asymmetry, and open-phase operation are ubiquitous (Omar and Rahim, 2012; Kekatos et al., 2016). Moreover, rooftop PVs and electrical vehicles aggravate unbalance in low-voltage DN (Kamh and Iravani, 2010; Yan and Saha, 2012). Therefore, the three balanced assumptions will introduce large errors in DN operation, and adopting the multi-phase model in the unbalanced system has been widely accepted (Kamh and Iravani, 2010; Wang et al., 2015). In Daratha et al. (2014), a coordinated optimization model is developed for unbalanced DN, which coordinates OLTC, CBs, and reactive output of DGs to control DN bus voltage and reduce active power loss. In addition, Mostafa et al. (2013) proposed a multi-objective optimization method for operating DN co-operating a large number of single-phase solar generators, and the current unbalance and energy loss are minimized via reactive compensation devices and reconfiguration switches. Moreover, both the bus active and reactive power injection impact the bus voltage significantly due to the high R/X ration in DN. It is complex that the active power and reactive power output of DGs are coupled tightly, which may need other measures when the inverter active power is high and the inverter remaining capacity cannot compensate overvoltage adequately. Consequently, Kulmala et al. (2014) present a sensitivity-based active and reactive power coordinated control algorithm. In the case of overvoltage, reactive power control should be carried out preferentially. If the reactive power control method cannot restore the bus voltage, the active power control is implemented, which usually includes DG active power output curtailment. However, in the aforementioned method, the active and reactive powers are controlled individually, which is not consistent with the fact that DG active and reactive powers are highly coupled.

To fill the research gaps shown as above, a unified active and reactive power coordinated optimization (ARPCO) method is proposed for unbalanced DN incorporating distributed grid-connected PV generations. The proposed method coordinates active and reactive output powers of PVs *via* the constructed optimization model, which could maximize the active power output of PVs as well as minimize active power loss on the premise of supply voltage qualification under various operation statuses of DN. Moreover, the proposed ARPCO is highly applicable in both radial and looped topologies.

The main contributions of this paper are described as follows:

(1) With consideration of high coupling between active and reactive power outputs of DGs, the ARPCO model which is unified in radial and looped topologies is established to maximize the unitization of DGs and minimize active power loss of DN.
(2) A trust region sequential linear programming (SLP) algorithm is proposed to solve the ARPCO model effectively. The proposed SLP is effective in nonconvex and nonlinear model solving, while its accuracy and convergence speed are improved evidently compared with the existing fixed step-size SLP.

The rest of the paper is organized as follows: **Section 2** presents the established ARPCO model. In **Section 3**, the trusted region SLP algorithm is illustrated detailedly in the ARPCO model solution. The multi-scenario case study based on modified IEEE 123 node unbalanced DN is described in **Section 4**, which validates the proposed method. **Section 5** concludes this paper.

2 COORDINATED OPTIMIZATION MODEL

2.1 Objective Functions

The main objectives of this study are as follows:

— To minimize active power loss of the unbalanced radial and looped DN.
— To maximize active power utilization of the grid-connected DGs.

For an unbalanced DN with N nodes, the active power loss equals the sum of active power injections of all nodes including the slack bus or substation bus

$$P_{loss} = \sum_{i=1}^{N} \sum_{\varphi=A,B,C} P_i^{\varphi} \tag{1}$$

where P_i^{φ} is the active power injection of phase φ at node i.

The second objective is to maximal utilization of DG's active power, and all the DGs' active power output is summed as

$$P_{DG} = \sum_{(i,\varphi)\in G_{DG}} P_{i,DG}^{\varphi} \tag{2}$$

where $P_{i,DG}^{\varphi}$ is the DG active power of φ phase at node i. $(i,\varphi) \in G_{DG}$ represents that there is a DG connected to phase φ at node i.

Whole injection of each node can be described as

$$\begin{aligned} P_i^{\varphi} &= \begin{cases} P_{i,DG}^{\varphi} + P_{i,load}^{\varphi} & (i,\varphi) \in G_{DG} \\ Q_i^{\varphi} P_{i,load}^{\varphi} & otherwise \end{cases} \\ &= \begin{cases} Q_{i,DG}^{\varphi} + Q_{i,load}^{\varphi} & (i,\varphi) \in G_{DG} \\ Q_{i,load}^{\varphi} & otherwise \end{cases} \end{aligned} \tag{3}$$

where $P_{i,load}^{\varphi}$ and $Q_{i,load}^{\varphi}$ represent the active and reactive power loads in i node phase φ, respectively, while $Q_{i,load}^{\varphi}$ is the reactive power output of DG.

Combing **Eqs 1**, **2**, the objective function is determined by

$$P_{loss} - P_{DG} = \sum_{\varphi=A,B,C} P_1^{\varphi} + \sum_{i=2}^{N} \sum_{\varphi=A,B,C} P_{i,load}^{\varphi} \tag{4}$$

where node 1 is the slack bus.

In **Eq. 4**, load data are given and fixed. Therefore, minimizing $P_{loss} - P_{DG}$ is equivalent to minimize slack bus active power injection, which is a function of DGs' active and reactive power output. It can be understood that when DGs' active power output is maximized and active power loss is minimized with a certain load, the slack bus active power injection should be minimized. Thus, the active power absorbed from the transmission network by DN is minimized. Consequently, the objective function of the coordinated optimization is achieved by

$$\min f = \sum_{\varphi=A,B,C} P_1^{\varphi} \tag{5}$$

2.2 Constraints

In the coordinated optimization model, the state variable, voltage of each node, and the control variable, active and reactive power output of the grid-connected DGs, must satisfy the following constraints:

$$\mathbf{S}^{ABC} = diag\left[\mathbf{V}^{ABC}\right] \cdot \left[\mathbf{Y}^{ABC}\right] \cdot \left[\mathbf{V}^{ABC}\right]^{*} \tag{6}$$

$$u^{min} \le u_i^{\varphi} \le u^{max} \tag{7}$$

$$0 \le P_{i,DG}^{\varphi} \le P_{i,frc}^{\varphi} \quad \forall (i,\varphi) \in G_{DG} \tag{8}$$

$$\begin{cases} -\alpha S_{i,DG}^{\varphi} \le Q_{i,DG}^{\varphi} \le \alpha S_{i,DG}^{\varphi} & 0 < \alpha < 1 \\ \left(P_{i,DG}^{\varphi}\right)^2 + \left(Q_{i,DG}^{\varphi}\right)^2 \le \left(S_{i,DG}^{\varphi}\right)^2 & \forall (i,\varphi) \in G_{DG} \end{cases} \tag{9}$$

where **Eq. 6** is the power flow equation for an unbalanced system; $\mathbf{S}^{ABC}$, $\mathbf{V}^{ABC}$, and $\mathbf{V}^{ABC}$ represent the bus power injections, bus voltage vector, and system admittance matrix, respectively, and more details about the unbalanced power flow equations can be seen in the reference (Nguyen, 1997); u_i^{φ} is voltage magnitude of i node φ phase, and u^{min} and u^{max} are the allowable lower bound and upper bound, respectively; $P_{i,frc}^{\varphi}$ is the maximum active output of the DG by forecast; $S_{i,DG}^{\varphi}$ is the inverter capability of the DG, and α is a coefficient, which limits the reactive power output of the DG.

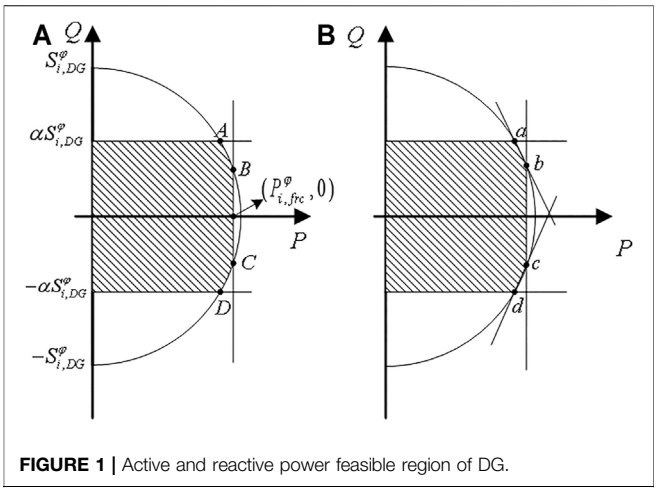

FIGURE 1 | Active and reactive power feasible region of DG.

The feasible region of a DG generated by **Constraints 8**, **9** is shown as the shadow in **Figure 1A**. In this study, the nonlinear constraint of DG is linearized by approximating arcs AB and CD in **Figure 1A** with lines $\overline{ab}$ and $\overline{cd}$ in **Figure 1B**, respectively.

Then, the shadow in **Figure 1B**, namely, the feasible region of each DG, can be described by four linear constraints:

$$\begin{cases} 0 \le P_{i,DG}^{\varphi} \le P_{i,frc}^{\varphi} \\ -\alpha S_{i,DG}^{\varphi} \le Q_{i,DG}^{\varphi} \le \alpha S_{i,DG}^{\varphi} \quad 0 < \alpha < 1 \\ Q_{i,DG}^{\varphi} - Q_{i,frc}^{\varphi} - t\left(P_{i,DG}^{\varphi} - P_{i,frc}^{\varphi}\right) \le 0 \\ Q_{i,DG}^{\varphi} + Q_{i,frc}^{\varphi} + t\left(P_{i,DG}^{\varphi} - P_{i,frc}^{\varphi}\right) \ge 0 \end{cases} \tag{10}$$

where

$$t = \frac{\alpha S_{i,DG}^{\varphi} - Q_{i,frc}^{\varphi}}{\sqrt{1-\alpha^2} \times S_{i,DG}^{\varphi} - P_{i,frc}^{\varphi}} \tag{11}$$

$$Q_{i,frc}^{\varphi} = \sqrt{\left(S_{i,DG}^{\varphi}\right)^2 - \left(P_{i,DG}^{\varphi}\right)^2} \tag{12}$$

To sum up, the coordinated optimization model is achieved by

$$\begin{cases} \mathbf{min}\ f \\ s.t\,(6),\,(7),\,(10) \end{cases} \tag{13}$$

3 TRUST REGION SLP METHOD

The proposed ARPCO model is a nonlinear and nonconvex program due to the power balance **Constraints 7**. In recent papers, many heuristic algorithms based on artificial intelligence have been proposed to find good solutions to the optimization problem, such as the genetic algorithm (Moradi and Abedini, 2012), differential evolution (Basu, 2016), particle

swarm optimization (Gomez-Gonzalez et al., 2012; Schweickardt et al., 2016), and so forth. Moreover, the effective mathematical methods such as SLP (Olofsson et al., 1995; Mohapatra et al., 2013) and successive quadratic programing (SQP) (Palma-Behnke et al., 2004) are also proposed. However, artificial intelligence heuristic algorithms do not guarantee an optimal solution and are unreliable for practical applications. As for the SLP and SQP, they suffer from choosing an appropriate step size; for example, the small step size usually leads to slow convergence and the large step size decreases the convergence accuracy. Thus, in this paper, a trust region SLP method is proposed to achieve both a fast convergence speed and high accuracy by designing a self-adaptive step size.

3.1 Trust Region Technology

Trust region methods are a class of numerical methods for optimization, which compute a trial step by solving a trust region subproblem (Yuan, 2015). To be more specific, for a general optimization problem

$$\min_{x\in X} f(x) \tag{14}$$

where $f(x)$ is the objective function and X is the feasible set generated by all the constraints.

At the k_{th} iteration, a trust region algorithm obtains a trial step d_k by solving the following trust region subproblem:

$$\begin{cases} \min\limits_{\mathrm{d}\in \mathrm{X_k}} \mathrm{m_k}(d) \\ s.t \parallel \mathrm{d}\parallel_{\mathrm{W_k}} \le \Delta_{\mathrm{k}} \end{cases} \tag{15}$$

where $m_k(d)$ is a model function that approximates the objective function $f(x_k + d)$ near the current iteration point x_k, X_k is an approximation to the feasible set, $||\cdot||W_k$ is a norm, and $\Delta_{\mathrm{k}} > 0$ is the trust region radius, which is altered with iteration.

3.2 Linear Approximation

One of the essential parts of trust region methods is the choice of trust region subproblem. Linear programing (LP) has been proved efficient by many scholars; thus, LP is combined with the trust region algorithm in this paper.

Assuming that ($\mathbf{u}_0$, $\mathbf{x}_0$) is a certain operation status of unbalanced DN, the linear approximation of the ARPCO model can be described as

$$\begin{cases} \min F(u_0, x_0) + \Delta_u F \Delta u + \nabla_x F \Delta x \\ s.t.\, \Delta_u h \Delta u + \Delta_x h \Delta x + h(u_0, x_0) = 0 \\ \Delta_u g \Delta u + \Delta_x g \Delta x + g(u_0, x_0) \le 0 \end{cases} \tag{16}$$

where F(x) is the objective function, $h(u, x)$ represents the equality constraints, $g(u, x)$ represents the inequality constraints, $\mathbf{u}$ and $\mathbf{x}$ represent the state and controllable variables, respectively, $F(u_0, x_0)$ is the objective function value for the operation status ($\mathbf{u}_0$, $\mathbf{x}_0$), $\nabla_{(.)}F(.)$ is the gradient of objective F, and $\Delta(.)$ shows the variation of variable.

Therefore, at the k_{th} iteration, the LP-based trust region subproblem of (14) is

$$\begin{cases} \min \sum\limits_{\varphi=\mathrm{A,B,C}} \Delta P_{1,k}^{\varphi} + P_{1,0}^{\varphi} \\ \begin{bmatrix} \Delta P_k^{ABC} \\ \Delta P_k^{ABC} \end{bmatrix} = J_k \begin{bmatrix} \Delta \theta_k^{ABC} \\ \Delta U_k^{ABC} \end{bmatrix} \\ s.t.\, u^{min} \le u_{i,k}^{\varphi} + \Delta u_{i,k}^{\varphi} \le u^{max} \\ 0 \le P_{i,DG,k}^{\varphi} + \Delta P_{i,DG,k}^{\varphi} \le P_{i,frc}^{\varphi} \\ -\alpha S_{i,DG}^{\varphi} \le Q_{i,DG,0}^{\varphi} + \Delta Q_{i,DG}^{\varphi} \le \alpha S_{i,DG}^{\varphi} \\ Q_{i,DG,k}^{\varphi} + \Delta Q_{i,DG,k}^{\varphi} - Q_{i,frc}^{\varphi} - t\left(P_{i,DG,k}^{\varphi} + \Delta P_{i,DG,k}^{\varphi} - P_{i,frc}^{\varphi}\right) \le 0 \\ Q_{i,DG,k}^{\varphi} + \Delta Q_{i,DG,k}^{\varphi} + Q_{i,frc}^{\varphi} + t\left(P_{i,DG,k}^{\varphi} + \Delta P_{i,DG,k}^{\varphi} - P_{i,frc}^{\varphi}\right) \ge 0 \\ \parallel u_k \parallel_{\infty} \le \Delta_k \end{cases} \tag{17}$$

where subscript k represents the value of the kth iteration, Δu_k is the vector of control variables' variation, namely, $\Delta P_{i,DG,k}^{\varphi}$ and $\Delta Q_{i,DG,k}^{\varphi}$, and J is the Jacobian matrix of power flow **Eq. 6**.

3.3 Trust Region Radius

The essential part of the trust region algorithm is to determine an appropriate trust region radius during each iteration. At the k_{th} iteration, let d_k be a trial step which solves the trust region subproblem (15). Then, the predicted reduction of the original optimization model (14) is computed by

$$Pred_k = m_k(0) - m_k(d_k) \tag{18}$$

and the actual reduction of (15) is

$$Ared_k = f(x_k) - f(x_k + d_k) \tag{19}$$

The ratio is defined by

$$r_k = \frac{Ared_k}{Pred_k} \tag{20}$$

Then, the trust region radius of the next iteration is determined by

$$\Delta_{k+1} = \begin{cases} max[\Delta_k, 4 \parallel d_k \parallel_{\infty}] & r_k > 0.9 \\ \Delta_k & 0.1 \le r_k \le 0.9 \\ min[\Delta_k/4, \parallel d_k \parallel_{\infty}/2] & r_k < 0.1 \end{cases} \tag{21}$$

It is proven in Powell and Yuan, 1990 that the trust region method features global convergence and local superlinear convergence.

The actual implementation of the proposed trust region SLP method is summarized as below:

Step 1. Initialization.

- Set the iteration counter k = 1;
- Initialize error bound err1 and err2, trust region radius Δ_0;
- Initialize control variables u_0, namely, $P_{i,DG,0}^{\varphi}$ and $Q_{i,DG,0}^{\varphi}$, and solve the power flow **Eq. 6** with u_0 to acquire the state variables x_0, namely, $u_{i,0}^{\varphi}$ and $\theta_{i,0}^{\varphi}$, as well as the Jacobian matrix J_0.

Step 2. Solve the trust region subproblem.

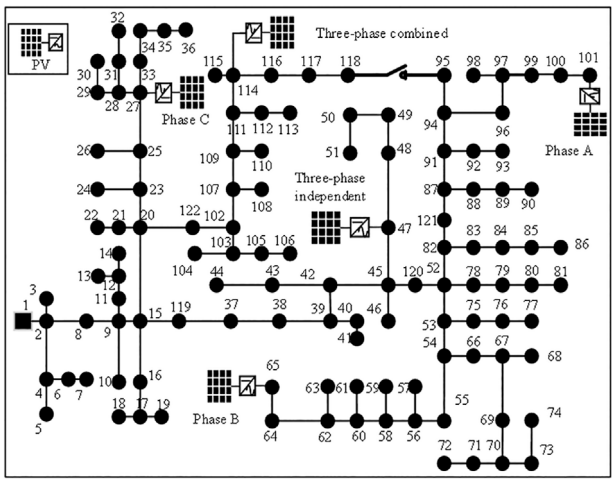

FIGURE 2 | Diagram of the modified IEEE 123 nodes test feeder.

- Generate the LP-based trust region subproblem (17);
- Solve LP (17) and acquire $\Delta \mathbf{u}_k$, namely, $\Delta P^{\varphi}_{i,DG,k}$ and $\Delta Q^{\varphi}_{i,DG,k}$;
- Calculate $Pred_k$, $Ared_k$, and r_k by (18), (19), and (20), respectively.

Step 3. Check convergence.

- Calculate the initial operation point of the next iteration:

$$\mathrm{u}_{k+1} = \begin{cases} \mathrm{u}_k & r_k < 0 \\ \mathrm{u}_k + \Delta \mathrm{u}_k & r_k > 0 \end{cases} \tag{22}$$

- If both $0 < Ared_k < err_1$ and $\| u_k \|_\infty < err_2$ hold, jump to **Step 4**, else continue;
- Solve the power flow **Eq.6** with u_{k+1} and calculate trust region radius of the next iteration by (21);
- Increase the iteration counter by $k = k+1$, then jump to **Step 2**.

Step 4. Acquire the optimal solutions.

- Solve the power flow **Eq. 6** with $\mathbf{u}_{k+1}$, get state variables x_{k+1}, and calculate the optimal objective function by $\mathbf{F}(\mathbf{x}_{k+1}, \mathbf{u}_{k+1})$

4 CASE STUDY

In order to verify the effectiveness of proposed ARPCO method for unbalanced DN, the case study is implemented on the modified IEEE 123 node unbalanced test feeder (Feeders, 1991) employing the MATLAB software. A Newton–Raphson power flow solver is developed, and the LP-based subproblem is modeled and solved in YALMIP (Lofberg, 2004) by the Cplex solver. The hardware environment is Intel i5 @ 3.3 GHz CPU with 4 GB RAM. The OS is win7 64 bit, the MATLAB version is R2015a, the YALMIP version is 20150204, and the Cplex version is 12.6.

4.1 The Modified IEEE 123 Node Test Feeder

The IEEE 123 node unbalanced distribution test feeder is used and modified by installing several distributed PVs, as is shown in **Figure 2**.

The voltage level of the test system is 4.16 kV, and the slack bus (node 1) voltage is set as 1.05 p.u. The total active load is 3,490 kW, while the total reactive load is 1,925 kVar. Due to large load difference up to hundreds of kilowatts among different phases and asymmetric line parameters, the three-phase unbalance is severe in this system. Moreover, it has many zero self-impedance as well as zero mutual-impedance branches and single-phase or two-phase branches; thus, its numerical conditions are very complex.

In the test system, three single-phase PVs whose capacity is 500 kVA are connected to node 27 phase C (PV 27), node 65 phase B (PV 65), and node 101 phase A (PV 101), respectively. Then, two three-phase PVs are installed at node 47 (PV47) and node 114 (PV114), while the capacity of each phase PV is 600 kVA. PV114 is three-phase combined, and the output power of each phase can just be controlled simultaneously. PV47 is three-phase-independent, and the output power of each phase can be controlled independently.

TABLE 1 | Comparison of active and reactive power outputs before and after optimization.

PV generators	Phase	Before optimization		After optimization	
		Active/kW	Reactive/kVar	Active/kW	Reactive/kVar
PV27	C	350	0	350	97.0
	A	400	0	400	259.4
PV47	B	400	0	400	30.4
	C	400	0	400	300
PV65	B	350	0	350	33.8
PV101	A	350	0	350	−32.7
	A	400	0	400	−17.9
PV114	B	400	0	400	−17.9
	C	400	0	400	−17.9

TABLE 2 | Comparison of active power losses before and after optimization.

Loss before optimization (kW)	Loss after optimization (kW)	Reduction ratio (%)
52.3	40.0	23.5

In this study, three typical scenarios are designed with a secure voltage range of all nodes set from 0.95 p.u. to 1.05 p.u. and the reactive power output limitation coefficient α set on 0.5.

4.2 Optimal Reactive Power Allocation for Loss Reduction

In scenario 1, all the PVs operate at the forecasted maximum active power point without the reactive power output before optimization, while all the PVs keep tracking the forecasted maximum active power point with the reactive power output instructed by the proposed strategy after optimization, as is shown in **Table 1**.

Through this study, DGs like PV should undertake more responsibility for the system optimization, such as voltage regulation and loss reduction. Due to three-phase unbalance, the reactive power output differs among three phases, such as PV47, which is more accurate. The active power loss comparison before and after optimization is shown in **Table 2**.

Usually, PV inverters own considerable remaining capability, which can be used as reactive compensators if optimal allocated for loss reduction.

4.3 Voltage Support Under a Heavy Load

In scenario 2, the active power outputs of PVs are set as 0, which shows that the phenomenon occurs during night or cloudy days. The active and reactive load is enlarged by 1.3 times considering load increase in the future. Consequently, severe undervoltage problems would happen. By the ARPCO method, PV inverters are used as reactive compensators to support the system voltage, guaranteeing supply voltage security, as is shown in **Figure 3**.

It can be seen that the voltage magnitude from bus 52 to bus 101 in phase A exceeds the lower voltage secure bound before optimization. In comparison, the voltage magnitude of the whole system is lifted and the voltage of all buses and all phases is kept within the system secure voltage limitation with application of ARPCO. What is more, the voltage rise degree of different

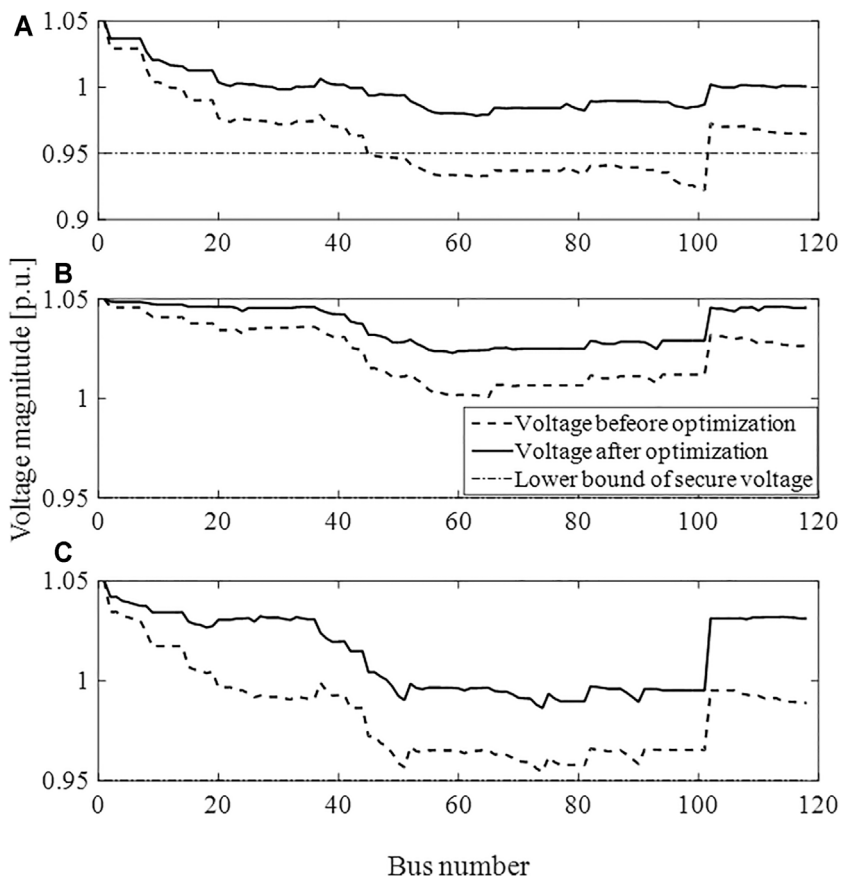

FIGURE 3 | Voltage magnitude comparison between before and after optimization: **(A)** phase A, **(B)** phase B and **(C)** phase C.

TABLE 3 | Relationship between active power loss and maximum reactive compensation capability.

Coefficient α	Loss (kW)	Reduction ratio (%)
0	197.4	—
1/4	160.0	18.94
1/2	148.6	24.74
3/4	146.7	25.63

phases differs from each other because detailed unbalanced models are adopted and all PVs except PV114 could be controlled in the single phase. As a result, unbalanced reactive power compensation schemes are adopted according to the actual situation of each phase and voltage unbalance is alleviated.

The active power losses are also reduced in this scenario. The relationship between the active power loss and maximum reactive compensation capability of each PV inverter quantified by coefficient α is studied, as is shown in **Table 3**.

From **Table 3**, it can be concluded that the bigger reactive compensation capability usually brings bigger active power loss reduction. However, when the system reactive power reserve is adequate, the active power loss improvement is inconspicuous with the increase of reactive power compensation capability. For example, the active power loss decreases only 2.1 kW when the maximum reactive power compensation capability increases from 1/2 of PV capability to 3/4 of PV capability. Therefore, the present load demand, future load increase, and reactive power compensation demand should be taken into comprehensive consideration when determining optimal installation capability of DGs at the planning stage. Also, in this study, reactive power is considered as "free;" thus a more accurate model which quantifies "the price of reactive power" should be included in future work.

4.4 Maximize Active Power Output of DGs When Overvoltage Occurs

In scenario 3, the maximum active power output equals the installation capability for each PV, which generally occurs at noon. If all the PVs keep on the MPPT mode, the inverters retain no reactive power supply and severe overvoltage happens due to voltage rise caused by high power injection of PVs. To keep DN secure, either certain voltage regulators

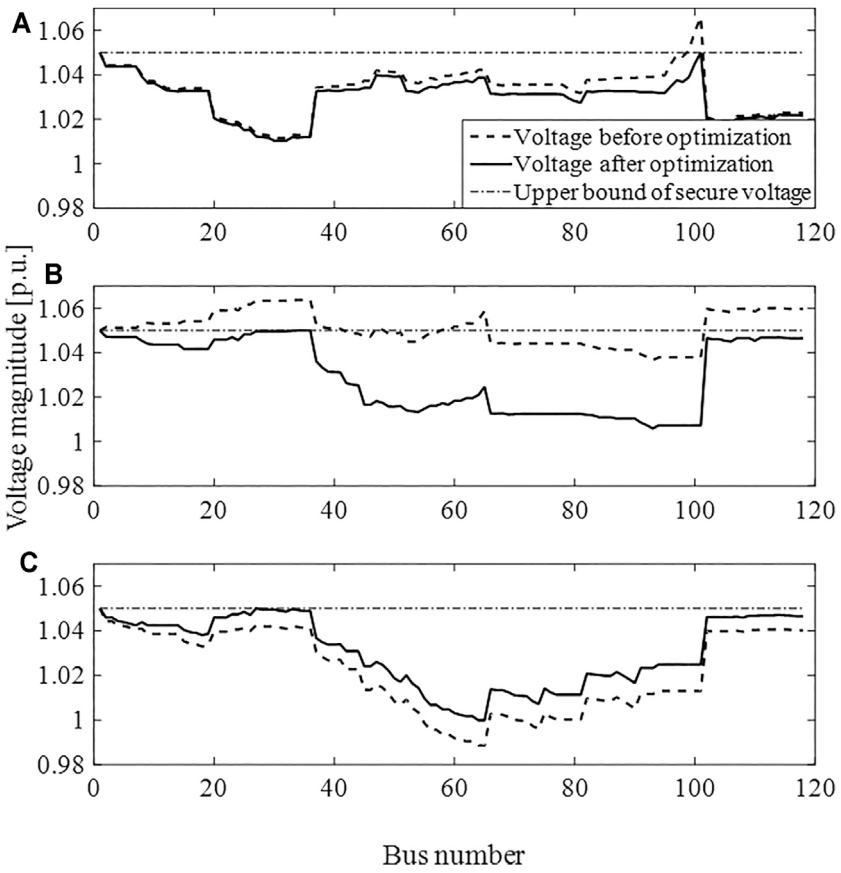

FIGURE 4 | Voltage magnitude comparison between before and after optimization: **(A)** phase A, **(B)** phase B and **(C)** phase C.

TABLE 4 | Active power output comparison among different strategies.

PV generators	Phase	Active power output		
		Maximum (kW)	Coordinated (kW)	Maximum (kW)
PV27	C	500	486	316
	A	600	600	600
PV47	B	600	536	20
	C	600	600	600
PV65	B	500	492	500
PV101	A	500	476	500
	A	600	600	600
PV114	B	600	600	600
	C	600	600	600

TABLE 5 | Relationship between active power loss and maximum reactive compensation capability.

Coefficient α	Iteration times/CPU time		
	Trust region	Δ = 0.001	Δ = 0.0002
Scenario 1	14/6.32 s	33/16.67 s	134/66.15 s
Scenario 2	16/7.20 s	oscillatory	105/56.65 s
Scenario 3	9/4.15 s	63/32.69 s	311/143.61 s

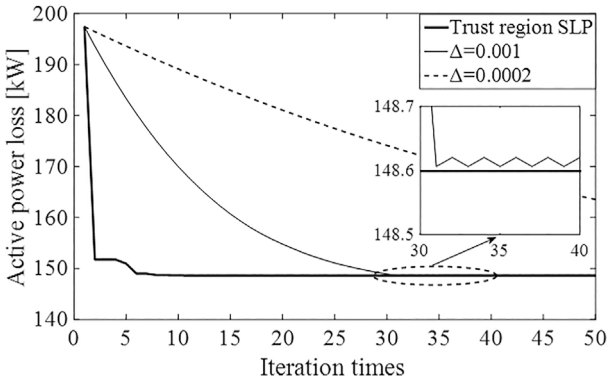

FIGURE 5 | Active power loss variation in scenario 2.

should be installed, such as OLTC, CBs, and SVCs, or the active output of the PVs should be curtailed. By the proposed APRCO, the active power output of the PVs is maximized, that is, PV curtailment is minimized, to limit the voltage magnitude within the allowable range, needless for extra devices.

As is shown in **Figure 4**, severe overvoltage happens especially in phase B due to PV power injection. Employing the ARPCO, the voltages of all buses are regulated within the allowable range. Moreover, the voltage unbalance is alleviated, while the voltage in phases A and B drops with the voltage in phase C rises slightly. This is because the ARPCO model is constructed with consideration of high coupling between the three phases.

As the active power and reactive power output of PVs are optimized simultaneously, there is more PV active power absorbed by DN than the active power curtailment method, as shown in **Table 4**.

As shown in **Table 4**, PV27 needs to curtail 14 kW, PV47 needs to curtail 64 kW, PV 65 needs to curtail 8 kW, and PV101 needs to curtail 24 kW by APRCO. In contrast, at least 764 kW needs to be curtailed if only the active power curtailment method is employed. Then, there are about 7 times renewable energy source waste in the traditional active power curtailment method compared to APRCO.

4.5 Computational Performance Analysis

To validate effectiveness of the proposed trust region SLP method, computational analysis is done toward the proposed trust region SLP and two basic SLP methods with fixed step sizes of 0.001 and 0.0002 apparently in the aforementioned three scenarios. The convergence accuracy is set on err1 = 10-6 and err2 = 2 × 10-3 apparently. The result is given in **Table 5**.

The proposed trust region SLP method performs better in terms of both convergence speed and convergence accuracy. This is because the self-adaptive step size overcomes the conflict between speed and accuracy. When the fixed step size is adopted, either the convergence speed or the convergence accuracy is low. For example, a step size of 0.001 convergences much faster than 0.0002, while it fails to converge in scenario 2. Also, the convergence progress of scenario 2 by different methods is analyzed in **Figure 5**.

It can be inferred from **Figure 5** that trust region SLP converges much faster than the two SLPs with a fixed step size. When choosing Δ = 0.0002, it still has not converged after 50 iterations, while it starts to oscillate after about 30 iterations when choosing Δ = 0.001.

5 CONCLUSION

In order to fulfill the demand of operating radial and looped unbalanced DN with increasing penetration of DGs, a unified

ARPCO model is established and a trust region SLP method is proposed to solve the constructed nonlinear and nonconvex models in this paper. The multi-scenario case study based on the modified IEEE 123 node test feeder shows that (1) active power loss could be reduced and overvoltage as well as undervoltage problems could be restrained by coordinated optimization of DGs' active and reactive power output; thus, it increases the ability of DN absorbing DGs; (2) the proposed trust region SLP method preforms well in both aspects of convergence speed and computational accuracy, superior to the fixed step SLP method. Meanwhile, it can satisfy the online optimization requirement of unbalanced DN incorporating a large amount of DGs.

DATA AVAILABILITY STATEMENT

The original contributions presented in the study are included in the article/supplementary material; further inquiries can be directed to the corresponding author.

AUTHOR CONTRIBUTIONS

YZ: APRCO model construction, trust region SLP algorithm development, and writing the paper. YW: DG model construction and programming. PL: literature review and APRCO model construction.

REFERENCES

Barr, J., and Majumder, R. (2014). Integration of Distributed Generation in the Volt/VAR Management System for Active Distribution Networks. *IEEE Trans. Smart Grid* 6 (2), 274–284. doi:10.1109/TSG.2014.2363051

Basu, M. (2016). Quasi-oppositional Differential Evolution for Optimal Reactive Power Dispatch. *Int. J. Electr. Power Energ. Syst.* 78, 29–40. doi:10.1016/j.ijepes.2015.11.067

Calderaro, V., Galdi, V., Lamberti, F., and Piccolo, A. (2014). A Smart Strategy for Voltage Control Ancillary Service in Distribution Networks. *IEEE Trans. Power Syst.* 30 (1), 494–502. doi:10.1109/TPWRS.2014.2326957

Chen, S. X., Foo, Y. S. E., Gooi, H. B., Wang, M. Q., and Lu, S. F. (2015). A Centralized Reactive Power Compensation System for LV Distribution Networks. *IEEE Trans. Power Syst.* 30 (1), 274–284. doi:10.1109/tpwrs.2014.2326520

D'Adamo, C., Jupe, S., and Abbey, C. (2009). "Global Survey on Planning and Operation of Active Distribution Networks-Update of CIGRE C6. 11 Working Group Activities," in Proc. 20th Int. Conf. and Exhibition on Electricity Distribution: -Part 1, Prague, Czech, 8-11 June 2009, 1–4. doi:10.1049/cp.2009.0836

Daratha, N., Das, B., and Sharma, J. (2014). Coordination between OLTC and SVC for Voltage Regulation in Unbalanced Distribution System Distributed Generation. *IEEE Trans. Power Syst.* 29 (1), 289–299. doi:10.1109/tpwrs.2013.2280022

Eftekharnejad, S., Vittal, V., Heydt, G. T., Keel, B., and Loehr, J. (2013). Impact of Increased Penetration of Photovoltaic Generation on Power Systems. *IEEE Trans. Power Syst.* 28 (2), 893–901. doi:10.1109/tpwrs.2012.2216294

Farivar, M., Neal, R., and Clarke, C. (2012). "Optimal Inverter Var Control in Distribution Systems with High PV Penetration," in IEEE Power and Energy Society General Meeting, San Diego, CA, USA, 22-26 July 2012, 1–7. doi:10.1109/PESGM.2012.6345736

Feeders, R. (1991). IEEE Distribution Planning Working Group Report. *IEEE Trans. Power Syst.* 6 (3), 975–985. 10.1109/59.119237.

Gao, H., Liu, J., and Wang, L. (2018). Robust Coordinated Optimization of Active and Reactive Power in Active Distribution Systems. *IEEE Trans. Smart Grid* 9 (5), 4436–4447. doi:10.1109/tsg.2017.2657782

Gomez-Gonzalez, M., López, A., and Jurado, F. (2012). Optimization of Distributed Generation Systems Using a New Discrete PSO and OPF. *Electric Power Syst. Res.* 84 (1), 174–180. doi:10.1016/j.epsr.2011.11.016

Kamh, M. Z., and Iravani, R. (2010). Unbalanced Model and Power-Flow Analysis of Microgrids and Active Distribution Systems. *IEEE Trans. Power Deliv.* 25 (4), 2851–2858. doi:10.1109/tpwrd.2010.2042825

Kekatos, V., Zhang, L., Giannakis, G. B., and Baldick, R. (2016). Voltage Regulation Algorithms for Multiphase Power Distribution Grids. *IEEE Trans. Power Syst.* 31 (5), 3913–3923. doi:10.1109/tpwrs.2015.2493520

Kulmala, A., Repo, S., and Jarventausta, P. (2014). Coordinated Voltage Control in Distribution Networks Including Several Distributed Energy Resources. *IEEE Trans. Smart Grid* 5 (4), 2010–2020. doi:10.1109/tsg.2014.2297971

Lemkens, K., Geth, F., Vingerhoets, P., and Deconinck, G. (2013). "Reducing Overvoltage Problems with Active Power Curtailment—Simulation Results," in IEEE PES ISGT Europe 2013, Lyngby, Denmark, 6-9 Oct. 2013, 1–5. doi:10.1109/ISGTEurope.2013.6695298

Li, P., Wu, Z., Wang, Y., Dou, X., Hu, M., and Hu, J. (2018). Adaptive Robust Optimal Reactive Power Dispatch in Unbalanced Distribution Networks with High Penetration of Distributed Generation. *IET Generation, Transm. Distribution* 12 (6), 1382–1389. doi:10.1049/iet-gtd.2017.0674

Li, P., Zhang, C., Wu, Z., Xu, Y., Hu, M., and Dong, Z. (2020). Distributed Adaptive Robust Voltage/var Control with Network Partition in Active Distribution Networks. *IEEE Trans. Smart Grid* 11 (3), 2245–2256. doi:10.1109/tsg.2019.2950120

Lofberg, J. (2004). "YALMIP: 'A Toolbox for Modeling and Optimization in MATLAB'," in IEEE International Symptom Computer Aided Control Systems Design, Taipei, Taiwan, 2-4 Sept. 2004, 284–289. doi:10.1109/cacsd.2004.1393890

Mohapatra, A., Bijwe, P. R., and Panigrahi, B. K. (2013). Efficient Sequential Non-linear Optimal Power Flow Approach Using Incremental Variables. *IET Generation, Transm. Distribution* 7 (12), 1473–1480. doi:10.1049/iet-gtd.2012.0750

Moradi, M. H., and Abedini, M. (2012). A Combination of Genetic Algorithm and Particle Swarm Optimization for Optimal DG Location and Sizing in Distribution Systems. *Int. J. Electr. Power Energ. Syst.* 34 (1), 66–74. doi:10.1016/j.ijepes.2011.08.023

Mostafa, H. A., El-Shatshat, R., and Salama, M. M. A. (2013). Multi-objective Optimization for the Operation of an Electric Distribution System with a Large Number of Single Phase Solar Generators. *IEEE Trans. Smart Grid* 4 (2), 1038–1047. doi:10.1109/tsg.2013.2239669

Nguyen, H. (1997). Newton-raphson Method in Complex Form Power System Load Flow Analysis. *IEEE Trans. Power Syst.* 12 (3), 1355–1359. doi:10.1109/59.630481

Olofsson, M., Andersson, G., and Soder, L. (1995). Linear Programming Based Optimal Power Flow Using Second Order Sensitivities. *IEEE Trans. Power Syst.* 10 (3), 1691–1697. doi:10.1109/59.466472

Omar, R., and Rahim, N. A. (2012). Voltage Unbalanced Compensation Using Dynamic Voltage Restorer Based on Supercapacitor. *Int. J. Electr. Power Energ. Syst.* 43 (1), 573–581. doi:10.1016/j.ijepes.2012.05.015

Palma-Behnke, R., Vargas, L. S., Perez, J. R., Nunez, J., and Torres, R. A. (2004). OPF with SVC and UPFC Modeling for Longitudinal Systems. *IEEE Trans. Power Syst.* 19 (4), 1742–1753. doi:10.1109/tpwrs.2004.836260

Powell, M., and Yuan, Y. (1990). A Trust Region Algorithm for equality Constrained Optimization. *Math. Programming* 49 (1), 189–211. doi:10.1007/bf01588787

Schweickardt, G., Alvarez, J. M. G., and Casanova, C. (2016). Metaheuristics Approaches to Solve Combinatorial Optimization Problems in Distribution Power Systems. An Application to Phase Balancing in Low Voltage Three-phase Networks. *Int. J. Electr. Power Energ. Syst.* 76, 1–10. doi:10.1016/j.ijepes.2015.09.023

Tonkoski, R., Lopes, L. A. C., and El-Fouly, T. H. M. (2011). Coordinated Active Power Curtailment of Grid Connected PV Inverters for Overvoltage Prevention. *IEEE Trans. Sustain. Energ.* 2 (2), 139–147. doi:10.1109/tste.2010.2098483

Tonkoski, R., Turcotte, D., and EL-Fouly, T. H. M. (2012). Impact of High PV Penetration on Voltage Profiles in Residential Neighborhoods. *IEEE Trans. Sustain. Energ.* 3 (3), 518–527. doi:10.1109/tste.2012.2191425

Wang, S., Han, L., and Wu, L. (2015). Uncertainty Tracing of Distributed Generations via Complex Affine Arithmetic Based Unbalanced Three-phase Power Flow. *IEEE Trans. Power Syst.* 30 (6), 3053–3062. doi:10.1109/tpwrs.2014.2377042

Wang, Z., Chen, H., Wang, J., and Begovic, M. (2014). Inverter-less Hybrid Voltage/var Control for Distribution Circuits with Photovoltaic Generators. *IEEE Trans. Smart Grid* 5 (6), 2718–2728. doi:10.1109/tsg.2014.2324569

Wu, H., Huang, C., Ding, M., Zhao, B., and Li, P. (2017). Distributed Cooperative Voltage Control Based on Curve-Fitting in Active Distribution Networks. *J. Mod. Power Syst. Clean. Energ.* Vol. 5 (5), 777–786. doi:10.1007/s40565-016-0236-1

Yan, R., and Saha, T. K. (2012). Voltage Variation Sensitivity Analysis for Unbalanced Distribution Networks Due to Photovoltaic Power Fluctuations. *IEEE Trans. Power Syst.* 27 (2), 1078–1089. doi:10.1109/tpwrs.2011.2179567

Yuan, Y.-x. (2015). Recent Advances in Trust Region Algorithms. *Math. Program* 151 (1), 249–281. doi:10.1007/s10107-015-0893-2

Zhang, C., Xu, Y., Dong, Z., and Ravishankar, J. (2019). Three-stage Robust Inverter-Based Voltage/var Control for Distribution Networks with High-Level PV. *IEEE Trans. Smart Grid* 10 (1), 782–793. doi:10.1109/tsg.2017.2752234

Zheng, W., Wu, W., Zhang, B., Sun, H., and Liu, Y. (2016). A Fully Distributed Reactive Power Optimization and Control Method for Active Distribution Networks. *IEEE Trans. Smart Grid* 7 (2), 1021–1033.

Conflict of Interest: Author YW is employed by State Grid Jiangsu Electric Power Co., Ltd.

The remaining authors declare that the research was conducted in the absence of any commercial or financial relationships that could be construed as a potential conflict of interest.

Publisher's Note: All claims expressed in this article are solely those of the authors and do not necessarily represent those of their affiliated organizations or those of the publisher, the editors, and the reviewers. Any product that may be evaluated in this article or claim that may be made by its manufacturer is not guaranteed or endorsed by the publisher.

frontiers in Energy Research

ORIGINAL RESEARCH
published: 16 March 2022
doi: 10.3389/fenrg.2022.841269

Control Strategy of Distributed Energy Micro-Grid Involving Distribution System Resilience

Jun Wu[1], *Rui Qiu*[1]*, *Mingyue Wang*[2], *Rui Han*[1], *Wenxin Huang*[1] *and Zihui Guo*[1]

[1]School of Electrical Engineering and Automation, Wuhan University, Wuhan, China, [2]School of Electronic Information and Electrical Engineering, Shanghai Jiao Tong University, Shanghai, China

To realize low-carbon energy systems, distributed energy storage systems and flexible loads have been integrated into power grids. System reliability, economy, and resilience, therefore, face significant challenges. This article presents modeling of a distributed energy micro-grid including wind turbines, micro gas turbines, waste heat recovery devices, electric boilers, direct-fired boilers, battery energy storage, interruptible loads, and transferable loads. At the same time, the optimal configuration of energy storage and the demand-side response modeling are studied, and the combined optimization control strategy of the two is demonstrated. The simulation results indicate that the proposed control strategy has better performance than the traditional operation. In addition, this article also clarifies the impact of control strategy on distribution system resilience. The results show that the control strategy proposed in this article can achieve the resource complementarity of demand-side response and energy storage, and realize the integrated coordination of source, network, load, and storage. The distributed energy micro-grid under this control strategy has the best overall economic benefit and the best capacity to accommodate load growth.

Keywords: distributed energy micro-grid, demand-side response, battery storage, network modeling, distribution system resilience

OPEN ACCESS

Edited by:
Hantao Cui,
Oklahoma State University,
United States

Reviewed by:
Qiwei Zhang,
the University of Tennessee, Knoxville,
United States
Guodong Liu,
Oak Ridge National Laboratory (DOE),
United States

***Correspondence:**
Rui Qiu
1259015932@qq.com

Specialty section:
This article was submitted to Smart Grids, a section of the journal Frontiers in Energy Research

Received: *22 December 2021*
Accepted: *11 January 2022*
Published: *16 March 2022*

Citation:
Wu J, Qiu R, Wang M, Han R, Huang W and Guo Z (2022) Control Strategy of Distributed Energy Micro-Grid Involving Distribution System Resilience. Front. Energy Res. 10:841269. doi: 10.3389/fenrg.2022.841269

INTRODUCTION

It has been extensively reported that distributed renewable energy power generation technology provides useful solutions to the energy crisis and excessive carbon emissions (Iqbal and Siddiqui, 2017). However, the direct connection between distributed renewable energy units and distribution networks will affect the original power flow distribution status and short-circuit current characteristics (Zho et al., 2021). The uncertainty of renewable energy is likely to cause problems in the reliability of the energy supply, leading to the reconfiguration of protection and control systems (Tian et al., 2020). A distributed energy micro-grid is a good solution to these problems. The United States Electrical Reliability Technical Measures Solutions Association and the European Union Micro-grid Project define a micro-grid (Muhammad Arif et al., 2020) as a small energy system composed of distributed units, loads, energy storage, power electronic devices, communication equipment, power transmission lines, and other facilities. It supplies users with energy such as cooling, heating, and electricity and can be regarded as a unified and schedulable whole. The distributed energy micro-grid is mainly divided into two types according to the operation mode: grid-connected and independent (Wenwu et al., 2018). The independent micro-grid has a weak connection with the utility grid. Because of its small scale and great sensitivity to uncertain

factors, it has high requirements on flexible resource utilization, operating economy, and energy supply reliability. With the help of the independent micro-grid, it is possible to supply loads in areas far from the utility grid such as mountainous areas, islands, offshore oil platforms, etc. Besides, it can achieve complementary coordination of cooling, heating, and electricity. This micro-grid can bring superior social benefits (FENG et al., 2020). Therefore, it is of great significance to study the modeling of distributed energy micro-grid and explore how to establish a control strategy for fully and flexibly calling toward the various resources in the micro-grid, which makes the micro-grid better in operational reliability, economy, and resilience.

Power system resilience is an important criterion to assess the ability of a system to adapt and recover from the significant power outages caused by accidents, deliberate attacks, or natural disasters. During this period, electric utilities desire to serve as much load as possible and to minimize the penalty cost for load shedding, which is a critical measure of distribution system resilience (Ma et al., 2018). There are approaches to enhance resilience, one of them is to increase the penetration of distributed energy resources (Shi et al., 2020). For some areas, rapid load growth is also a threat to system resilience. Therefore, studying the impact of a distributed energy system on load growth after adopting a control strategy can reflect the impact on system resilience. The operation of a micro-grid requires the support of various resources that can be flexibly invoked. In terms of power supply, the scheduling technology for conventional units has matured. However, problems such as uncertain output and wind abandonment still exist. As far as energy load, demand-side response (DR) resources can be flexibly invoked, and the DR technology enables both sides of supply and demand to participate in the optimal scheduling simultaneously. Qi et al. (2021) proposed a scheduling strategy that considers DR classification and segmented participation in multi-timescale source–load coordination. This method can effectively reduce the cost of scheduling operations and promote the utilization of renewable energy. Duan (2016) introduced a price-based demand bidding mechanism, which effectively stabilizes load fluctuations in dispatch. This bidding mechanism brings the surplus adjustable capacity to the source side and increases the social welfare of the power system. China has already implemented guidelines and interface standards for power systems and DR technology. Nonetheless, large-scale and automatic DR cannot be carried out with the limitation of imperfect policies and regulations (Zhang et al., 2014). Meanwhile, the personalized demand on the load side prevents excessive interference in energy usage upon scheduling. Therefore, only a few loads can participate in DR. When considering DR in the process of optimizing operation, it is necessary to arrange an appropriate load response plan to achieve a win–win situation between supply and demand. In addition, energy storage has attracted attention due to its advantages including bidirectional power flow, energy transfer across time, and low environmental impact. The configurations of electric energy storage and power control in the micro-grid can resolve uncertainties and improve the reliability of the energy supply (Bahramirad et al., 2012). Hajipour et al. (2015) carried out a micro-grid electric energy storage plan based on the Monte Carlo method. This plan proved that electric energy storage can effectively handle uncertain factors and possess economic competitiveness. Ding et al. (2011) adopted a new type of battery to optimize the operation of the micro-grid. This type of energy storage has a special operating environment and high management costs, and it has little effect on the cost cutting of the micro-grid operation. Considering the high cost and environmental pollution, it is important to configure electrical energy storage rationally before optimizing an operation. In the process of optimizing the configuration of energy storage, the complementation of resources in the distributed energy micro-grid should be considered. At this time, considering DR is expected to make the plan more economical and has better operating performance. Tao et al. (2017) employed variable participation frequency to control refrigerator temperature control load and optimized the configuration of electric energy storage based on the probability planning method. The results demonstrated that the DR resource can partially replace the electric energy storage and improve the economics of the micro-grid. Shi (2018) optimized the dual-layer configuration of wind power and energy storage with the load transfer, translation, and reduction being considered. The result proved that the proposed DR method can cut operating costs, improve power supply reliability, and reduce the configuration requirements for electrical energy storage.

Existing research does not comprehensively consider factors such as reservation of conventional units, thermal power compensation, and waste heat depletion of the combined heat and power (CHP) system or clarify the impact on distribution system resilience. Based on the establishment of a distributed energy micro-grid model, the control strategy introduced in this article explores the abovementioned problems. The strategy uses the integrated time series of typical days in the four seasons and the idea of cost discounting to optimize the configuration of energy storage. It also implements the flexible deployment of multiple resources such as conventional units, wind turbines, DR, and electrical energy storage in multiple time nodes. In the process of energy storage configuration optimization, this article compares the difference between whether to involve DR. The results show that involving DR is beneficial to reduce energy storage configuration capacity. This article creates four combination modes of DR and energy storage, and the control model is solved by GAMS to minimize the accumulative cost for dispatchable DER operation. According to the results, the operational reliability, economy, and interference to energy consumption behavior of the four modes are compared. Calculations are performed to illustrate the impact on distribution system resilience. This article reveals a control strategy that comprehensively considers reservation of conventional units, thermal power compensation, waste heat depletion of the combined heat and power system, optimal configuration of energy storage and the DR, and the impact on distribution system resilience. The strategy shows good performance in promoting the integrated coordination of source, network, load, and storage of a distributed energy micro-grid, improving the reliability of energy supply, cutting operating costs, reducing the interference to energy consumption,

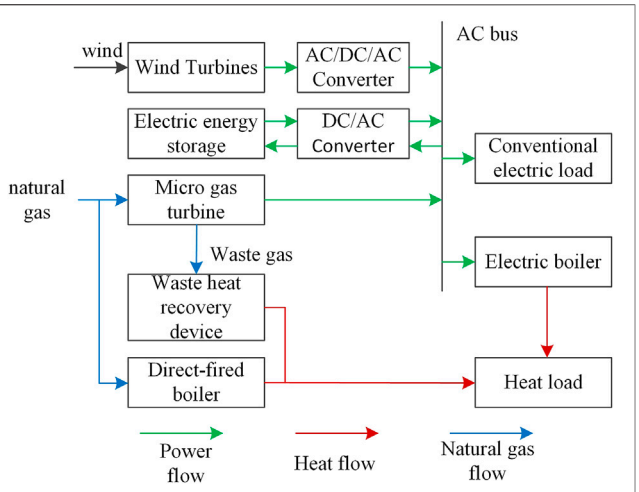

FIGURE 1 | Schematic diagram of an isolated combined heat and power micro-grid.

increasing system resilience, and advocating a way to guide the planning of work in areas with a high load growth rate.

RESOURCE MODELING IN INDEPENDENT MICRO-GRID

Main Structure of Independent Micro-Grid

The main structure of a CHP-independent micro-grid is shown in **Figure 1**. The micro gas turbine is a gas–electric coupling device. The waste heat recovery device is a gas–heat coupling device. The direct-fired boiler is a gas–heat coupling device, and the electric boiler is an electric–heat coupling device. The electric load is divided into conventional electric load and electric boiler. Both conventional electric load and heat load participates in DR partly. The electric energy storage is treated as an electric energy transfer station.

Unit Modeling

The mathematical models of conventional controllable distributed thermal power units such as micro gas turbines and waste heat recovery devices, electric boilers, and direct-fired boilers are given in **Supplementary Appendix** (Tao et al., 2017). And the active power output characteristics of wind turbines can be found in the **Supplementary Appendix** (Shi, 2018).

DR Resources

The current DR strategy is mainly composed of price type and incentive type (Luo et al., 2020). The price-based DR uses a pricing mechanism to guide users to respond to changes in energy supply prices actively. Incentive DR signs an agreement between the energy supply side and the user side and grants subsidies to users to obtain direct load management rights. The real-time power balance of the system is maintained by invoking interruptible and transferable loads and other resources. The agreement routinely stipulates the limit on the number of loads participating in DR and other factors. Compared with the price-based DR, incentive type one has a shorter response time, more flexible method, and more obvious effect. The subsidy paid in this way is smaller than the penalty fee caused by load shedding, which is beneficial to cutting operating costs. In this article, the independent micro-grid does not involve electronic transactions with the utility grid. The user-side information is not transparent. The responses under the price-based DR cannot be certainly described and is difficult to be reflected in the optimization model. Therefore, the incentive-based DR is selected. Taking into account the incentive-type DR, the electric and heat load components are decomposed as in **Eqs 1**, **2**:

$$P_{\mathrm{ldr}}(i,t) = P_{\mathrm{ld}}(i,t) + P_{\mathrm{in}}(i,t) - P_{\mathrm{out}}(i,t) - P_{\mathrm{itr}}(i,t) - P_{\mathrm{lsh}}(i,t) \tag{1}$$

$$Q_{\mathrm{ldr}}(i,t) = Q_{\mathrm{ld}}(i,t) + Q_{\mathrm{in}}(i,t) - Q_{\mathrm{out}}(i,t) - Q_{\mathrm{itr}}(i,t) - Q_{\mathrm{lsh}}(i,t), \tag{2}$$

where

$P_{\mathrm{ld}}(i,t)$ is active power load at node i before DR is implemented in time period t,
$P_{\mathrm{ldr}}(i,t)$ is active power load at node i after DR is implemented in time period t,
$P_{\mathrm{in}}(i,t)$ is active power load planned to be moved in,
$P_{\mathrm{out}}(i,t)$ is active electrical load planned to be removed,
$P_{\mathrm{itr}}(i,t)$ is active power load planned to be interrupted,
$P_{\mathrm{lsh}}(i,t)$ is active electrical load cut off outside the agreement, and
Q represents the heat load, where the subscripts have the same meaning as those mentioned above, and the units of the above load items are all kW.

Electric Energy Storage

Electric energy storage is mainly divided into power type and energy type according to their technical characteristics. As far as the independent micro-grid optimization, the main consideration is the energy-type electric energy storage possessing high energy density. Pumped water storage and compressed air energy storage are not commonly used due to the constriction of resource and geographical conditions. Battery storage (BS) has been widely used in modern power systems owing to its characteristics of commercialization and large-scale energy storage. For example, BS can be used for the operating power supply of power plants and substations or as the backup energy of AC uninterrupted power supply (Zhu et al., 2014). Recently, the performance of BS has been improved, and the cost has declined. With rational configuration, its technical benefits and economic investment can be balanced. Therefore, we selected BS to form an electric energy storage system and involved the flexible invocation of BS resources in the independent micro-grid optimal scheduling.

For BS unit b, the main technical parameters are as follows: rated capacity $E_{\max}(b)$ (kWh), self-discharge rate σ (h^{-1}), charging efficiency $\eta_{\mathrm{c}}(b)$, discharge efficiency $\eta_{\mathrm{d}}(b)$, maximum state of charge $SOC^{\max}(b)$, minimum state of charge $SOC^{\min}(b)$, maximum charging power $P_{\mathrm{c}}^{\max}(b)$ (kW), maximum discharge power $P_{\mathrm{d}}^{\max}(b)$ (kw), set unit b with power in time period t as

$E(b,t)$ (kW), external charging power for unit b $P_c(b,t)$ (kW), and external discharge power of unit b $P_d(b,t)$ (kW). The definition and calculation of the state of charge in the time period t are shown in **Eqs 3**, **4**, respectively.

$$SOC(b,t) = \frac{E(b,t)}{E_{\max}(b)}, \tag{3}$$

$$SOC(b,t) = (1-\sigma)SOC(b,t-1) + \left[\frac{P_c(b,t)\eta_c(b) - P_d(b,t)/\eta_d(b)}{E_{\max}(b)}\right], \tag{4}$$

OPTIMIZATION MODEL

Cost Calculation

1) Total cost of independent micro-grid operating expenses:

The calculation of the total cost of independent micro-grid operating expenditures within the simulation duration C_{total} (Yuan) can be calculated by **Eq. 5**:

$$C_{\text{total}} = C_{\text{cw}} - C_{\text{uw}} + C_{\text{ss}} + C_{\text{gas}} + C_{\text{CO}_2} + C_{\text{op}} + C_{\text{ld}} + C_{\text{DR}}, \tag{5}$$

where

C_{cw} is wind abandonment penalty cost (Yuan),
C_{uw} is consumption of wind power subsidies (Yuan),
C_{ss} is operating cost of micro gas turbine switch (Yuan),
C_{gas} is sum of fuel costs of micro gas turbines and direct-fired boilers (Yuan),
C_{CO_2} is cost of treating carbon dioxide released by micro gas turbines and direct-fired boilers (Yuan),
C_{op} is operation and management cost of conventional controllable distributed thermal power unit (Yuan),
C_{ld} is load shedding penalty cost (including heat load and electric load) (Yuan), and
C_{DR} is cost of DR subsidies (Yuan).

The specific calculation formula of the above variables are given in **Supplementary Appendix**.

C_{total} involves various cost items that reflect the economics, environmental protection, and power supply reliability of an independent micro-grid operation.

2) Cost of BS configuration conversion:

The calculation of the cost of optimizing the configuration of the BS converted to the value C_{bat} (Yuan) within the simulation duration is shown in **Eq. 6**:

$$C_{\text{bat}} = K_{\text{bat}} \sum_{i=1}^{N_{\text{Bus}}} N_{\text{BS}}(i), \tag{6}$$

where

K_{bat} is the investment of a BS unit, which is converted to the value within the simulation duration considering the idea of cost discounting [Yuan/(quantity × simulation time length)], and

$N_{\text{BS}}(i)$ is the number of BS units at node i.

Constraints

3) The switch state of the micro-gas turbine and action variable constraints can be found in Yun et al. (2020), and the specific computational formulas are provided in the **Supplementary Appendix**.
4) The upper and lower limits of the active output of the micro gas turbine:

Standby is the additional unit capacity of the power system to ensure safe and stable operation when the power system is subject to uncertain factors. The adjusted reserve is used to balance the forecast error of the wind turbine output, and the spinning reserve is used to deal with accidents. The upper and lower limits of the active power output of the micro gas turbine are shown in **Eq. 7**:

$$\begin{aligned} P_{\text{CG}}(m,t) &\le u(m,t)\left[P_{\text{CG}}^{\max}(m) - R_{CG}(m,t) - S_{CG}(m,t)\right] \\ P_{\text{CG}}(m,t) &\ge u(m,t)\left[P_{\text{CG}}^{\min}(m) + R_{CG}(m,t)\right], \end{aligned} \tag{7}$$

where $P_{\text{CG}}^{\min}(m)$ is the minimum active power output of gas turbine (kW), $P_{\text{CG}}^{\max}(m)$ is the maximum active power output of gas turbine (kW), $u(m,t)$ is the switch machine state 0-1 variable in time period t, $R_{CG}(m,t)$ is the adjust reserve capacity (kW), and $S_{CG}(m,t)$ is the spinning reserve capacity (kW).

5) The climbing constraints of micro gas turbines are detailed in the **Supplementary Appendix**.
6) The upper and lower limits of the power of the electric boiler and the heating power of the direct-fired boiler are given in the **Supplementary Appendix**.
7) The actual active power output of the wind turbine and the wind curtailment power constraints are given in the **Supplementary Appendix**.
8) The load shedding power constraints are given in **Eqs 8**, **9**:

$$0 \le Q_{\text{lsh}}(i,t) \le R_{\text{lsh}}^{\text{H}} Q_{\text{ld}}(i,t), \tag{8}$$

$$0 \le P_{\text{lsh}}(i,t) \le R_{\text{lsh}}^{\text{E}} P_{\text{ld}}(i,t), \tag{9}$$

where $R_{\text{lsh}}^{\text{H}}$ is the coefficient of the heat load that the node allows to remove, $R_{\text{lsh}}^{\text{E}}$ is the coefficient of the electric load that the node allows to remove, $Q_{\text{ld}}(i,t)$ is the node heat load, and $P_{\text{ld}}(i,t)$ is the node electric load.

9) The DC power flow constraints are provided in the **Supplementary Appendix**. The independent micro-grid in this work has less load and the phenomenon of branch power flow exceeding the limit is not easy to occur. Thus, only the direct current wave is considered, and this can meet the requirements for the electric network part.
10) Constraints in DR:

(a) The upper and lower limits of interruptible and transferable load are given in **Eqs 10**–**15**:

$$0 \le Q_{\text{itr}}(i,t) \le R_{\text{itr}}^{\text{H}} Q_{\text{ld}}(i,t), \tag{10}$$

$$0 \le P_{\text{itr}}(i,t) \le R_{\text{itr}}^{\text{E}} P_{\text{ld}}(i,t), \tag{11}$$

$$0 \le Q_{\text{in}}(i,t) \le R_{\text{sft}}^{\text{H}} Q_{\text{ld}}(i,t), \tag{12}$$

$$0 \le P_{\text{in}}(i,t) \le R_{\text{sft}}^{\text{E}} P_{\text{ld}}(i,t), \tag{13}$$

$$0 \le Q_{\text{out}}(i,t) \le R_{\text{sft}}^{\text{H}} Q_{\text{ld}}(i,t), \tag{14}$$

$$0 \le P_{\text{out}}(i,t) \le R_{\text{sft}}^{\text{E}} P_{\text{ld}}(i,t), \tag{15}$$

where $R_{\text{itr}}^{\text{H}}$ is the ratio of the maximum interruptible heat load of a node to the original load, $R_{\text{itr}}^{\text{E}}$ is the ratio of the maximum interruptible electric load of a node to the original load, $R_{\text{sft}}^{\text{H}}$ is the ratio of the maximum transferable heat load of a node to the original load, and $R_{\text{sft}}^{\text{E}}$ is the ratio of the maximum transferable electric load of a node to the original load.

(b) Interruption duration constraint of the interruptible load is given by:

$$T_{\text{d}}(i) \le T_{\text{d max}}(i), \tag{16}$$

where

$T_{\text{d max}}(i)$ is the upper limit of the interruption duration allowed by the node each time.

(c) Constraint on the total number of cut offs of interruptible loads is given by:

$$\sum_{\text{t}=1}^{N} U(i,t) \triangle T \Big/ T_d(i) \le \text{y}(i), \tag{17}$$

where $\text{y}(i)$ is the total number of interruptions allowed by the node per day.

(d) Interruption time interval constraint of the interruptible load is given by:

$$\sum_{\text{t}}^{\text{t}+n(\text{i})} V(i,t) \le 1, \tag{18}$$

where $\text{n}(i)$ is the minimum value of the time interval between the two load cut off of the node, and $\text{V}(i,t)$ is the 0–1 variable that indicates whether the node is interrupted during the t period.

(e) Constraints of transferable load balance

It is assumed that the transferable load needs to be met within 1 day to control the impact of load movement on users. Then, the total load moved in by a node in 1 day should equal the total load moved out by the node:

$$\begin{gathered} \sum_{t=24(l-1)+1}^{24l} Q_{\text{in}}(i,t) = \sum_{t=24(l-1)+1}^{24l} Q_{\text{out}}(i,t) \\ \sum_{t=24(l-1)+1}^{24l} P_{\text{in}}(i,t) = \sum_{t=24(l-1)+1}^{24l} P_{\text{out}}(i,t) \\ \forall i = 1,\ldots,N_{\text{Bus}}; \forall l = 1,\ldots,L, \end{gathered} \tag{19}$$

where L is the number of days included in the simulation duration.

11) BS operation constraints:

Assuming that the parameters of all BS units are the same and that the initial state of charge and charging and discharging behaviors of the BS units of the same node are consistent, the constraints that need to be met by the BS unit group of a node can be listed as follows:

(a) The upper and lower limits of charge and discharge power and the upper and lower limits of the state of charge are given in the **Supplementary Appendix**.
(b) BS power constraint at the end of the cycle:

At the end of a BS work cycle (1 day), the power stored in the BS unit group of each node $E(i, t = 24l), l = 1,\ldots,L$ (kWh) needs to be limited to the upper limits $SOC_{\text{end}}^{\max}$ and lower limits $SOC_{\text{end}}^{\min}$, so there is a remaining power at the beginning of the next work cycle that can be charged and discharged. The BS rated capacity is kept unchanged during the simulation. This constraint can be equivalent to the upper and lower bound constraints of the BS state of charge at the end of each working cycle, as shown in **Eq. 20**:

$$SOC_{\text{end}}^{\min} \le SOC(i, t = 24l) \le SOC_{\text{end}}^{\max}. \tag{20}$$

12) BS configuration constraints which include constraints on the number of BS units allowed to be installed on a single node and the total number of BS units allowed to be installed in the network has been provided by Yun et al. (2020). See the **Supplementary Appendix** for specific formulas.
13) Power balance constraint
(a) Considering the active power balance constraint of DR and BS configuration at the same time, as given in **Eq. 21**:

$$\begin{gathered} \sum_{m=1}^{M_i} P_{\text{CG}}(m,t) + \sum_{n=1}^{N_i} P_{\text{uw}}(n,t) + P_{\text{d}}(i,t) - P_{\text{c}}(i,t) \\ - \sum_{h=1}^{H_i} P_{\text{EB}}(h,t) - P_{\text{ld}}(i,t) = \sum_{j \in \Omega(i)} P(i,j,t), \end{gathered} \tag{21}$$

where M_i is the number of micro gas turbines installed at the node, N_i is the number of wind turbines installed at the node, H_i is the number of electric boilers installed at the node, and $\Omega(i)$ is the collection of nodes connected by the branches between nodes.

(b) Considering the thermal power balance constraint of the DR and BS configuration at the same time, as given in **Eq. 22**:

$$\begin{gathered} \sum_{h=1}^{N_{\text{EB}}} Q_{\text{EB}}(h,t) + \sum_{d=1}^{N_{\text{DB}}} Q_{\text{DB}}(d,t) \\ + \sum_{m=1}^{N_{WHRU}} Q_{WHRU}(l,t) \ge R_{\text{c}} \sum_{i=1}^{N_{\text{Bus}}} Q_{\text{ldr}}(i,t). \end{gathered} \tag{22}$$

Because heat is easy to lose during transmission, a thermal power compensation coefficient R_{c} larger than 1 is included to reserve thermal power margin.

Strategy of BS Optimal Configuration Considering DR

The BS optimal configuration based on specific data is an important prerequisite for optimal scheduling. The modeling

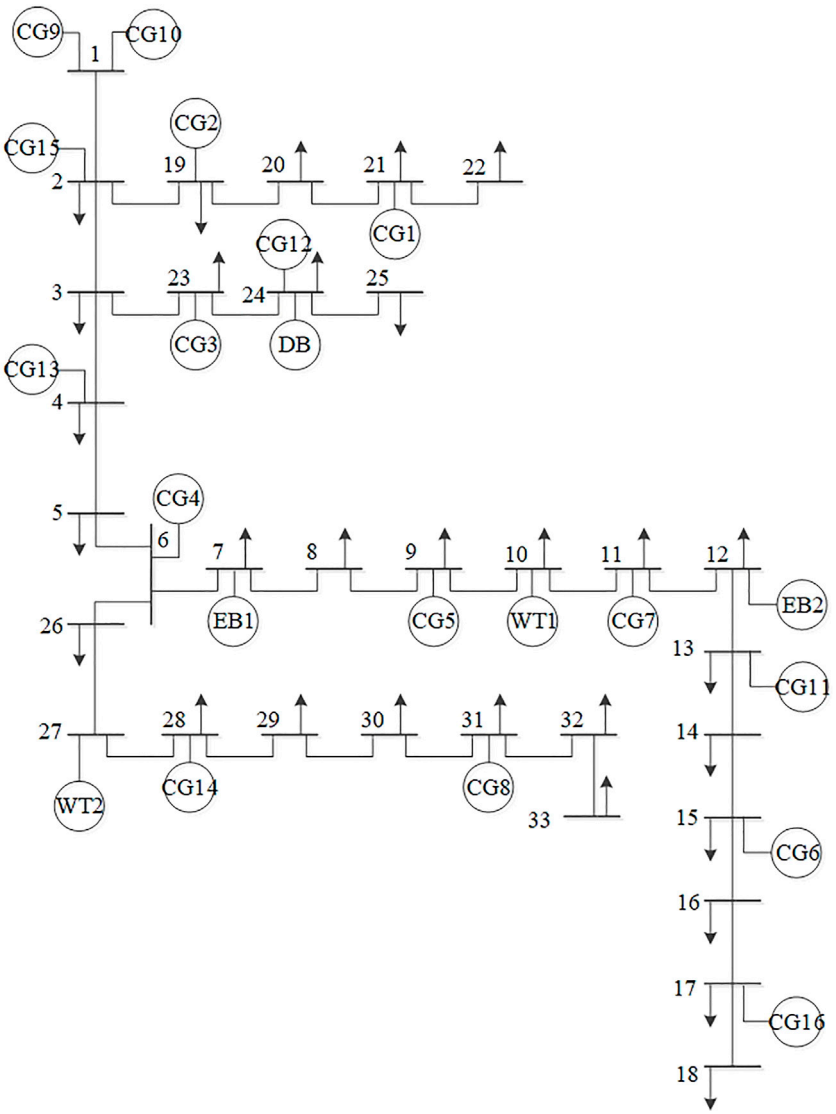

FIGURE 2 | Diagram of network of the isolated micro-grid.

of configuration includes two aspects: constraints and optimization goals.

14) Constraints: all constraints listed in *Constraints*.
15) Optimization goals: solving the number of access nodes and units of the BS to minimize the value of C'_{total}. The purpose is to optimize the overall economy of the independent micro-grid when configuring the BS. The calculation of this is shown in **Eq. 23**:

$$C'_{\text{total}} = C_{\text{total}} + C_{\text{bat}}. \tag{23}$$

Control Strategy Considering DR and BS Configuration

16) Constraints: constraints (1)–(9) and (11) in *Constraints*.
17) Optimization objective: solving the planned output value of the thermal power unit, the consumed wind power and abandoned wind power, and the thermal power load removal during the day to be dispatched. To formulate the BS charge and discharge, load interruption, and transfer plan to minimize the value of C_{total}. The BS is configured according to the solution results of the model in *Strategy of BS Optimal Configuration Considering DR*.

CALCULATION EXAMPLES AND ANALYSIS

Basic Parameter Settings

We built an independent micro-grid model of combined heat and power based on the IEEE 33-node system. Based on the

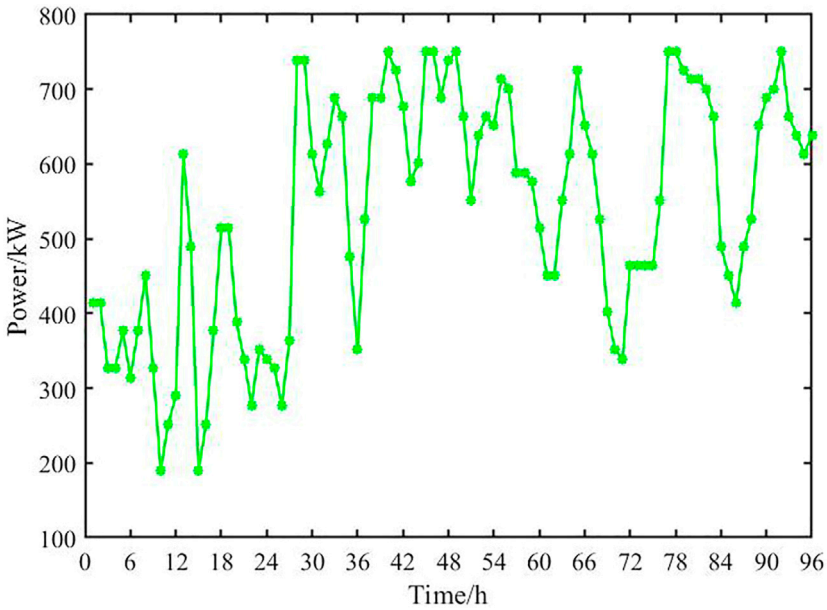

FIGURE 3 | Forecast values of the output of single wind turbine during typical days of four seasons.

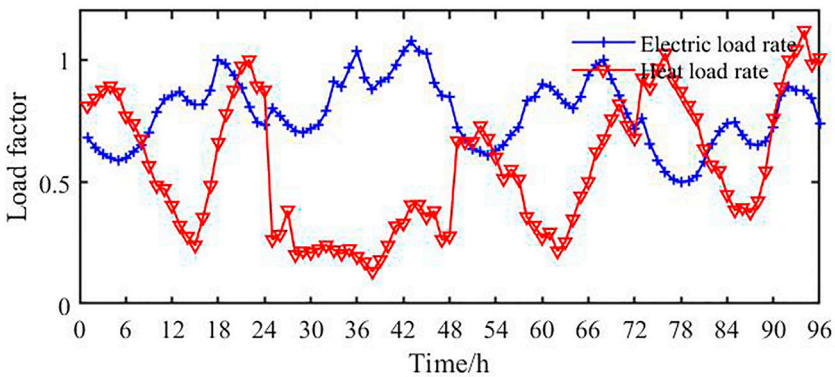

FIGURE 4 | Forecast values of electric and heat load rate during typical days of four seasons.

optimized configuration of BS, the independent micro-grid optimized dispatching takes into account DR and the configuration of BS. The model contains 30 load nodes, 32 lines (numbered branch1–branch32), 16 micro gas turbines and the corresponding heat recovery devices (numbered CG1–CG16), two wind turbines (WT1 and WT2), one direct-fired boiler (DB), and two electric boilers (EB1 and EB2). Assuming that the access node of the unit has been given, the information of each node in the micro-grid can be obtained and is provided in **Supplementary Appendix Table SB1**. The system voltage is 10 kV, and the reference capacity S base is 10 MVA. Thus, the standard unit value of the electrical network parameters can be obtained and is listed in **Supplementary Appendix Table SB2**. The configuration of the independent micro-grid network is shown in **Figure 2**. Node 13 is a phase reference node.

WT1 and WT2 have the same parameters: P_{Wr} = 750 kW, v_{in} = 2.5 m/s, v_{r} = 12 m/s, and v_{out} = 20 m/s. The parameters of EB1 and EB2 are the same: η_{EH} = 92.5%, $K_{\mathrm{EB}}^{\mathrm{op}}$ = 1.35 Yuan/kwh, $P_{\mathrm{EB}}^{\mathrm{max}}$ = 120 kw, and $P_{\mathrm{EB}}^{\mathrm{min}}$ = 0 kw. The technical parameters of DB are as follows: η_{DB} = 85%, $G_{\mathrm{DB}}^{\mathrm{CO_2}}$ = 0.3 kg/kwh, $P_{\mathrm{DB}}^{\mathrm{max}}$ = 500 kw, $P_{\mathrm{DB}}^{\mathrm{min}}$ = 0 kw, and $K_{\mathrm{DB}}^{\mathrm{op}}$ = 2.25 Yuan/kwh. The parameters of CG1–CG16 are shown in **Supplementary Appendix Table SB3**: R_{c} = 1.1, K_{cw} = 0.75 Yuan/kwh, K_{uw} = 0.55 Yuan/kwh, K_{gas} = 2.4 Yuan/m^3, $P^{\mathrm{max}}(i, j)$ = 1.15 (p.u.), and $K_{\mathrm{CO_2}}$ = 0.25 Yuan/kg.

It is assumed that the predicted values of the electrical load and thermal load of node i in time period t are expressed in the form

TABLE 1 | Optimal configuration results of battery storage (BS) in the isolated micro-grid considering DR.

Access node	4	11	19
Number of connected BS units	16	83	200
Total number of configured BS units		299	

TABLE 2 | Optimal configuration results of battery storage (BS) in the isolated micro-grid without considering demand-side response (DR).

Access node	6	10	22	24	31	32
Number of connected BS units	104	9	200	167	55	10
Total number of configured BS units			545			

of "load base value at node *i* predicted value of load rate in time period t." The base value of the electrical load and thermal load of each node is shown in **Supplementary Appendix Table SB4**. The DR related parameters were set as follows: $R_{itr}^{H} = 0.2\%$, $R_{itr}^{E} = 0.2\%$, $R_{sft}^{E} = 8\%$, $R_{sft}^{H} = 10\%$, $K_{itr}^{E} = 3$ Yuan/kWh, $K_{itr}^{H} = 2$ Yuan/kwh, $K_{sft}^{E} = 1.85$ Yuan/kWh, and $K_{sft}^{H} = 1.35$ Yuan/kWh.

The BS unit parameters are selected as follows: $N_{BS}^{Busmax} = 200$, $N_{BS}^{ALLmax} = 2{,}000$, $K_{bat} = 30$ Yuan/(quantity *96 h), $\eta_c = 95\%$, $\eta_d = 95\%$, $E_{max} = 6$ kWh, $SOC^{max} = 0.98$, $SOC^{min} = 0.2$, $SOC_{end}^{min} = 0.35$, $SOC_{end}^{max} = 0.75$, $SOC\,(t = 0) = 0.5$, $\sigma = 0.01\%\ h^{-1}$, $P_c^{max} = 1.2$ kW, and $P_d^{max} = 1.2$ kW.

BS Optimized Configuration Parameter Settings

Considering long-term operation and multiple load conditions, we selected the typical daily data of the independent micro-grid for the four seasons to optimize the configuration of the number of BS access nodes and units. To avoid the different configuration results of each typical day caused by solving in the unit of day, the four curves of typical days in the four seasons are integrated into a single curve which are in the order of spring, summer, autumn, and winter. The forecast values of the output of a single wind turbine is shown in **Figure 3**, and the forecast values of the electric and heat load rate are shown in **Figure 4**. Then, the simulation time of the BS optimal configuration model T(96 h) can be obtained, including the number of BS working cycles, $L = 4$. Additionally, both are set as 0.1%.

Solution and Analysis of BS Optimal Configuration

The CPLEX solver in GAMS is used to solve the independent micro-grid BS optimal configuration model that takes DR into account. The model is a mixed integer linear programming problem, and the results are given in **Table 1**.

Regardless of DR, the same parameter settings are used to solve the BS optimal configuration model, and the results are provided in **Table 2**.

Under the same conditions, compare the total number of configured BS units in **Tables 1**, **2**, and it can be seen that the total number has reduced by 45.14% after the implementation of the incentive-type DR, indicating that the incentive-type DR can effectively reduce the overall configuration requirements of the independent micro-grid.

Optimized Scheduling Parameter Setting of Independent Micro-Grid

We take the simulation duration of the scheduling model as $T = 24$ h. Assuming that the forecasted wind speed of the area where the independent micro-grid is located in each period of the day that needs to be dispatched is given, the forecasted value of the active power output of a single wind turbine can be calculated according to the model in *Main Structure of Independent Micro-Grid*. The results are presented in **Figure 5**. The predicted values of the electric load and heat load rate on the day that needs to be dispatched are shown in **Figure 6**. Both R_{lsh}^{H} and R_{lsh}^{E} are set as 0.

Solution and Analysis of Optimal Scheduling of Independent Micro-Grid

Taking the results in **Table 1** as the BS configuration scheme, the CPLEX solver in GAMS is utilized to solve the mixed integer linear programming problem. Taking the BS of node 11 as an example, the

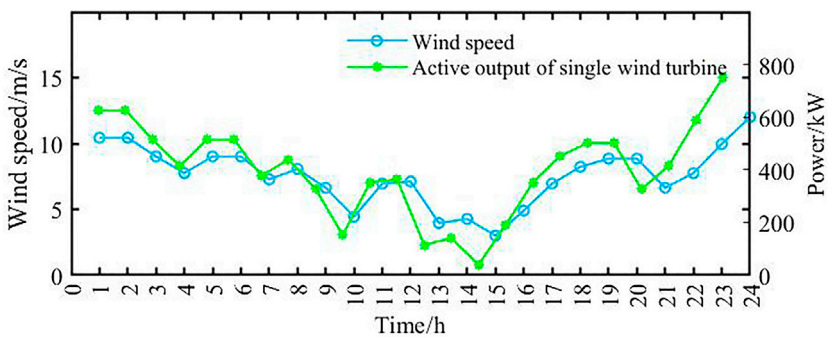

FIGURE 5 | Forecast values of wind speed and a single wind turbine's output during the day to be dispatched.

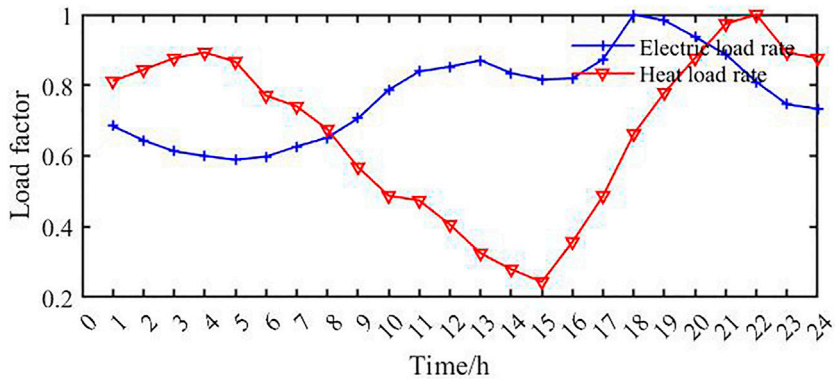

FIGURE 6 | Forecast values of electric and heat load rate during the day to be dispatched.

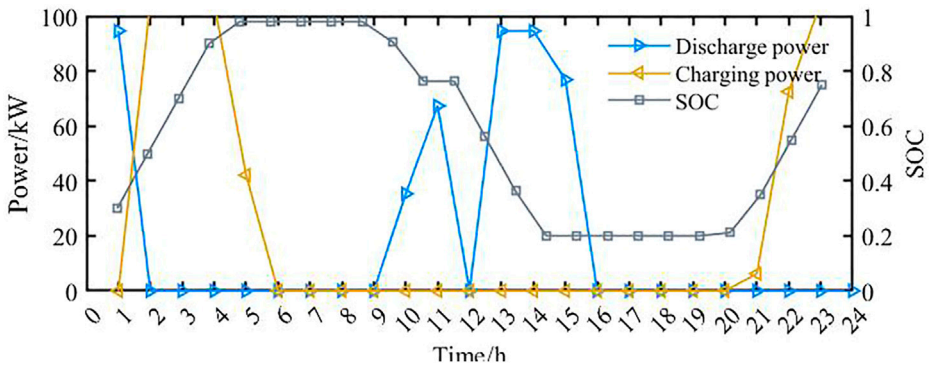

FIGURE 7 | Charging or discharging behaviors and state of charge of battery storage units at node 11.

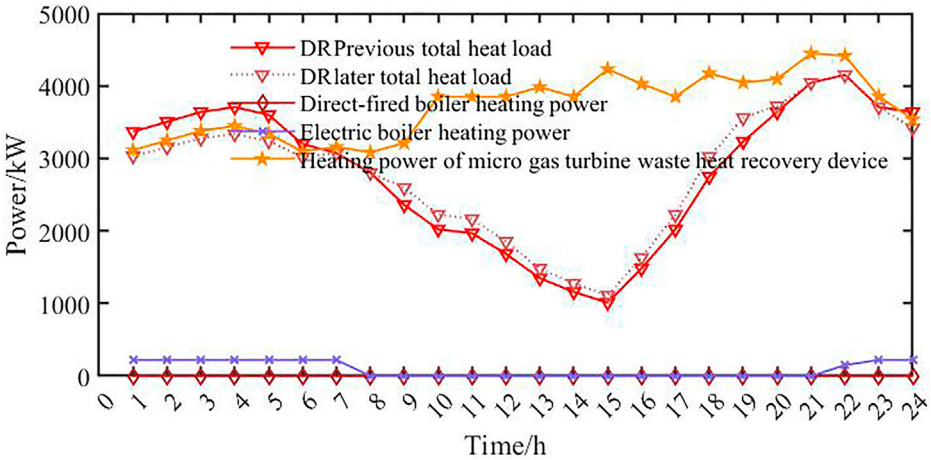

FIGURE 8 | Planned values of heat power items during the day to be dispatched.

planned charging and discharging, and state-of-charge curves are shown in **Figure 7**. The BS characteristics of the other nodes are analogous to node 11.

Considering the DR and BS configuration of independent micro-grid, the results of the plan values of heat power, active power, and thermal power on the scheduling day are shown in

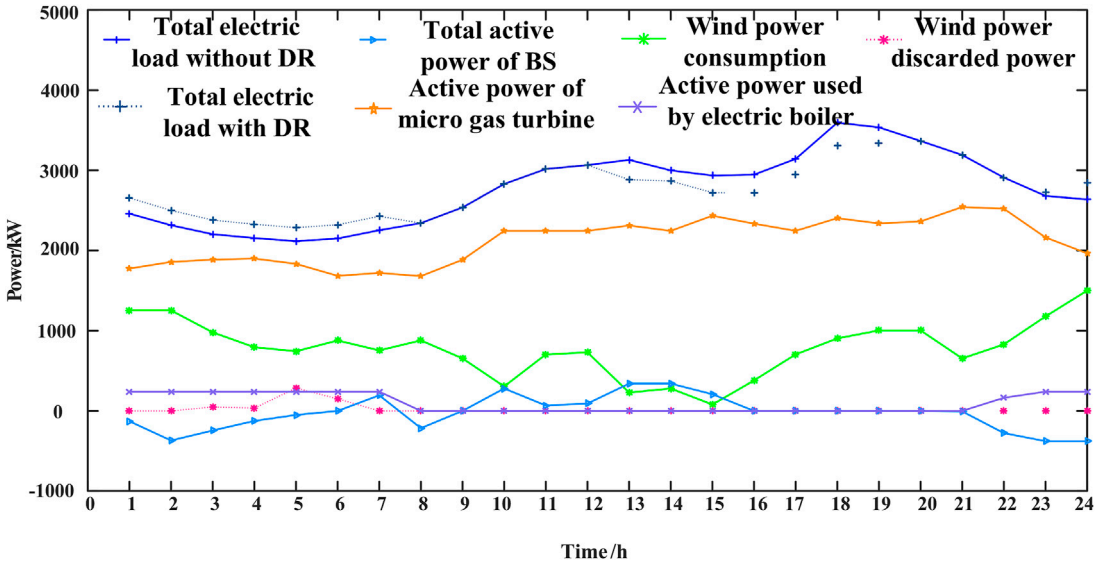

FIGURE 9 | Planned values of active power items during the day to be dispatched.

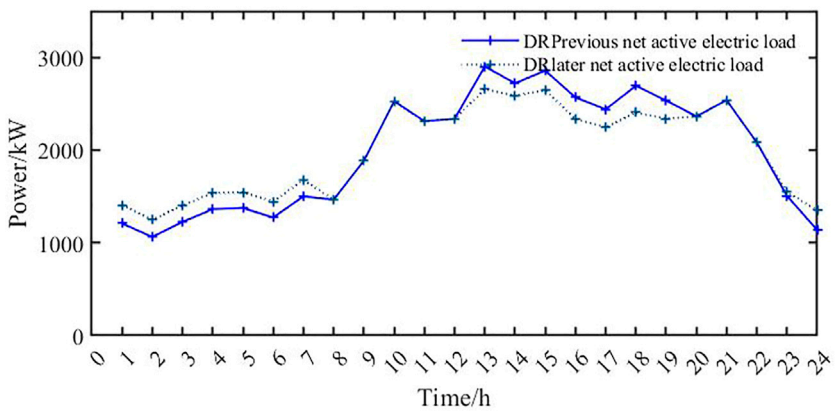

FIGURE 10 | Net active load values before and after considering demand-side response (DR).

Figures 8, **9**, **10**, respectively. If the total active power of the BS is negative, it is in the charging state. On the other hand, the total active power indicates the discharging state.

It can be seen from **Figure 8** that the removed heat load is satisfied when it is transferred to a low heat load rate and a high electric load rate. On this occasion, the increase in heat load helps to make effective use of waste heat. It can be seen from **Figure 9** that the overall BS is charged from 1 to 6 o'clock and 21 to 24 o'clock when the electricity load rate is low and wind power resources are abundant. On the other hand, it is discharged from 9 to 16 o'clock when the electricity load rate is high and wind power resources have been consumed and cooperate with the micro gas turbine to supply the electric load in the grid.

In addition, the following configurations are taken for independent micro-grids: 1) DR is not implemented, and BS is not connected; 2) DR is not implemented, and BS is configured according to **Table 2**; 3) DR is implemented, and BS is not connected. Subsequently, the same parameters are used to solve the independent micro-grid optimization scheduling. The comparison of the planned expenditures of the independent micro-grid on the day of scheduling and the total cost of operating expenditures in the four scenarios are given in **Table 3**. For each scenario, the comparison of the total cost of independent micro-grid expenditures considering the BS investment converted to the value on the day that needs to be scheduled is shown in **Figure 11**. In addition, to give priority to the stable operation of the power system, the remaining heat of the micro gas turbine is dissipated when the heat load is light and the heat resources are abundant (not "using heat to determine electricity"). The comparison of the remaining heat dissipated in each scenario is shown in **Figure 12**.

TABLE 3 | Comparison of cost items of optimized dispatching plans under various scenarios.

Value (unit: Yuan)	No DR, No BS access	No DR, BS access	DR, No BS access	DR, BS access
C_{cw}	3744.96	1664.75	1500.00	389.55
C_{uw}	7800.22	9325.70	9446.52	10260.85
C_{ld}	0.00	0.00	0.00	0.00
C_{itrE}	0.00	0.00	0.00	0.00
C_{itrH}	0.00	0.00	0.00	0.00
C_{sftE}	0.00	0.00	3039.41	2775.51
C_{sftH}	0.00	0.00	2958.15	2951.15
C_{ss}	202.37	100.02	152.73	100.02
C_{DB}^{gas}	38.74	16.16	0.00	0.00
C_{CG}^{gas}	39899.54	38364.94	37732.30	36987.60
$C_{DB}^{CO_2}$	11.75	4.90	0.00	0.00
$C_{CG}^{CO_2}$	8813.54	8487.61	8330.76	8170.01
C_{EB}^{op}	3138.30	2806.31	3146.52	2901.47
C_{DB}^{op}	299.68	125.05	0.00	0.00
C_{CG}^{op}	26280.37	23519.28	23635.59	22662.00
C_{total}	74629.03	65763.32	71048.94	66676.45

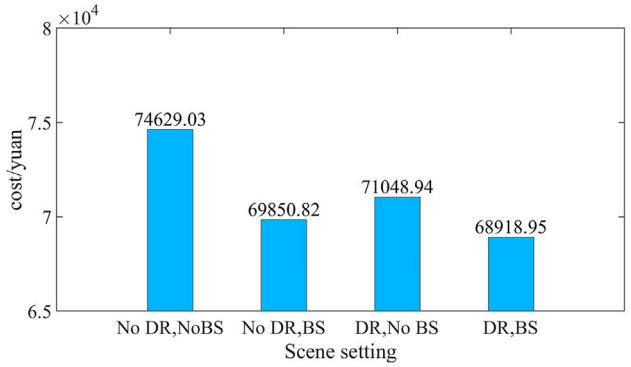

FIGURE 11 | Total expenditures of the isolated micro-grid considering the cost of electrical energy storage.

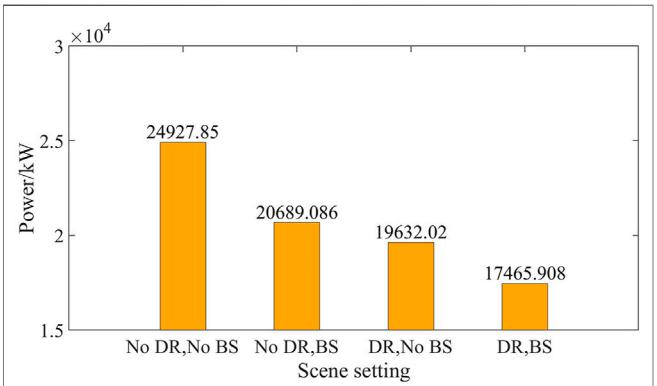

FIGURE 12 | Residual heat dissipation under various scenarios.

For the same calculation example, after the independent micro-grid implements the incentive DR and optimally configures the BS, the comparison results with other scenarios are as follows:

(1) It can be seen from **Table 3** that there is no load removal and interruption in the plan, indicating that the model can guarantee the reliability of energy supply at the plan level and realize economic dispatch on the source side. From **Figures 8–10**, it can be seen that the transferable load makes the thermal and electrical load curves achieve "peak shaving and valley filling." Regarding the electric load, the rise of the trough section allows part of the wind power that was originally abandoned due to surplus to be absorbed. The reduction in the peak section reduces the power supply pressure of the unit and the dissipation of the waste heat. Regarding the heat load, the reduction of the peak period reduces the heating pressure, and the cost of the direct-fired boiler is reduced to zero.

(2) It can be concluded from **Table 3** that C_{cw} reduces by 89.598% compared with the situation where no measures are taken. This is the minimum value in all scenarios. C_{uw} is increased by 31.546% after no method is invoked, which is the maximum value in all scenarios. The total cost of the thermoelectric unit is reduced by 9.993% compared with when no measures are taken, which is the minimum value in all scenarios. Even considering the investment of the BS equivalent to the dispatch date 30/4 = 7.5 yuan/(quantity·24 h), $C_{total}^{'}$ is also reduced by 7.651% when compared with when no measures are taken, which is the minimum value in all scenarios. In addition, it can be seen in **Figure 12** that the remaining heat dissipation is reduced by 29.934% when no measures are taken, which is the minimum value in all scenarios. Hence, it can be concluded that the model proposed in this article has the best overall economics

TABLE 4 | Critical rate of load growth in the isolated micro-grid under various scenarios.

Scenes	R_{LI}^{max}
No DR, No BS access	1.0197
No DR, BS access	1.3051
DR, No BS access	1.2400
DR, BS access	1.3397

compared with other configurations and can further realize the energy saving and emission reduction of independent micro-grids.

(3) It can be concluded from **Table 3** that for the same incentive type DR, the transferable load is reduced after the BS is optimized, especially for the transferable electric load, which is reduced by 8.683%. This shows that the introduction of BS can reduce the interference to energy consumption. Combined with the analysis in *Solution and Analysis of BS Optimal Configuration*, the simultaneous use of the two resources has achieved complementary effects.

Impact on the Distribution System Resilience

In the real system, the load will increase over time, and the source side needs to be upgraded regularly to meet the load demand. As mentioned earlier, studying the impact on load growth after adopting a control strategy can reflect the impact on system resilience. By examining the data reported here, we can see that there exist redundant configurations of energy in the network, indicating that a certain load increase is acceptable. After considering the incentive DR or the configuration of BS (see *Solution and Analysis of Optimal Scheduling of Independent Micro-Grid*), the reduction of the energy supply pressure during the peak load period means the redundant capacity of the source side increases, and it has the potential to accommodate more load growth. In this section, the typical days of the four seasons are selected as the time series, and the thermal load and electrical load of each period are set to increase at the same rate (R_{LI}) based on the original load. The control strategy corresponding to each scenario is employed to calculate the operation status until a convergence solution cannot be obtained. Then, the previous value of R_{LI} is recorded as the critical load growth rate R_{LI}^{max} of the micro-grid in this scenario to measure its ability to accommodate load growth. The model is programmed with GAMS, and the solution is carried out by the CPLEX solver. The results are shown in **Table 4**. Since only the parameter R_{LI} is under control, if the model does not have a convergent solution, it indicates that the scheduling plan under the value of R_{LI} cannot be implemented as required, rather than there being a problem within GAMS.

It can be seen from **Table 4** that R_{LI}^{max} reaches the smallest when DR is not implemented and BS is not configured, R_{LI}^{max} is the largest when incentive-type DR is implemented and BS is configured. This shows that the effective control of BS and DR is beneficial to accommodate more load. The control strategy with BS and DR at the same time shows the most effective way to improve system resilience. This can further delay the upgrade of the micro-grid and brings long-term comprehensive benefits for the micro-grid while maintaining the required reliability of energy supply.

CONCLUSION

Based on the establishment of a distributed energy micro-grid model, this article carried out the control strategy for flexible invocation of multiple types of resources such as conventional thermal power generators, wind turbines, and incentive-type DR, BS, etc. The interference of different resources combination on network reliability, economy, and energy consumption behavior was also compared. The impact on distribution system resilience was demonstrated. Our simulation results show:

(1) The method we proposed realizes the unified and flexible call of various resources in the distributed energy micro-grid and the integrated coordination of the elements of source, network, load, and storage.
(2) The incentive DR reduces the configuration requirements of the BS when optimizing the operation of micro-grid. The access of the BS can reduce the interference to the energy consumption behavior during the optimization schedule. The two resources achieve complementary effects.
(3) Without sacrificing the reliability of energy supply, our method enables the distributed energy system to achieve economically optimal operation, greatest energy saving, emission reduction, and the best system resilience.

This article expects the coordination and optimization of active and reactive resources of distributed energy micro-grid, more detailed energy storage models, more complex DR strategies, and uncertainty modeling of wind turbine and load in subsequent research so that the performance of the micro-grid can be further optimized.

DATA AVAILABILITY STATEMENT

The original contributions presented in the study are included in the article/**Supplementary Material**, and further inquiries can be directed to the corresponding author.

AUTHOR CONTRIBUTIONS

JW was mainly responsible for article guidance and modeling optimization work, RQ was responsible for the writing part and data analysis of the article, MW was responsible for part of the data collection and part of the writing, and the other authors were responsible for the material arrangement and part of the writing of the article.

FUNDING

This work was supported by the National Key Research and Development Program of China, China (No. 2018YFB0904800).

SUPPLEMENTARY MATERIAL

The Supplementary Material for this article can be found online at: https://www.frontiersin.org/articles/10.3389/fenrg.2022.841269/full#supplementary-material

REFERENCES

Bahramirad, S., Reder, W., and Khodaei, A. (2012). Reliability-constrained Optimal Sizing of Energy Storage System in a Microgrid[J]. *IEEE Trans. Smart Grid* 03 (04), 2056–2062. doi:10.1109/tsg.2012.2217991

Chen, Cixuan., and Xiang, Tieyuan. (2016). *Fundamentals of Electrical Engineering*. Third Edition, Vol. II. Beijing: China Electric Power Press, 150–158. [M].

Ding, Ming., Zhang, Yingyuan., Mao, Meiqin., and Liu, X. (2011). Economic Operation Optimization for Microgrids Including Na/S Battery Storage [J]. *Proc. CSEE* 31 (04), 7–14.

Duan, Qinwei. (2016). in A price-based demand response scheduling model in day-ahead electricity market[C]//2016 IEEE Power and Energy Society General Meeting (PESGM), July 17-21, 2016 (Boston, MA, USA, 1–5.

Feng, Lejun., Dai, Xiaoye., Junrong, M. O., and Lin, S. H. I. (2020). Feasibility Analysis of the Operation Strategies for Combined Cooling,Heating and Power Systems (CCHP) Based on the Energy-Matching Regime[J]. *J. Therm. Sci.* 29 (05), 1149–1164. doi:10.1007/s11630-020-1314-2

Gilani, Mohammad. Amin., Kazemi, Ahad., and Ghasemi, Mostafa. (2020). Distribution System Resilience Enhancement by Microgrid Formation Considering Distributed Energy Resources[J]. *Energy* 191 (C). doi:10.1016/j.energy.2019.116442

Hajipour, E., Bozorg, M., and Fotuhi-Firuzabad, M. (2015). Stochastic Capacity Expansion Planning of Remote Microgrids with Wind Farms and Energy Storage [J]. *IEEE Trans. Sust. Energ.* 06 (02), 491–498. doi:10.1109/tste.2014.2376356

Iqbal, F., and Siddiqui, A. S. (2017). Optimal Configuration Analysis for a Campus Microgrid-A Case Study. *Prot. Control. Mod. Power Syst.* 2 (03), 245–256. doi:10.1186/s41601-017-0055-z

Luo, Yanhong., Zhang, Xinwen., Yang, Dongsheng., and Sun, Qiuye. (2020). Emission Trading Based Optimal Scheduling Strategy of Energy Hub with Energy Storage and Integrated Electric Vehicles[J]. *J. Mod. Power Syst. Clean Energ.* 8 (02), 267–275. doi:10.35833/mpce.2019.000144

Ma, S., Su, L., Wang, Z., Qiu, F., and Guo, G. (2018). Resilience Enhancement of Distribution Grids against Extreme Weather Events. *IEEE Trans. Power Syst.* 33 (5), 4842–4853. doi:10.1109/tpwrs.2018.2822295

Muhammad Arif, Syed., Hussain, Akhtar., Syed Muhammad Ahsan, Tek. Tjing. Lie., and Khan, Hassan. Abbas. (2020). Analytical Hybrid Particle Swarm Optimization Algorithm for Optimal Siting and Sizing of Distributed Generation in Smart Grid[J]. *J. Mod. Power Syst. Clean Energ.* 8 (06), 1221–1230.

Phylicia, Cicilio., David, Glennon., Adam, Mate., Arthur, Barnes., Vishvas, Chalishazar., Eduardo, Cotilla. Sanchez., et al. (2021). Resilience in an Evolving Electrical Grid[J]. *Energies* 14 (3).

Qi, Jianghao., Li, Fengting., and Zhang, Gaohang. (2021). Multi-time Scale Scheduling Strategy for Source-Load Coordination Considering Demand Response Block Participation [J]. *Power Syst. Prot. Control.* 49 (11), 61–69.

Shi, Nian. (2018). *Research on Coordinated Planning of Wind Power and Energy Storage in Distribution Network Considering Demand Response [D]*. Wuhan: Huazhong University of Science and Technology.

Shi, Q., Li, F., Olama, M., Dong, J, Xue, Y, Strake, M, et al. (2020). Network Reconfiguration and Distributed Energy Resource Scheduling for Improved Distribution System Resilience [J]. *Int. J. Electr. Power Energ. Syst.* 124, 1–10. doi:10.1016/j.ijepes.2020.106355

Shi, Qingxin., Li, Fangxing., Olama, Mohammed., Jin, Dong., Xue, Yaosuo., Starke, Michael., et al. (2021). Network Reconfiguration and Distributed Energy Resource Scheduling for Improved Distribution System Resilience[J]. *Int. J. Electr. Power Energ. Syst.* 124. doi:10.1016/j.ijepes.2020.106355

Soroudi, A. (2017). Power Plant Dispatching, *Power System Optimization Modeling in GAMS [M]*. First Edition. Switzerland: Springer Nature, 65–93. doi:10.1007/978-3-319-62350-4_3

Tao, Qiong., Li, Chunlai., and Mu, Yunfei. (2017). Statistical Capacity Planning Method for Battery Energy Storage System of Island Microgrid Considering Demand Response[J]. *Proc. CSU-EPSA* 29 (01), 37–44.

Tian, Liting., Cheng, Lin., Guo, Jianbo., and Wu, Kuihua. (2020). System Modeling and Optimal Dispatching of Multi-Energy Microgrid with Energy Storage[J]. *J. Mod. Power Syst. Clean Energ.* 8 (05), 809–819. doi:10.35833/mpce.2020.000118

Wenwu, Y., Chaojie, L., Xinghuo, Y., Wen, G., and Jinhu, L. (2018). Economic Power Dispatch in Smart Grids: a Framework for Distributed Optimization and Consensus Dynamics[J]. *Sci. China(Information Sciences)* 61 (01), 233–248.

Yun, Yunyun., Dong, Haiying., and Ma, Zhicheng., (2020). Optimization Economic Dispatch of a Multi-Source System Considering the Participation of Demand Response and Concentrating Solar Power Plant[J]. *Power Syst. Prot. Control.* 48 (14), 140–149.

Zhang, Jing., Wang, Ting., and Li, Bin. (2014). Research on Technical Standardization for Electric Demand Response [J]. *Proc. CSEE* 34 (22), 3623–3629.

Zho, Bin., Zou, Jianting., Chung, Chi. Yung., Wang, Huaizhi., Liu, Nian., Voropai, Nikolai., et al. (2021). Multi-microgrid Energy Management Systems: Architecture, Communication, and Scheduling Strategies[J]. *J. Mod. Power Syst. Clean Energ.* 9 (03), 463–476. doi:10.35833/mpce.2019.000237

Zhu, L., Zheng, Y., Yang, X., and Fu, Y. (2014). Integrated Resources Planning in Microgrid Based on Modeling Demand Response [J]. *Proc. CSEE* 34 (16), 2621–2628.

Conflict of Interest: The authors declare that the research was conducted in the absence of any commercial or financial relationships that could be construed as a potential conflict of interest.

Publisher's Note: All claims expressed in this article are solely those of the authors and do not necessarily represent those of their affiliated organizations, or those of the publisher, the editors, and the reviewers. Any product that may be evaluated in this article, or claim that may be made by its manufacturer, is not guaranteed or endorsed by the publisher.

frontiers | Frontiers in Energy Research

ORIGINAL RESEARCH
published: 01 April 2022
doi: 10.3389/fenrg.2022.875706

Fast and Accurate Traction Induction Machine Performance Calculation Method for Integrated Onboard Charging in Vehicle to Grid Application

Haiwei Cai[1], Ru Huang[1], Hao Zhai[1], Honghua Xu[2], Shaojun Liu[2] and Jingzhou Xu[2]*

[1]School of Electrical Engineering, Southeast University, Nanjing, China, [2]Nanjing Power Supply Company State Grid Jiangsu Electric Power CO., LTD, Nanjing, China

Reusing traction electric machine windings in electric vehicles as an integrated filtering inductor is a promising solution to reduce the size of the vehicle to grid (V2G) charging/discharging system. Obviously, the integrated inductors need to meet the requirements of traction and charging/discharging, which brings challenge for the design of traction machines. As one of the most popular traction electric machine types, the high-speed induction machine usually has large electrical time constant and consequently unacceptably long transient time in the design stage when finite element analysis is adopted. In this article, a method is proposed to quickly and accurately calculate the steady state performance of the induction machine by time-stepping transient magnetic finite element analysis. First, the stator current magnitude is ramped up from zero to full magnitude gradually to control the DC component in rotor flux and torque. Second, a multistep equivalent resistance method is adopted to decrease rotor time constant and suppress slot-tooth harmonic transient response. The proposed method can predict the FEA computation load before running the calculation, and it does not rely on the machine parameter and feedback signal. Its performance is tested by an example induction machine. The result shows that the proposed method can reduce the finite element calculation time of a high-speed operating point by 99%.

Keywords: finite element, induction machine, torque, transient response, high-speed, equivalent resistance, V2G, harmonic

OPEN ACCESS

Edited by:
Qingxin Shi,
North China Electric Power University, China

Reviewed by:
Jianyu Pan,
Chongqing University, China
Yanpu Zhao,
Wuhan University, China

****Correspondence:***
Haiwei Cai
haiweicai@seu.edu.cn

Specialty section:
This article was submitted to Smart Grids, a section of the journal Frontiers in Energy Research

Received: *14 February 2022*
Accepted: *01 March 2022*
Published: *01 April 2022*

Citation:
Cai H, Huang R, Zhai H, Xu H, Liu S and Xu J (2022) Fast and Accurate Traction Induction Machine Performance Calculation Method for Integrated Onboard Charging in Vehicle to Grid Application. Front. Energy Res. 10:875706. doi: 10.3389/fenrg.2022.875706

1 INTRODUCTION

As an emerging type of distributed energy resources (DERs), the electric vehicle is increasingly connected to the power grid in the two-way charging and discharging manner (Haghbin et al., 2013; Khaligh and D'Antonio, 2019). To suppress the harmonics brought by the grid-connected inverters, filter inductors are usually required to be installed between the inverter and the power grid. Integrated filter inductors reused traction electric machine windings instead of adding an

Abbreviation: I_s, i_{ds}, i_{qs}, stator current magnitude and dq components; i_{dr}, i_{qr}, rotor current dq components; λ_{dr}, λ_{qr}, rotor flux dq components; R_s, R_r, stator resistance and rotor resistance; L_s, L_r, L_m, stator, rotor, and mutual inductance; t_{syn}, electrical synchronous period; ω_e, synchronous angular frequency, $\omega_e = \frac{2\pi}{t_{syn}}$; τ, rotor electrical time constant, $\tau = \frac{L_r}{R_r}$; n, rotor mechanical speed in round per minute; ω_r, rotor speed, $\omega_r = 2\pi\frac{poles}{2}\frac{n}{60}$; ω_{slip}, s, slip frequency in rad/s and slip, $\omega_{slip} = s\omega_e = \omega_e - \omega_r$; T_e, electromagnetic torque; *Peak*, subscript denoting the peak value; $'$, $''$, superscripts denoting 1st and 2nd order derivatives, respectively; P, number of poles; *ss*, subscript denoting the steady state value.

extra set of inductors for the purpose of reducing the charging system size (Xiao et al., 2019; Metwly et al., 2020; Wang et al., 2020). It is well known that the vehicle traction application requires the machine to have high efficiency and small size, while the V2G application focuses more on the power quality such as harmonic components. Hence, it is necessary to make sure the machine can satisfy the requirements of both applications.

Induction machines (IMs) are commonly used in electric and hybrid vehicle traction (Zhu and Howe, 2007; El-Refaie, 2013). To improve machine efficiency, the IMs need to operate at high speed, which results in a large rotor electrical time constant ($\tau = \frac{L_r}{R_r}$) and consequently a very time-consuming transient response before obtaining steady state performance (Yamazaki et al., 2012). Because finite element analysis (FEA) can accurately calculate electric machine performance, it is commonly used in the machine design stage. However, the accuracy comes at the cost of large amount of computation load and time; it becomes impractical to design an IM that meets the traction and V2G applications in an acceptable time length (Le Besnerais et al., 2010; Kim et al., 2019).

To reduce the calculation time, many researchers have proposed different ideas to calculate the initial steady state performance in a relatively short time. The locked-rotor method sets the rotor speed to be zero and increases rotor resistance by a factor of $\frac{1}{s}$ to obtain a $\frac{1}{s}$ times faster transient response time (Lin et al., 2017). However, to consider the tooth/slot harmonics, the rotor speed must be changed back to the normal speed, but such transition will introduce a new transient response. In Lin et al. (2017), a compensation voltage is added to original sinusoidal voltage excitation to eliminate the DC flux to suppress the transient response, which works on permanent magnet machines, but works on IMs because the two machine types are very different.

The current excitation is transitioned to a voltage excitation in Di et al. (2019), which reduces the transient time by as much as 66%. However, the research does not provide theoretical analysis on the optimal transition moment. The time-harmonic (TH) FEA and larger time step methods are also studied (Fu et al., 2012; Rainer et al., 2012). However, these methods cannot guarantee the accuracy of the result. Hence, they face the same transition transient response issue when switched back to the accurate time-stepping FEA model.

This article proposes a two-step IM performance calculation method to accelerate the machine design process. The first step is to control the DC component in rotor flux and torque by gradually ramping up stator current magnitude. The second step is to reduce the rotor time constant by slowing down rotor speed and increasing rotor resistance simultaneously.

The content of this article is organized as follows: in **Section 2**, the transient dynamic of the IM under current source excitation is discussed. The performance of several existing methods is analyzed. **Section 3** presents and discusses the proposed method. Then, the performance of the proposed method is tested by an example induction machine in **Section 4**. **Section 5** concludes the article.

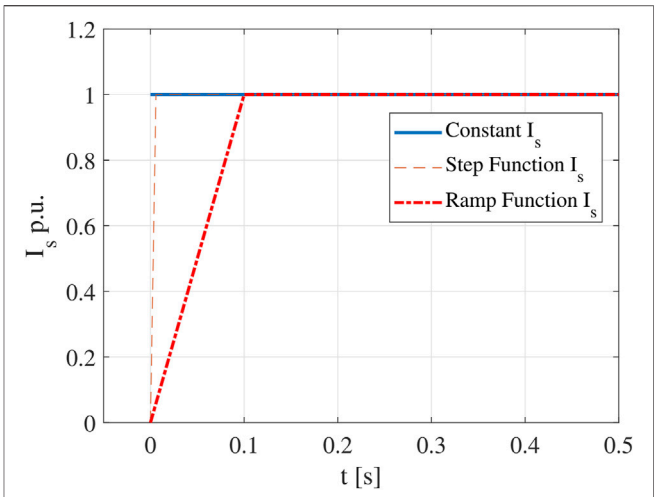

FIGURE 1 | I_s waveform of the three methods (analytical model).

2 PERFORMANCE OF EXISTING METHODS

2.1 Steady State Model in the DQ Reference Frame

The rotor flux, current, and torque of an IM in synchronous $d-q$ reference frame can be expressed by **(1–5)**. Since current excitation is supplied to the stator winding, the transient response is mainly on the rotor flux and current. Hence, the stator voltage and flux equations are not included.

$$0 = R_r i_{dr} - s\omega_e \lambda_{qr} + \lambda'_{dr} \tag{1}$$

$$0 = R_r i_{qr} + s\omega_e \lambda_{dr} + \lambda'_{qr} \tag{2}$$

$$\lambda_{dr} = L_r i_{dr} + L_m i_{ds} \tag{3}$$

$$\lambda_{qr} = L_r i_{qr} + L_m i_{qs} \tag{4}$$

$$T_e = \frac{3P}{4}\frac{L_m}{L_r}\left(\lambda_{dr} i_{qs} - \lambda_{qr} i_{ds}\right). \tag{5}$$

The reference d-axis is selected such that i_{ds} and i_{qs} satisfy (6) and (7), respectively, in the steady state.

$$i_{dsss} = 0 \tag{6}$$

$$i_{qsss} = I_{sss}. \tag{7}$$

Regardless of the transient waveform of the stator current, as long as the steady state inputs I_s and ω_{slip} are known, solving (1–4) and setting all differential terms to be zero can obtain the steady state rotor flux value as expressed by **8** and **9**.

$$\lambda_{drss} = \frac{\tau\omega_{slip}}{1 + \tau^2\omega_{slip}^2} L_m I_{sss} \tag{8}$$

$$\lambda_{qrss} = \frac{1}{1 + \tau^2\omega_{slip}^2} L_m I_{sss}. \tag{9}$$

When the current source is imposed on stator winding, the transient response of the IM is mainly referring to oscillation of the rotor current, flux, and torque. (10) and (11) can be derived

from **(1–4)**. Note that rotor speed ω_r is an input value in the FEA calculation, so slip frequency $\omega_{slip} = s\omega_e = \omega_e - \omega_r$ can be designated.

$$\lambda_{dr}'' + \frac{2}{\tau}\lambda_{dr}' + \left(\frac{1}{\tau^2} + \omega_{slip}^2\right)\lambda_{dr} = \frac{L_m}{\tau}\left(i_{ds}' + \frac{1}{\tau}i_{ds} + \omega_{slip}i_{qs}\right) \quad (10)$$

$$\lambda_{qr}'' + \frac{2}{\tau}\lambda_{qr}' + \left(\frac{1}{\tau^2} + \omega_{slip}^2\right)\lambda_{qr} = \frac{L_m}{\tau}\left(i_{qs}' + \frac{1}{\tau}i_{qs} - \omega_{slip}i_{ds}\right). \quad (11)$$

Three existing methods, including constant I_s method, step function I_s method, and ramp function I_s method, will be discussed in the following subsections (Cai, 2020). They are different because of the different input stator current waveforms as shown in **Figure 1**.

2.2 Existing Method 1—Constant I_s

In the constant I_s method, the steady state sinusoidal current is supplied to stator winding from time zero until the steady state is reached. (12) and (13) can be derived from **10** and **11**.

$$\lambda_{dr1} = \lambda_{drss}e^{-\frac{t}{\tau}}\left(\tau\omega_{slip}\,sin\omega_{slip}t - cos\omega_{slip}t\right) + \lambda_{drss} \quad (12)$$

$$\lambda_{qr1} = \lambda_{drss}e^{-\frac{t}{\tau}}\left(\tau\omega_{slip}\,cos\omega_{slip}t + sin\omega_{slip}t\right) + \lambda_{qrss}. \quad (13)$$

The transient electromagnetic torque can be calculated by substituting (6), (7), (12), and (13) into (5). The result is shown in **14**, where $T_{ess} = \frac{3P}{4}\frac{L_m}{L_r}\lambda_{drss}I_{sss}$.

$$T_{e1} = \frac{3P}{4}\frac{L_m}{L_r}\lambda_{dr}i_{qs} = T_{ess}e^{-\frac{t}{\tau}}\left(\tau\omega_{slip}\,sin\omega_{slip}t - cos\omega_{slip}t\right) + T_{ess}. \quad (14)$$

The ratio between the magnitude of the oscillating component $T_{os1} = T_{ess}e^{-\frac{t}{\tau}}(\tau\omega_{slip}\sin\omega_{slip}t - \cos\omega_{slip}t)$ and the steady state component T_{ess}, i.e., the torque error, can be calculated by **15**. Then, the number of synchronous electrical cycles k_{ω_e} needed to make the error smaller than ε_{T_e1} (practical steady state in numerical computation) can be calculated by **16**, which is a function of s and $\tau\omega_{slip}$.

$$\varepsilon_{T_e1} = e^{-\frac{t}{\tau}}\sqrt{1 + \tau^2\omega_{slip}^2} \quad (15)$$

$$k_{\omega_e1} = \frac{\tau\omega_{slip}}{2\pi s}ln\left(\frac{\sqrt{1 + \tau^2\omega_{slip}^2}}{\varepsilon_{T_e1}}\right). \quad (16)$$

2.3 Existing Method 2—Step Function for I_s

In the step function I_s method, the input stator current magnitude can be expressed by **17**. When $t > 0$, (18) and (19) can be derived.

$$i_{qs} = \begin{cases} 0 & t = 0 \\ I_{sss} & t > 0 \end{cases}; \quad (17)$$

$$\lambda_{dr2} = \lambda_{drss}e^{-\frac{t}{\tau}}\left(-\frac{1}{\tau\omega_{slip}}sin\omega_{slip}t - cos\omega_{slip}t\right) + \lambda_{drss} \quad (18)$$

$$\lambda_{qr2} = \lambda_{drss}e^{-\frac{t}{\tau}}\left(-\frac{1}{\tau\omega_{slip}}cos\omega_{slip}t + sin\omega_{slip}t\right) + \lambda_{qrss}. \quad (19)$$

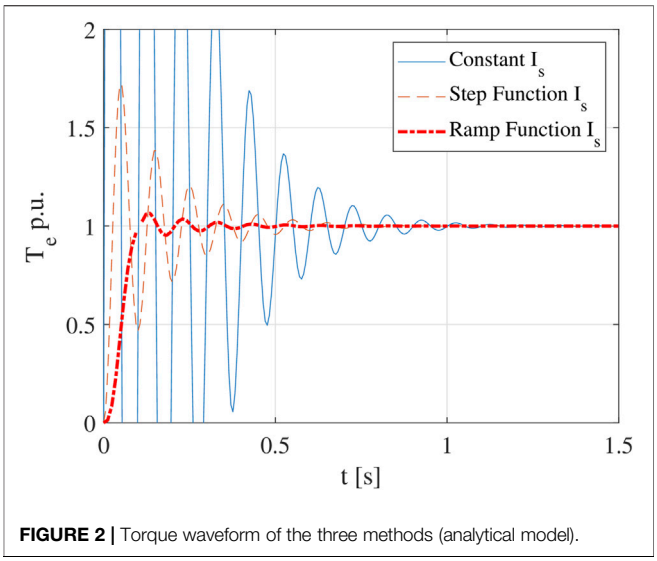

FIGURE 2 | Torque waveform of the three methods (analytical model).

Similar to (16), the number of synchronous electrical cycles needed to reach a given error ε_{T_e2} can be derived as (20).

$$k_{\omega_e2} = \frac{\tau\omega_{slip}}{2\pi s}ln\left(\frac{\sqrt{1 + \tau^2\omega_{slip}^2}}{\tau\omega_{slip}\varepsilon_{T_e2}}\right). \quad (20)$$

2.4 Existing Method 3—Ramp Function for I_s

In the ramp function I_s method, I_s is expressed by **21**.

$$i_{qs} = \begin{cases} \frac{I_{sss}}{t_0}t & t \le t_0 \\ I_{sss} & t > t_0 \end{cases} \quad (21)$$

When $t \le t_0$, the rotor flux is expressed by **22** and **23**, where $\theta_3 = atan(\frac{\tau^2\omega_{slip}^2 - 1}{\tau\omega_{slip}})$.

$$\lambda_{dr3} = \frac{\lambda_{drss}}{k_0 2\pi}\left[e^{-\frac{t}{\tau}}cos\left(\omega_{slip}t + \theta_3\right) - cos\theta_3 + \omega_{slip}t\right] \quad (22)$$

$$\lambda_{qr3} = \frac{\lambda_{drss}}{k_0 2\pi}\left[-e^{-\frac{t}{\tau}}sin\left(\omega_{slip}t + \theta_3\right) + sin\theta_3 + \frac{1}{\tau}t\right]. \quad (23)$$

When $t > t_0$ and $i_{qs} = I_{sss}$, rotor flux can be calculated by **24** and **25**, where $t^\star = t - t_0$, $C_1^\star = \lambda_{dr30} - \lambda_{drss}$, and $C_2^\star = \lambda_{qr30} - \lambda_{qrss}$. Note that λ_{dr30} and λ_{qr30} can be calculated by letting $t = t_0 = k_0\frac{2\pi}{\omega_{slip}}$ in **22** and **23**.

$$\lambda_{dr3} = e^{-\frac{t^\star}{\tau}}\left[C_2^\star\,sin\omega_{slip}t^\star + C_1^\star\,cos\omega_{slip}t^\star\right] + \lambda_{drss}; \quad (24)$$

$$\lambda_{qr3} = e^{-\frac{t^\star}{\tau}}\left[C_2^\star\,cos\omega_{slip}t^\star - C_1^\star\,sin\omega_{slip}t^\star\right] + \lambda_{qrss}. \quad (25)$$

Similar to (16) and (20), the synchronous electrical periods needed to make the error smaller than ε_{T_e3} can be derived as (26).

$$k_{\omega_e3} = \frac{k_0}{s} + \frac{\tau\omega_{slip}}{2\pi s}ln\left(\frac{\sqrt{e^{-2\frac{k_0 2\pi}{\tau\omega_{slip}}} - 2e^{-\frac{k_0 2\pi}{\tau\omega_{slip}}}cos\left(k_0 2\pi\right) + 1}}{k_0 2\pi\varepsilon_{T_e3}}\right). \quad (26)$$

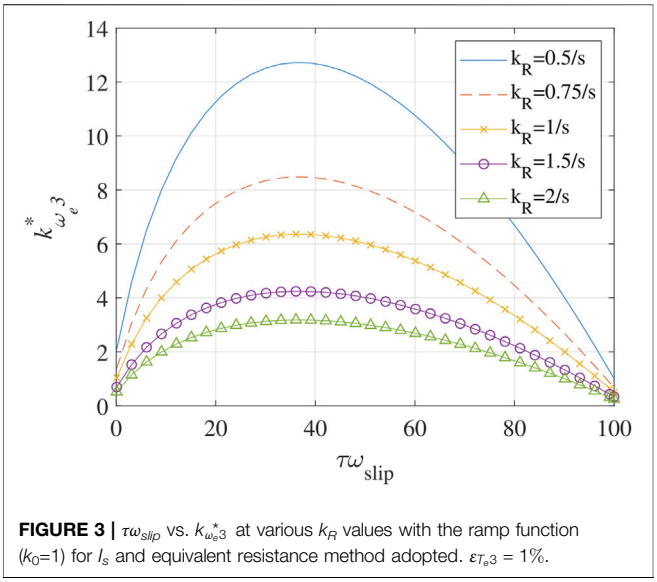

FIGURE 3 | $\tau\omega_{slip}$ vs. $k^*_{\omega_e 3}$ at various k_R values with the ramp function (k_O=1) for I_s and equivalent resistance method adopted. $\varepsilon_{T_e 3}$ = 1%.

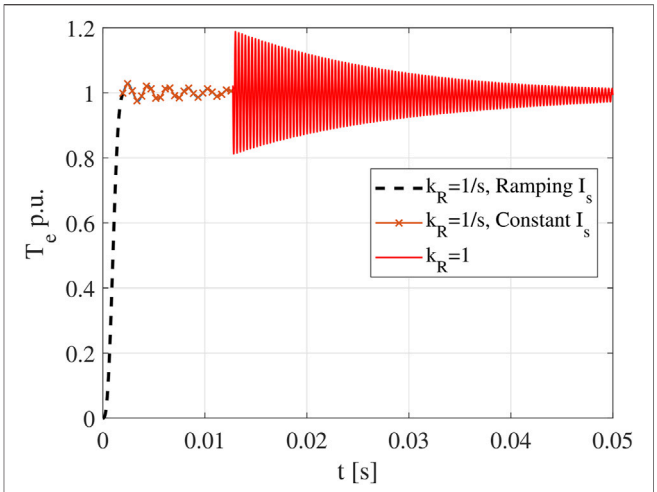

FIGURE 4 | Traditional single-step equivalent resistance method.

Performance of the three existing methods are evaluated with an example IM, when $\omega_e = 2\pi \times 510$, $\tau\omega_{slip} = 30$, and $s = 0.0196$, and the torque waveforms of the three methods are shown in **Figure 2**. It should be pointed out that for simplicity of initial discussion, the example uses an analytical model rather than a finite element model, so the nonlinear behaviors have not been considered yet.

Even though the ramp function I_s method can significantly reduce the transient response time when compared with the other two methods, it still takes hundreds of cycles to reach the steady state. In fact, it takes much longer time to decay from 10 to 1% error than that from zero to 10% error.

3 PROPOSED METHOD—MULTISTEP EQUIVALENT RESISTANCE METHOD

To further reduce the transient time, this article proposes the multistep equivalent resistance method. It is well known that as long as the value of $\frac{R_r}{s}$ is not changed, the steady state torque and flux (fundamental component) of the IM will remain the same. By increasing R_r in proportion to s, the oscillation time of rotor flux and torque can be reduced since $\tau = \frac{L_r}{R_r}$ becomes smaller. This approach is called the equivalent resistance (ER) method.

To implement the ER method, when R_r needs to be increased by a factor of k_R, then the rotor bar resistivity and rotor slip should also be multiplied by k_R, and the rotor mechanical speed should be modified as $n^* = n\ (1 - sk_R)/(1 - s)$.

To calculate the accurate IM performance, it is necessary to switch from the ER model back to the original model. Since the ramp function method has shown obvious advantages over the other two methods, if it can be combined with the ER method, the transient response time can be further reduced. Thus, $k_{\omega_e 3}$ can be updated as (27).

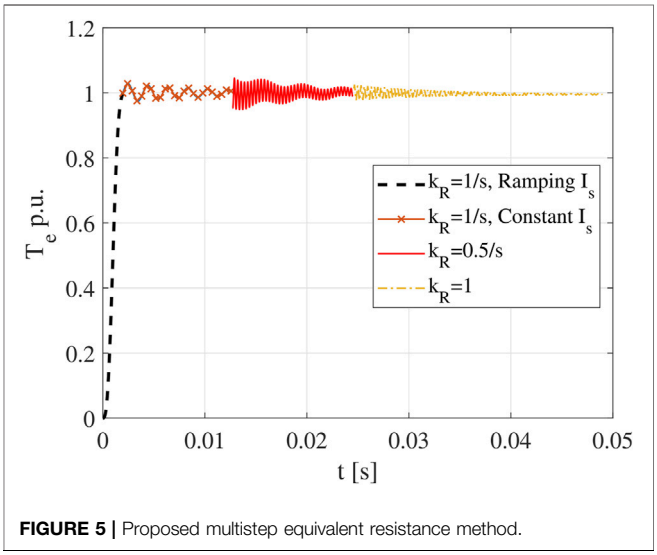

FIGURE 5 | Proposed multistep equivalent resistance method.

$$k^\star_{\omega_e 3} = \frac{1}{k_R s}\left[1 + \frac{\tau\omega_{slip}}{2\pi} ln\left(\frac{e^{-\frac{2\pi}{\tau\omega_{slip}}} - 1}{2\pi\varepsilon_{T_e 3}}\right)\right]. \quad (27)$$

The relationship between $\tau\omega_{slip}$ and $k^\star_{\omega_e 3}$ at various k_R values is plotted in **Figure 3**, which shows that the peak value of $k^\star_{\omega_e 3}$ is inversely proportional to k_R. More importantly, the peak value of $k^\star_{\omega_e 3}$ is 6.38, indicating that the IM can reach the steady state in less than 6.5 synchronous periods. In contrast, the existing methods will need hundreds or thousands of periods. Hence, it seems reasonable to select k_R to be as large as possible. However, larger k_R will lead to larger t_{add}, and the total transient response time may become longer instead.

To mitigate this problem, the multistep ER method is proposed. The basic idea is to use a time-varying k_R value to smooth the transition, such that t_{add} can be greatly reduced. As shown in **Figure 4** ($\omega_e = 2\pi \times 510Hz$ and $s = 0.0196$), the one-step ER method will introduce large oscillation when the

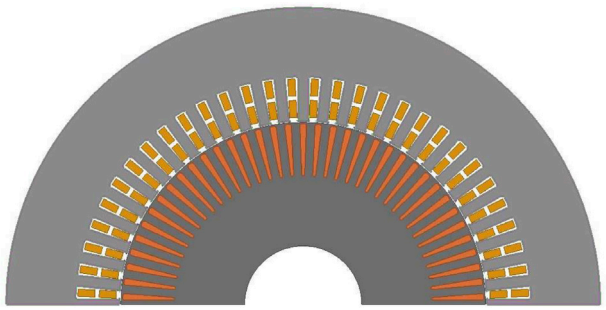

FIGURE 6 | Cross section of the example traction induction machine.

TABLE 1 | Specifications of the example induction machine.

Quantity	Unit	Value
Number of poles		4
Stator/rotor slot number		60/74
Stack length	mm	153
Stator OD/ID	mm	254/157
Rotor OD/ID	mm	155.6/50
DC bus voltage	V	300
Slip (s)		0.0196
Stator current (Peak)	A	1,273
Rotor speed	RPM	15,000

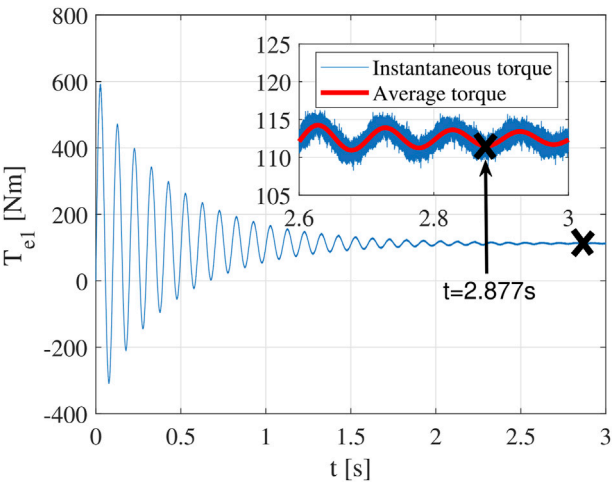

FIGURE 7 | Torque of the constant I_s method (FEA result).

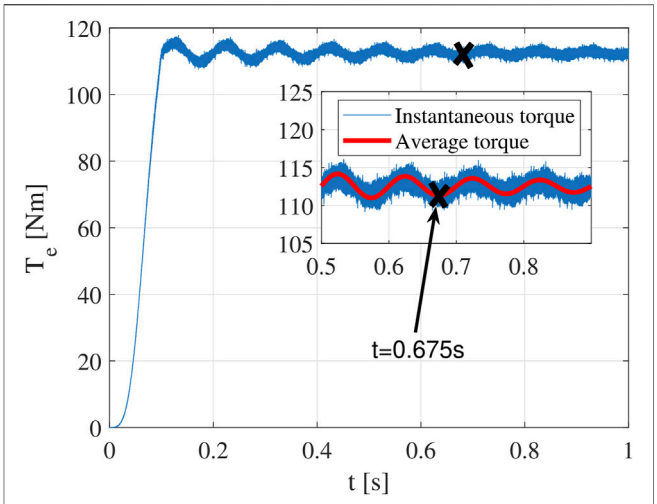

FIGURE 8 | Torque of the ramp function I_s method (FEA result).

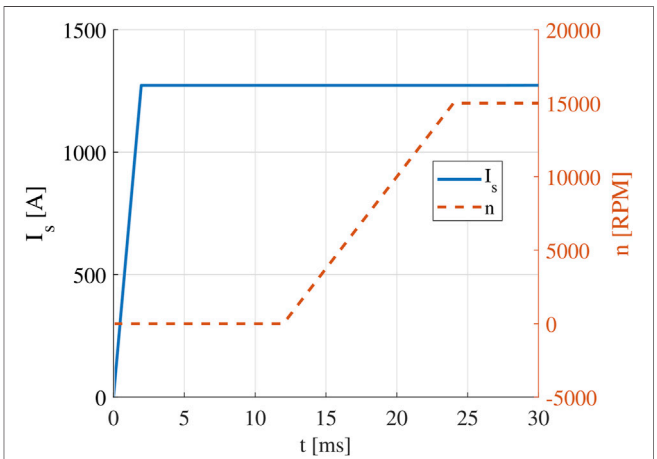

FIGURE 9 | I_s and n waveform of the ramp function I_s with the multistep ER method (FEA result).

transition happens. While in **Figure 5**, when a two-step ER method is adopted, t_{add} becomes much shorter. It should be pointed out if the rotor speed is increased to the actual speed following a constant slope (ramp function) after the transition, it becomes a special case of the multistep ER method.

Note that **Figures 4**, **5** are schematic waveforms; the actual response of the finite element IM model involves complex nonlinear behavior that is difficult to be expressed by accurate analytical equations. Hence, the effectiveness of the proposed multistep ER method will be proven in the next section by the FEA model directly.

In short, the proposed method has two parts. First, stator current magnitude I_s is increased following a ramp function and applied on q-axis while keeping the d-axis current to be zero (arbitrary synchronous reference frame). Second, a multistep equivalent resistance method is adopted.

4 VALIDATION OF THE PROPOSED METHOD

A high-speed traction IM is selected for investigation as shown in **Figure 6** (cross section) and **Table 1** (specs). For easiness of understanding, the steady state value of $\tau\omega_{slip}$ is calculated after the simulation, which is around 30. For the purpose of comparison, the transient response of different methods

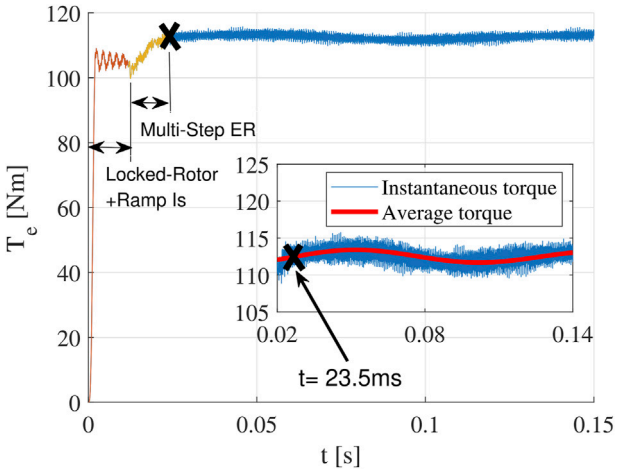

FIGURE 10 | Toque of the ramp function I_s method with the multistep ER method (FEA result).

TABLE 2 | Performance comparison of different methods.

Method	Transient time (ms)	Transient period	%
Constant I_s	2,877	1,467	100
Step function I_s	2,200	1,122	76.5
Ramp function I_s	675	344	23.5
Ramp function I_s + multistep ER	23.5	12	0.82

including the three existing methods discussed earlier is also calculated. The torque waveforms for constant I_s and ramp function I_s methods are shown in **Figures 7**, **8**, respectively.

To validate the effectiveness of the multistep ER method, the rotor speed is increased from 0 to 15000RPM following a constant slope from t = $6t_{syn}$ = 11.8 ms to t = $12t_{syn}$ = 23.5 ms (**Figure 9**). The torque waveform is shown in **Figure 10**. It is found that there is almost no additional transient response after the rotor speed reaches 15000RPM. Hence, the total transient time is only $12t_{syn}$ (23.5 ms). As shown, the average value of the steady state torque is 112.5 N m.

The number of electrical cycle needed to reach 1% torque error is listed in **Table 2**. Since the constant I_s method takes the longest time to reach the practical steady state (1%), its computation time is used as the reference for other methods. It is observed that the transient response time of the FEA models is longer than that of the theoretical analysis, which is the result of nonlinearity of the core material (saturation).

The finite element results show that the calculation time has been reduced from 2.877 s (constant Is method as shown in **Figure 7**) to 23.5 ms (proposed method as shown in **Figure 10**). Hence, the calculation time is reduced by more than 99% for the test case. In fact, this test case is a very challenging operating point in terms of finite element calculation, which is the maximum speed (15000 rpm) and low torque point. It is important to point out that the end time of calculation is decided by the most challenging and time-consuming points, rather than the average calculation time of all operating points. To be more specific, if the constant I_s method takes 24 h to get the result, with the proposed method, the calculation time is reduced to less than 12 min.

Compared with the other two existing methods (step function Is method and ramp function Is method), the proposed method that combines the ramp function I_s method and the multistep ER method can reduce transient response time by 98.9% and 96.5%, respectively.

5 CONCLUSION

A method to significantly accelerate the time-stepping magnetic transient FEA calculation of steady state performance of the high-speed traction IM is proposed. The proposed method includes two parts.

The first part is the ramp function I_s method, which increases the stator current magnitude from zero to full magnitude following a constant slope, such that the DC component can be controlled at a very low level from the beginning. This part alone can reduce FEA calculation time by 76.5%.

The second part is the multistep equivalent resistance method, which adjusts the rotor resistance inversely proportional to the slip multiple times during the transient stage, such that the additional transient response due to the transition from the equivalent model to original model is suppressed to a negligible level.

Note that these two parts can work separately and together, either way can significantly reduce the FEA calculation time. The proposed method has two important features. First, the maximum

electrical cycle needed to reach the steady state can be easily calculated before running the FEA model. Hence, the computation load and time are predictable. Second, the proposed method does not require knowing the parameter or feedback signal of the machine. Hence, its performance is very stable and robust.

The performance of the proposed method is validated by the FEA model of a typical high-speed traction IM. The result shows that the proposed method can reduce the FEA calculation time by 99%. Since the example calculation point is a very challenging test case, it is reasonable to believe that assuming error tolerance is 1%, the ramping up time of I_s can be set at $6t_{syn}$ and the multi-step ER method can be set to increase the rotor speed gradually within $6t_{syn}$, then the transient response time can be limited within $12t_{syn}$ in most cases.

DATA AVAILABILITY STATEMENT

The raw data supporting the conclusion of this article will be made available by the authors, without undue reservation.

AUTHOR CONTRIBUTIONS

HC: IM FEA model construction and writing the manuscript. RH and HZ: programming. HX, SL, and JX: literature review and writing the manuscript.

FUNDING

This work was supported by the Science and Technology Project of State grid Cooperation of China: Research on Harmonic Pollution of Non-Ideal AC Filter Inductor in V2G System and Countermeasures (5400-202099287A-0-0-00).

ACKNOWLEDGMENTS

The authors would like to thank ANSYS Inc., for providing the finite element analysis tool Maxwell.

REFERENCES

Cai, H. (2020). "A Fast Calculation Method for Steady State Performance of High Speed Traction Induction Machine by Finite Element Analysis," in 2020 IEEE Energy Conversion Congress and Exposition (ECCE), 4284–4291. doi:10.1109/ECCE44975.2020.9236417

Di, C., Petrov, I., Pyrhonen, J. J., and Chen, J. (2019). Accelerating the Time-Stepping Finite-Element Analysis of Induction Machines in Transient-Magnetic Solutions. *IEEE Access* 7, 122251–122260. doi:10.1109/ACCESS.2019.2938269

El-Refaie, A. (2013). Motors/generators for Traction/propulsion Applications: A Review. *IEEE Veh. Technol. Mag.* 8, 90–99. doi:10.1109/MVT.2012.2218438

Fu, W. N., Ho, S. L., and Zhou, P. (2012). Reduction of Computing Time for Steady-State Solutions of Magnetic Field and Circuit Coupled Problems Using Time-Domain Finite-Element Method. *IEEE Trans. Magn.* 48, 3363–3366. doi:10.1109/TMAG.2012.2199285

Haghbin, S., Lundmark, S., Alakula, M., and Carlson, O. (2013). Grid-connected Integrated Battery Chargers in Vehicle Applications: Review and New Solution. *IEEE Trans. Ind. Electron.* 60, 459–473. doi:10.1109/TIE.2012.2187414

Khaligh, A., and D'Antonio, M. (2019). Global Trends in High-Power On-Board Chargers for Electric Vehicles. *IEEE Trans. Veh. Technol.* 68, 3306–3324. doi:10.1109/TVT.2019.2897050

Kim, Y., Koo, B., and Nam, K. (2019). Induction Motor Design Strategy for Wide Constant Power Speed Range. *IEEE Trans. Ind. Electron.* 66, 8372–8381. doi:10.1109/TIE.2018.2885691

Le Besnerais, J., Fasquelle, A., Hecquet, M., Pelle, J., Lanfranchi, V., and Harmand, S. (2010). Multiphysics Modeling: Electro-Vibro-Acoustics and Heat Transfer of Pwm-Fed Induction Machines. *IEEE Trans. Ind. Electronics* 57, 1279–1287. doi:10.1109/TIE.2009.2029526

Lin, D., Zhou, P., Chen, N., Lu, C., and Christini, M. (2017). "Fast Methods for Reaching Ac Steady State in Fe Transient Analysis," in 2017 IEEE International Electric Machines and Drives Conference (IEMDC), 1–6. doi:10.1109/IEMDC.2017.8001996

Metwly, M. Y., Abdel-Majeed, M. S., Abdel-Khalik, A. S., Hamdy, R. A., Hamad, M. S., and Ahmed, S. (2020). A Review of Integrated On-Board Ev Battery Chargers: Advanced Topologies, Recent Developments and Optimal Selection of Fscw Slot/pole Combination. *IEEE Access* 8, 85216–85242. doi:10.1109/ACCESS.2020.2992741

Rainer, S., Biro, O., Stermecki, A., and Weilharter, B. (2012). Frequency Domain Evaluation of Transient Finite Element Simulations of Induction Machines. *IEEE Trans. Magnetics* 48, 851–854. doi:10.1109/TMAG.2011.2173164

Wang, Z., Zhang, Y., You, S., Xiao, H., and Cheng, M. (2020). An Integrated Power Conversion System for Electric Traction and V2g Operation in Electric Vehicles with a Small Film Capacitor. *IEEE Trans. Power Electronics* 35, 5066–5077. doi:10.1109/TPEL.2019.2944276

Xiao, Y., Liu, C., and Yu, F. (2019). An Integrated On-Board Ev Charger with Safe Charging Operation for Three-phase Ipm Motor. *IEEE Trans. Ind. Electronics* 66, 7551–7560. doi:10.1109/TIE.2018.2880712

Yamazaki, K., Kuramochi, S., Fukushima, N., Yamada, S., and Tada, S. (2012). Characteristics Analysis of Large High Speed Induction Motors Using 3-d Finite Element Method. *IEEE Trans. Magnetics* 48, 995–998. doi:10.1109/TMAG.2011.2172919

Zhu, Z. Q., and Howe, D. (2007). Electrical Machines and Drives for Electric, Hybrid, and Fuel Cell Vehicles. *Proc. IEEE* 95, 746–765. doi:10.1109/JPROC.2006.892482

Conflict of Interest: HX, SL, and JX were employed by Nanjing Power Supply Company State Grid Jiangsu Electric Power Co., Ltd.

The remaining authors declare that the research was conducted in the absence of any commercial or financial relationships that could be construed as a potential conflict of interest.

Publisher's Note: All claims expressed in this article are solely those of the authors and do not necessarily represent those of their affiliated organizations, or those of the publisher, the editors, and the reviewers. Any product that may be evaluated in this article, or claim that may be made by its manufacturer, is not guaranteed or endorsed by the publisher.

frontiers | Frontiers in Energy Research

ORIGINAL RESEARCH
published: 25 April 2022
doi: 10.3389/fenrg.2022.884886

Robust Bi-Level Planning Method for Multi-Source Systems Integrated With Offshore Wind Farms Considering Prediction Errors

Qingzhi Jian[1], *Xiaoming Liu*[1], *Xinye Du*[2]*, *Yuyue Zhang*[1], *Nan Wang*[1] *and Yonghui Sun*[2]

[1]Economic and Technological Research Institute, State Grid Shandong Electric Power Co., LTD., Jinan, China, [2]College of Energy and Electrical Engineering, Hohai University, Nanjing, China

Considering the economy, reliability, and output characteristics of multiple power sources (MPS) and energy storage (ES) comprehensively, a multi-source system integrated with offshore wind farms (OWFs) and its construction cost, and operating and maintenance cost model are established. The system is mainly composed of OWFs, thermal power plants, gas turbine power plants, and pumped hydro storage plants. Given the economy of the power system and offshore wind power accommodation, a bi-level optimal capacity configuration and operation scheduling method is proposed for the multi-source system integrated with OWF clusters with the objective function of optimal total cost. Then, a robust bi-level planning method for the multi-source system integrated with OWFs considering the dual uncertainty of load and offshore wind power prediction is proposed, in which the upper and lower models are solved by an improved particle swarm optimization (PSO) algorithm and CPLEX solver, respectively. Based on the method, the cost-optimal capacity configuration and operation scheduling scheme of an MPS and ES can be obtained. Finally, an OWF group in Shandong Province is taken as an example to check the validity and feasibility of the proposed method.

Keywords: offshore wind power integration, generation expansion planning, bi-level optimization, uncertainty, economic optimization, improved PSO

OPEN ACCESS

Edited by:
Qinran Hu,
Southeast University, China

Reviewed by:
Wei Qian,
Henan Polytechnic University, China
Yan Wang,
Zhejiang Sci-Tech University, China

***Correspondence:**
Xinye Du
duxinye1018@163.com

Specialty section:
This article was submitted to Smart Grids, a section of the journal Frontiers in Energy Research

Received: *27 February 2022*
Accepted: *22 March 2022*
Published: *25 April 2022*

Citation:
Jian Q, Liu X, Du X, Zhang Y, Wang N and Sun Y (2022) Robust Bi-Level Planning Method for Multi-Source Systems Integrated With Offshore Wind Farms Considering Prediction Errors. Front. Energy Res. 10:884886. doi: 10.3389/fenrg.2022.884886

1 INTRODUCTION

Onshore wind turbines have shown the trend of production saturation in recent years due to excessive competition. As a new direction of new energy development, offshore wind power has significant advantages (such as no occupation of onshore land, high wind speed, stable wind direction, and proximity to the load center), creating a new situation in the development of wind power all over the world (Nian et al., 2019; Wu et al., 2019). However, the anti-peak characteristics of offshore wind power are particularly noticeable. The degree and probability of strong anti-peak regulation of offshore wind power are greater than those of onshore wind power. Large-scale offshore wind power integration will increase the difficulty of peak regulation of an electric power system. The problem of poor controllability of a high proportion of new energy power generation can be solved effectively with a multi-source complementary strategy. Therefore, power system dispatching establishes the coordination mechanism of multi-source complementary advantages and realizes the optimal planning of multiple power sources (MPS) and energy storage (ES) on the premise of safety and stability,

which is of great significance to reduce the power supply cost and to improve the operation economy of the power system and the level of renewable energy consumption.

In recent years, offshore wind power has developed rapidly and has broad market prospects. So far, extensive research has been conducted on offshore wind power (Kang et al., 2019; Costoya et al., 2020; Zhang et al., 2020; Riboldi et al., 2021). Li et al. (2020)compared and evaluated the characteristics and wind energy potential of onshore and offshore wind power based on the original wind records of onshore and offshore wind measured at wind towers in the southeast coastal area of China. Jiang (2021) proposed the review of the offshore wind turbine installation technology, and the future development of four technical fields was prospected to guide the development of offshore wind turbine installation. The opportunity for combining offshore wind turbines and wave energy converters was analyzed through a spatial planning method, and the possibility of combining different renewable technologies was considered based on existing pressures and vulnerabilities through quantitative indicators (Azzellino et al., 2019). Yang et al. (2020), considering potential maintenance opportunities brought by the dynamic speed of the winds, constructed a novel weather-centered operation and maintenance framework to combine the impact of wind on energy production and maintenance plans. Ji et al. (2020), considering the effects of an offshore station, DC cable, and onshore station, proposed an offshore AC side impedance model of an MMC-HVDC system for wind power integration. Most of the aforementioned studies focus on the technical problems of offshore wind turbines and the grid connection technology of offshore wind farms (OWFs), while research on the power system suitable for the integration of offshore wind power clusters with obvious anti-peak characteristics is rarely mentioned.

Power planning is a significant and essential preliminary work in the development of the power industry. As an important part of power system expansion planning, it has many positive effects, and there have already been a large number of relevant studies (Gan et al., 2020; Lv et al., 2020; Chen et al., 2021; Xie et al., 2021). Deng and Lv. (2020), to study the changes in optimization models caused by the large penetration of variable renewable energy, screened some studies on power system planning considering the addition of variable renewable energy, and these models were further deconstructed and compared. Li et al. (2021), given various uncertainties and multi-energy demand-side management, proposed a risk-averse method for heterogeneous energy storage deployment in a residential multi-energy microgrid. Hu et al. (2021)proposed a complementary power generation model of wind-hydropower-pumped storage systems, which used hydropower and pumped storage to adjust the fluctuation of wind power. Considering different vehicle-to-building schedules, a robust energy planning approach for hybrid photovoltaic and wind energy systems in a typical high-rise residential building was proposed (Liu et al., 2021). In the study by da Costa et al. (2021),a method of incorporating reliability constraints into the optimal expansion planning of power systems was proposed based on the loss of load probability and expected power of power systems, and the risk

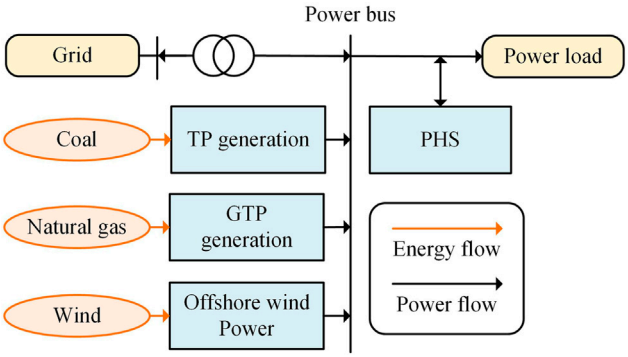

FIGURE 1 | Model of multi-source system integrated with OWFs.

measurement value-at-risk and conditional value-at-risk. However, for the multi-source system with offshore wind power having prediction errors that cannot be ignored, the methods of optimizing the power capacity configuration and operation scheduling are rarely mentioned.

Therefore, a robust bi-level planning method for a multi-source system integrated with OWFs is proposed to realize the optimal capacity configuration and operation optimization in the receiving-end grid. Aiming at the disadvantages of strong intermittency, large fluctuations, and the apparent anti-peak characteristics of offshore wind power, in this study, a multi-source system model suitable for the integration of offshore wind power clusters is established. Based on the coordination and optimization strategies of MPS and ES, a robust bi-level planning model of the system is proposed, completely considering the economy of the power system, the consumption level of offshore wind power, and the prediction error of offshore wind power and load. The improved particle swarm optimization (PSO) algorithm with adaptive inertia weight is used to solve its upper model, and through the case study, it is verified that under the same population size and iteration times, the convergence accuracy of the results is improved.

The remaining sections of this study are organized as follows: The multi-source system integrated with OWFs is constructed in **Section 2**. The robust bi-level planning model for the system considering prediction errors is proposed in **Section 3**. Then, the solution approach of the robust bi-level planning model is proposed in **Section 4**. Case studies, results' comparisons, and analyses are conducted in **Section 5**. Finally, the conclusions of this study are provided in **Section 6**.

2 MULTI-SOURCE SYSTEMS INTEGRATED WITH OFFSHORE WIND FARMS

Based on the research on the output characteristics of MPS and ES, selecting the appropriate equipment types is the basis for the rational planning and coordinated operation of the power system with offshore wind power. The model of the multi-source system integrated with OWFs is shown in **Figure 1**. It can be seen from **Figure 1** that the multi-source system is mainly composed of

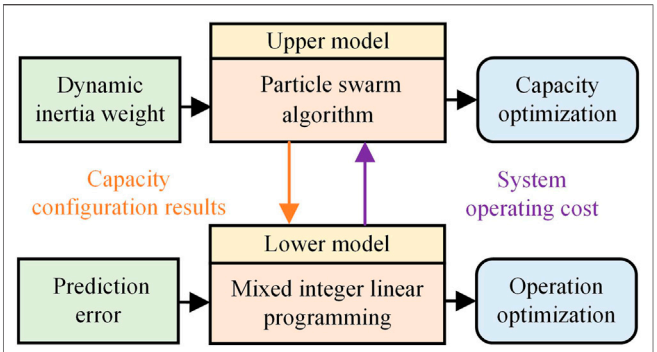

FIGURE 2 | Structure of the robust bi-level planning model.

offshore wind power, thermal power (TP) generation, gas turbine power (GTP) generation, and pumped hydro storage (PHS). TP units are hardly affected by the geographical environment and climate. Furthermore, TP plants have the characteristics of flexible site selection, stable and reliable operation, and fast and deep peak load regulation in the power system with offshore wind power. The capacity configuration and operation mode of a gas turbine (GT) are flexible, and the unit can quickly adjust the power. On the premise of safety and reliability, the GT unit can effectively improve the flexibility of the power system to reduce the impact of offshore wind power fluctuation on the system. PHS has high reliability and fast response speed, which can reduce the peak-valley differences of the system, and plays a certain role in reducing the effects of the anti-peak characteristics of offshore wind power. When the output of offshore wind power changes rapidly, the PHS system can make corresponding adjustments to its fluctuations in time.

3 ROBUST BI-LEVEL PLANNING MODEL OF MULTI-SOURCE SYSTEMS

On the basis of considering the prediction error of offshore wind power and load, a robust bi-level planning model of the multi-source system integrated with OWFs is constructed to optimize the capacity configuration and operation scheduling of MPS and ES. The model structure is shown in **Figure 2**. The improved PSO algorithm is used to optimize the capacity of MPS and ES in the upper model. Taking into account the prediction error, the operation scheduling scheme with the optimal cost is generated in the lower model based on the capacity configuration results. Through the optimization iteration of the upper and lower models, the planning scheme of the multi-source system with the best cost is obtained.

Upper Model

In this study, the coordinated planning of MPS and ES of a multi-source system integrated with OWFs is carried out from the perspective of realizing the optimal economy of the system. The upper model takes the minimum total cost of the system including construction, operating, and maintenance costs as the objective function, and its decision variables are the capacity of MPS and ES. To minimize the total cost of a typical day, the objective function of the upper model can be expressed by

$$\min C_{\mathrm{TOTAL}} = C_{\mathrm{IM}} + C_{\mathrm{OP}}, \tag{1}$$

where C_{TOTAL}, C_{IM}, and C_{OP} are the total cost, construction and maintenance cost, and operating cost of the multi-source system in a scheduling cycle, respectively.

The system construction and maintenance costs are allocated to each scheduling cycle in the life cycle through the discount rate, and its mathematical model is given by

$$C_{\mathrm{IM}} = \sum_{\varphi}\left(1+\beta_{\varphi}\right)P_{\varphi}W_{\varphi}\lambda\left(1+\lambda\right)^{L_{\varphi}}\Big/\left(365\left(\left(1+\lambda\right)^{L_{\varphi}}-1\right)\right), \tag{2}$$

where β_{φ} is the ratio of the maintenance cost and construction cost of system φ, including TP, GTP, and PHS systems. P_{φ} is the unit cost of system φ. W_{φ} is the capacity of system φ. L_{φ} is the life cycle of the unit in system φ. λ is the discount rate.

The capacity constraints of MPS and ES are considered in the upper model, and its mathematical model is shown as

$$W_{\varphi\min} \le W_{\varphi} \le W_{\varphi\max}, \tag{3}$$

where $W_{\varphi\max}$ and $W_{\varphi\min}$ are the upper and lower limits of the planned capacity of system φ, respectively.

Lower Model

3.1.1 Objective Function

Considering the operating cost of TP, GTP, and PHS systems, the minimum operating cost of the multi-source system is taken as the objective in the lower model. The mathematical model of the objective function is formulated as

$$\min C_{\mathrm{OP}} = \sum_{t=1}^{T}\left(C_{\mathrm{FO}}\left(t\right)+C_{\mathrm{TO}}\left(t\right)+C_{\mathrm{PO}}\left(t\right)\right), \tag{4}$$

where $C_{\mathrm{FO}}\left(t\right)$, $C_{\mathrm{TO}}\left(t\right)$, and $C_{\mathrm{PO}}\left(t\right)$ are the operating costs of TP, GTP, and PHS systems at time t, respectively. T is the number of times in a scheduling cycle.

The operating cost of the TP system is the coal consumption cost of TP units, and its mathematical model can be described by

$$C_{\mathrm{FO}}\left(t\right) = \sum_{j=1}^{N_{\mathrm{F}}}\left(a_{j}P_{\mathrm{F},j}\left(t\right)^{2}+b_{j}P_{\mathrm{F},j}\left(t\right)+c_{j}\right), \tag{5}$$

where a_j, b_j, and c_j are the operating cost correlation coefficients of TP unit j. $P_{\mathrm{F},j}\left(t\right)$ is the output power of TP unit j at time t. N_{F} is the total number of TP units.

The mathematical model of the operating cost of the GTP system can be expressed by

$$C_{\mathrm{TO}}\left(t\right) = p_{\mathrm{n}}\sum_{g=1}^{N_{\mathrm{T}}}P_{\mathrm{T},g}\left(t\right)\div\eta, \tag{6}$$

where p_{n} is the unit fuel consumption cost of natural gas. $P_{\mathrm{T},g}\left(t\right)$ is the output power of GT unit g at time t. η is the generation efficiency of GT unit g. N_{T} is the total number of GT units.

The mathematical model of the operating cost of the PHS system is given as

$$C_{\mathrm{PO}}(t)=\sum_{k=1}^{N_{\mathrm{H}}}\left(S_{\mathrm{gen},k}(t)+S_{\mathrm{pum},k}(t)\right), \tag{7}$$

$$\begin{cases} S_{\mathrm{gen},k}(t)=s_{\mathrm{gen},k}u_{\mathrm{gen},k}(t)\left(u_{\mathrm{gen},k}(t)-u_{\mathrm{gen},k}(t-1)\right) \\ S_{\mathrm{pum},k}(t)=s_{\mathrm{pum},k}u_{\mathrm{pum},k}(t)\left(u_{\mathrm{pum},k}(t)-u_{\mathrm{pum},k}(t-1)\right) \end{cases}, \tag{8}$$

where $S_{\mathrm{gen},k}(t)$ and $S_{\mathrm{pum},k}(t)$ are the start-up costs of PHS unit k operating in generating and pumping modes at time t, respectively. N_{H} is the total number of PHS units. $s_{\mathrm{gen},k}$ and $s_{\mathrm{pum},k}$ are the start-up costs of PHS unit k operating in generating and pumping modes, respectively. $u_{\mathrm{gen},k}(t)$ and $u_{\mathrm{pum},k}(t)$ are used to verify whether PHS unit k is in generating and pumping modes at time t, respectively.

3.1.2 Constraints

1) Power balance constraint

$$\sum_{k=1}^{N_{\mathrm{H}}}P_{\mathrm{gen},k}(t)+\sum_{j=1}^{N_{\mathrm{F}}}P_{\mathrm{F},j}(t)+\sum_{g=1}^{N_{\mathrm{T}}}P_{\mathrm{T},g}(t)+\sum_{w=1}^{N_{\mathrm{W}}}P_{\mathrm{W},w}(t)-\sum_{w=1}^{N_{\mathrm{W}}}P_{\mathrm{E},w}(t) =\sum_{d=1}^{D}P_{d}(t)+\sum_{k=1}^{N_{\mathrm{H}}}P_{\mathrm{pum},k}(t), \tag{9}$$

where $P_{\mathrm{gen},k}(t)$ and $P_{\mathrm{pum},k}(t)$ are the generating and pumping power of PHS unit k at time t, respectively. $P_{\mathrm{W},w}(t)$ is the predicted value of the wind power of OWF w at time t. $P_{\mathrm{E},w}(t)$ is the wind power curtailment of OWF w at time t. $P_{d}(t)$ is the predicted value of active power of the load of node d at time t. N_{W} is the total number of OWFs. D is the number of load nodes.

2) Offshore wind power curtailment constraint

$$0\le\sum_{t=1}^{T}\sum_{w=1}^{N_{\mathrm{W}}}P_{\mathrm{E},w}(t)\le e\times\sum_{t=1}^{T}\sum_{w=1}^{N_{\mathrm{W}}}P_{\mathrm{W},w}(t), \tag{10}$$

where e is the upper limit of the curtailment rate of offshore wind power.

3) Equipment operating constraint

The operating constraints of TP units and GT units can be uniformly expressed as

$$\begin{cases} u_{n}(t)P_{\mathrm{min},n}\le P_{n}(t)\le u_{n}(t)P_{\mathrm{max},n} \\ r_{\mathrm{d},n}\Delta t\le P_{n}(t)-P_{n}(t-1)\le r_{\mathrm{u},n}\Delta t \end{cases}, \tag{11}$$

where $u_{n}(t)$ and $P_{n}(t)$ are the on/off state and output power of unit n at time t, respectively. $P_{\mathrm{min},n}$ and $P_{\mathrm{max},n}$ are the minimum and maximum output power allowed by unit n, respectively. $r_{\mathrm{d},n}$ and $r_{\mathrm{u},n}$ are the speed limits of power reduction and power rise of unit n in unit time, respectively. Δt is the scheduling interval.

Power constraints of PHS units and storage capacity constraints of the PHS plant can be referred to the study by Lai et al. (2020).

Robust Bi-Level Planning Model Considering Prediction Errors

The robust optimization problem with uncertain parameters can be summarized as

$$\begin{cases} \min\limits_{x\in R^{n}} f(x,\varepsilon) \\ \text{s.t. } g_{i}(x,\varepsilon)\le 0\ \forall\varepsilon\in U, i=1,2,\ldots m. \end{cases}, \tag{12}$$

where x is the decision variable. ε is an uncertain parameter and belongs to a bounded closed set U. f is the objective function. g is the constraint.

Because of uncertainty factors such as an abnormal offshore wind regime, errors often occur in prediction results of offshore wind power. According to experience, the actual value of offshore wind power and load can be equivalent to uncertain parameters with an unknown probability distribution in the given sets. Robust optimization is applicable to optimization problems with such uncertain parameters, and the uncertainty is completely considered in the modeling (Ratanakuakangwan and Morita, 2021). Therefore, a robust bi-level planning model is proposed for two uncertain parameters which are the predicted values of offshore wind power and load. The modified constraints (9) and (10) in the lower model can be expressed as

$$\begin{cases} \sum\limits_{k=1}^{N_{\mathrm{H}}}P_{\mathrm{gen},k}(t)+\sum\limits_{j=1}^{N_{\mathrm{F}}}P_{\mathrm{F},j}(t)+\sum\limits_{g=1}^{N_{\mathrm{T}}}P_{\mathrm{T},g}(t)+\sum\limits_{w=1}^{N_{\mathrm{W}}}P_{\mathrm{Wu},w}(t)-\sum\limits_{d=1}^{D}P_{\mathrm{u},d}(t)-\sum\limits_{k=1}^{N_{\mathrm{H}}}P_{\mathrm{pum},k}(t)\ge 0 \\ \sum\limits_{t=1}^{T}\left(\sum\limits_{k=1}^{N_{\mathrm{H}}}P_{\mathrm{gen},k}(t)+\sum\limits_{j=1}^{N_{\mathrm{F}}}P_{\mathrm{F},j}(t)-\sum\limits_{d=1}^{D}P_{\mathrm{u},d}(t)-\sum\limits_{k=1}^{N_{\mathrm{H}}}P_{\mathrm{pum},k}(t)\right)\le(e-1)\sum\limits_{t=1}^{T}\sum\limits_{w=1}^{N_{\mathrm{W}}}P_{\mathrm{Wu},w}(t) \end{cases}, \tag{13}$$

where $P_{\mathrm{Wu},w}(t)$ and $P_{\mathrm{u},d}(t)$ are, respectively, the wind power value of OWF w and load value of node d considering prediction errors at time t, which are random variables.

4 SOLUTION APPROACH

The aforementioned model is a mixed-integer nonlinear bi-level planning model. The upper model is solved by the improved PSO algorithm to generate a capacity configuration scheme of MPS and ES. The inertia weight is fixed in PSO (Tsai et al., 2020), which is easy to make the algorithm fall into local optimization. The improved PSO algorithm changing the fixed weight into the dynamic weight adjusted based on the premature convergence and fitness value is adopted in this study.

The dynamic weight formula is shown as

$$\omega=\begin{cases} \omega_{\min}+\dfrac{\left[f_{j}-f_{\min}\right]\times(\omega_{\max}-\omega_{\min})}{f_{\mathrm{av}}-f_{\min}} & f_{j}\le f_{\mathrm{av}} \\ \omega_{\max} & f_{j}>f_{\mathrm{av}} \end{cases}, \tag{14}$$

where f_{j} is the fitness value of the j^{th} particle. f_{av} and $f_{\min}$ are the average fitness and minimum fitness, respectively. $\omega_{\max}$ and $\omega_{\min}$ are the upper and lower limits of dynamic inertia weights, respectively. Corresponding to the bi-level planning model, f_{j} is the objective function of the upper model, that is, the total cost of the system including construction, operating, and maintenance costs. The location of the swarm corresponds to the capacity of MPS and ES planned by the upper model.

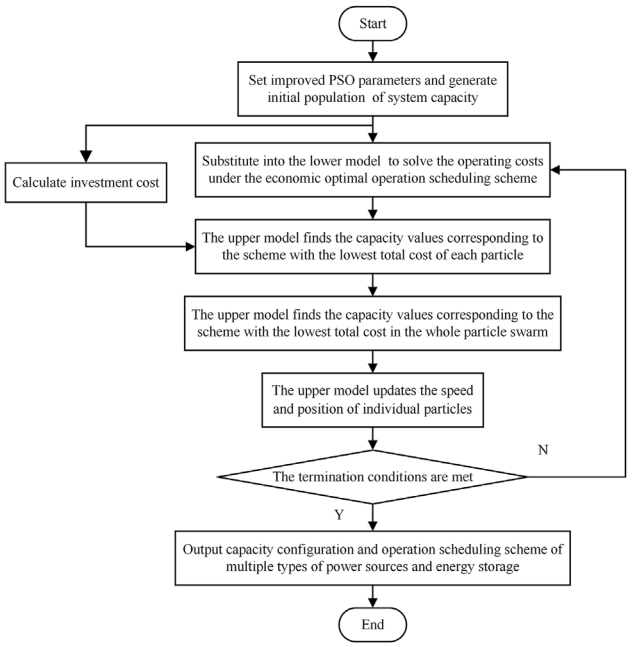

FIGURE 3 | Flowchart of the robust bi-level planning method for the multi-source system.

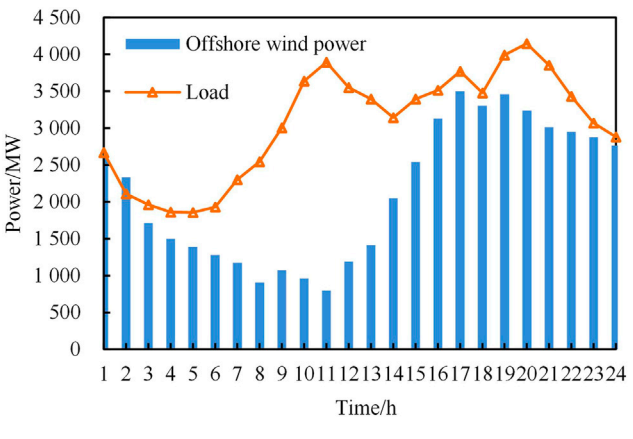

FIGURE 4 | Prediction curves of offshore wind power and load.

The lower layer of the robust bi-level planning model is a mixed-integer quadratic programming (MIQP) problem, and the parameter uncertainty is taken into account. The CPLEX solver is used to solve the lower model and generate an operation scheduling scheme of MPS and ES with minimum cost. The flow of the robust bi-level planning method for the multi-source system integrated with OWFs is shown in **Figure 3**.

5 CASE STUDY

The typical daily power prediction of an OWF group in Shandong Province, China, is used to verify the effectiveness of the proposed robust bi-level planning method. The prediction curves of offshore wind power and load in a scheduling cycle are shown in **Figure 4**.

TABLE 1 | Unit construction cost and life cycle.

Types	Construction cost (×10^3¥/MW)	Life cycle of unit (year)
TP plant	182.00	30
GTP plant	125.00	20
PHS plant	528.57	80

The unit construction cost and life cycle of the TP, GTP, and PHS plants are shown in **Table 1**. The discount rate is 6.7%. The power generation efficiency of the GT unit is 33%. The fuel consumption cost of natural gas is ¥ 25 million/MW (¥ is the unit of CNY).

Considering the uncertain factors in the prediction process, three scenarios are designed for comparative analysis.

Scenario 1: Bi-level planning for the multi-source system integrated with OWFs without considering prediction errors.

Scenario 2: Robust bi-level planning that takes the prediction errors of offshore wind power into account, and the prediction error of offshore wind power is within 10%.

Scenario 3: Robust bi-level planning that considers the dual uncertainty of load and offshore wind power prediction. The prediction error of offshore wind power is within 10%, and the load prediction error is within 2.5%.

In the solution algorithm of the lower model, the population size of the particle swarm is set to 100, the number of iterations is set to 50, and the maximum and minimum inertia weights are 0.8 and 0.4, respectively. The capacity configuration scheme with the optimal total cost under each scenario is shown in **Table 2**. The construction cost corresponding to a scheduling cycle is shown in **Table 3**, and the operating and maintenance costs of each scenario in a scheduling cycle are shown in **Table 4**. As can be seen, the total cost of the corresponding planning scheme in scenario 1 is the lowest. With the increase of prediction uncertainty, the planning scheme of scenarios 2 and 3 increases part of the power capacity and operating and maintenance costs compared with scenario 1. Combined with **Table 3** and **Table 4**, it can be seen that the operating and maintenance costs account for the largest proportion of the total cost of the TP and GTP systems. The minimum total cost of the system is taken as the objective function in the robust bi-level planning model proposed in this study. Therefore, the planning results will give priority to the cost. It can be inferred that the total cost and output of the TP and GTP systems are largely determined by the operating cost.

The optimal scheduling results according to the capacity configuration scheme in each scenario are shown in **Figure 5**, **Figure 6**, and **Figure 7**, respectively. In scenario 1, according to the optimization results, the wind power curtailment is controlled within 0.2%. It can be seen that under the planning scheme, renewable energy is completely utilized on the basis of ensuring the safe and stable operation of the power system. The PHS system uses the excess electric energy at time 2 to pump water to the upper reservoir and converts it into high-value electric energy

TABLE 2 | Optimal capacity configuration results for each scenario.

Scenarios	TP system (MW)	GTP system (MW)	PHS system (MW)	Total cost (×10^5¥)
S1	1,246.00	1,856.44	187.44	952.45
S2	1,231.57	1,496.26	328.67	1,166.49
S3	1,616.44	1,538.11	623.45	1,278.99

TABLE 3 | Construction cost for each scenario.

Scenarios	TP system (×10^3¥)	GTP system (×10^3¥)	PHS system (×10^3¥)	Total construction cost (×10^3¥)
S1	485.68	586.20	182.88	1,254.76
S2	480.05	472.47	320.68	1,273.20
S3	630.07	485.68	608.30	1,724.05

TABLE 4 | Operating and maintenance costs for each scenario.

Scenarios	TP system (×10^5¥)	GTP system (×10^5¥)	PHS system (×10^3¥)	Total operating and maintenance costs (×10^5¥)
S1	479.70	459.60	60.24	939.90
S2	685.97	465.37	241.68	1,153.76
S3	729.70	529.02	302.70	1,261.75

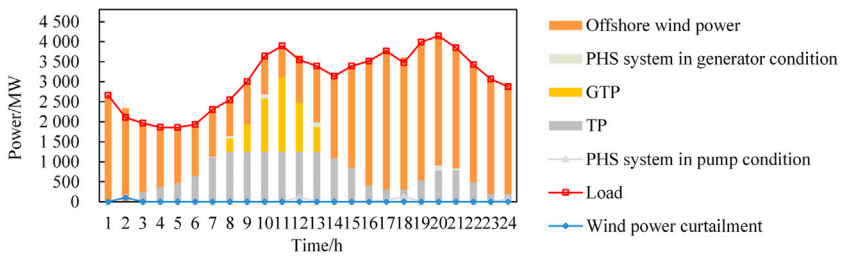

FIGURE 5 | Operation planning result for scenario 1.

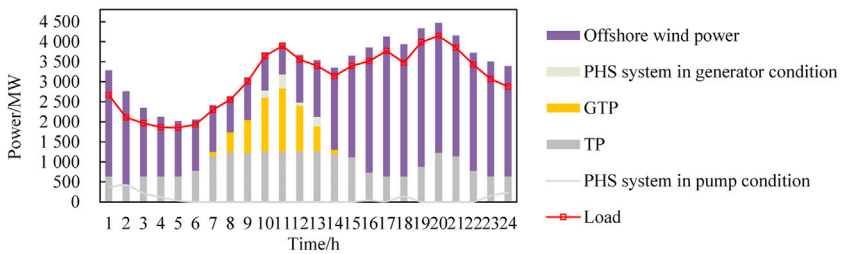

FIGURE 6 | Operation planning result for scenario 2.

when the load demand is large, which ensures the safe operation of the power system and solves the contradiction of supply and demand during the climax and ebb periods of the power grid effectively. It is known that in addition to time 2, when the wind power value of the OWF cluster is greater than the load, theoretically, there is no need for the PHS system to work in the pumping mode at other times. In the actual situation, considering the climbing constraints of the unit, the output power cannot drop to 0 quickly in a short time. Therefore, the excess power output from the OWF cluster and other power

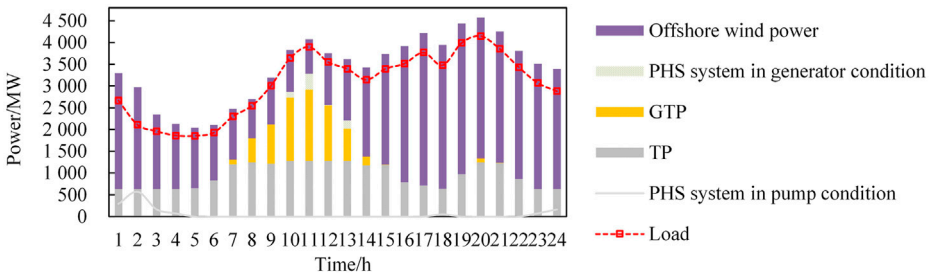

FIGURE 7 | Operation planning result for scenario 3.

TABLE 5 | Comparison of solution results.

Scenarios	Total cost (×10^5¥)	
	PSO	Improved PSO
S2	1169.28	1,166.49
S3	1,279.71	1,278.99

sources is absorbed by the PHS system as ES at 12, 18, and other times. The same is true for scenarios 2 and 3. Because the climbing constraint of the unit cannot fit the load curve, part of the output power is converted into ES through the PHS system and absorbed. According to **Figure 5**, **Figure 6**, **Figure 7**, and **Table 4**, the TP system can maintain the minimum demand in the power system, and its total cost is lower than that of GTP and PHS systems. The GT unit features outstanding dynamic characteristics and strong peak-load regulation capability, and can quickly adjust the power output. Therefore, it is used as the supplementary power source of the TP unit to meet the load demand. The PHS system is not the main output power source of the power system but mainly the power source for regulation because of the constraints of unit capacity and reservoir capacity.

In the interest of verifying the performance of the improved PSO algorithm with dynamic inertia weight in solving the robust bi-level planning model, the traditional PSO algorithm is applied to solve the upper model in scenarios 2 and 3 under the same population size and iteration times, and the solution results of the two methods are shown in **Table 5**. It can be seen that the optimal cost of the schemes solved by the improved PSO algorithm in scenarios 2 and 3 are 278.87 (×10^3¥) and 71.85 (×10^3¥) lower than that of the traditional PSO algorithm, respectively. This proves that the PSO algorithm with dynamic inertia weight has a stronger global optimization ability, and the power capacity configuration and operation scheduling scheme with a lower total cost can be obtained when using this algorithm to solve the robust bi-level planning model.

6 CONCLUSION

To adapt to the consumption of offshore wind power clusters, a multi-source system model was constructed, which included the offshore wind power, TP, GTP, and PHS systems. Moreover, considering the system economy and offshore wind power consumption level, and taking into account the dual uncertainty of load and offshore wind power prediction, a robust bi-level planning method for the multi-source system was proposed, in which the improved PSO algorithm with dynamic weight was used to solve the model. The economic optimal capacity configuration and operation scheduling scheme of MPS and ES were generated based on the method proposed in this study. The planning scheme realized the balance of supply and demand between power sources and load and the peak load shifting in the power grid. In addition, the method proposed in this study improved the inclusiveness of prediction errors and made the system have the advantages of good stability and high reliability.

DATA AVAILABILITY STATEMENT

The original contributions presented in the study are included in the article/Supplementary Material, further inquiries can be directed to the corresponding author.

AUTHOR CONTRIBUTIONS

QJ: methodology, software, writing—original draft, and data curation. XL: investigation, software, writing—original draft, and data curation. XD: conceptualization of this study, software, and supervision. YZ: investigation, and review and editing. NW: data curation and review and editing. YS: writing—review and editing.

FUNDING

This study was funded by the Science and Technology Program of the State Grid Shandong Electric Power Company under Grant 52062519000R.

REFERENCES

Azzellino, A., Lanfredi, C., Riefolo, L., De Santis, V., Contestabile, P., and Vicinanza, D. (2019). Combined Exploitation of Offshore Wind and Wave Energy in the Italian Seas: A Spatial Planning Approach. *Front. Energ. Res.* 7, 42. doi:10.3389/fenrg.2019.00042

Chen, H., Fu, L., Bai, L., Jiang, T., Xue, Y., Zhang, R., et al. (2021). Distribution Market-Clearing and Pricing Considering Coordination of DSOS and Iso: An EPEC Approach. *IEEE Trans. Smart Grid* 12 (4), 3150–3162. doi:10.1109/TSG.2021.3061282

Costoya, X., deCastro, M., Carvalho, D., and Gómez-Gesteira, M. (2020). On the Suitability of Offshore Wind Energy Resource in the United States of America for the 21st century. *Appl. Energ.* 262, 114537. doi:10.1016/j.apenergy.2020.114537

da Costa, L. C., Thome, F. S., Garcia, J. D., and Pereira, M. V. F. (2021). Reliability-Constrained Power System Expansion Planning: a Stochastic Risk-Averse Optimization Approach. *IEEE Trans. Power Syst.* 36 (1), 97–106. doi:10.1109/TPWRS.2020.3007974

Deng, X., and Lv, T. (2020). Power System Planning with Increasing Variable Renewable Energy: A Review of Optimization Models. *J. Clean. Prod.* 246, 118962. doi:10.1016/j.jclepro.2019.118962

Gan, W., Shahidehpour, M., Yan, M., Guo, J., Yao, W., Paaso, A., et al. (2020). Coordinated Planning of Transportation and Electric Power Networks with the Proliferation of Electric Vehicles. *IEEE Trans. Smart Grid* 11 (5), 4005–4016. doi:10.1109/TSG.2020.2989751

Hu, S., Xiang, Y., Liu, J., Li, J., and Liu, C. (2021). A Two-Stage Dispatching Method for Wind-Hydropower-Pumped Storage Integrated Power Systems. *Front. Energ. Res.* 9, 646975. doi:10.3389/fenrg.2021.646975

Ji, K., Tang, G., Pang, H., and Yang, J. (2020). Impedance Modeling and Analysis of MMC-HVDC for Offshore Wind Farm Integration. *IEEE Trans. Power Deliv.* 35 (3), 1488–1501. doi:10.1109/TPWRD.2019.2946450

Jiang, Z. (2021). Installation of Offshore Wind Turbines: A Technical Review. *Renew. Sustain. Energ. Rev.* 139, 110576. doi:10.1016/j.rser.2020.110576

Kang, J., Sun, L., and Guedes Soares, C. (2019). Fault Tree Analysis of Floating Offshore Wind Turbines. *Renew. Energ.* 133, 1455–1467. doi:10.1016/j.renene.2018.08.097

Lai, X., Li, C., Zhou, J., Zhang, Y., and Li, Y. (2020). A Multi-Objective Optimization Strategy for the Optimal Control Scheme of Pumped Hydropower Systems under Successive Load Rejections. *Appl. Energ.* 261, 114474. doi:10.1016/j.apenergy.2019.114474

Li, Y., Huang, X., Tee, K. F., Li, Q., and Wu, X.-P. (2020). Comparative Study of Onshore and Offshore Wind Characteristics and Wind Energy Potentials: A Case Study for Southeast Coastal Region of China. *Sustainable Energ. Tech. Assessments* 39, 100711. doi:10.1016/j.seta.2020.100711

Li, Z., Xu, Y., Feng, X., and Wu, Q. (2021). Optimal Stochastic Deployment of Heterogeneous Energy Storage in a Residential Multienergy Microgrid with Demand-Side Management. *IEEE Trans. Ind. Inf.* 17 (2), 991–1004. doi:10.1109/TII.2020.2971227

Liu, J., Cao, S., Chen, X., Yang, H., and Peng, J. (2021). Energy Planning of Renewable Applications in High-Rise Residential Buildings Integrating Battery and Hydrogen Vehicle Storage. *Appl. Energ.* 281, 116038. doi:10.1016/j.apenergy.2020.116038

Lv, Z., Kong, W., Zhang, X., Jiang, D., Lv, H., and Lu, X. (2020). Intelligent Security Planning for Regional Distributed Energy Internet. *IEEE Trans. Ind. Inf.* 16 (5), 3540–3547. doi:10.1109/TII.2019.2914339

Nian, V., Liu, Y., and Zhong, S. (2019). Life Cycle Cost-Benefit Analysis of Offshore Wind Energy under the Climatic Conditions in Southeast Asia - Setting the Bottom-Line for Deployment. *Appl. Energ.* 233-234, 1003–1014. doi:10.1016/j.apenergy.2018.10.042

Ratanakuakangwan, S., and Morita, H. (2021). Hybrid Stochastic Robust Optimization and Robust Optimization for Energy Planning - A Social Impact-Constrained Case Study. *Appl. Energ.* 298, 117258. doi:10.1016/j.apenergy.2021.117258

Riboldi, L., Alves, E. F., Pilarczyk, M., Tedeschi, E., and Nord, L. O. (2021). Optimal Design of a Hybrid Energy System for the Supply of Clean and Stable Energy to Offshore Installations. *Front. Energ. Res.* 8, 607284. doi:10.3389/fenrg.2020.607284

Tsai, J.-T., Chou, P.-Y., and Chou, J.-H. (2020). Color Filter Polishing Optimization Using ANFIS with Sliding-Level Particle Swarm Optimizer. *IEEE Trans. Syst. Man. Cybern, Syst.* 50 (3), 1193–1207. doi:10.1109/TSMC.2017.2776158

Wu, X., Hu, Y., Li, Y., Yang, J., Duan, L., Wang, T., et al. (2019). Foundations of Offshore Wind Turbines: A Review. *Renew. Sustain. Energ. Rev.* 104, 379–393. doi:10.1016/j.rser.2019.01.012

Xie, P., Jia, Y., Chen, H., Wu, J., and Cai, Z. (2021). Mixed-Stage Energy Management for Decentralized Microgrid Cluster Based on Enhanced Tube Model Predictive Control. *IEEE Trans. Smart Grid* 12 (5), 3780–3792. doi:10.1109/TSG.2021.3074910

Yang, L., Li, G., Zhang, Z., Ma, X., and Zhao, Y. (2020). Operations & Maintenance Optimization of Wind Turbines Integrating Wind and Aging Information. *IEEE Trans. Sustain. Energ.* 12 (1), 211–221. doi:10.1109/TSTE.2020.2986586

Zhang, R., Jiang, T., Li, F., Li, G., Chen, H., and Li, X. (2020). Coordinated Bidding Strategy of Wind Farms and Power-To-Gas Facilities Using a Cooperative Game Approach. *IEEE Trans. Sustain. Energ.* 11 (4), 2545–2555. doi:10.1109/TSTE.2020.2965521

Conflict of Interest: Authors QJ, XL, YZ, and NW were employed by the Economic and Technological Research Institute, State Grid Shandong Electric Power Co., LTD. The funder had the following involvement with study: providing parameters of equipment in the multi-source system and the predicted power data of an offshore wind farm group in Shandong Province, China.

The remaining authors declare that the research was conducted in the absence of any commercial or financial relationships that could be construed as a potential conflict of interest.

frontiers | Frontiers in Energy Research

ORIGINAL RESEARCH
published: 25 April 2022
doi: 10.3389/fenrg.2022.875499

Optimal Capacity Allocation Model for Integrated Energy Microgrids Considering Aggregation of Prosumers Under Multi-Market Mechanisms

Xinwen Wang[1,2], *Xiaoqing Bai*[1,2]* *and Puming Wang*[1,2]

[1]School of Electrical Engineering, Guangxi University, Nanning, China, [2]Key Laboratory of Guangxi Electric Power System Optimization and Energy-Saving Technology, Guangxi University, Nanning, China

Traditional energy consumers gradually change to the new form of aggregation of prosumers (AOP) in the integrated energy microgrid (IEM) on the demand side. The emergence of the AOPs has led to the IEM's structure changes, resulting in the emergence of two major stakeholders, the integrated energy microgrid service providers (IEMSPs) and the AOPs. The primary studies of this study are to configure the capacity for devices managed by IEMSP and AOPs with minimal costs. To achieve satisfaction for both IEMSP and AOPs, the approach of the non-cooperative game is used to allocate the capacity of devices managed by IEMSP and devices of AOPs. In detail, the IEMSP acts as a leader who determines the electricity pricing to minimize the cost, while the AOPs respond with electricity purchase or sales as the followers according to the price information provided by IEMSP. Moreover, electricity trading between AOPs is considered to reduce transmission losses and promote energy consumption nearby. To investigate the application of the multi-market mechanism in the optimal capacity allocation of IEM, a coupling mechanism of green certificate trading, carbon emission trading, and the electricity market is built in the proposed model. The cases are studied to verify the effectiveness of the proposed model in terms of saving the configuration capacity, reducing carbon emissions, and increasing the environmental benefits.

Keywords: aggregation of prosumers, integrated energy microgrid, integrated energy microgrid service provider, linear ladder carbon trading, non-cooperative game capacity allocation, multi-market mechanism

OPEN ACCESS

Edited by:
Tao Chen,
Southeast University, China

Reviewed by:
Guifu Du,
Soochow University, China
Yunting Yao,
Cardiff University, United Kingdom
Xiaoling Su,
Qinghai University, China

***Correspondence:**
Xiaoqing Bai
baixq@gxu.edu.cn

Specialty section:
This article was submitted to Smart Grids, a section of the journal Frontiers in Energy Research

Received: *14 February 2022*
Accepted: *17 March 2022*
Published: *25 April 2022*

Citation:
Wang X, Bai X and Wang P (2022) Optimal Capacity Allocation Model for Integrated Energy Microgrids Considering Aggregation of Prosumers Under Multi-Market Mechanisms. Front. Energy Res. 10:875499. doi: 10.3389/fenrg.2022.875499

1 INTRODUCTION

A large amount of greenhouse gas emissions has created an enormous burden on the earth's environment, and the power system has the most carbon emissions of all industrial systems (Chen et al., 2010). The integrated energy microgrid (IEM) provides a new way to realize energy conservation and emission reduction (Wang et al., 2019). There are substantial studies to solve challenges in the optimal capacity allocation of the IEM. Akram et al. (2018) proposed two constraint-based iterative search algorithms to size the devices in a wind/solar/battery grid-connected microgrid in an optimal way. Atia and Yamada (2016) presented a model based on mixed-integer linear programming to optimize an energy system with battery storage in its

residential microgrids. Quashie et al. (2018) proposed bilevel planning of microgrids and optimized storage capacity under the management of a distribution system operator. Clairand et al. (2019) discussed the generation planning problem in diesel-based island microgrids with renewable energy sources. However, based on the abovementioned studies, the research on the capacity allocation of the IEM needs to pay attention to the introduction of emerging things in the IEM, such as prosumers which can not only consume but also produce energy (Parag and Sovacool, 2016).

Distributed energy sources in the IEM have the natural ability to act as prosumers because they are located on the demand side. Some studies have paid attention to the energy sharing and trading among adjacent prosumers. The interaction and optimization solution technology of the prosumer management system are introduced by Zafar et al. (2018). Chen et al. (2018) pointed out that the local energy sharing mode of the interaction between the prosumers in the distribution network has research value. Wang et al. (2020) proposed the P2P energy trading based on the urban community microgrid and considered the differentiated characteristics of prosumers so as to realize the coordination and complementarity of resources. Multiple prosumers can aggregate together to be the aggregation of prosumers (AOPs). In terms of the study of the AOP, Shafie-Khah et al. (2017) proposed an operational household energy management system to deal with the problem of operation of the production and consumer groups, and Liu et al. (2017) put forward the dispatch strategy of the prosumers to encourage users to participate in energy sharing by a lower price than the internal electricity price than the grid electricity price. A multi-microgrid hybrid energy sharing framework is presented for a heat-electricity IEM with combined heat and power by Liu et al. (2019). However, the abovementioned questions do not discuss the impact of the emergence of AOPs on the capacity allocation of the IEM.

At present, the most of existing traditional optimization models only focus on the benefits of the comprehensive IEM or the AOPs, lacking research on the optimization of the IEM considering AOPs. This study introduces the AOPs into the capacity allocation of IEM and considers the internal transactions between AOPs. The emergence of the AOPs has led to the IEM's structure changes, resulting in the emergence of the game between the IEMSP and the AOPs. The energy trading process between the IEMSP and AOPs conforms to the game situation of the non-cooperative game, so the non-cooperative game is used to allocate the capacity of devices managed by IEMSP and devices of AOPs.

Game-theoretic methods have been widely applied in the interactions between prosumers (Teotia et al., 2020) and the interactions between power companies and consumers (Yu and Hong (2016) and Maharjan et al. (2013)). There has been some research on the non-cooperative game in the integrated energy system and demand response; for example, Yang et al. (2019) constructed a multi-investor dynamic decision-making game model for integrated energy system joint planning. Hu et al. (2020) established a non-cooperative game model with the power supplier as the main party and the electricity consumer as the slave party and formulated the optimal time-of-use price strategy with the goal of reducing the peak-to-valley difference. Demand response is described as a Stackelberg game in the energy pricing and dispatch problem for smart grid retailers by Wei et al. (2015). Pan et al. (2021) developed a multi-retail e-commerce retailer based on non-cooperative game package design and multi-level market power purchase strategy analysis.

In addition, with the proposal of carbon neutrality goals and the establishment of a new renewable portfolio standards policy in the document (National Energy Administration, 2021), it is urgent to study the flexible application of market mechanisms for carbon emission reduction of IEMs. An optimal planning model was proposed by Ge et al. (2021) for IEMs considering both distributed generators' output uncertainties and carbon emission punishments. Lu et al. (2021) established a bilayer scheduling method for the community-integrated energy service system based on carbon trading. Helgesen and Tomasgard (2018) constructed a multi-regional comprehensive green certificate and electricity market model and analyzed the economic impact of tradable green certificates on promoting renewable energy power generation. Cai et al. (2020) put forward the implementation scheme of the green certificate trading platform and built the underlying network and application environment of blockchain. To sum up, the research on the multi-market mechanism has attracted the attention of the academic community, but there is a lack of research on how to apply it in the capacity allocation of the IEM.

To investigate the application of the multi-market mechanism in the optimal capacity allocation of IEM, the study proposes a coupling mechanism of green certificate trading, carbon emission trading, and the electricity market as an example to introduce the multi-market mechanism into the capacity allocation model. The contributions of this study mainly include the following:

1) AOPs are considered in the capacity allocation of IEM, which can save the configuration capacity of the device under the same load and avoid waste of energy in IEM.
2) The approach of the non-cooperative game is used to solve the optimal capacity allocation model for IEM considering AOPs, thus obtaining the optimal capacity allocation results of the capacity of devices managed by IEMSP and devices of AOPs in IEM.
3) The multi-market mechanism is built based on the coupling mechanism of green certificate trading, carbon emission trading, and the electricity market to stimulate renewable energy equipment and increase environmental benefits in the IEM in the study.

The rest of this study is organized as follows: **Section 2** introduces the AOPs in IEM and presents a model for devices managed by IEMSP and devices of AOPs in IEM, respectively. **Section 3** describes the modeling of the multi-market mechanism. **Section 4** establishes the optimal capacity allocation method model for IEMSP and AOPs. The IEMSP-AOPs non-cooperative capacity allocation method is proposed in **Section 5**. In **Section 6**, the effectiveness of the proposed method

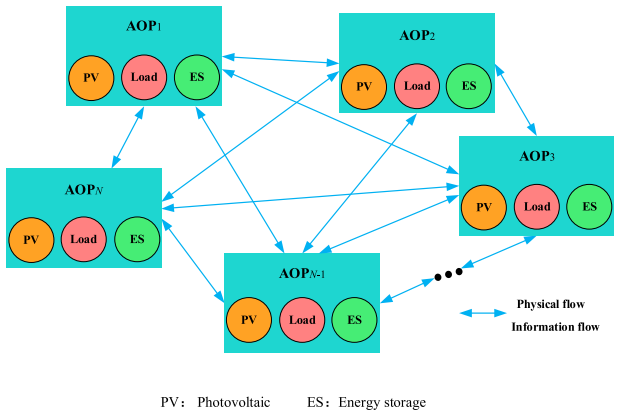

FIGURE 1 | The frame of AOP transactions and modeling the devices in the AOP.

is verified by cases. Conclusions are in **Section 7**. **Section 8** deals with future work.

2 INTEGRATED ENERGY MICROGRID CONSIDERING AGGREGATION OF PROSUMERS

2.1 Modeling of Aggregation of Prosumers

With the development and further promotion of distributed generation, small-scale energy users participate in energy market transactions as prosumers in an IEM. Multiple prosumers are aggregated together to form an AOP. Electricity transactions can be made between AOPs. **Figure 1** shows the process of AOP transactions

$$\begin{aligned} &0 \le P_{m,t}^{pv} \le P_{m}^{\max\, pv} \\ &P_{m,t}^{\mathrm{PV,U}} + P_{m,t}^{\mathrm{PV,S}} = P_{m,t}^{pv} \end{aligned} \tag{1}$$

where $P_{m,t}^{\mathrm{PV}}$ is the actual output PV value of the mth AOP in t periods; $P_{m}^{\max \mathrm{PV}}$ is the maximum PV predicted according to historical data; and $P_{m,t}^{\mathrm{PV,U}}$ and $P_{m,t}^{\mathrm{PV,S}}$ are the part of PV generation used by the AOP and the part of PV generation sold to the IEMSP, respectively. AOPs also have energy storage devices, and their models are as follows:

$$\begin{aligned} &P_{m,t}^{ESScharge} \le \beta_{m,t} \cdot u_{m}^{charge} \\ &P_{m,t}^{ESSdischarge} \le \left(1-\beta_{m,t}\right) \cdot u_{m}^{discharge} \\ &P_{m,t}^{\mathrm{ESS},U} + P_{m,t}^{\mathrm{ESS},S} = \lambda_{m,t}^{\mathrm{ESS}} \cdot P_{m,t}^{ESSdischarge} \end{aligned} \tag{2}$$

where $P_{m,t}^{ESScharge}$ and $P_{m,t}^{ESSdischarge}$ are the power charge and discharge of the energy storage device at time t, respectively; $\beta_{m,t}$ is a binary variable. When the state of the energy storage device is charging, the value is 1; otherwise, it is 0. u_{m}^{charge} is the maximum charge rate; $u_{m}^{\mathrm{discharge}}$ is the maximum discharge rate; $P_{m,t}^{\mathrm{ESS,U}}$ and $P_{m,t}^{\mathrm{ESS,S}}$ are the part of energy storage used by the AOP and the part of energy storage sold to the IEMSP, respectively; and $\lambda_{m,t}^{\mathrm{ESS}}$ is the discharge efficiency of the mth energy storage device.

Since the charging state of the battery is related to the charging state of the previous time and the charging and discharging powers of the equipment, its mathematical model is described as follows:

$$\begin{aligned} SOCE_{m,t} = SOCE_{m,t-1} &+ \left(P_{m,t}^{ESScharge}\eta_{m}^{\mathrm{charge}}\Delta t\right) \\ &- \left(P_{m,t}^{ESSdischarge}\eta_{m}^{\mathrm{discharge}}\Delta t\right) \end{aligned} \tag{3}$$

where $SOCE_{m,t}$ is the state of charge of the wth ES at time t; $\eta_{m}^{\mathrm{charge}}$ and $\eta_{m}^{\mathrm{discharge}}$ are the charge and discharge efficiency for the battery, respectively; and Δt is the charging time.

AOPs include inflexible load (IL) and translatable load (TL):

$$\begin{aligned} &P_{m,t}^{\min\ \mathrm{TL}} \le P_{m,t}^{\mathrm{TL}} \le P_{m,t}^{\max\ \mathrm{TL}} \\ &\sum_{t=1}^{T} P_{m,t}^{\mathrm{TL,shif}} = 0 \end{aligned} \tag{4}$$

where $P_{m,t}^{\mathrm{TL}}$ is the load translation amount of the TL user at time t and $P_{m,t}^{\min \mathrm{TL}}$ and $P_{m,t}^{\max \mathrm{TL}}$ are the upper and lower limits of TL load translation, respectively; when $P_{m,t}^{\mathrm{TL,shif}}$ is positive, it means that the translatable electrical load is transferred out, and on the contrary, it means that it is transferred in.

2.2 Integrated Energy Microgrid Architecture Considering Aggregation of Prosumers

Figure 2 shows a typical schematic diagram of an IEM structure considering AOPs.

The components involved in **Figure 2** are IEMSP, AOPs, general users, and so on. IEMSPs purchase electricity/natural gas from the superior electricity/gas network, cooperate with their own energy supply (PV, CHP, GB) and energy storage equipment (ES, HS), and supply energy to various users and obtain benefits in this way. AOPs install energy supply (PV) and energy storage equipment (ES) according to their conditions and purchase heat from IEMSP. General users purchase electricity and heat from IEMSP according to their electric and heating load needs.

2.3 Modeling of devices managed by IEMSP

1 Combined heat and power system model

CHP uses gas as fuel and high-quality thermal energy to drive gas turbines for power generation. The thermal energy and electric energy of CHP are obtained by consuming natural gas, and the mathematical model is

$$\begin{aligned} &P_{\mathrm{H},t}^{\mathrm{CHP}} = P_{\mathrm{G},t}^{\mathrm{CHP}}\eta^{\mathrm{CHP,H}} \\ &P_{\mathrm{E},t}^{\mathrm{CHP}} = P_{\mathrm{G},t}^{\mathrm{CHP}}\eta^{\mathrm{CHP,E}} \\ &P_{\min}^{\mathrm{CHP}} \le P_{\mathrm{H},t}^{\mathrm{CHP}} \le P_{\max}^{\mathrm{CHP}} \end{aligned} \tag{5}$$

where $P_{\mathrm{H},t}^{\mathrm{CHP}}$ and $P_{\mathrm{E},t}^{\mathrm{CHP}}$ respectively represent the heating power and electric power of CHP at time t; $P_{\mathrm{G},t}^{\mathrm{CHP}}$ represents the natural gas power consumed by CHP at time t; $\eta^{\mathrm{CHP,H}}$ and $\eta^{\mathrm{CHP,E}}$ represent the heating efficiency and power supply efficiency of CHP, respectively; and $P_{\min}^{\mathrm{CHP}}$ and $P_{\max}^{\mathrm{CHP}}$ represent the upper and lower limits of CHP heating power, respectively.

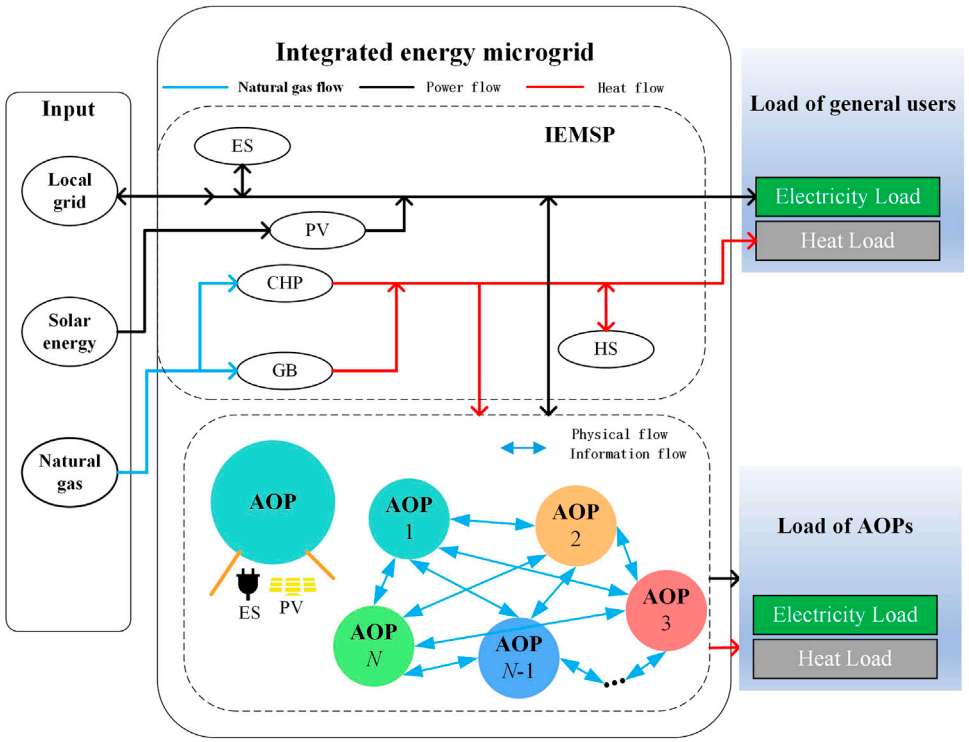

FIGURE 2 | IEM architecture considering AOPs.

2 Photovoltaic Model

Based on data of a typical day, the actual power consumed by the PV at time t cannot exceed the maximum predicted output at that time

$$P_{\mathrm{PV},t} \le P_{\max}^{PV} \tag{6}$$

where $P_{\mathrm{PV},t}$ represents the absorptive power at time t and $P_{\max}^{PV}$ is the maximum output power predicted on a typical day.

3 Gas Boiler Model

As systematic heat-generating equipment, GB can convert the chemical energy generated by natural gas combustion into high-grade heat energy, and its mathematical relationship is

$$\begin{aligned} P_{\mathrm{H},t}^{\mathrm{GB}} &= \eta_{\mathrm{GB}} P_{\mathrm{G},t}^{\mathrm{GB}} \\ P_{\min}^{\mathrm{GB}} \le P_{H,t}^{\mathrm{GB}} &\le P_{\max}^{\mathrm{GB}} \end{aligned} \tag{7}$$

where $P_{\mathrm{H},t}^{\mathrm{GB}}$ and $P_{\mathrm{G},t}^{\mathrm{GB}}$ respectively represent the electric power consumed and the natural gas power consumed; η_{GB} represents the heating efficiency of gas boilers; and $P_{\min}^{\mathrm{GB}}$ and $P_{\max}^{\mathrm{GB}}$ respectively represent the upper and lower limits of GB heating power.

4 Electric Boiler Model

The thermal output and electric consumption of EB are constrained as follows:

$$\begin{aligned} P_{\mathrm{H},t}^{\mathrm{EB}} &= \eta_{\mathrm{EB}} P_{\mathrm{E},t}^{\mathrm{EB}} \\ P_{\min}^{\mathrm{EB}} \le P_{\mathrm{H},t}^{\mathrm{EB}} &\le P_{\max}^{\mathrm{EB}} \end{aligned} \tag{8}$$

where $P_{\mathrm{H},t}^{\mathrm{EB}}$ and $P_{\mathrm{E},t}^{\mathrm{EB}}$ are the production power and input electric power of electric boiler equipment, respectively, and η_{EB} represents the power generation efficiency of the EB.

5 Energy Storage Device Model

There are two types of energy storage devices in the microgrid structure in this study, namely, the electricity storage unit (ES) and the heat storage unit (HS).

1 Electricity Storage Unit Model

SOCE is the state of charge of the battery, which is the ratio of the remaining storage capacity E_{re} to the configured capacity E_{ne}, generally expressed as follows:

$$SOCE = \frac{E_{re}}{E_{ne}} \times 100\% \tag{9}$$

Since the state of battery charge is related to the state of charge at the last moment and the power of the device, its mathematical model is described as follows:

$$SOCE_t = SOCE_{t-1} + \Delta T u_{ech}\frac{P_e^{\mathrm{ch}}\eta_e^{\mathrm{ch}}}{E_{ne}} - \Delta T u_{edis}\frac{P_e^{\mathrm{dis}}}{E_{ne}\eta_e^{\mathrm{dis}}} \quad (10)$$

where P_e^{ch} and P_e^{dis} are the battery charging and discharging powers, respectively; η_e^{ch} and η_e^{dis} are the charging and discharging efficiencies for the battery, respectively; ΔT is the charging time; and u_{ech} and u_{edis} represent the status flags of battery charging and discharging, respectively.

2 Heat Storage Unit Model

SOCH is the state of the heat storage unit, which is the ratio of the remaining heat storage E_{rh} to the configured capacity E_{nh}, and its percentage form is as follows:

$$SOCH = \frac{E_{rh}}{E_{nh}} \times 100\% \quad (11)$$

Similarly, the current heat storage capacity of the heat storage device is related to the previous heat storage state and the charging and discharging heat of the device. The mathematical model is described as follows:

$$SOCH_t = SOCH_{t-1} + \Delta T u_{hch}\frac{P_H^{\mathrm{ch}}\eta_h^{\mathrm{ch}}}{E_{nh}} - \Delta T u_{hdis}\frac{P_{H,t}^{dis}}{E_{nh}\eta_h^{\mathrm{dis}}} \quad (12)$$

where P_h^{ch} and P_h^{dis} are the charging heat and discharging heat of the heat storage device, respectively; η_h^{ch} and η_h^{dis} are respectively the charging efficiency and discharging efficiency of the heat storage device; ΔT is the heat storage time; and u_{hch} and u_{hdis} represent the status flags of the charging and discharging of the heat storage device, which can only be 0 or 1.

3 MODELING OF THE MULTI-MARKET MECHANISM

The flexible application of market mechanisms has become an essential means to break through the bottleneck of new energy development in China, and the IEM can not only participate in green electricity trading, carbon emission trading, and green certificate trading but also use the electricity market mechanism and other multi-market mechanisms to promote renewable energy consumption and reduce carbon emissions. The study considers three of these market mechanisms: the green certificate transactions among AOPs, the linear ladder carbon trading (LLCT) considered in the IEMSP, and the electricity market, which are described below.

3.1 Green Certificate Transactions Considered in the Aggregation of Prosumers

3.1.1 Green Certificate Transactions

It is assumed that the AOPs can participate in green certificate transactions. Some researchers used green certificate cross-chain transactions according to the number of green certificates obtained by the AOPs (Luo et al., 2021), and cross-chain transactions will be carried out on three blockchains of AOPs, green certificate transactions, and renewable energy.

The three blockchains constitute a chain group, which belongs to the category of alliance chains. Blockchains are only open to members participating in the green certificate trading market and provide a guarantee for the information security of participants. Smart contracts are contracted programs composed of Turing complete program codes, and chain code technology is a further development of smart contracts. As shown in **Figure 3**, new energy generators, AOPs, green certificate transaction platforms, and administrative supervision departments operate jointly through the blockchain green certificate transaction chain code.

First of all, a unified green certificate trading market should be established, in which the number of green certificates is shown in **Eq. 13**:

$$N_{GRE} = \sum_{w=1}^{W}\frac{P_c^w \cdot \Delta t}{1000} \quad (13)$$

where N_{GRE} represents the number of green certificates participating in the transaction in the system, P_c^w is the actual consumption of the wth renewable energy equipment, and W is the number of renewable energy generators in the system.

The green certificate transaction model is shown in **Eq. 14**. According to the comparison of realistic renewable energy power generation and the prescribed quota, the model is as follows:

$$C_{GRE}^t = \begin{cases} [-(E_R - P_{GRE})] \cdot T_{GRE} & P_{GRE} > E_R \\ (P_{GRE} - E_R)T_{GRE} & E_R - Q < P_{GRE} < E_R \\ [Q \cdot P_{GRE} \cdot T_{GRE} - (E_R - P_{GRE} - Q)] \cdot F_{GRE} & P_{GRE} \le E_R - Q \end{cases} \quad (14)$$

where C_{GRE}^t is the green certificate transaction, T_{GRE} is the price of green certificate transactions, P_{GRE} is the actual consumption of renewable energy, E_R is the amount of renewable energy quota, F_{GRE} is the penalty price, and Q is the penalty margin of the green certificate system.

Green certificate quota constraints:

$$\sum_{i=1}^{v} G\alpha_i P_i - N_{GRE} = G\sum_{i=1}^{v}\eta_i P_{io} \quad (15)$$

where G is the quantitative coefficient, N_{GRE} represents the number of green certificates that can be obtained for a unit of green electricity production, α_i is the proportion of the ith power generation company's renewable power generation within the specified time, P_i is the ith power generation company's initial distribution of electricity, η_i is the actual power generation of the ith power generation company, and P_{io} is the initial distribution of power for the ith power generation company.

3.2 The Linear Ladder Carbon Trading Considered in the IEMSP Capacity Allocation

The initial assignation of carbon emission rights in the IEMSP mainly includes gas boilers and CHP. A ladder carbon price can

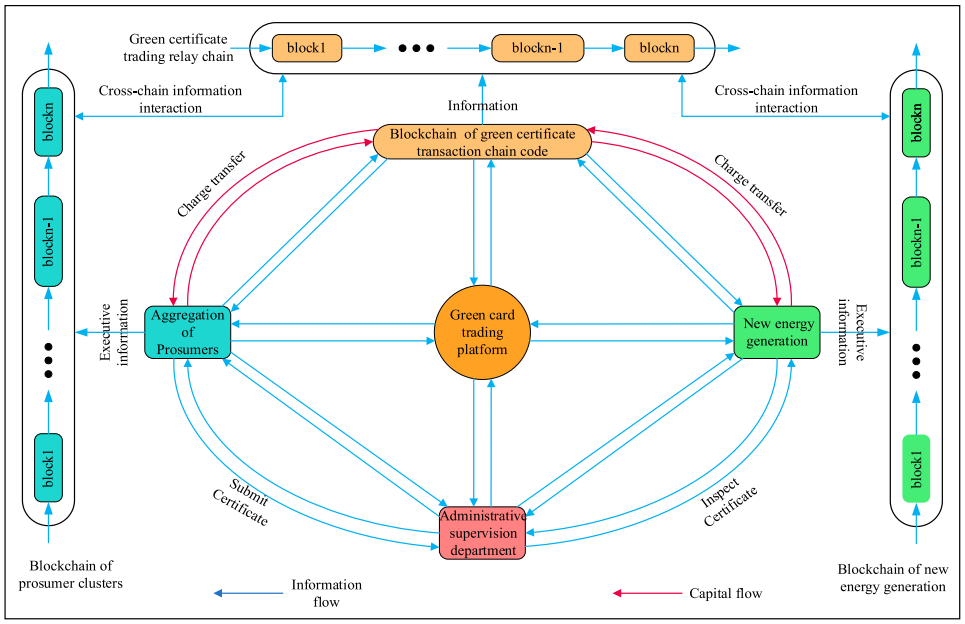

FIGURE 3 | Green certificate transaction framework.

increase the carbon trading cost of large emission units, and the ladder carbon price model in this study is as follows:

$$\begin{aligned} E_c &= E_{chp} + E_{gb} \\ E_{gb} &= \delta_h \cdot P_d \\ E_{chp} &= \delta_h \cdot \left(P_a + \varphi P_b\right) \end{aligned} \tag{16}$$

where E_c is free carbon emission quota; E_{chp} and E_{gb} are free carbon emission quota for CHP units and gas boilers, respectively; δ_h is the carbon emission quota per unit heat supply; P_d is heat supply for gas boilers; φ is the conversion coefficient from power generation to heat supply; and P_a and P_b are the heating capacity and power generation capacity of the CHP unit, respectively.

$$P_{CO_2} = \begin{cases} P_0 - U\alpha & E_P \le E_C - U\nu \\ \vdots & \vdots \\ P_0 - \alpha & E_C - 2\nu \le E_P \le E_C - \nu \\ P_0 & E_C \le |E_P| \le E_C + \nu \\ P_0 + \theta & E_C + \nu \le E_P \le E_C + 2\nu \\ \vdots & \vdots \\ P_0 + U\theta & E_P \ge E_C + U\nu \end{cases} \tag{17}$$
$$\sum_{u=0}^{|U|+1} E_u = E_P - E_C$$

where P_{CO_2} is the price of each ladder of carbon emission rights, θ is the increment of carbon price, α is the reward coefficient, ν is the increment of carbon quota, and E_P represents the actual carbon emissions.

When the carbon emission is less than the free allocation of carbon emissions, the energy supply company can sell excess carbon emission quotas in the carbon trading market. The lower the carbon emission, the higher the carbon trading price; when the carbon emission is greater than the carbon emission amount allocated for free, the energy supply company needs to purchase carbon emission rights in the carbon trading market. The total cost of carbon trading is a linear function and the linear function of the total carbon transaction cost C_{CO_2} is calculated according to the stepped carbon price, which can be expressed as follows:

$$\begin{aligned} C_{CO_2} &= \begin{cases} \sum_{u}^{U+1} \left[P_{CO_2} + (u-1)\theta\right] E_u & E_P \ge E_C \\ \sum_{|u|}^{|U|+1} \left[P_{CO_2} + (u-1)\alpha\right] E_u & E_P \le E_C \end{cases} \end{aligned} \tag{18}$$

where E_u is the carbon emission range of the uth stage.

3.3 Grid Time-Of-Use Tariff Model

Time-of-use (TOU) refers to the power grid encouraging users to arrange the electricity time reasonably. Different electricity prices are formulated for each time period according to the load change

$$\boldsymbol{c}_G \triangleq \left[c_G^1, \ldots, c_G^T\right] \tag{19}$$

where $\boldsymbol{c}_G$ represents the electricity prices for the grid.

3.4 IEMSP Electricity Price Model

$$\begin{aligned} \boldsymbol{c}_{ES} &\triangleq \left[c_{ES}^1, \ldots, c_{ES}^T\right] \\ \boldsymbol{c}_{EB} &\triangleq \left[c_{EB}^1, \ldots, c_{EB}^T\right] \end{aligned} \tag{20}$$

$$\begin{aligned} c_{ES}^t &= c_G^t - \beta_S\left(c_G^t\right) \\ c_{EB}^t &= c_G^t + \beta_B\left(c_G^t\right) \end{aligned} \tag{21}$$

$$\beta_S + \beta_B < 1 \tag{22}$$

$$c_{EB}^{t} < c_{ES}^{t} \tag{23}$$

where c_{ES} is the electricity sales price for IEMSP, c_{EB} is the electricity purchase price for IEMSP, β_S is the adjustment coefficient for the electricity sales price of the IEMSP, and β_B is the adjustment coefficient for the purchase price of the IEMSP.

4 OPTIMAL CAPACITY ALLOCATION MODEL FOR INTEGRATED ENERGY MICROGRID CONSIDERING AGGREGATION OF PROSUMERS

4.1 Optimal Capacity Allocation Model of IEMSP

The optimization objective of the IEMSP capacity allocation model proposed in the study is to minimize the net present value of the total cost within the capacity allocation period, in which the total cost includes investment costs, operation costs, maintenance costs, equipment residual value, and carbon transaction costs. The carbon transaction costs are from the linear ladder carbon trading (LLCT) considered in the IEMSP capacity allocation as shown in **Section 3.2**

$$\min C^{IEMSP} = C_{inv}^{IEMSP} + \sum_{k=1}^{N} \frac{C_{ope}^{k} + C_{mai}^{k} + C_{CO_2}^{k}}{(1+r)^{k}} - \frac{C_{rv}^{IEMSP}}{(1+r)^{N}}$$

$$C_{inv}^{k} = \sum_{i=1}^{I} \left(c_{inv}^{i} \cdot \boldsymbol{q}^{k}\right) \tag{24}$$

$$C_{mai}^{k} = \sum_{i=1}^{I} \left(c_{mai}^{i} \cdot \boldsymbol{p}^{k}\right)$$

where r is the coefficient of the present value; C^{IEMSP} is the total cost for IEMSP; N is the planning period; C_{inv}^{k} is the investment cost of IEMSP for the kth year similarly; C_{ope}^{k} is the operating cost for the kth year; C_{mai}^{k} is the maintenance cost; $C_{CO_2}^{k}$ is the carbon transaction cost for the kth year; C_{rv}^{IEMSP} is the total residual value for IEMSP; i represents the types of candidate equipment; c_{inv}^{i} and c_{mai}^{i} represent the investment cost per unit capacity and the variable maintenance cost per unit power for the ith equipment, respectively; the matrix $\boldsymbol{q}^{k} = [q_i^k]_{1\times i}$ represents the ith device configuration capacity at time t in the kth year; and $\boldsymbol{p}^{k} = [p_{i,t}^{k}]_{i\times 8760}$ represents the ith device power at time t in the kth year

$$\begin{aligned} C_{rv}^{IEMSP} &= \sum_{i=1}^{M} \left(C_{inv,i} - \sum_{n=1}^{N} C_{dep,i}\right) \\ C_{dep,i} &= C_{inv,i}\left(1-\delta_i\right) \Big/ N_i \\ C_{inv,i} &= c_{inv,i} \times q_i \end{aligned} \tag{25}$$

The average age method is used to calculate the depreciation of equipment in the study. Suppose that the life of the ith device is N_i; the depreciation expense for each year is $C_{dep,i}$; δ_i is the net salvage rate of the ith device; $C_{inv,i}$ is the investment cost of the ith device; $c_{inv,i}$ is the unit capacity investment cost of the ith device, related to the type to which they belong; and q_i is the configured capacity for the ith device

$$\begin{aligned} C_{ope}^{k} &= \sum_{k=1}^{N} 365 \sum_{n=1}^{d} p_{n,k} C_{ope}^{n,k} \\ C_{ope}^{n,k} &= \sum_{t=1}^{T} \left(c_G^t P_{\text{grid}}(t)\Delta t + c_{\text{gas}} G_{\text{gas}}(t)\Delta t\right) - C_P^L - C_P^{ex} - C_H^{ex}) \\ C_P^{ex} &= \sum_{t=1}^{T} c_{EB}^t P_{pro,buy}(t)\Delta t + c_{ES}^t P_{pro,sell}(t)\Delta t \\ C_P^L &= \sum_{t=1}^{T} c_{ES}^t P_{Load}(t)\Delta t \\ C_H^{ex} &= \sum_{t=1}^{T} c_{HB}^t \left(H_{pro,buy}(t) + H_{Load}(t)\right)\Delta t \end{aligned} \tag{26}$$

where n indicates the nth typical daily operation scenario; $C_{ope}^{n,k}$ is the daily operating cost of IEMSP, which consists of the purchase cost of electricity by the superior power grid, the gas purchase cost of the superior gas network, the power transaction of the AOPs C_P^{ex}, the heat transaction C_H^{ex}, and the daily purchase profit of the general load C_P^L; c_G^t is the electricity price for the grid; c_{gas} is the gas price for natural gas; $P_{\text{grid}}(t)$ and $G_{\text{gas}}(t)$ are the electricity purchased from the grid and the natural gas bought from the gas grid, respectively.

4.2 IEMSP Operation Constraints

1 Electric Power Balance Constraint

$$P_{grid,t} + P_{E,t}^{CHP} + P_{PV,t} + P_{e,t}^{dis} + P_{pro,sell}(t) = P_{pro,buy}(t) + P_e^{\text{ch}} + P_{L,t} \tag{27}$$

where $P_{\text{grid},t}$ represents the power purchased from the grid at the tth time, $P_{L,t}$ is the general electrical load at the tth time, and $P_{pro,sell}(t)$ and $P_{pro,buy}(t)$ are the electricity sold by the AOPs and the electricity purchased by the AOPs, respectively.

2 Thermal Power Balance Constraint

$$P_{H,t}^{CHP} + P_{H,t}^{GB} + P_{H,t}^{dis} = P_{H,t}^{ch} + H_{L,t} + H_{pro,buy}(t) \tag{28}$$

where $H_{\text{L},t}$ represents the heat load at time t and $H_{pro,buy}(t)$ is the heat sold by the AOPs.

3 Natural Gas Bus Constraint

$$G_{\text{gas}}(t) = P_{\text{G},t}^{\text{CHP}} + P_{\text{G},t}^{\text{GB}} \tag{29}$$

where $G_{\text{gas}}(t)$ represents the natural gas purchased from the gas network at time t.

4 The Upper Output Limit of the Equipment and Investment Capacity Constraints Are Shown in the Following Equation

$$\begin{aligned} 0 \le P_{i,dev} \le P_{i,dev}^{\max} \\ 0 \le q_i^k \le Q_i \end{aligned} \tag{30}$$

where $P_{i,dev}^{\max}$ is the upper limit of the output of the ith device and Q_i is the upper limit of the construction capacity of the ith device.

5 The Power Constraint of the Contact Line Between the Grid and the IEMSP Is as Follows

$$P_{grid}^{\min} \le P_{grid,t} \le P_{grid}^{\max} \tag{31}$$

where $P_{grid}^{\min}$ and $P_{grid}^{\max}$ are the upper and lower limits of power constraint of the contact line between the grid and the IEMSP, respectively.

4.3 Aggregation of Prosumer Capacity Configuration Model

$$\min C^{AOP} = C_{AOP}^{inv} + \sum_{k=1}^{N} \frac{C_{AOP,ope}^{k} + C_{AOP,mai}^{k} + C_{gre}^{k}}{(1+r)^{k}} - \frac{C_{rv}^{AOP}}{(1+r)^{N}} \tag{32}$$

where C^{AOP} represents the capacity allocation cost of the AOPs, C_{AOP}^{inv} is the investment cost, $C_{AOP,ope}^{k}$ is the operation cost, $C_{AOP,mai}^{k}$ is the maintenance cost, C_{rv}^{AOP} is the equipment residual value, and C_{gre}^{k} is the green certificate transaction cost. Green certificate transactions considered in the AOPs are shown in **Section 3.1**, the maintenance cost and equipment residual value are similar to those in the IEMSP capacity configuration model, and the operation cost is shown in **Eq. 32**. $C_{ope,AOP}^{n,k}$ is the daily operating cost for AOPs

$$\begin{aligned} C_{AOP,ope}^{k} &= \sum_{k=1}^{N} 365 \sum_{n=1}^{d} p_{n,k} C_{ope,AOP}^{n,k} \\ C_{ope,AOP}^{n,k} &= C_{P}^{ex} + C_{H}^{ex} \end{aligned} \tag{33}$$

4.4 Aggregation of Prosumer Trading Constraints

1 Power Balance

$$\begin{aligned} p_{m,t}^{in} + P_{m,t}^{pv} + P_{m,t}^{ESS} &= P_{m,t}^{TL} + L_{m,t} + P_{m,t}^{ESScharge} \\ P_{m,t}^{toIEMSP} &= P_{m,t}^{\mathrm{PV,S}} + P_{m,t}^{\mathrm{ESS,S}} \end{aligned} \tag{34}$$

where $p_{m,t}^{in}$ is the total power input of the mth AOP and $P_{m,t}^{toIEMSP}$ is the power sold to the IEMSP.

2 Tie Line Power Constraints

Tie line power constraints are introduced in the following formula:

$$\begin{aligned} p_{h,t}^{in} &= \sum_{\mathrm{j}} \left(p_{h,j,t} \cdot \sigma_{h,j} \right) + p_{h,t}^{fromIEMSP} \\ p_{j,t}^{out} &= \sum_{\mathrm{h}} \left(p_{h,j,t} \cdot \sigma_{h,j} \right) + p_{j,t}^{toIEMSP} \\ \sigma_{h} &= k \cdot \left| p_{h,x,t} \right| + r \cdot p_{h,x,t}^{2} \\ p_{h,j,t} &\le \bar{\sigma}_{h,j} \end{aligned} \tag{35}$$

where $p_{h,t}^{in}$ represents the total power input of AOP h, which is the sum of all powers obtained from other users on the network, equal to the power exchanged from AOP h to AOP j at time t multiplied by tie line losses σ_h, and then plus the power purchased from IEMSP $p_{h,t}^{fromIEMSP}$. The approximation of tie line losses σ_h is made by a quadratic function of the power flow; k and r are coefficients. The total power output equation can be obtained similarly. In addition, the green certificate transaction constraints among AOPs are shown in **Section 3.1**. The unit of k is [.], and the unit of r is [kW^{-1}]. The approximation of tie line losses is linearized using the Special-Order Sets of Type 2 as follows:

$$\begin{aligned} \sum\nolimits_{r \in R} X_{h,h,t}^{\sim} &= 1 \\ P_{h,h,t}^{IEMSP} &= \sum\nolimits_{r \in R} A_r X_{h,h,t} \end{aligned} \tag{36}$$

5 IEMSP-AOPS NON-COOPERATIVE CAPACITY ALLOCATION METHOD

IEMSPs purchase electricity/natural gas from the superior electricity/gas network, cooperate with their own equipment, supply energy to various users, and obtain benefits in this way. According to the abovementioned description, the optimization of IEMSP and AOPs is based on the quoted price of IEMSP, and their optimization results will react to the IEMSP quotation. This energy trading process conforms to the game situation of the non-cooperative game, so the non-cooperative game theory is used to solve the problem of considering both AOP profits and IEMSP profits in the study. The game is performed frequently in each iteration.

Algorithm 1. IEMSP-AOPs non-cooperative capacity allocation algorithm

1. Initialize all relevant parameters of the IEM. IEMSP receives grid electricity prices, gas prices, load information, and PV information.

2. IEMSP sends c_{EB}^{t} and c_{ES}^{t} to AOPs and general users.

3. While (3) do: Optimal configuration of AOPs begin.

4a: Receive c_{EB}^{t} and c_{ES}^{t}, according to formula (31), combined with the load information of the AOPs, the green certificate cross-chain transactions and the transactions between the AOPs, etc. C^{AOP} are optimized.

4b: Send $P_{pro,buy}(t)$, $P_{pro,sell}(t)$, and $H_{pro,buy}(t)$ to IEMSP. 5a: According to **Eq. 23**, IEMSP confirms its optimal configuration scheme.

5b: IEMSP updates the c_{EB}^{t} and c_{ES}^{t}.

6: Solve $(c_{EB}^{t*}, c_{ES}^{t*}) = \mathrm{argmin}\ C^{IEMSP}(c_{EB}^{t}, c_{ES}^{t}, P_{pro,buy}(t), P_{pro,sell}(t))$ and update $(c_{EB}^{t*}, c_{ES}^{t*})$; $(P_{pro,buy}(t)^{*}, P_{pro,sell}(t)^{*}) = \mathrm{argmin}\ C^{AOP}(c_{EB}^{t}, c_{ES}^{t}, P_{pro,buy}(t), P_{pro,sell}(t))$ and update $(P_{pro,buy}(t)^{*}, P_{pro,sell}(t)^{*})$.

7: Stopping criteria: if $\left\{ \begin{array}{l} \left| C^{IEMSk} - C^{IEMSk-1} \right| \le \varepsilon \\ \left| C^{PROk} - C^{PROk-1} \right| \le \varepsilon \end{array} \right\}$ break.

8: Else: $k = k+1$

9: End if

10: End while.

The particle swarm optimization algorithm has simple principles and easy implementation and a fast convergence speed and can completely save the local optimal solutions and

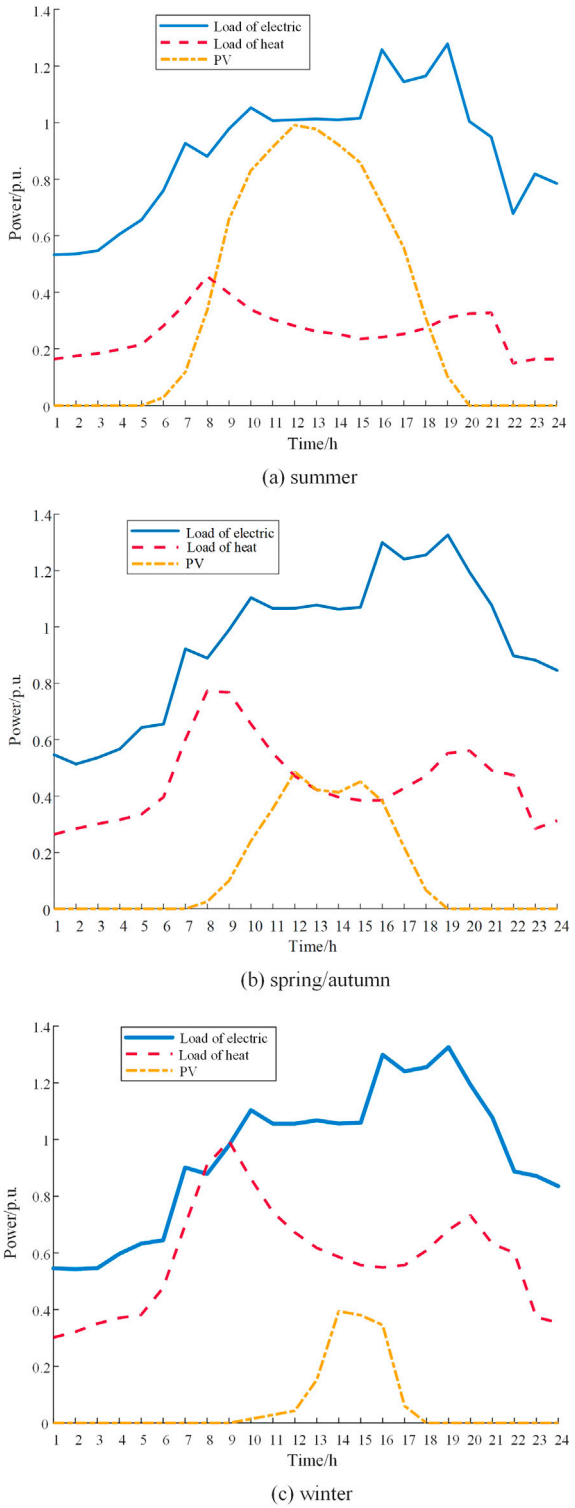

FIGURE 4 | Load curve.

global optimal solutions of all particles in the iterative process; it is very suitable for analyzing the non-cooperative game process in this study. In the particle swarm optimization algorithm, the number of iterations is set to 80, the number of populations is 60, and the maximum allowable error of iterative convergence ε is 10^{-3}.

Nonlinear programming problems need to be solved for the IEMSP as shown in **Eq. 37**:

$$\begin{cases} \min\ C^{IEMSP} \\ s.t.\ (16) - (23), (27) - (31) \end{cases} \tag{37}$$

The optimization capacity allocation model is implemented in MATLAB R2019b. For AOPs, the calculation of strategies and cost is solved by GUROBI, and the nonlinear programming problems need to be solved as shown in **Eq. 38**:

$$\begin{cases} \min\ C^{AOP} \\ s.t.\ \ (1) - (4), (34), (35) \end{cases} \tag{38}$$

6 SIMULATION AND RESULTS

6.1 Simulation Settings

Simulation data come from a certain northern electric, gas, and thermal coupling IEM (Cao et al., 2020) to study the optimal capacity allocation model for IEM considering AOPs. The load curve of IEM is shown in **Figure 4**. The capacity allocation period is 8 years, and seven candidate devices can be selected for IEMSP, which are shown in the **Supplementary Appendix**. This study only discusses the purchase and sale prices of electricity; the heat demand of the AOP is provided by IEMSP, the heat sale price of IEMSP is still \$0.07/kWh, and the grid electricity price is shown in the **Supplementary Appendix**. The fixed price for natural gas is \$0.39/m^3, the low calorific value of gas is 9.7 kW h/m^3, and the converted natural gas grid is \$0.04/kWh. The coefficient of the present value is 8%. The carbon trading cost is settled at the end of each year. The carbon emission of GB and CHP units is 0.065 t/GJ (Qu et al., 2018), the carbon transaction price is \$38/t, and the incentive coefficient and carbon price increment are 0.2; the carbon quota increment v = 85000t (Li et al., 2021). The green certificate price is set at \$10 (Luo et al., 2021). If one of the parties to the transaction breaches the contract or fails to meet the quota standard, a penalty price will be formulated, which is three times the green certificate.

To demonstrate the superiority of the proposed capacity allocation method for IEM considering AOPs under the multi-market mechanism in the study, four cases are compared in **Section 6.2**.

***Case 1*:** Traditional capacity allocation for IEM without considering AOPs or the green certificate and carbon trading.

***Case 2*:** Capacity allocation for IEM considering green certificate and carbon trading, but electricity trading between AOPs is not considered.

***Case 3*:** Capacity allocation for IEM considering electricity trading between AOPs, but without considering green certificate and carbon trading.

***Case 4*:** Capacity allocation for IEM considering trading between AOPs and the green certificate and carbon trading using the proposed model.

TABLE 1 | Capacity allocation result of four cases.

case		1	2	3	4
IEMSP	PV/kW	478	279	169	230
	CHP/kW	260	276	321	260
	ES/kWh	678	316	306	306
	HS/kWh	699	469	344	389
	GB/kW	67	72	98	68
AOPs	PV/kW	0	170	106	116
	ES/kWh	0	85	69	59

Among the cases, case 1 is the base case in which neither AOPs nor green certificates and carbon trading are considered. AOPs in the IEM are considered in the other three cases; the electricity and heat load demand of the AOPs account for 15% of the total load, and the general user load demand accounts for 85% of the total load in cases 2–4. Case 4 uses the proposed model in this study.

6.2 Optimal Result Analysis

Tables 1, **2** show the optimal allocation results and costs for four cases. First of all, it can be seen from **Tables 1**, **2** that the overall configuration capacity of IEM and carbon emissions in case 1 is the most, and these in case 4 are the least under the same load; the comprehensive costs for capacity allocation in case 1 are the highest and that in case 4 is the lowest, proving the superiority of the proposed model in case 4. Next, the impact of trading between AOPs on the capacity allocation of IEM considering AOPs is analyzed by comparing case 2 and case 4, and the impact of green certificate and carbon trading on the capacity allocation of IEM considering AOPs is analyzed by comparing case 3 and case 4.

6.2.1 Comparative Analysis of IEM Capacity Allocation Considering Trading Between Aggregation of Prosumers or Not

This section compares case 2 with case 4.

1 Optimization game results of the purchase and sell prices

Based on the proposed method, when the AOP and the IEMSP reach game equilibrium, the final electricity price adjustment coefficient (PAC) is 0.895, the purchase PAC is 0.10 in case 4, the sale PAC in case 2 is 0.893, and the purchase PAC is 0.09. By formula (20), we can obtain the corresponding IEMSP electricity sell and purchase prices as shown in **Figure 5**.

IEMSP purchase and sell price optimization results in case 2 and IEMSP purchase and sell price optimization results in case 4 are provided.

2 Equipment Selection and Capacity Configuration Results

Comparing case 2 and case 4 in **Table 1**, we can obtain that when the electricity trading between AOPs is not considered, both the capacity configurations of AOPs and IEMSP have increased significantly. For example, the PV capacity configuration has increased from 230 kW to 279 kW in IEMSP, and AOP's PV capacity configuration increases from 116 to 170 kW. To conserve the equipment configuration capacity, the electricity trading between AOPs should be considered on the AOP-involved optimal capacity allocation method for IEM.

3 Economic Results

Comparing case 2 and case 4 from **Table 2**, when the electricity trading between AOPs is not considered, both comprehensive costs of AOP and IEMSP have increased, IEMSP's comprehensive costs have increased by 26.9%, and AOPs' comprehensive costs have increased by 53.2%, which illustrates that the consideration of the electricity trading between AOPs will save a lot of costs and improve the economy of the capacity configuration.

6.2.2 Analysis of the Impact of the Green Certificate and Carbon Trading

This section compares case 3 with case 4.

1) Equipment Selection and Capacity Configuration Results

Case 3 did not consider green certificates and carbon trading compared with case4; comparing case 3 and case 4 in **Table 1**, it can be seen that for IEMSP, the PV configuration capacity decreases from 230 kW in case 4 to 169 kW in case 3, and the CHP configuration capacity increases from 260 kW in case 4 to 321 kW in case 3. For AOPs, the PV configuration capacity decreases from 116 to 106 kW. Due to the high cost and small carbon emissions of PV units compared to CHP units, the green certificates and the carbon trading model used in case1 select the PV configuration with small carbon emissions, which demonstrates that the participation of the multi-market

TABLE 2 | Cost of four cases.

case		1	2	3	4
IEMSP	Carbon emission trading costs/$\times 10^4$ $	0	−3.06	0	−2.18
	Carbon emission/t	4.99	3.69	2.88	2.40
	Operating costs/$\times 10^4$ $	212.54	157.68	103	126.00
	Capacity allocation costs/$\times 10^4$ $	47.01	42.97	26.88	30.01
	Comprehensive costs/$\times 10^4$ $	259.55	203.59	138.88	159.98
AOPs	Green certificate transaction costs/$\times 10^4$ $	0	−0.45	0	−0.29
	Carbon emission/t	0	0.56	0.42	0.34
	Operating costs/$\times 10^4$ $	0	26.45	15.78	17.29
	Capacity allocation costs/$\times 10^4$ $	0	5.46	2.99	4.33
	Comprehensive costs/$\times 10^4$ $	0	37.55	21.76	24.50

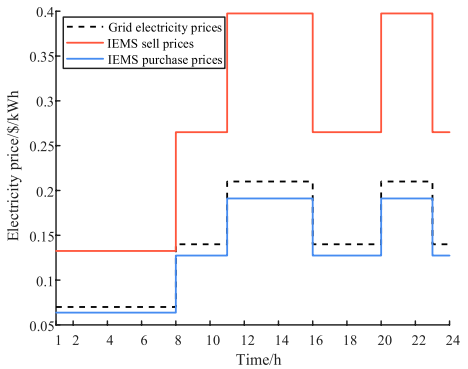

IEMSP purchase and sell price optimization results in Case 2

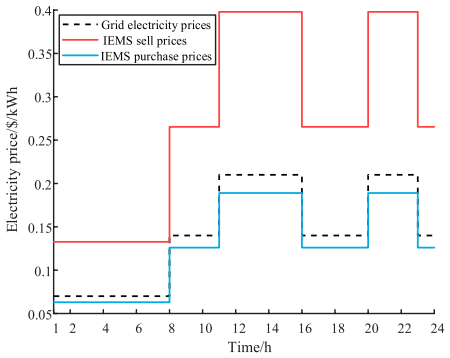

IEMSP purchase and sell price optimization results in Case 4

FIGURE 5 | IEMSP purchase and sell price optimization results in case 2 and case 4.

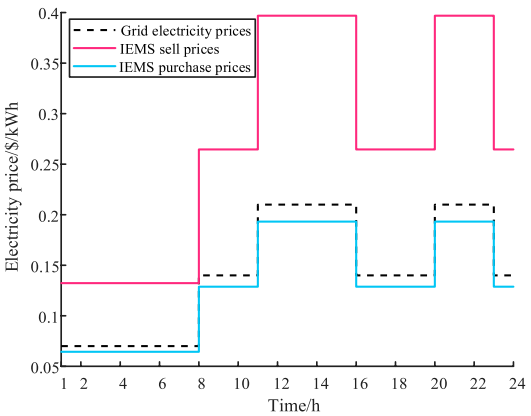

IEMSP price optimization results when penetration of AOPs is 50%

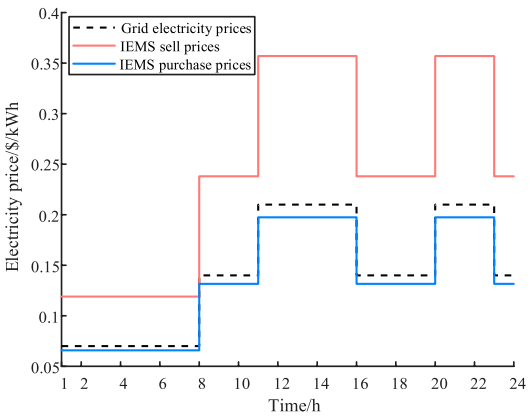

IEMSP price optimization results when Penetration of AOPs is 85%

FIGURE 6 | IEMSP purchase and sell price optimization results of different penetrations of AOPs.

mechanism proposed in this study improves the enthusiasm of green equipment and reducing carbon emissions.

2) Economic Results

Comparing case 3 and case 4 from **Table 2**, we can first get that the carbon emission trading costs and green certificate transaction costs are zero when carbon emission trading and green certificate transactions are not considered. Second, both costs of IEMSP and AOP decrease in case 3, and IEMSP's comprehensive costs decrease by 13.2%; AOP's comprehensive costs decrease by 11.2% due to the fact that the system tends to choose devices with small costs but large carbon emissions when not considering market mechanisms. However, both carbon emissions of IEMSP and AOP decrease in case 4 compared to case 3, IEMSP's carbon emission decreases by 16.7%, and AOP's carbon emission decreases by 20%.

6.3 Comparative Analysis of Different Penetrations of Aggregation of Prosumers in the Integrated Energy Microgrid

Penetration of AOPs refers to the proportion of AOPs that exist in IEM. The penetration rate of case 4 is 15%. In this section, the penetration rate is increased to 50 and 85% on the basis of case 4 for comparison. The corresponding IEMSP electricity sell and purchase prices are shown in **Figure 6**. With the change of penetration of AOPs in IEM, the optimization results of the purchase and sale price game and capacity configuration results are also changing.

1) Optimization Game Results of the Purchase and Sell Prices

The selling PAC is 0.895 and the purchase PAC is 0.10 in case 4 when the penetration of AOPs is 15%. When the penetration is 50%, the selling PAC is 0.89 and the purchase PAC is 0.08. When

TABLE 3 | Capacity allocation results of different penetrations of AOPs.

Penetration of AOPs		0	15%	30%	50%	85%
IEMSP	PV/kW	502	230	196	145	105
	CHP/kW	240	250	230	214	183
	ES/kWh	677	306	278	255	90
	HS/kWh	698	389	305	212	99
	GB/kW	67	67	67	68	68
AOPs	PV/kW	0	116	199	249	390
	ES/kWh	0	59	87	145	201

the penetration is 85%, the selling PAC is 0.7 and the purchase PAC is 0.06. With the increase in penetration of AOPs, the IEMSP purchase prices gradually increase, gradually approaching the grid price. Increased penetration of the AOP makes it more advantageous for them to fight for their interests in the price game, while the sell prices of IEMSP are slightly lowered.

2) Capacity Configuration Results

As shown in **Table 3**, with the increase of penetration of AOPs, the capacity configuration of AOPs has gradually increased and the capacity configuration of IEMSP has gradually decreased. From the perspective of the overall IEM, the overall capacity allocation is greatly reduced with the increase of penetration of AOPs under the same load of the overall IEM, which demonstrates that the increase of penetration of AOPs can effectively reduce the allocation of capacity in the IEM and save resources, which also proves that it is necessary to take the behavior of AOPs in the configuration of IEM into account.

6.4 Impact of Carbon Trading Price on Operation Costs of IEMSP

From **Figure 7**, we can see that the carbon trading price has little impact on the operation cost under the low price. When the carbon trading price rises to $35, the IEMSP operation cost increases obviously and the carbon trading cost decreases significantly. With the continuous growth of carbon trading prices, the system can profit through carbon trading. The photovoltaic device reaches the upper limit when the carbon trading price reaches $45/T. As the carbon trading price rises, the carbon emission of the system will not change significantly, and the operation state of the system tends to be stable. The analysis shows that the carbon trading price fluctuation impacts the system operation cost and carbon trading cost. Reasonable carbon prices are beneficial for the capacity allocation of IEMSP.

6.5 Analysis of Earnings of Aggregation of Prosumers Under Different Green Certificate Prices

The price of the green certificate is adjusted from $6 to $12 and the change in the income of the green certificate of the AOPs is observed as shown in **Figure 8**.

It is assumed that the AOPs can participate in green certificate transactions and green certificate cross-chain transactions according to the number of green certificates obtained by the AOPs to get a green income. It can be found from **Figure 8** that the higher the unit price of the green certificate, the more the earnings obtained through cross-chain transactions.

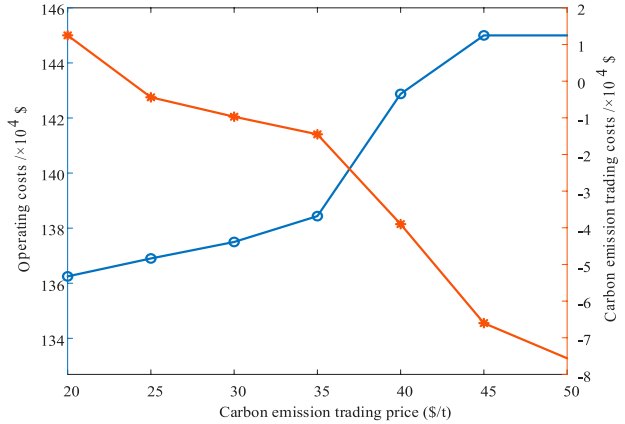

FIGURE 7 | Operating costs and carbon emission trading costs of IEMSP under different carbon emission trading prices.

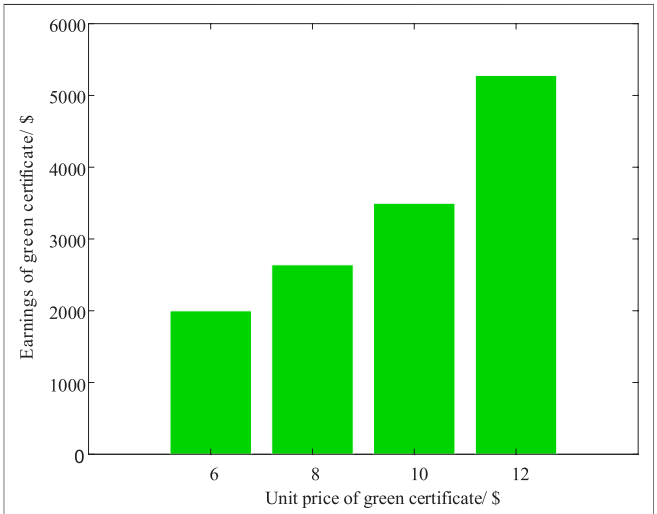

FIGURE 8 | Earnings under different green certificate prices.

7 CONCLUSION

To configure capacity for devices managed by IEMSP and devices of AOPs in IEM with minimal costs, an IEMSP capacity configuration cost model considering LLCT and an AOP capacity configuration cost model considering green cross-chain transactions are established. Electricity trading between AOPs is considered to reduce transmission losses and promote energy consumption nearby. The IEMSP-AOPs non-cooperative capacity allocation algorithm is used to consider electricity price trading between IEMSP and AOPs.

When trading between AOPs is considered under the 15% penetration of AOPs in the IEM, IEMSP's comprehensive costs have decreased by 26.9% and AOPs' comprehensive costs have reduced by 53.2%, which illustrates that the consideration of the electricity trading between AOPs will save a lot of costs and improve the economy of the capacity configuration under the same load; participation of the multi-market mechanism improves the enthusiasm of green equipment and reduces carbon emissions. When the multi-market mechanism is considered under the 15% penetration of AOPs, both the carbon emission of IEMSP and AOP decrease, IEMSP's carbon emission decreases by 16.7% and AOP's carbon emission decreases by 20%. In addition, simulation results demonstrate that the increase of the penetration of AOPs enables the allocation capacity of devices in IEM to decrease under the same load.

8 FUTURE WORK

The heating and gas network constraints will be considered in the next research work; subsequent research will consider enhancing the originality and complexity of device modeling of IEM considering AOPs; this study uses the particle swarm algorithm to solve the proposed game model, which may cause the solution results to fall into local optimum. How to make the solution the result of the game model faster and more accurate will be further studied in the future.

DATA AVAILABILITY STATEMENT

The original contributions presented in the study are included in the article/**Supplementary Material**, further inquiries can be directed to the corresponding author.

AUTHOR CONTRIBUTIONS

1. AOPs are considered in the capacity allocation of IEM, which can save the configuration capacity of the device under the same load and avoid waste of energy in IEM. 2. The approach of the non-cooperative game is used to solve the optimal capacity allocation model for IEM considering AOPs, thus obtaining the optimal capacity allocation results of the capacity of devices managed by IEMSP and devices of AOPs in IEM. 3. The multi-market mechanism is built based on the coupling mechanism of green certificate trading, carbon emission trading, and the electricity market to stimulate renewable energy equipment and increase environmental benefits in the IEM in the study.

SUPPLEMENTARY MATERIAL

The Supplementary Material for this article can be found online at: https://www.frontiersin.org/articles/10.3389/fenrg.2022.875499/full#supplementary-material

REFERENCES

Akram, U., Khalid, M., and Shafiq, S. (2018). Optimal Sizing of a Wind/solar/battery Hybrid Grid-connected Microgrid System. *IET Renew. Power Generation* 12, 72–80. doi:10.1049/iet-rpg.2017.0010

Atia, R., and Yamada, N. (2016). Sizing and Analysis of Renewable Energy and Battery Systems in Residential Microgrids. *IEEE Trans. Smart Grid* 7, 1204–1213. doi:10.1109/TSG.2016.2519541

Cai, Y., Gu, Y., Luo, G., Zhang, X., and Chen, Q. (2020). Blockchain Based Trading Platform of Green Power Certificate: Concept and Practice. *Dianli Xitong Zidonghua/automation Electr. Power Syst.* 44, 1–9. doi:10.7500/AEPS20200222003

Cao, Y., Mu, Y., Jia, H., Yu, X., Song, Y., and Wu, K. (2020). Multi-stage Planning of Park-Level Integrated Energy System Considering Construction Time Sequence. *Zhongguo Dianji Gongcheng Xuebao/proceedings Chin. Soc. Electr. Eng.* 40, 6815–6827. doi:10.13334/j.0258-8013.pcsee.200622

Chen, Q., Kang, C., Xia, Q., and Zhong, J. (2010). Power Generation Expansion Planning Model towards Low-Carbon Economy and its Application in china. *IEEE Trans. Power Syst.* 25, 1117–1125. doi:10.1109/TPWRS.2009.2036925

Chen, Q., Wang, K., Chen, S., and Xia, Q. (2018). Transactive Energy System for Distributed Agents: Architecture, Mechanism Design and Key Technologies. *Dianli Xitong Zidonghua/automation Electr. Power Syst.* 42, 1–7+31. doi:10.7500/AEPS20171031002

Clairand, J.-M., Arriaga, M., Canizares, C. A., and Alvarez-Bel, C. (2019). Power Generation Planning of Galapagos' Microgrid Considering Electric Vehicles and Induction Stoves. *IEEE Trans. Sustain. Energ.* 10, 1916–1926. doi:10.1109/TSTE.2018.2876059

Ge, L., Liu, H., Yan, J., Zhu, X., Zhang, S., and Li, Y. (2021). Optimal Integrated Energy System Planning with DG Uncertainty Affine Model and Carbon Emissions Charges. *IEEE Trans. Sustain. Energ.* 3029, 1. doi:10.1109/tste.2021.3139109

Helgesen, P. I., and Tomasgard, A. (2018). An Equilibrium Market Power Model for Power Markets and Tradable green Certificates, Including Kirchhoff's Laws and Nash-Cournot Competition. *Energ. Econ.* 70, 270–288. doi:10.1016/j.eneco.2018.01.013

Hu, P., Ai, X., Zhang, S., and Pan, X. (2020). Modelling and Simulation Study of TOU Stackelberg Game Based on Demand Response. *Dianwang Jishu/power Syst. Technol.* 44, 585–592. doi:10.13335/j.1000-3673.pst.2019.0387

Li, H., Liu, D., and Yao, D. (2021). Analysis and Reflection on the Development of Power System towards the Goal of Carbon Emission Peak and Carbon Neutrality. *Zhongguo Dianji Gongcheng Xuebao/proceedings Chin. Soc. Electr. Eng.* 41, 6245–6258. doi:10.13334/j.0258-8013.pcsee.210050

Liu, N., Wang, J., and Wang, L. (2019). Hybrid Energy Sharing for Multiple Microgrids in an Integrated Heat-Electricity Energy System. *IEEE Trans. Sustain. Energ.* 10, 1139–1151. doi:10.1109/TSTE.2018.2861986

Liu, N., Yu, X., Wang, C., Li, C., Ma, L., and Lei, J. (2017). Energy-Sharing Model with Price-Based Demand Response for Microgrids of Peer-To-Peer Prosumers. *IEEE Trans. Power Syst.* 32, 3569–3583. doi:10.1109/TPWRS.2017.2649558

Lu, Q., Guo, Q., and Zeng, W. (2021). Optimization Scheduling of an Integrated Energy Service System in Community under the Carbon Trading Mechanism: A Model with Reward-Penalty and User Satisfaction. *J. Clean. Prod.* 323, 129171. doi:10.1016/j.jclepro.2021.129171

Luo, Z., Qin, J., Liang, J., Zhao, M., Wang, H., and Liu, K. (2021). Operation Optimization of Integrated Energy System with Green Certificate Cross-Chain Transaction. *Dianwang Jishu/power Syst. Technol.* 45, 1311–1319. doi:10.13335/j.1000-3673.pst.2020.1940

Maharjan, S., Zhu, Q., Zhang, Y., Gjessing, S., and Basar, T. (2013). Dependable Demand Response Management in the Smart Grid: A Stackelberg Game Approach. *IEEE Trans. Smart Grid* 4, 120–132. doi:10.1109/TSG.2012.2223766

National Energy Administration (2021). *Notice of the National Energy Administration on Issuing the "Key Points of Energy Supervision Work in 2021.*

Pan, H., gao, H., Yanhong, y., Wang, m., Yinbo, z., and Junyong, l. (2021). "Multi-type Retail Packages Design and Multi-Level Market Power purchase Strategy

for Electricity Retailers Based on Master-Slave Game," in *Zhongguo Dianji Gongcheng Xuebao/Proceedings Chinese Soc. Electr. Eng.*, 1–16. Available at: https://kns.cnki.net/kcms/detail/11.2107.TM.20210728.1035.006.html.

Parag, Y., and Sovacool, B. K. (2016). Electricity Market Design for the Prosumer Era. *Nat. Energ.* 1. doi:10.1038/nenergy.2016.32

Qu, K., Huang, L., Yu, T., and Zhang, X. (2018). Decentralized Dispatch of Multi-Area Integrated Energy Systems with Carbon Trading. *Zhongguo Dianji Gongcheng Xuebao/proceedings Chin. Soc. Electr. Eng.* 38, 697–707. doi:10.13334/j.0258-8013.pcsee.170602

Quashie, M., Marnay, C., Bouffard, F., and Joós, G. (2018). Optimal Planning of Microgrid Power and Operating reserve Capacity. *Appl. Energ.* 210, 1229–1236. doi:10.1016/j.apenergy.2017.08.015

Shafie-Khah, M., Javadi, S., Siano, P., and Catalao, J. P. S. (20172017). *Optimal Behavior of Smart Households Facing with Both price-based and Incentive-Based Demand Response Programs*. IEEE Manchester PowerTech. doi:10.1109/PTC.2017.7981248

Teotia, F., Mathuria, P., and Bhakar, R. (2020). Peer-to-peer Local Electricity Market Platform Pricing Strategies for Prosumers. *IET Generation, Transm. Distribution* 14, 4388–4397. doi:10.1049/iet-gtd.2019.0578

Wang, Y., Wang, Y., Huang, Y., Yang, J., Ma, Y., Yu, H., et al. (2019). Operation Optimization of Regional Integrated Energy System Based on the Modeling of electricity-thermal-natural Gas Network. *Appl. Energ.* 251, 113410. doi:10.1016/j.apenergy.2019.113410

Wang, Z., Yu, X., Mu, Y., and Jia, H. (2020). A Distributed Peer-To-Peer Energy Transaction Method for Diversified Prosumers in Urban Community Microgrid System. *Appl. EnergyEnergy* 260, 114327. doi:10.1016/j.apenergy.2019.114327

Wei, W., Liu, F., and Mei, S. (2015). Energy Pricing and Dispatch for Smart Grid Retailers under Demand Response and Market Price Uncertainty. *IEEE Trans. Smart Grid* 6, 1364–1374. doi:10.1109/TSG.2014.2376522

Yang, N., Huang, Y., Dong, B., Xin, P., Liu, S., Ye, D., et al. (2019). Research on the Joint Planning Method of Electricity-Gas Integrated Energy System Based on Multi-Agent Game. *Zhongguo Dianji Gongcheng Xuebao/proceedings Chin. Soc. Electr. Eng.* 39, 6521–6532. doi:10.13334/j.0258-8013.pcsee.182021

Yu, M., and Hong, S. H. (2016). Supply-demand Balancing for Power Management in Smart Grid: A Stackelberg Game Approach. *Appl. Energ.* 164, 702–710. doi:10.1016/j.apenergy.2015.12.039

Zafar, R., Mahmood, A., Razzaq, S., Ali, W., Naeem, U., and Shehzad, K. (2018). Prosumer Based Energy Management and Sharing in Smart Grid. *Renew. Sust. Energ. Rev.* 82, 1675–1684. doi:10.1016/j.rser.2017.07.018

Conflict of Interest: The authors declare that the research was conducted in the absence of any commercial or financial relationships that could be construed as a potential conflict of interest.

Publisher's Note: All claims expressed in this article are solely those of the authors and do not necessarily represent those of their affiliated organizations or those of the publisher, the editors, and the reviewers. Any product that may be evaluated in this article or claim that may be made by its manufacturer is not guaranteed or endorsed by the publisher.

frontiers | Frontiers in Energy Research

ORIGINAL RESEARCH
published: 26 April 2022
doi: 10.3389/fenrg.2022.883602

A Low-Carbon Dispatch Strategy for Power Systems Considering Flexible Demand Response and Energy Storage

Haiteng Han, Tiantian Wei, Chen Wu, Xiuyan Xu, Haixiang Zang, Guoqiang Sun and Zhinong Wei*

College of Energy and Electrical Engineering, Hohai University, Nanjing, China

The consumption of traditional fossil energy brings inevitable environmental protection problems, which also makes the low-carbon transition in industrial development imminent. In the process of low-carbon transition, the power industry plays a very important role. However, the large-scale integration of renewable energy resources such as wind power and photovoltaic brings new characteristics to power system dispatch. How to design a dispatch strategy that considers both low-carbon demand and economic cost has become a major concern in power systems. The flexible resources such as demand response (DR) and energy storage (ES) can cooperate with these renewable energy resources, promoting the renewable energy generation and low-carbon process. Thus, a low-carbon dispatch strategy for power systems considering flexible DR and ES is proposed in this article. First, models of DR and ES based on their behavior characteristics are established. Then, a carbon emission index is presented according to China's Clean Development Mechanism (CDM). Finally, the low-carbon dispatch strategy for power systems is proposed through the combination of the carbon emission index and flexible resource dispatch models. The simulation results show that the proposed dispatch strategy can significantly improve wind power consumption and reduce carbon emission.

Keywords: power system dispatch, flexible resources, demand response, energy storage, low-carbon dispatch strategy

OPEN ACCESS

Edited by:
Qinran Hu,
Southeast University, China

Reviewed by:
Minjian Cao,
Tsinghua University, China
Xin Zhao,
Southeast University, China
Xun Dou,
Nanjing Tech University, China

****Correspondence:***
Haiteng Han
hanht@hhu.edu.cn

Specialty section:
This article was submitted to Smart Grids, a section of the journal Frontiers in Energy Research

Received: *25 February 2022*
Accepted: *21 March 2022*
Published: *26 April 2022*

Citation:
Han H, Wei T, Wu C, Xu X, Zang H, Sun G and Wei Z (2022) A Low-Carbon Dispatch Strategy for Power Systems Considering Flexible Demand Response and Energy Storage. Front. Energy Res. 10:883602. doi: 10.3389/fenrg.2022.883602

1 INTRODUCTION

Energy crisis and environmental protection issues are receiving more attention worldwide. Many countries are focusing on the development of sustainable renewable energy resources. China is in the stage of energy transformation, facing the challenge of carbon neutrality target by 2060. The strategy of energy revolution has emerged, which paves the way for low-carbon industrial development. In addition, in the process of energy structure transformation, flexible resources are important to achieve low-carbon advancement in power systems.

The trend of clean power integration is irreversible. The uncertainties brought by large-scale integration of renewable energy resources pose a higher challenge to the secure and stable operation of power systems (Shan et al., 2018; Cheng et al., 2021). On the one hand, customers are guided to stagger power consumption and optimize the load structure through reasonable demand response

(DR) (Shu et al., 2017). On the other hand, high-quality ES systems should be selected to match the generation dispatch of the power system (Shan et al., 2018; Zhang et al., 2018). Generally, DR in power systems refers to the electricity customer behavior of changing their electricity consumption activities according to market regulation signals (Hobbs et al., 1993; Federal Energy Regulatory Commission, 2007; Zhang et al., 2008). The DR in the electricity market can be classified into price-based response (PDR) and incentive-based response (IDR) according to the response mode. In addition, the electricity customers are guided to respond to the power system dispatch in long-term and short-term time scales (Wang et al., 2021). As an effective method for optimal dispatch of power systems, DR has been proposed in a large number of countries, helping change the electricity consumption pattern. It supports not only the grid's peak-shaving and valley-filling but also renewable power consuming (Gao et al., 2014; Aghaei and Alizadeh, 2013) IDR can combine with PDR to improve the reliability and flexibility of DR and make DR dispatched precisely in real time (Xu et al., 2019). Zhang et al. (2021) propose an optimal DR dispatch model considering supply–demand balance and security constraints; the imbalance pressure caused by renewable energy is alleviated. In the study by Hong-Tao et al. (2018), Chen establishes a wind–solar power consumption model, and it verifies the effectiveness of DR on reducing the curtailment of wind and solar power. In the study by Gao et al. (2019), Gao characterizes the uncertainty of DR participation by considering the risk attitudes. It shows that the introducing DR can improve the adequacy of generation systems including wind power. In the study by Li et al. (2021), Li develops an optimal DR dispatch strategy for DR dispatch coordinated with the load aggregator to achieve joint optimization of entity benefits. Furthermore, the application of automatic DR in smart grids can greatly enhance the security of power system operation (Taorong et al., 2020). DR can be applied in frequency modulation to balance the active power (Zhu et al., 2021) and ensure sufficient voltage balancing control capacity (Tan and Shaaban, 2020).

Similar to DR, energy storage (ES) also has the function of flexible regulation. The renewable power curtailment can be reduced by introducing ES into the system. Thus, the ES configuration strategy is regarded as an effective approach to enhance the friendliness of wind and solar power generation (Zhang et al., 2022). It is also helpful for the stability and economic efficiency of power systems (Ani, 2021). Dorahaki developed an optimal VPP dispatch model which contains distributed wind power and ES devices. The ES device can smooth the fluctuations caused by wind power in the study by Dorahaki et al. (2020). In addition, the joint operation of wind power and ES can relieve the contradiction of renewable energy supply and reprogram the tariff profit (Zhang J. et al., 2020). The storage duration, capacity, and charging/discharging frequency of ES are investigated in the study by Hargreaves and Jones, (2020) to make it suitable for renewable energy systems. The combination of DR and ES is more beneficial to promote the optimal operation of the power systems (Wang et al., 2016; He et al., 2021). The adverse impacts of wind power uncertainties on power system stability can be solved by introducing DR and ES. Su integrates DR to a hybrid Wind-PV-ES system, achieving a goal of zero-curtailment of renewable power based on the correlation analysis (Su et al., 2020). In the study by Firouzmakan et al. (2019), DR and ES are considered in comprehensive stochastic energy management system containing micro-CHP units and renewable energy to implement resource complementarity and improve integral revenue. A multi-energy microgrid with wind–solar power generation considering DR and ES is constructed to provide a reasonable plan for multiple energy applications (Shen et al., 2022). In conclusion, the integration of DR and ES offers additional sources of flexibility in the system (Mimica et al., 2022).

Carbon emission trading is an effective way to promote global emission reduction through the market mechanism. In the study by Lou et al. (2017), Lou includes carbon emission trading cost in the objective function based on the concept of low-carbon economy. It optimizes the power generation dispatch under the random charging/discharging behavior of EVs and effectively reduces the system's carbon emission. At the same time, the focus on carbon emission stimulates the demand for EVs, which helps take the lead in achieving the goal of "carbon peak" and "carbon neutrality" (Nie et al., 2022). Melgar-Dominguez et al. (2020) demonstrates that implementing a carbon emission trading scheme can make reduction in costs of the supplied energy and purchase of emission allowances. By incorporating the cost of carbon emission trading into a multi-energy complementary system, the environmental factors and system operating characteristics can be fully considered. Thus, wind and photovoltaic power curtailment and load shedding are reduced while minimizing system operating costs (Zhu et al., 2019). In the study by Zhang W. et al. (2020), Zhang quantitively evaluates the operation efficiency of different carbon emission trading systems to determine whether they are profitable to the economy and environment. Flexible resources such as DR and ES can cooperate with renewable energy to optimize power system dispatch and promote renewable power consumption. In addition, the import of the carbon emission trading market model can quantify the impacts of the dispatch strategy on carbon emission.

The existing literature has examined the response characteristics of DR and ES from various perspectives, showing the enhancing functions of DR and ES on carbon emission reduction. However, the integrated utilization of flexible resources still needs to be further explored, especially during the low-carbon transition period of power systems. Therefore, we propose a low-carbon dispatch strategy that combines carbon emission index and flexible DR and ES resources in this study. The strategy that realizes the reasonable coupling of conventional thermal power units, flexible resources, and carbon trading can effectively reduce wind power curtailment and quantitatively evaluate the reduction of carbon emission.

The remainder of this study is organized as follows. First, **Section 2** establishes the models of DR and ES based on their

behavioral characteristics. Subsequently, **Section 3** proposes a low-carbon dispatch strategy through the combination of carbon market with the flexible DR resources and ES models. **Section 4** demonstrates the effectiveness of the proposed strategy with simulation results. Finally, **Section 5** draws the conclusion of this work.

2 MODELS OF FLEXIBLE RESOURCES IN POWER SYSTEM DISPATCH

2.1 The Response and Configuration Model of Multiple Demand Response Resources

We consider incentive-based DR (IDR) and price-based DR (PDR) in this study. Here, three types of IDR including interruptible load (IL), direct load control (DLC), and transferable load (TL) are modeled.

Generally, IL and DLC adjust the response amount and duration within a period according to a dispatch plan as there is a supply–demand balance problem in the system.

The cost of IL and DLC can be expressed as

$$C_u(t) = \mu_u \cdot f_u \cdot \left|Q_u(t)\right| \cdot X_u(t)/t_{u.\mathrm{int}} \tag{1}$$

The dispatch of TL can shift part of the load from the peak hours to the valley hours, releasing the load pressure and reducing thermal unit start-ups and shutdowns.

The cost of TL response can be expressed as

$$C_v(t) = P_v(t) \cdot Q_v(t) \cdot X_v(t) \tag{2}$$

The PDR participates in system dispatch according to price signals, and the response amount and cost of PDR can be expressed as

$$Q_w(t) = \begin{cases} q_w(t) - q_{w,\max} & q_w(t) > q_{w,\max}, lmp(t) \geq lmp_1 \\ q_{w,\min} - q_w(t) & q_{w,\min} > q_w(t), lmp(t) \leq lmp_2 \\ 0 & \text{othercases} \end{cases} \tag{3}$$

When the locational marginal price is not in the threshold interval, the PDR resource can choose whether to respond and adjust to the specified load level. PDR can obtain the corresponding economic compensation from the system. The PDR acquisition response cost can be expressed as

$$C_w(t) = P_w(t) \cdot Q_w(t) \cdot X_w(t) \tag{4}$$

The cost model of multiple DR is introduced above. Generally, DR also requires considering the constraints such as response duration, interval time, and amount constraints. The constraints on DR resources are as follows.

- Maximum response duration constraint:

$$\sum_{t=k}^{k+T_{u\max}} X_u(t) \leq T_{u\max}, k = 1, 2, \ldots, T \tag{5}$$

- Maximum response count constraint:

$$\sum_{t=1}^{T} X_u(t)[1 - X_u(t)] \leq N_{u\max}. \tag{6}$$

- Minimum response interval time constraint:

$$\left[T_{u,\mathrm{int}}(t-1) - T_{u,\min}\right]\left[X_u(t) - X_u(t-1)\right] \geq 0 \tag{7}$$

- Load response amount constraint:

$$Q_{u\min} \cdot X_u(t) \leq |Q_u(t)| \leq Q_{u\max} \cdot X_u(t) \tag{8}$$

2.2 Energy Storage Model

The ES of power systems are modeled as follows. It is established based on its charging/discharging power, charging/discharging efficiency, maximum charging/discharging rate, self-discharging rate, and state of charge (SOC).

- Charging and discharging power constraints:

$$\begin{cases} 0 \leq p^{ch}(t) \leq p_r^{ch} \cdot X_{ES}(t) \\ 0 \leq p^{dis}(t) \leq p_r^{dis} \cdot X_{ES}(t) \end{cases} \tag{9}$$

- Charging and discharging capacity constraints:

$$\begin{cases} G^{ch}(t) = \eta^{ch} \cdot p^{ch}(t) \cdot \Delta t, \quad G^{ch}(t) \leq G^{ch}_{\max} \\ G^{dis}(t) = \dfrac{1}{\eta^{dis}} \cdot p^{dis}(t) \cdot \Delta t, G^{dis}(t) \leq G^{dis}_{\max} \end{cases} \tag{10}$$

- Self-discharging capacity constraint:

$$E^{self}(t) = ES(t-1) \cdot (1 - r) \tag{11}$$

- Storage capacity:

$$ES(t) = ES(t-1) - E^{self}(t) + G^{ch}(t) - G^{dis}(t) \tag{12}$$

- SOC constraint:

$$SOC_{\min} \leq \frac{ES(t)}{ES_{\max}} \leq SOC_{\max} \tag{13}$$

3 THE LOW-CARBON DISPATCH MODEL CONSIDERING FLEXIBLE DEMAND RESPONSE AND ENERGY STORAGE

3.1 A Carbon Market Model Based on Clean Development Mechanism Trading Mechanism

The carbon emission trading mechanism is proposed to promote CO_2 emission reduction. Based on the current economic situation, China participates in the Clean Development Mechanism (CDM) market. The large-scale grid integration of wind power is in accordance with the objective of the CDM. It can meet the demand of low-carbon dispatch of power systems. With

the introduction of the CDM, power generation entities are pre-assigned a certain baseline of CO_2 emissions, and the actual carbon emission is monitored (Lou et al., 2017).

Depending on the actual situation in China, the allowance allocation method is feasible. The allowance can influence the trading scale of the emission trading market and is regarded as an important factor of carbon emission trading cost. Therefore, allowances need to be measured in advance to assess the cost.

Enterprises responsible for emission reduction obligations attend the initial allocation of carbon emission trading allowances. The competent department of carbon emission trading distributes carbon emission allowances to them through legal means.

Enterprises obtain carbon emission rights through the initial allocation of carbon emission allowances. A reasonable allocation method is conducive to the optimal allocation of resources. It can enable enterprises to produce in a low-carbon and economically efficient way (Lou et al., 2017). We adopt the industry baseline method to calculate the free carbon emission allowances for power producers.

$$M = \sum_{t=1}^{T}\sum_{i=1}^{G}\xi_C \cdot p_i(t) \cdot \Delta t. \tag{14}$$

The amount of carbon allowances and the distribution method set by the government directly affects the effect of the supply of carbon emission rights. It further impacts the trading price in the carbon emission trading market. If an enterprise does not get enough allowances, it will enter the secondary market of trading to buy more. Conversely, when an enterprise emits less carbon than its allowances, it can earn revenue by selling the excess emission allowances. Therefore, the carbon emission of the participating carbon market in the model can be expressed as

$$M_C = \sum_{t=1}^{T}\sum_{i=1}^{G}\xi_i^C \cdot p_i(t) \cdot \Delta t. \tag{15}$$

The different allocation methods lead to different amounts of allowances for each enterprise. Thus, it indirectly affects the reasonableness of the supply of allowances. As a result, the motivation of enterprises to reduce emissions also changes, which affects the trading price.

The cost of emission C_C, namely, the costs incurred by carbon emission trading or paying penalties for the excess can be expressed as

$$C_C = f(M, M_C) \tag{16}$$

3.2 The Dispatch Model Considering Flexible Demand Response and Energy Storage Resources.

3.2.1 The Objective Function of the Dispatch Model

The dispatch model consists of five main parts: f_1, f_2, f_3 , f_4, and f_5, representing the thermal unit dispatch cost, carbon emission trading cost, penalty cost of wind power curtailment, DR participation cost, and ES operation cost, respectively.

- Thermal unit dispatch cost

The thermal unit dispatch process includes the start-up and shutdown cost and fuel cost.

The shutdown cost of thermal units is generally set to a small constant independent of the duration of continuous operation, and the start-up cost is set as an exponential function of the time constant for the shutdown time. The start-up and shutdown costs of thermal units are set as fixed parameters to simplify the analysis in this article, which can be expressed as

$$C_i^{up}(t) = m_i(t) \cdot c_i^{up} \tag{17}$$

$$C_i^{down}(t) = n_i(t) \cdot c_i^{down} \tag{18}$$

Then, the start-up and shutdown costs of thermal units in a dispatch cycle can be expressed as

$$C_1 = \sum_{t=1}^{T}\sum_{i=1}^{G}\left[C_i^{up}(t) + C_i^{down}(t)\right] \tag{19}$$

The fuel cost of thermal units is usually a binomial of its power output, which can be expressed as

$$C_2 = \sum_{t=1}^{T}\sum_{i=1}^{G}\left[a_i \cdot p_i(t)^2 + b_i \cdot p_i(t) + c_i \cdot u_i(t)\right] \tag{20}$$

Thus, the total cost of thermal unit dispatch is expressed as

$$f_1 = C_1 + C_2 \tag{21}$$

- Carbon emission trading cost

Based on CDM, the cost of carbon emission trading is as follows (Lou et al., 2017):

$$f_2 = C_C = K_{CDM} \cdot \Delta M_{CDM} + K_p \cdot \Delta M_p - K_{CDM} \cdot \Delta M'_{CDM} \tag{22}$$

$$\begin{cases} \Delta M_{CDM} = \max\left[0, \min\left(M_C - M, M_{CDM}^{\max}\right)\right] \\ \Delta M_p = \max\left(0, M_C - M - \Delta M_{CDM}\right) \\ \Delta M_{CDM}' = \max\left[0, \min\left(M - M_C, M_{CDM}^{\max}\right)\right] \end{cases} \tag{23}$$

When $M_C > M$, it means that the actual emission is higher than the allowances. In that case, it is required to obtain allowances for the excess part through CDM trading or paying penalty. The operating cost of the power systems will be increased accordingly. When $M_C \le M$, it means the actual emission is lower than the allowances. Then, the power systems can sell the surplus allowances for profit, hence equivalently reducing the integrated system cost.

- Penalty cost for wind power curtailment

$$f_3 = \sum_{t=1}^{T} p_w(t) \cdot W_{pw} \tag{24}$$

- DR participation cost

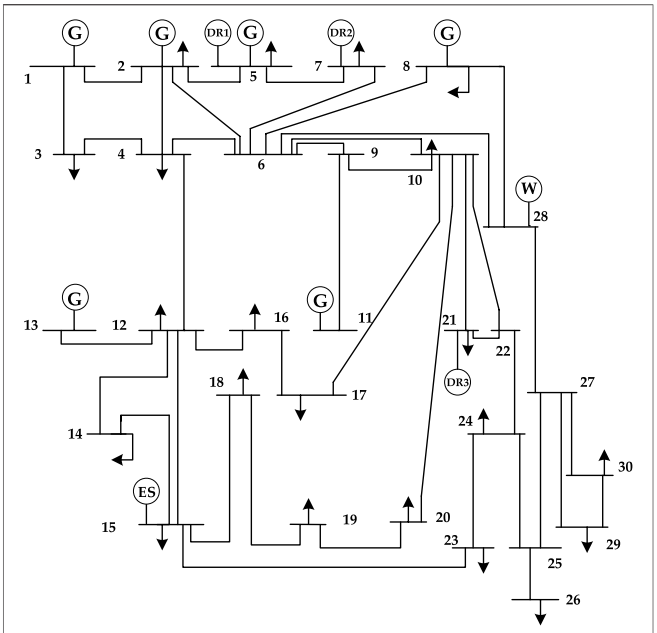

FIGURE 1 | Modified IEEE 30-bus test system.

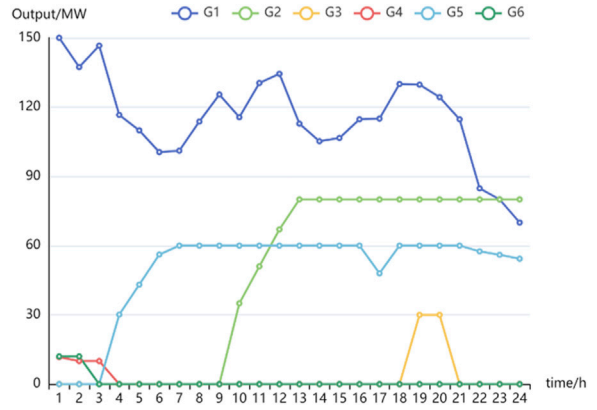

FIGURE 2 | Outputs of thermal units at each period in Scenario 1

The DR participation cost in a dispatch cycle can be expressed as

$$f_4 = \sum_{t=1}^{T}\left[\sum_{u=1}^{N_u} C_u(t) + \sum_{v=1}^{N_v} C_v(t) + \sum_{w=1}^{N_w} C_w(t)\right] \tag{25}$$

- ES operation cost

According to the ES model presented in 2.2, the operation cost of ES can be expressed as

$$f_5 = \sum_{t=1}^{T}\left[G^{ch}(t)\cdot V_{ch}(t) - G^{dis}(t)\cdot V_{dis}(t)\right] \tag{26}$$

Through integration of the aforementioned five subobjectives, the main objective function can be expressed as

$$\min f = f_1 + f_2 + f_3 + f_4 + f_5 \tag{27}$$

3.2.2 The Constraints of the Dispatch Model

The model also includes constraints on the operation of thermal power units and relative constraints of DR and ES.

- Spinning reserve constraint:

$$\sum_{i=1}^{G} y_i(t)\cdot p_{si}(t) + \sum_{j=1}^{k} X_v(t)\cdot Q_v(t) \geq \gamma\cdot L(t) \tag{28}$$

- Power balance constraint:

$$\sum_{i=1}^{G} p_i(t) + \sum_{u=1}^{Nu} Q_u(t) + \sum_{v=1}^{N_v} Q_v(t) + \sum_{w=1}^{N_w} Q_w(t) + W(t) - p_w(t) + E(t) = L(t). \tag{29}$$

- Upper and lower limit constraints of thermal unit output:

$$y_i(t)\cdot p_{i,\min} \leq p_i(t) \leq y_i(t)\cdot p_{i,\max} \tag{30}$$

- Minimum start-up and shutdown time constraints:

$$\begin{cases} [y_i(t-1) - y_i(t)][T_{i,on}(t-1) - T_{u,i}] \geq 0 \\ [y_i(t) - y_i(t-1)][T_{i,off}(t-1) - T_{d,i}] \geq 0 \end{cases} \tag{31}$$

- Ramping constraints:

$$\begin{cases} p_i(t) - p_i(t-1) \leq R_{u,i} \\ p_i(t-1) - p_i(t) \leq R_{d,i} \end{cases} \tag{32}$$

- Maximum start-up and shutdown power constraints:

$$\begin{cases} \bar{p}_i(t) \leq S_{d,i}\cdot n_i(t+1) + p_{i,\max}\cdot[y_i(t) - n_i(t+1)] & \text{shutdowns at time } t+1 \\ p_i(t) \geq p_i(t-1) - R_{d,i}\cdot y_i(t) - S_{d,i}\cdot n_i(t) & \text{shutdowns at time } t \\ \bar{p}_i(t) \leq p_i(t-1) + R_{u,i}\cdot y_i(t-1) + S_{u,i}\cdot m_i(t) & \text{startsup at time } t \end{cases} \tag{33}$$

- System stability requirement:

$$\sum_{i=1}^{N_G} p_i^s(t) \geq L(t)\cdot\beta \tag{34}$$

Constraints of DR resources in **Eqs 1–8** (35)
Constraints of ES resources in **Eqs 9–13** (36)

TABLE 1 | Amount of wind power curtailment at each period.

Time/h	1	2	3	4	5	6	7	8	9	10	11	12
Amount/MW	**31.9**	**44.3**	**31**	**37.5**	**11**	**5.6**	**38.7**	**52.9**	**30**	**5.6**	**0**	**0**
Time/h	13	14	15	16	17	18	19	20	21	22	23	24
Amount/MW	0	0	10.6	10.5	13.4	5.2	36.3	40.1	27.1	18.5	26.8	20.1

TABLE 2 | Daily operation cost of the system in Scenario 1

Total cost/$	Thermal unit dispatch cost/$	Carbon emission trading cost/$	Wind power curtailment penalty/$
105,512	87,614	2,985	14,913

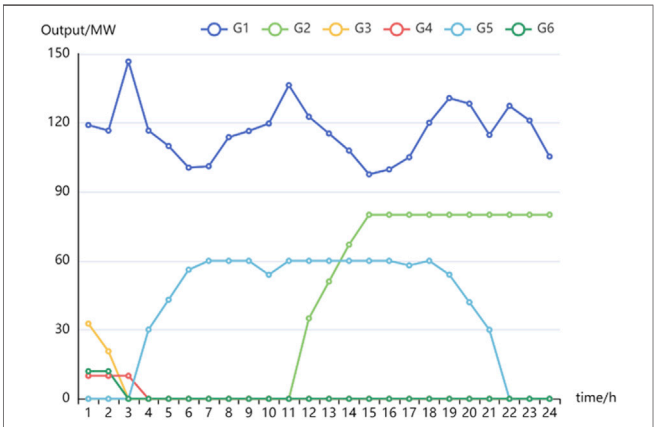

FIGURE 3 | Outputs of thermal units at each period in Scenario 2

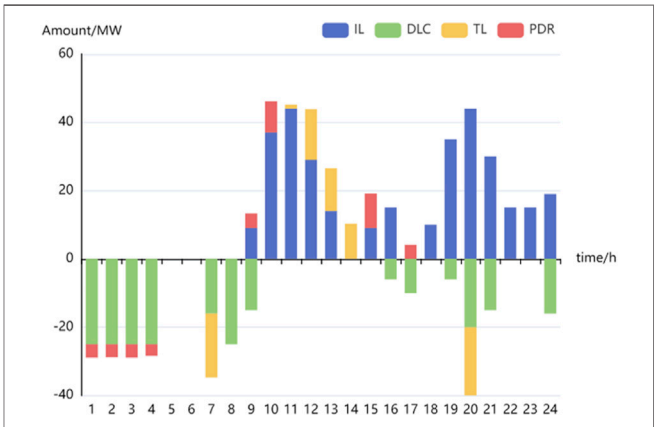

FIGURE 4 | Response values of DRs at each period in Scenario 2

4 CASE STUDY

To verify the effectiveness of our proposed low-carbon dispatch strategy, a modified IEEE30-bus test system is selected and shown in **Figure 1**. It has six thermal units and 41 lines. The system is assembled with three DR aggregators (named as D1, D2, and D3 in **Figure 1**) containing different DR resources at Bus 5, 7, and 21, respectively. D1 and D2 each contain three IDRs, and D3 contains one PDR resource. A wind farm with a total capacity of 45 MW is located at Bus 28. An ES module with a capacity of 500 MW·h is located at Bus 15. The relevant parameters of thermal power units, DR resources, ES device, system load forecast, and wind power forecast output are given in **Supplementary Material S1**. The model proposed in this study is solved by GAMS on a 16-core CPU/16G RAM PC. To quantitively access the impact of flexible DR and ES resources on the wind power consumption and carbon reduction, three scenarios are designed as follows.

Scenario 1

In this scenario, DR resources do not participate in the system dispatch process.

The outputs of thermal units are shown in **Figure 2**. The amount of wind power curtailment and daily operation costs of the system are shown in and **Tables 1**, **2**, respectively.

It can be found from **Table 1** that the wind power curtailment occurs frequently in Scenario 1. In **Table 2**, the total cost of system operation is $105512, of which the thermal unit dispatch cost, carbon emission trading cost, and wind power curtailment penalty are $87613, $2,985, and 14913, respectively.

Scenario 2:

In this scenario, only DR resources participate in the system dispatch process.

The characteristic parameters of IDR and PDR resources are listed in **Supplementary Material S1** and the LMP curves of PJM.

The outputs of thermal units, values of DR response, and amount of wind curtailment are shown in **Figures 3**, **4**; **Table 3**, respectively. The daily operation costs of the system are listed in **Table 4**.

The wind power curtailment amount in Scenario 1 and Scenario 2 are 497.10 and 242.00 MW, respectively. Compared with Scenario 1, the participation of DR resources in Scenario 2 helps reduce the wind power curtailment by 51.32%. In addition, it is worth noting that the carbon emission trading cost before and

TABLE 3 | Amount of wind curtailment at each period in Scenario 2

Time/h	**1**	**2**	**3**	**4**	**5**	**6**	**7**	**8**	**9**	**10**	**11**	**12**
Amount/MW	**3**	**15.5**	**2.1**	**9.1**	**11**	**5.6**	**4**	**27.9**	**19.3**	**14.7**	**0**	**0**
Time/h	13	14	15	16	17	18	19	20	21	22	23	24
Amount/MW	0	0	20.7	4.5	7.5	5.2	30.3	0.1	12.1	18.5	26.8	4.1

TABLE 4 | Daily operation costs of system in Scenario 2

Total cost/$	**Thermal unit dispatch cost/$**	**Carbon emission trading cost/$**	**Wind power curtailment penalty/$**	**DR response cost/$**
97418	81,479	2,776	7,260	5,902

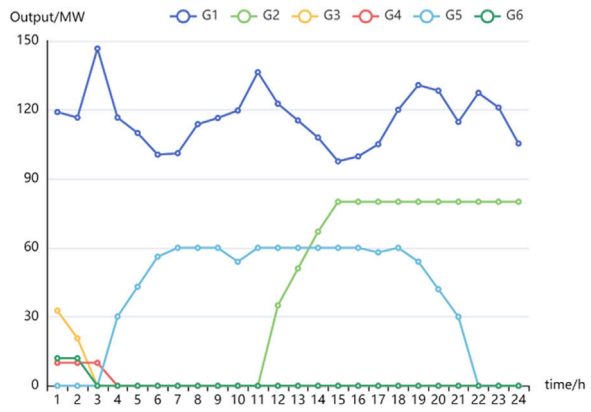

FIGURE 5 | Outputs of thermal units at each period in Scenario 3

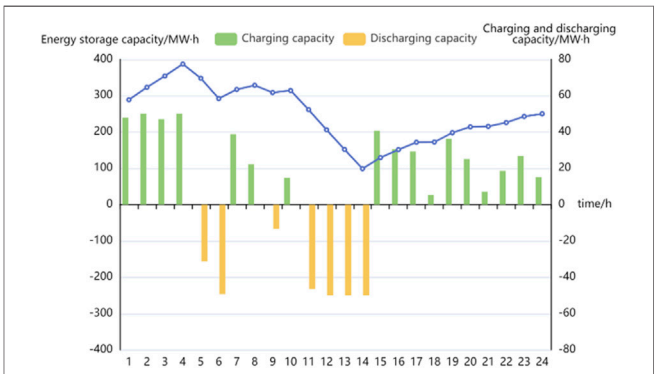

FIGURE 7 | Variation of ES capacity at each period in Scenario 3.

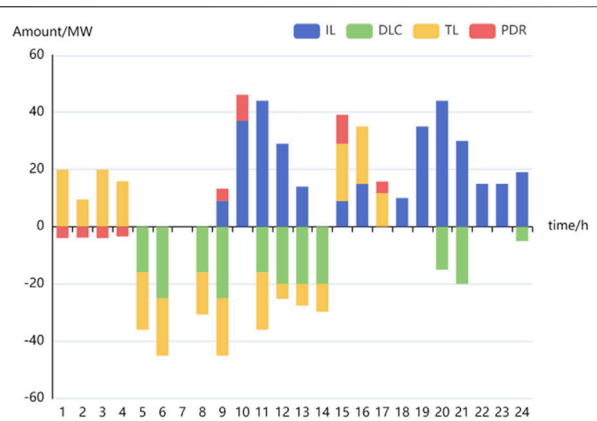

FIGURE 6 | Response values of DRs at each period in Scenario 3

after DR participation is $2,985 and $2,776 respectively. With DR participation in the system dispatch, the overall outputs of thermal power units decrease. In addition, the peak-to-valley gap of the system is reduced, which directly reduces carbon emission. DR provides more opportunity for wind power generation and avoids frequent start-up and shutdown actions of the thermal units. Therefore, it also helps relieving the pressure of high load peaking.

Scenario 3

In this scenario, both DR and ES participate in the system dispatch process.

The outputs of thermal units, values of DR response, and variation of ES capacity are shown in **Figure 5**, **Figure 6**, and **Figure 7**, respectively. The blue curve representing energy storage capacity in **Figure 7** is associated with the left *Y*-axis, and the green and yellow bars representing the charging and discharging capacity are associated with the right *Y*-axis. The daily operation costs of the system are listed in **Table 5**.

In Scenario 3, the time distribution of wind power resources is further optimized with the participation of ES in the system operation process. The wind power here is completely consumed. The flexible dispatch strategy and superior response performance of DR resources and ES play an important role in wind power consumption and system power balance maintenance. Moreover, ES helps with relieving the pressure of peaking. In carbon emission reduction, the effect of ES is reflected in the consumption of wind power to reducing carbon emission at the source-side.

TABLE 5 | Daily operation costs of the system in Scenario 3

Total cost/$	Thermal unit dispatch costs/$	Carbon emission trading cost/$	Wind power curtailment penalty/$	DR response cost/$	ES cost/$
90988	81,479	2,776	0	6,189	544

TABLE 6 | Comparison of costs in each scenario.

Scenario	Total cost/$	Thermal unit dispatch cost/$	Carbon emission cost/$	Wind power curtailment penalty/$	DR response cost/$	ES cost/$
1	105,512	87,614	2,985	14,913	0	0
2	97,418	81,479	2,776	7,260	5,902	0
3	90,988	81,479	2,776	0	6,189	544

As can be found from **Table 6**, the participation of DR in the system dispatch process has optimized the operation of thermal units, reducing their peaking pressure and the costs arising from frequent start-ups and shutdowns. In addition, the increase in wind power consumption results in significant reduction in wind power curtailment penalty. The improvement of thermal unit outputs has reduced the carbon emission trading cost of the system by 7.00% with DR participation. Although the involvement of ES brings added costs to the system, it is notably less than the decrease in the wind power curtailment penalty. Thus, compared with Scenario 1 and 2, the total cost in Scenario 3 decreases by 7.67 and 13.77%, respectively.

5 CONCLUSION

In this article, we propose a low-carbon dispatch strategy for power systems considering flexible DR and ES. First, the models of flexible DR resources and ES is established based on their behavior characteristics. Second, by combining the carbon market model with the flexible DR resources and ES model, the low-carbon dispatch strategy is proposed. Finally, the effectiveness of the proposed strategy is verified with simulations.

From the presented work, general conclusions can be drawn as follows:

1) The cooperation of DR and ES has a remarkable impact on the power system dispatch. The combined operation mode of DR and ES effectively promotes peak-shaving and valley-filling.
2) The combined DR–ES dispatch has a notable function on wind power consumption. Through the dispatch of flexible resources, the wind power curtailment can be greatly reduced.
3) The low-carbon dispatch strategy can quantitatively evaluate the reduction of carbon emission, realizing the reasonable coupling of conventional thermal power units, flexible resources, and carbon trading. It can help design carbon reduction policies according to DR and ES activities.

In the future work, we plan to combine the uncertainties derived from power and load with our framework and make the proposed model appropriate for short-time scale dispatch environment.

DATA AVAILABILITY STATEMENT

The original contributions presented in the study are included in the article/**Supplementary Material**; further inquiries can be directed to the corresponding author.

AUTHOR CONTRIBUTIONS

HH conceptualized and formed the methodology. TW prepared the original draft. HH, TW, and XX reviewed and edited the article. HH, CW, and TW supervised the study. ZW, HZ and GS administered the project. HH funded the acquisition. All authors have read and agreed to the published version of the manuscript.

FUNDING

This research was funded in part by the Fundamental Research Funds for the Central Universities under Grant B200201016 and in part by the Postdoctoral Research Funding Program of Jiangsu Province under Grant 2021K622C.

SUPPLEMENTARY MATERIAL

The Supplementary Material for this article can be found online at: https://www.frontiersin.org/articles/10.3389/fenrg.2022.883602/full#supplementary-material

REFERENCES

Aghaei, J., and Alizadeh, M.-I. (2013). Demand Response in Smart Electricity Grids Equipped with Renewable Energy Sources: A Review. *Renew. Sustain. Energ. Rev.* 18, 64–72. doi:10.1016/j.rser.2012.09.019

Ani, V. A. (2021). Development of an Intelligent Power Management System for Solar PV-Wind-Battery-Fuel-Cell Integrated System. *Front. Energ. Res.* 9. doi:10.3389/fenrg.2021.613958

Cheng, L., Zang, H., Wei, Z., Ding, T., Xu, R., and Sun, G. (2022). Short-term Solar Power Prediction Learning Directly from Satellite Images With Regions of Interest. *IEEE Trans. Sustain. Energy* 13, 629–939. doi:10.1109/TSTE.2021.3123476

Dorahaki, S., Dashti, R., and Shaker, H. R. (2020). Optimal Energy Management in the Smart Microgrid Considering the Electrical Energy Storage System and the Demand-Side Energy Efficiency Program. *J. Energ. Storage* 28, 101229. doi:10.1016/j.est.2020.101229

Federal Energy Regulatory Commission (2007). The Content You Are Looking for Is Currently Archived in eLibrary. Available at: http://www.ferc.gov/legal/staff-reports/demand-response.pdf (Accessed February 15, 2022).

Firouzmakan, P., Hooshmand, R.-A., Bornapour, M., and Khodabakhshian, A. (2019). A Comprehensive Stochastic Energy Management System of Micro-CHP Units, Renewable Energy Sources and Storage Systems in Microgrids Considering Demand Response Programs. *Renew. Sustain. Energ. Rev.* 108, 355–368. doi:10.1016/j.rser.2019.04.001

Gao, C. W., Liang, T. T., and Li, Y. (2014). A Review of the Theory and Practice of Automatic Demand Response. *Power Sys Techno* 352, 359. doi:10.13335/j.1000-3673.pst.2014.02.013

Gao, J., Ma, Z., and Guo, F. (2019). The Influence of Demand Response on Wind-Integrated Power System Considering Participation of the Demand Side. *Energy* 178, 723–738. doi:10.1016/j.energy.2019.04.104

Hargreaves, J. J., and Jones, R. A. (2020). Long Term Energy Storage in Highly Renewable Systems. *Front. Energ. Res.* 8. doi:10.3389/fenrg.2020.00219

He, P., Chi, F., and Zhao, Z. B. (2021). A Research on a Scheduling Method of Wind Power Energy Storage System with Demand Response Participation. *Comput. Digital Eng.* 1936, 1940. doi:10.3969/j.issn.1672-9722.2021.09.039

Hobbs, B. F., Rouse, H. B., and Hoog, D. T. (1993). Measuring the Economic Value of Demand-Side and Supply Resources in Integrated Resource Planning Models. *IEEE Trans. Power Syst.* 8, 979–987. doi:10.1109/59.260903

Hong-Tao, C., Jian-Xue, C., Yang, D., Meng, Y., and Ge, P. (2018). "Local Consumption Model of Wind and Photovoltaic Power Based on Demand Side Response," in 2018 China International Conference on Electricity Distribution (CICED), Tianjin, China, 17-19 Sept. 2018. doi:10.1109/CICED.2018.8592126

Li, W., Han, R. D., and Sun, C. (2021). Optimal Incentive Contract and Incentive Strategy for Levelable Load Participation in Demand Response Based on Electricity Consumption Preference. *Proc. Chin. Soc. Electr. Eng* 185, 193. doi:10.13334/j.0258-8013.pcsee.202593

Lou, S., Zhang, L., Wu, Y., and Wang, Y. (2017). Coordinated and Optimal Operation between Electric Vehicle Cluster and Power System in Low Carbon Economy. *Trans. China Electrotechnical Soc.* 176, 183. doi:10.19595/j.cnki.1000-6753.tces.2017.05.021

Melgar-Dominguez, O. D., Pourakbari-Kasmaei, M., Lehtonen, M., and Sanches Mantovani, J. R. (2020). An Economic-Environmental Asset Planning in Electric Distribution Networks Considering Carbon Emission Trading and Demand Response. *Electric Power Syst. Res.* 181, 106202. doi:10.1016/j.epsr.2020.106202

Mimica, M., Sinovčić, Z., Jokić, A., and Krajačić, G. (2022). The Role of the Energy Storage and the Demand Response in the Robust reserve and Network-Constrained Joint Electricity and reserve Market. *Electric Power Syst. Res.* 204, 107716. doi:10.1016/j.epsr.2021.107716

Nie, Q., Zhang, L., and Li, S. (2022). How Can Personal Carbon Trading Be Applied in Electric Vehicle Subsidies? A Stackelberg Game Method in Private Vehicles. *Appl. Energ.* 313, 118855. doi:10.1016/j.apenergy.2022.118855

Shan, F., Li, X., and Song, Y. (2018). Economic Dispatch of Regional Integrated Energy System Based on Improved Two-Stage Robust Optimization. *Electr. Meas. Instrumentation* 103, 108. doi:10.3969/j.issn.1001-1390.2018.23.017

Shen, Y., Hu, W., Liu, M., Yang, F., and Kong, X. (2022). Energy Storage Optimization Method for Microgrid Considering Multi-Energy Coupling Demand Response. *J. Energ. Storage* 45, 103521. doi:10.1016/j.est.2021.103521

Shu, Y., Zhang, Z., Guo, J., and Zhang, Z. (2017). Analysis of Key Factors of New Energy Consumption and Research on Solution Measures. *Proc. Chin. Soc. Electr. Eng* 1, 9. doi:10.13334/j.0258-8013.pcsee.162555

Su, S., Zhang, S., and You, Y. (2020). A Demand Response Strategy Based on Correlation Analysis for Complementary Wind and Storage. *Sci. Techn. Eng.* 6902, 6907. doi:10.3969/j.issn.1671-1815.2020.17.029

Tan, W.-S., and Shaaban, M. (2020). Dual-timescale Generation Scheduling with Nondeterministic Flexiramp Including Demand Response and Energy Storage. *Electric Power Syst. Res.* 189, 106821. doi:10.1016/j.epsr.2020.106821

Taorong, G., Ninghui, H., Jindou, Y., and Chao, Y. (2020). Demand Response Analysis of Large Electricity Consumer Based on Load Response Model. *Manage. Sci. Informatization Econ. Innovation Develop. Conf.* 81, 84. doi:10.1109/MSIEID52046.2020.00023

Wang, B., Ye, B., and Zhu, L. (2021). Practice and Exploration of Electricity Demand Response in China under Market Environment[J]. *Electricity demand-side Manag.* 91, 95. doi:10.3969/j.issn.1009-1831.2021.05.018

Wang, T. W., Gao, E., Jiang, M., and Du, T. (2016). Optimal Scheduling of Power System under Virtual Power Plant Counting and Distributed Wind Power and Energy Storage System. *Electric Power Construction* 108, 114. doi:10.3969/j.issn.1000-7229.2016.11.016

Xu, Y., Liao, Q., and Liu, D. (2019). Integrated Demand Response and Game-Based Intra-day Joint Optimal Dispatch of Regional Integrated Energy System with Multiple Subjects. *Power Sys Techno* 2506, 2518. doi:10.13335/j.1000-3673.pst.2018.2421

Zhang, H., Gong, C., Ju, W., Pan, G., and Wang, W. (2021). Optimization Dispatch Modeling for Demand Response Considering Supply and Demand Balance and Security Constraints. *Power Syst. Green Energ. Conf.* 166, 170. doi:10.1109/PSGEC51302.2021.9542507

Zhang, J., Guerra, O. J., Eichman, J., and Pellow, M. A. (2020). Benefit Analysis of Long-Duration Energy Storage in Power Systems with High Renewable Energy Shares. *Front. Energ. Res.* 8. doi:10.3389/fenrg.2020.527910

Zhang, L. D., Yuan, Y., and Sun, D. (2018). A Wind-Storage Joint Operation Scheduling Model Based on Two-Stage Robust Interval Optimization. *Electric Power Automation Equipment* 59, 66. doi:10.16081/j.issn.1006-6047.2018.12.009

Zhang, Q., Wang, X., Wang, J., and Feng, C. L. (2008). A Review of Demand Response Research under Power Market. *Automat Electron. Power Sys* 97, 106. doi:10.3321/j.issn:1000-1026.2008.03.022

Zhang, R. C., Zhai, D. J., and Zhang, Y. (2022). Distributed Model Predictive Control Based on Scenic Storage Double-Layer Bus Microgrid. *Mech. Des. Manufacture* 1, 6. doi:10.19356/j.cnki.1001-3997.20211115.040

Zhang, W., Li, J., Li, G., and Guo, S. (2020). Emission Reduction Effect and Carbon Market Efficiency of Carbon Emissions Trading Policy in China. *Energy* 196, 117117. doi:10.1016/j.energy.2020.117117

Zhu, Q., Wang, Y., Song, J., Jiang, L., and Li, Y. (2021). Coordinated Frequency Regulation of Smart Grid by Demand Side Response and Variable Speed Wind Turbines. *Front. Energ. Res.* 9. doi:10.3389/fenrg.2021.754057

Zhu, Y., Lan, Z. B., and Kui, Z. (2019). Optimal Operation of Wind-Storage Multi-Energy Complementary System Considering Carbon Emission Cost. *Power Syst. Prot. Control.* 127, 133. doi:10.19783/j.cnki.pspc.180659

Conflict of Interest: The authors declare that the research was conducted in the absence of any commercial or financial relationships that could be construed as a potential conflict of interest.

GLOSSARY

Indices

t Index of hours

i Index of thermal units

l Index of branches

Parameters

μ_u Weight factor of IL and DLC

lmp_1/lmp_2 Maximum and minimum locational marginal price ($/MW·h)

$q_{w,\min}/q_{w,\max}$ Maximum and minimum response amount of PDR (MW)

$T_{u\max}$ Maximum duration of a single DR response (h)

$N_{u\max}$ Maximum response hours of DR in a dispatch cycle (h)

T A dispatch cycle

G Number of the thermal units

$T_{u,\min}$ Minimum response interval of DR (h)

$Q_{u\max}/Q_{u\min}$ Maximum and minimum load response amounts of DR (MW)

$P_v(t)/P_w(t)$ Unit price of the compensation for TL/PDR in period t ($/MW·h)

p_r^{ch}/p_r^{dis} Rated charging and discharging power of the ES (MW)

η^{ch}/η^{dis} Charging and discharging efficiency of the ES

$G_{\max}^{ch}/G_{\max}^{dis}$ Maximum charging and discharging capacity of the ES (MW·h)

r Self-discharging rate of the ES

$SOC_{\max}/SOC_{\min}$ Maximum and minimum state of charge

$ES_{\max}$ Rated capacity of the ES (MW·h)

ξ_C Initial allocation factor of carbon emission

ξ_i^C Actual carbon emission intensity factor of the ith unit

c_i^{up}/c_i^{down} Fixed start-up and shutdown costs ($/MW·h)

$a_i/b_i/c_i$ Fuel cost factors of the ith thermal unit

K_{CDM}/K_p CDM unit price and unit excess penalty ($/ton)

$M_{CDM}^{\max}$ Maximum amount of allowance power systems can trade through the CDM (ton)

W_{pw} Unit price of wind power curtailment penalty ($/MW·h)

γ Reserve demand factor to deal with the system load forecasting error

$p_{i,\max}/p_{i,\min}$ Upper and lower limits on the output power of the ith thermal unit (MW)

$T_{d,i}/T_{u,i}$ Maximum and minimum continuous running time of the ith thermal unit (h)

$R_{u,i}/R_{d,i}$ Upward and downward ramping rates of the ith unit (MW/h)

$S_{u,i}/S_{d,i}$ Maximum start-up and shutdown power of the ith unit (MW/h)

β Minimum demand factor to meet the system stability requirement

Variables

$C_u(t)/C_v(t)/C_w(t)$ Response cost of IL and DLC/TL/PDR in period t ($)

$Q_u(t)/Q_v(t)/Q_w(t)$ Response amount of IL and DLC/TL/PDR in period t (MW)

$X_u(t)/X_v(t)/X_w(t)$ Response state of IL and DLC/TL in period t

f_u Response number of DR in a circle

$t_{u.\text{int}}$ Time interval after the last action of DR (h)

$q_w(t)$ Predicted day-ahead load in period t (MW)

$lmp(t)$ LMP in period t ($/MW·h)

$T_{u,\text{int}}(t)$ Accumulated interval from the last action of DR in period t (h)

$X_{ES}(t)$ Status constraint variable of the ES in period t

$p^{ch}(t)/p^{dis}(t)$ Charging and discharging power of the ES in period t (MW)

$G^{ch}(t)/G^{dis}(t)$ Charging and discharging capacity of the ES in period t (MW·h)

$E^{self}(t)$ Self-discharge energy of the ES in period t (MW·h)

$ES(t)$ Storage capacity of the ES in period t (MW·h)

M Free carbon emission allowance of the system (ton)

M_C Actual carbon emission of the system (ton)

C_C Cost incurred by carbon trading or paying penalty for the excess ($)

$p_i(t)$ Power output of the ith thermal unit in period t (MW)

f_1 Thermal unit dispatch cost in a dispatch cycle ($)

f_2 Cost of carbon emission trading in a dispatch cycle ($)

f_3 Penalty cost of wind power curtailment in a dispatch cycle ($)

f_4 Cost of DR participation in a dispatch cycle ($)

f_5 Cost of ES operation in a dispatch cycle ($)

$m_i(t)/n_i(t)$ Start-up and shutdown state of the ith thermal unit in period t

$C_i^{up}(t)/C_i^{down}(t)$ Start-up and shutdown cost of the ith thermal unit in period t

C_1 Start-up and shutdown cost in a dispatch cycle ($)

C_2 Fuel cost of thermal units ($)

$\Delta M_{CDM}/\Delta M'_{CDM}$ Allowance power systems purchased and sold through the CDM (ton)

ΔM_p Allowance power systems obtained through penalty payment (ton)

$p_w(t)$ Amount of wind power curtailment in period t (MW)

$V_{ch}(t)/V_{dis}(t)$ Contract price for ES charging and discharging in period t (MW·h)

$y_i(t)$ State of the ith thermal unit in period t

$p_{si}(t)$ Spinning reserve provided of the ith thermal unit in period t (MW)

$F_l(t)$ Active power of the branch l in period t (MW)

$\theta(t)$ Voltage phase-angle in period t

$W(t)$ Wind power output in period t (MW)

$E(t)$ Power supplied by the ES in period t (MW)

$L(t)$ Predicted load of the system in period t (MW)

$T_{i,off}(t)/T_{i,on}(t)$ Cumulative shutdown and start-up time of the ith unit in period t (h)

frontiers | Frontiers in Energy Research

ORIGINAL RESEARCH
published: 03 May 2022
doi: 10.3389/fenrg.2022.883598

Day-Ahead Operation of an Urban Energy System Considering Traffic Flows and Peak Shaving

Yan Peng[1], Junchao Ma[1], Chengyu Lu[1], Sheng Chen[2] and Lei Pei[2]*

[1]State Grid Zhejiang Electric Power Research Institute, Hangzhou, China, [2]The College of Energy and Electrical Engineering, Hohai University, Nanjing, China

With the increasing penetration of new-type loads such as electric vehicles and hydrogen fuel vehicles in urban power grids, the peak-to-valley load difference increases sharply, and a multi-energy coordination model is desirable. This article proposes a day-ahead operation model of an urban energy system considering traffic flows and peak shaving, which can positively contribute to multi-energy complement and low-carbon emission. The proposed model minimizes the total cost of electricity and gas by optimizing the charging and discharging strategies of energy storage, in which the output of the wind turbine and energy management of the energy hub are adaptively adjusted. The urban energy system is represented by a second-order cone (SOC) energy flow model, and hence, the optimization problem is modeled as a mixed integer SOC programming (MISOCP). Finally, test results on an integrated urban energy network indicate that the energy storage and multi-energy coordination can alleviate the peak load cutting and valley filling. The relationship between urban grid operation cost and peak-valley difference is also discussed. The maximum utilization of renewable energy sources using gasoline vehicles has been presented in this study to illustrate cost and emission reductions for a sustainable integrated electricity and transportation infrastructure.

Keywords: an urban energy system, peak shaving, traffic flows, multi-energy complement, low-carbon operation

OPEN ACCESS

Edited by:
Qinran Hu,
Southeast University, China

Reviewed by:
Hossam A. Gabbar,
Ontario Tech University, Canada
Chuan He,
Sichuan University, China
Shuai Lu,
Southeast University, China

****Correspondence:***
Sheng Chen
chenshenghhu@163.com

Specialty section:
This article was submitted to Smart Grids, a section of the journal Frontiers in Energy Research

Received: *25 February 2022*
Accepted: *28 March 2022*
Published: *03 May 2022*

Citation:
Peng Y, Ma J, Lu C, Chen S and Pei L (2022) Day-Ahead Operation of an Urban Energy System Considering Traffic Flows and Peak Shaving. Front. Energy Res. 10:883598. doi: 10.3389/fenrg.2022.883598

1 INTRODUCTION

1.1 Motivation

In recent years, energy consumption and global environmental problems have become increasingly serious, and the energy transition toward a low-carbon energy system is highly desirable (Zhao et al., 2017). The energy internet provides great potential for reliable power supply and an improved energy efficiency by integrating various energy production/conversion components, including renewable energy sources (RESs), energy storage systems (ESSs), hydrogen fuel vehicles (HVs), and electric vehicles (EVs) (Strasser et al., 2015; Meng and Wang, 2017; Yang and Fang, 2017). At the same time, interactions between urban electrical, transportation, and natural gas systems have become increasingly common due to the utilization of coupling components such as microturbines, combined heat and power (CHP), and power to gas units (Mancarella, 2014; Shabanpour-Haghighi and Seifi, 2015). The coupling of urban multi-energy networks positively contributes to the improved energy utilization efficiency, multi-energy complement, and the construction of a low-carbon sustainable energy system (Xu et al., 2020).

Traditionally, coupled energy systems have been operated and optimized independently (Chen et al., 2014). The urban distribution network that is inactive generally has limited ability to

regulate power flow, which results in the problem of a large difference between the daily peak and valley of the net load (Uddin et al., 2018). On the other hand, the traditional energy storage has relatively small storage capacity with a high investment cost, and hence, it is difficult to store energy effectively on a large scale and for a long time (Zhao et al., 2020). Considering the fact that the traditional urban distribution network cannot fully meet the electricity demand of new-type loads such as EVs and HVs, the development of day-ahead co-optimization of multi-energy systems is of considerable interest.

Owing to the aforementioned considerations, the present work develops a day-ahead co-optimization strategy for urban energy networks considering traffic flows.

1.2 Literature Review

1.2.1 Research on Power-Transportation Coordination

EVs and HVs have become a promising alternative to gasoline vehicles (GVs) for decarbonizing the transportation sector and combating climate change (IEA, Global EV Outlook, 2020). An integrated demand response framework is designed to regulate flexible resources in both networks through optimal road tolls and electricity tariffs in Lv et al., 2021a. In Rotering and Ilic (2011), the problem of growing peak load and grid overloading is addressed based on a forecast of future electricity prices, and the dynamic programming algorithm is employed to find the economically optimal solution for the vehicle owner. Hu et al. (2016) present an integrated optimization framework for battery sizing, charging, and on-road power management in plug-in hybrid EVs. The maximum utilization of RESs using GVs has been presented in Saber and Venayagamoorthy (2011) to achieve cost and emission reductions, which contributes to a low-carbon integrated electricity and transportation infrastructure. We note that most works consider the coupling between the transportation system and the power grid. However, the coupling between the power, natural gas, and the transportation system has not been well considered.

1.2.2 Coordinated Optimization of Multi-Energy Systems

A day-ahead optimal scheduling of the urban energy system is proposed by Jin et al., 2016, in which the flexible and reconfigurable topology of power distribution networks is considered. The joint and unified optimization decision of coupled power systems and natural gas systems is analyzed in Martínez-Mares et al. (2011). Correa-Posada and Sánchez-Martín (2015) determine the dynamic optimal operation strategy of the electricity–gas integrated energy system, which includes a transient natural-gas flow model. An integrated electricity–gas system with steady-state energy flow models considering the uncertainty of wind power is proposed in Gao and Li (2020). Additionally, a new Benders decomposition-based algorithm is proposed, which improves the solution efficiency for non-convex models (Gao and Li, 2021). A new external dependency model based on the energy hub (EH) is introduced to consider the possible uncertainty in customer decision through stochastic model processing (Neyestani et al., 2015). The stochastic optimal model is investigated with the comprehensive consideration of renewable generation and carbon-capture-based power-to-gas technology (Li et al., 2018). However, we note that most existing works on coordination optimization of integrated energy systems do not consider the existence of new-type loads such as EVs and HVs. Moreover, in most existing studies, a common assumption is that the driving mode of EVs is known. Arrival rates and times as well as the number of charging requests are specified in advance in a deterministic or stochastic manner, which can be determined from data-driven methods or queuing theory or modeled with probabilistic models through Markov decision processes. This assumption is reasonable for set-level research, such as residential parking management or a single CS management. However, it may not be appropriate if the system-level interdependency is under investigation, which is proposed in this article.

1.3 Contribution of This Study

To fill the research gaps summarized above, our model makes the following contributions:

1) We propose a mixed-UE traffic flow model based on an urban transportation system and divide the overall vehicular flows into five categories: GV traffic flow, EV traffic flow, HV traffic flow, HV charging flow, and EV charging flow. Our model, hence, accurately simulates the distribution of EVs and HVs in the urban transportation network.
2) We develop a day-ahead optimal dispatch of an urban energy system considering the transportation-network operation model, which includes the electric–gas co-optimization and the impact of traffic flows. Our model positively contributes to multi-energy complement and low-carbon operation. Moreover, the optimal energy management of EHs reduces the peak-valley difference caused by increasing penetrations of new-type loads such as EVs and HVs.

The remainder of this article is organized as follows: **Section 2** elaborates on the mathematical model of day-ahead operation for an urban energy system considering traffic flows. **Section 3** presents the performance of the proposed optimization model. Finally, **Section 4** presents the conclusions of the work.

2 DAY-AHEAD OPERATION OF AN URBAN ENERGY SYSTEM CONSIDERING PEAK LOAD SHAVING

This section first presents the day-ahead electricity–gas co-optimization for urban energy systems, which includes the operating constraint with regard to peak load shaving. Then, the joint optimal dispatch model considers the electricity charging load and hydrogen charging load on the traffic side. Finally, through the optimal control of ESS and energy management of EH, the peak shaving and valley filling of the urban system with

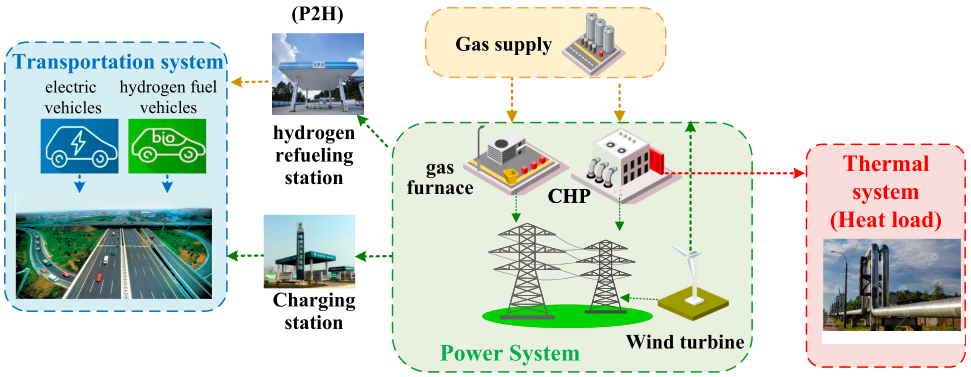

FIGURE 1 | Schematic diagram of multi-energy systems.

high penetrations of wind power are realized. The multi-energy systems are shown in **Figure 1**. There are many nodes connected to EH in the urban distribution network. EH provides hydrogen for the hydrogen charging station on the traffic side through the internal P2H device, meets the heat load demand through the CHP unit, and provides power for the charging station on the traffic side simultaneously through the converter and CHP unit.

Five key assumptions are made in our work:

1) We use a nonlinear day-ahead optimal dispatch model of an urban energy system that considers the transportation-network operation model.
2) We use fixed natural gas price information to coordinate the operation of electricity and natural gas systems. Unfixed gas pricing often leads to market inefficiencies.
3) We assume that the wind power output is deterministic, without considering the randomness of wind power output.
4) We use time-of-use price to calculate the cost of purchasing electricity in an urban energy system.

2.1 Branch Flow Model of the Urban Power Distribution Network

Since AC power flow constraints are non-convex, the day-ahead dispatch of the urban energy system is a non-convex optimization problem, which is difficult to solve. The second-order cone (SOC) relaxation based on the branch flow model is implemented to improve its computational tractability. Therefore, we use the branch flow model to replace the nonlinear power flow model of the urban distribution network (Baran and Wu, 1989):

$$\tilde{U}_{i,t} = U_{i,t}^2, \forall i \in \Omega^{node}, \forall t \in T, \tag{1}$$

$$\tilde{I}_{ij,t} = I_{ij,t}^2, \forall ij \in \Omega^{line}, \forall t \in T, \tag{2}$$

$$\begin{cases} \sum_{j \in M(i)} P_{ij,t} - \sum_{k \in N(i)} \left(P_{ki,t} - \tilde{I}_{ki,t} R_{ki,t}\right) = P_{i,t}^{inj} \\ \sum_{j \in M(i)} Q_{ij,t} - \sum_{k \in N(i)} \left(Q_{ki,t} - \tilde{I}_{ki,t} X_{ki,t}\right) = Q_{i,t}^{inj} \end{cases} \forall i \in \Omega^{node}, \forall t \in T, \tag{3}$$

$$\tilde{U}_{j,t} = \tilde{U}_{i,t} - 2\left(P_{ij,t} R_{ij,t} + Q_{ij,t} X_{ij,t}\right) + \tilde{I}_{ij,t}\left(R_{ij}^2 + X_{ij}^2\right) \forall ij \in \Omega^{node} \forall ij \in \Omega^{line}, \forall t \in T \tag{4}$$

$$\tilde{I}_{ij,t} \tilde{U}_{i,t} = P_{ij,t}^2 + Q_{ij,t}^2 \forall i \in \Omega^{node} \forall ij \in \Omega^{line}, \forall t \in T, \tag{5}$$

$$P_{i,t}^{inj} = P_{i,t}^{sub} + P_{i,t}^{DG} - P_{i,t}^{L} + P_{i,t}^{dis} - P_{i,t}^{ch} - P_{i,t}^{EH} - P_{i,t}^{GF} - P_{i,t}^{CHP} - P_{i,t}^{P2H}, \forall i \in \Omega^{node}, \forall t \in T, \tag{6}$$

$$Q_{i,t}^{inj} = Q_{i,t}^{sub} + Q_{i,t}^{DG} - Q_{i,t}^{L} \forall i \in \Omega^{node}, \forall t \in T. \tag{7}$$

Eqs 1, **2** replace the voltage and current quadratic terms in the original nonlinear power flow equation with new variables. The DistFlow model for radial electricity networks is formulated by **3**–**7**, in which variables of the squared voltage magnitude and squared branch current are employed. **Eqs 3**–**5** represent the active and reactive power flow balance. **Eqs 6**, **7** represent the injected active and reactive power of the node.

The operation of the urban AC distribution network should satisfy the following security constraints:

$$\begin{cases} P_{i\min}^{sub} \le P_{i,t}^{sub} \le P_{i\max}^{sub} \\ Q_{i\min}^{sub} \le Q_{i,t}^{sub} \le Q_{i\max}^{sub} \end{cases} \forall i \in \Omega^{sub}, \forall t \in T, \tag{8}$$

$$P_{ij,t}^2 + Q_{ij,t}^2 \le S_{ij\max}^2 \forall ij \in \Omega^{line}, \forall t \in T, \tag{9}$$

$$P_{i,t}^{DG} = P_{i\max}^{DG} \forall i \in \Omega^{DGN}, \forall t \in T, \tag{10}$$

$$Q_{i,t}^{DG} = P_{i,t}^{DG} \tan\varphi \forall i \in \Omega^{DGN}, \forall t \in T, \tag{11}$$

$$\tilde{U}_{i\min} \le \tilde{U}_{i,t} \le \tilde{U}_{i\max} \forall i \in \Omega^{node}, \forall t \in T. \tag{12}$$

Constraint (8) limits the transmission power capacity of the root node. Constraint (9) represents the feeder capacity constraint. Then, curtailment constraints with respect to distributed generation are given in **10**, **11**. Constraint (12) limits the operating range of the squared voltage magnitude.

ESS operation constraints include charge and discharge state constraints, storage capacity constraints, charge and discharge

power constraints, and daily allowable charge and discharge times constraints (Gabash and Li, 2012), which are provided as follows:

$$y_{i,t}^{ch} + y_{i,t}^{dis} \le 1, \forall i \in \Omega^{ESS}, \forall t \in T, \tag{13}$$

$$\begin{cases} 0 \le P_{i,t}^{dis} \le y_{i,t}^{dis} P_{\max}^{e} \\ 0 \le P_{i,t}^{ch} \le y_{i,t}^{ch} P_{\max}^{e} \end{cases}, \forall i \in \Omega^{ESS}, \forall t \in T, \tag{14}$$

$$\begin{cases} E_{i,t+1}^{ESS} = E_{i,t}^{ESS} + \alpha P_{i,t}^{ch} - \beta P_{i,t}^{dis} \\ 0.2E_i^{\max} \le E_{i,t}^{ESS} \le 0.9E_i^{\max} \end{cases}, \forall i \in \Omega^{ESS}, \forall t \in T, \tag{15}$$

$$\begin{cases} \sum_t \left| y_{i,t+1}^{ch} - y_{i,t}^{ch} \right| \le \lambda_{\max}^{ESS} \\ \sum_t \left| y_{i,t+1}^{dis} - y_{i,t}^{dis} \right| \le \lambda_{\max}^{ESS} \end{cases}, \forall i \in \Omega^{ESS}, \forall t \in T. \tag{16}$$

Constraint (13) denotes the charging and discharging states of ESS, and constraint (14) represents upper limit of charge and discharge. **Eqs 15**, **16** are energy constraints of ESS and daily allowable charge and discharge times constraints, respectively. Then, the quadratic equality (5) is further relaxed into the following SOC inequality (Taylor and Hover, 2012; Farivar and Low, 2013):

$$\left\| \begin{matrix} 2P_{ij,t} \\ 2Q_{ij,t} \\ \tilde{I}_{ij,t} - \tilde{U}_{i,t} \end{matrix} \right\|_2 \le \tilde{I}_{ij,t} + \tilde{U}_{i,t}, \forall i \in \Omega^{node} \forall ij \in \Omega^{line}, \forall t \in T, \tag{17}$$

where $\|.\|_2$ is the mathematical expression of the Euclid norm.

2.2 Model of the Energy Hub

The EH (Chen et al., 2019) depicted in **Figure 1A** represents the coupling between electricity and gas networks. CHP represents the key component of this EH, which generates electricity and heat simultaneously, and the urban distribution network provides the charging service for EVs through the EH. The energy conversion efficiency between the input and output energy flows of the EH is formulated in **18**

$$\begin{bmatrix} L_{i,t}^{e} \\ L_{i,t}^{h} \end{bmatrix} = \begin{bmatrix} \eta_{ee} & v\eta_{CHP,e} \\ 0 & v\eta_{CHP,h} + (1-v)\eta_{gh} \end{bmatrix} \begin{bmatrix} P_{i,t}^{EH} \\ F_{i,t}^{EH} \end{bmatrix}. \tag{18}$$

Eq. 19 represents the dispatch factor of the EH input gas flow

$$0 \le v \le 1. \tag{19}$$

Then, the EH also needs to satisfy the following operating constraints:

$$F_{EH,\min} \le F_{i,t}^{EH} \le F_{EH,\max}, \tag{20}$$

$$S_{chp,\min} \le vF_{i,t}^{EH} \le S_{chp,\max}, \tag{21}$$

$$S_{gf,\min} \le (1-v)F_{i,t}^{EH} \le S_{gf,\max}. \tag{22}$$

Constraint (20) gives the range of total gas purchases of EH. Constraints (20) and (21) represent the production capacity of CHP units and gas furnaces, respectively.

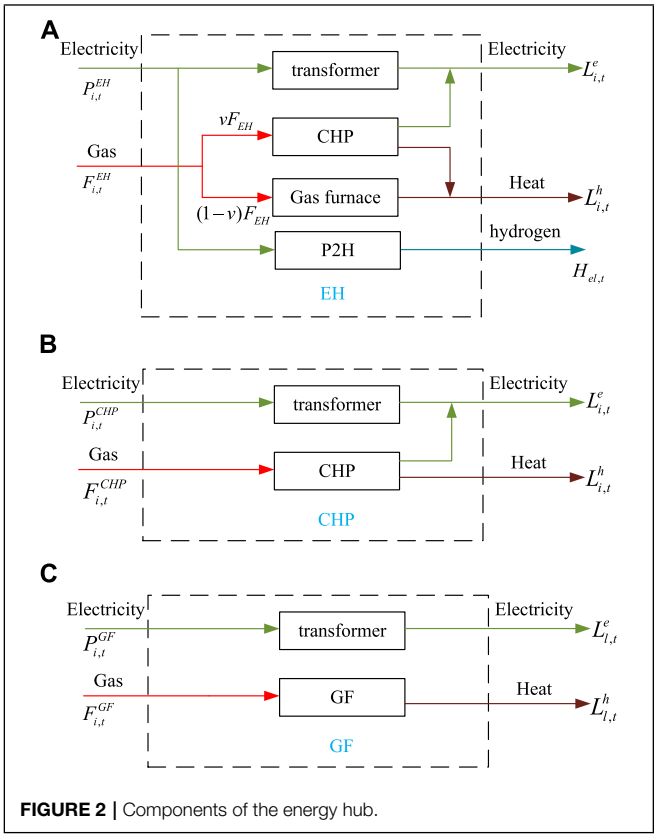

FIGURE 2 | Components of the energy hub.

For a specific case, the nodes of the distribution network are connected to some components of EH, for example, only CHP units or gas furnaces, as shown in **Figure 2**. On the other hand, the power distribution network converts electric power into hydrogen through P2H devices to provide hydrogen supply services for hydrogen-fueled vehicles on the traffic side (Korpas and Holen, 2006; Pan et al., 2021). The structure of P2H is shown in **Figure 3**.

The energy conversion efficiency between the input and output energy flows of P2H is given in **23** and **24**

$$H_{el,t} = \eta_{e2hy} P_{i,t}^{P2H} \Delta t / H_c, \tag{23}$$

$$0 \le H_{el,t} \le H_{el}^{\max}. \tag{24}$$

Constraint (23) calculates the energy conversion efficiency between the input and output energy flows of P2H. Constraint (24) limits the hydrogen production.

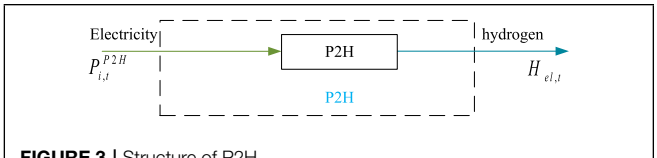

FIGURE 3 | Structure of P2H.

2.3 Transportation System Modeling

The user equilibrium (UE) model has been widely used to describe the urban transportation system in transportation research. In the case of the given traffic network and traffic demand, the UE model can output the current traffic state, namely, the traffic flow distribution on the road. The transportation system model in this article is based on the mixed-UE traffic flow model (Wei et al., 2018). We divide the overall vehicular flows into five categories: GV traffic flow, EV traffic flow, HV traffic flow, HV charging flow, and EV charging flow. The difference between traffic flow and charging flow lies in that the former represents the route choice of EVs and HVs, while the latter represents the charging choice of EVs and HVs. Traffic link has regular link, charging link, and bypass link. The charging links correspond to EV and HV queuing and charging events in EVCSs and HVCSs, and bypass links denote bypass events at EVCSs and HVCSs (Lv et al., 2021b; Teng et al., 2021).

The improved mixed-UE transportation model is a nonlinear complementary problem (NCP) consisting of four constraint sets

$$UE-NCP\begin{Bmatrix} Cons-Flow, Cons-Time \\ Cons-Cost, Cons-CP \end{Bmatrix} \tag{25}$$

where constraint sets are presented as follows:

Cons – Flow:

$$\sum_{\rho\in\lambda_g^{rs}} f_{\rho,rs,t}^{g} = \pi^{g} q_{rs,t}, \tag{26}$$

$$\sum_{\rho\in\lambda_e^{rs}} f_{\rho,rs,t}^{e} = \pi^{e} q_{rs,t}, \tag{27}$$

$$\sum_{\rho\in\lambda_h^{rs}} f_{\rho,rs,t}^{h} = \pi^{h} q_{rs,t}, \tag{28}$$

$$x_{a,t}^{g} = \sum_{rs}\sum_{\rho\in\lambda_g^{rs}} f_{\rho,rs,t}^{g}\delta_{a,\rho,rs}^{g} + \sum_{rs}\sum_{\rho\in\lambda_e^{rs}} f_{\rho,rs,t}^{e}\delta_{a,\rho,rs}^{e} + \sum_{rs}\sum_{\rho\in\lambda_h^{rs}} f_{\rho,rs,t}^{h}\delta_{a,\rho,rs}^{h}, \tag{29}$$

$$x_{a,t}^{e} = \sum_{rs}\sum_{\rho\in\lambda_e^{rs}} f_{\rho,rs,t}^{e}\delta_{a,\rho,rs}^{e}, \tag{30}$$

$$x_{a,t}^{h} = \sum_{rs}\sum_{\rho\in\lambda_h^{rs}} f_{\rho,rs,t}^{h}\delta_{a,\rho,rs}^{h}, \tag{31}$$

$$\pi^{g} + \pi^{e} + \pi^{h} = 1, \pi^{g}, \pi^{e}, \pi^{h} > 0. \tag{32}$$

Cons – Time:

$$t_{a,t}^{rg} = t_a^0\left[1 + 0.15\left(\frac{x_{a,t}^{g}}{c_a^{rg}}\right)^4\right], \tag{33}$$

$$t_{a,t}^{ch,e} = \frac{E^e}{p_{ser,e}} + t_{a,ch,e}^{\max}\left(\frac{x_{a,t}^{e}}{c_a^{ch,e}}\right)^3, x_{a,t}^{e} \le c_a^{ch,e}, \tag{34}$$

$$t_{a,t}^{ch,h} = \frac{E^h}{p_{ser,h}} + t_{a,ch,h}^{\max}\left(\frac{x_{a,t}^{h}}{c_a^{ch,h}}\right)^3, x_{a,t}^{h} \le c_a^{ch,h}. \tag{35}$$

Cons – Cost:

$$c_{\rho,rs,t}^{g} = \sum_{a}\omega t_{a,t}^{rg}\delta_{a,\rho,rs}^{g}, \tag{36}$$

$$c_{\rho,rs,t}^{e} = \sum_{a}\omega t_{a,t}^{rg}\delta_{a,\rho,rs}^{g} + \sum_{a}\left(\omega t_{a,t}^{ch,e} + \lambda_{a,t}^{e}E^{e}\right)\delta_{a,\rho,rs}^{e}, \tag{37}$$

$$c_{\rho,rs,t}^{h} = \sum_{a}\omega t_{a,t}^{rg}\delta_{a,\rho,rs}^{g} + \sum_{a}\left(\omega t_{a,t}^{ch,h} + \lambda_{a,t}^{h}E^{h}\right)\delta_{a,\rho,rs}^{h}. \tag{38}$$

Cons – Cp:

$$0 \le f_{\rho,rs,t}^{g} \perp c_{\rho,rs,t}^{g} - u_{rs,t}^{g} \ge 0, \tag{39}$$

$$0 \le f_{\rho,rs,t}^{e} \perp c_{\rho,rs,t}^{e} - u_{rs,t}^{e} \ge 0, \tag{40}$$

$$0 \le f_{\rho,rs,t}^{h} \perp c_{\rho,rs,t}^{h} - u_{rs,t}^{h} \ge 0. \tag{41}$$

Constraint set *Cons – Flow* describes flow conservation in the TN. Specifically, constraints (29)–(31) indicate that the traffic flow on each link is equal to the sum of the flows on all paths that pass through the link. Constraints (26)–(28) explain that the traffic flow on all paths connecting each O-D pair is equal to the corresponding traffic demand. Constraint set *Cons – Time* gives link travel time and estimation of different link types, respectively. For regular link $a \in T_A^{rg}$, constraint (33) uses the Bureau of Public Roads (BPR) function [Bureau of Public Roads (1, 1964)] to represent the link travel time as a function of x_a^g. In constraint (7), the first and second terms denote the charging time and queuing time, respectively. Constraint set *Cons – Cost* describes the travel costs of GVs, EVs, and HVs that choose path ρ. Note that the cost for EVs and HVs contains both travel cost and charging cost, respectively. Constraint set *Cons – Cp* represents the complementarity condition of the Wardrop UE principle (Sheffi, 1985), which indicates that no GV/EV/HV travelers could decrease their travel costs by unilaterally switching their route choices.

By changing the electricity price and hydrogen price for each period of time, we calculate the transportation network model 24 times. Then, we can get the load curve of each charging station and hydrogen charging station in a day according to **Eqs 42**, **43**. In addition, the heat load $L_{i,t}^{h}$ can be obtained from the literature (Soroudi, 2017)

$$L_{i,t}^{e} = E^{e}x_{a,t}^{e}, \tag{42}$$

$$L_{i,t}^{h} = E^{h}x_{a,t}^{h}. \tag{43}$$

2.4 The Day-Ahead Optimization Dispatch Model of an Urban Energy System

With the goal of minimizing the sum of gas purchase cost and electricity purchase cost, we established a day-ahead optimization dispatch model of an urban energy system, and the

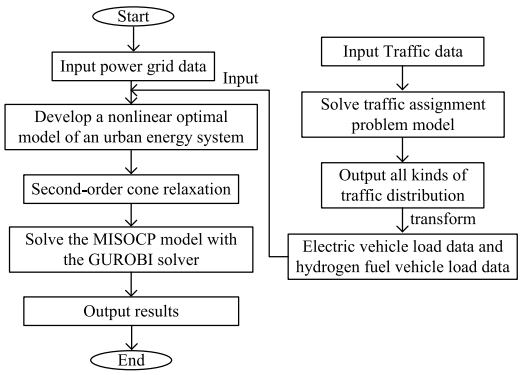

FIGURE 4 | Framework of the optimization dispatch model.

optimization model is summarized below (Lu et al., 2020; Bakeer and Hossam, 2021; Cheng et al., 2021; Lu et al., 2020; Bakeer and Hossam, 2021; Cheng et al., 2021).

The objective function is provided as

$$\min \mu_{e,t} P_{i,t}^{sub} + \mu_{g,t} \left(F_{i,t}^{EH} + F_{i,t}^{CHP} + F_{i,t}^{GF} \right). \tag{44}$$

The objective function (44) is subject to Day-ahead operation constraints: $\begin{cases} (1) - (4) \\ (6) - (17) \\ (18) - (24) \\ (42) - (43) \end{cases}$

Figure 4 shows the framework of the day-ahead optimization dispatch model of an urban energy system, which clarifies the interactions between power and transportation networks from the modeling perspective.

3 CASE STUDY

The urban energy system shown in **Figure 5** is composed of a transportation network and a 33-node urban electricity network with five EHs located at nodes 6, 16, 18, 21, and 30 and two P2H units at nodes 8 and 10. CS1–CS8 are charging stations which correspond to nodes 6, 16, 12, 27, 18, 25, 21, and 30 in the power network, respectively. HFS1–HFS7 are hydrogen charging stations which correspond to nodes 6, 16, 21, 30, 18, 10, and 8 in the power network, respectively. In addition, two 0.4-MW capacity wind farms are connected at nodes 14 and 33, while two 1.8-MW capacity ESSs are connected at nodes 11 and 29, respectively. The computational tests were conducted on a laptop with Intel Core 1.0 GHz CPU and 16 GB memory, and the MISOCP model was programmed in GAMS and solved with the GUROBI solver.

3.1 Electric Vehicle Charging Load and Hydrogen Load

Figure 6 shows the daily heat load, the charging load of EVs, and the hydrogen load of HVs on the traffic side. As can be observed from this figure, the charging load curve of EVs has the same trend with the hydrogen load curve of HVs, and both have the characteristic of double peaks. During the morning rush hour from 8:00 to 10:00 and the evening rush hour from 17:00 to 19:00, the electric load and hydrogen load on the traffic side are relatively high, while the heat load is higher during the day and lower at night (Ye et al., 2021). The trend of these three loads is consistent with that of the total load.

3.2 The Anti-Peak-Shaving Characteristic of Wind Power Production

Figure 7 shows the comparison of the wind power output curve, total original load curve, and total net load curve without considering energy storage. In this figure, load 0 represents the total original load curve, and load 1 represents the total net load curve without considering the energy storage. As can be observed from the figure, wind turbines produce more output at night, which results in a lower net load at the valley time. However, the output of wind turbines is less in the daytime, and hence, it cannot significantly reduce the peak load. Consequently, the daily wind power production results in a larger peak-to-valley difference of net load.

3.3 Coordination Between ESS and Wind Power Production

It is noteworthy that when the ESS participates in the power regulation of the power grid, the disadvantages brought by the anti-peak-shaving of wind power can be well compensated. As shown in **Figure 8**, load 3 represents the total net load considering energy storage and multi-energy regulation, and load 2 represents the total net load without considering multi-energy regulation. ESS charges at night when the power load is low and the wind power output is large and discharges during the day when the load is relatively high and the wind power output is small. As a result, peak cutting and valley filling of the power load are achieved.

3.4 Complementary Operation of Multi-Energy Coupling

Natural gas is simultaneously converted into heat and electricity through CHP units and only into heat through the gas furnace. **Figure 9** shows the total purchase of natural gas at each time period, from which we can observe that the amount of gas purchase of gas is larger at the time period when the power load is high than that at the time period when the power load is low. As shown in **Figure 8**, the difference between curve load 2 and load 3 is mainly due to the multi-energy complement. In addition, the EV load is relatively high at time periods from 7:00 to 17:00. To summarize, increasing the power supply of CHP units can effectively reduce the peak load, but this impact on valley filling is not obvious.

3.5 Impact of ESS Strategies on Urban Energy System Operation

As discussed above, ESS can play an important role in power systems. Reasonable ESS scheduling decisions can alleviate the impact of wind power on the distribution network and promote

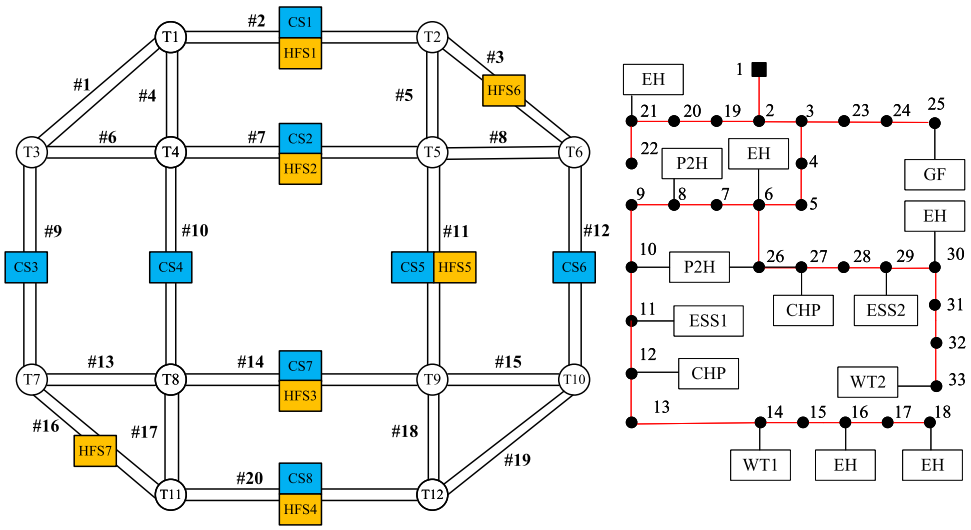

Coupling relationship between traffic side and power grid side

The traffic side	CS1/HFS1	CS2/HFS2	CS3	CS4	CS5/HFS5	CS6	CS7/HFS3	CS8/HFS4	HFS6	HFS7
The grid side	Node6	Node16	Node12	Node27	Node18	Node25	Node21	Node30	Node10	Node8

FIGURE 5 | Topology of the urban energy system.

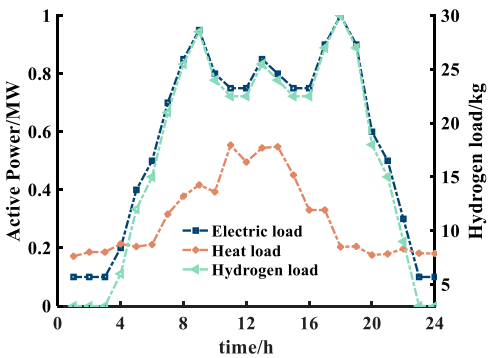

FIGURE 6 | Hourly multi-energy load.

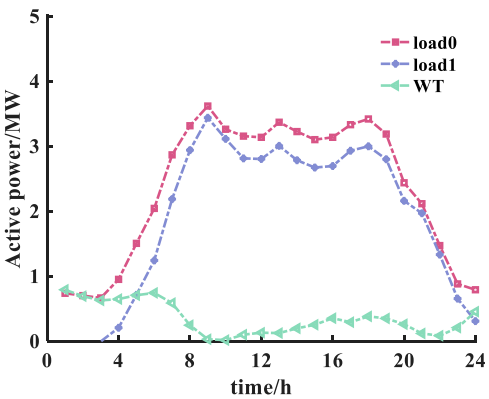

FIGURE 7 | Anti-peak-shaving characteristic of wind power production.

peak shaving and valley filling. **Figure 10** and **Figure 11** show the charge–discharge curve of ESS and the SOC state of charge of ESS, respectively. We can note that for time periods from 0:00 to 7:00, the net load is relatively with low power consumption and high wind power production, and ESS charges to satisfy the load electricity demand. The SOC state of charge rises in preparation for the next stage of the discharge process. For time periods from 8:00 to 11:00, the electricity price is high and the net load is relatively high. ESS reduces the load peak by discharging. From 16:00 to 19:00, the load reaches the peak again, and ESS continues to discharge, which reduces the power purchase cost from the main grid. At the same time, in order to ensure the normal operation of the next charge and discharge cycle, the ESS charges and returns to the original state of charge at time periods from 20:00 to 24:00.

We introduce an index δP_a to measure the average peak-valley difference:

$$\delta P_a = \sum_{t_{peak}} P_{i,t_{peak}} / N_{peak} - \sum_{t_{valley}} P_{i,t_{valley}} / N_{valley}. \quad (45)$$

Table 1 lists mean peak-valley differences and the total operation costs under different ESS capacities. As shown in this table, the increase in ESS capacity positively reduces the average peak-valley difference of power demands and reduces the total operating costs. This is because a higher energy storage capacity can provide more sufficient charging power in load valley and discharging power in load peak, which also reduces the purchase of power at the peak time, thus reducing the operating cost.

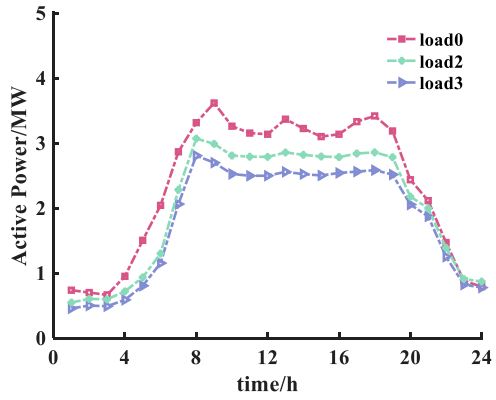

FIGURE 8 | Hourly load curves under three scenarios.

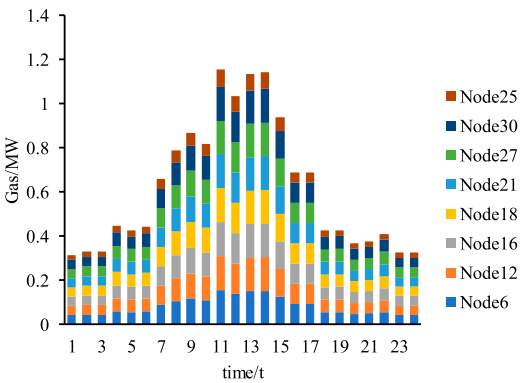

FIGURE 9 | Hourly total purchase of natural gas.

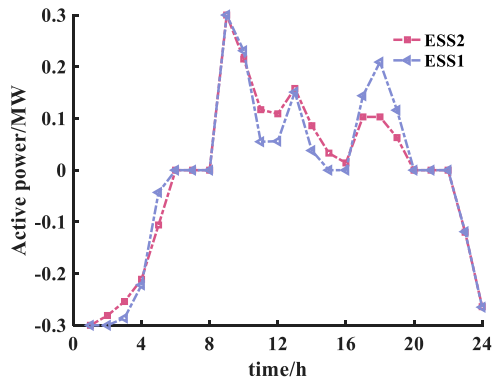

FIGURE 10 | Hourly charge–discharge curve of ESS.

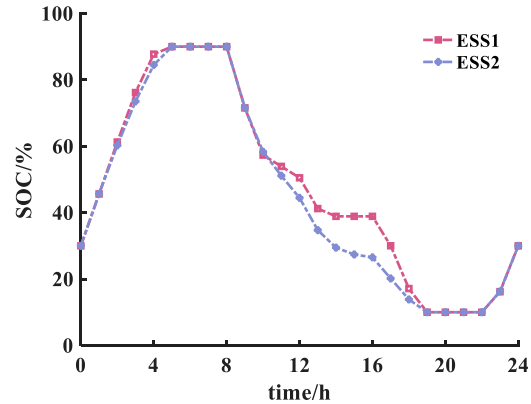

FIGURE 11 | Hourly SOC state of charge of ESS.

TABLE 2 | Cost comparison under different constraint values of average peak-valley difference.

λ/MW	1.37	1.27	1.15	1.10	1.05
Cost/$	25145.35	25282.07	25731.15	25952.80	26179.76

3.6 Cost Comparison Under Different Values of Average Peak-Valley Difference

To control the load peak-valley difference to an ideal level, we add an additional linear constraint (46) into the original model. Meanwhile, we set the energy storage capacity to be fixed at the original value

$$\delta P_a \leq \lambda. \tag{46}$$

λ denotes the load peak-valley difference which we want to get. By modifying the value of λ, we can obtain the corresponding operating costs under different requirements of average peak-valley difference, and the results are summarized in **Table 2**.

Generally, a more ideal peak-valley difference increases the total operating cost, which indicates that the operating cost and the requirement of peak shaving and valley filling are contradictory. The reason is that if we set the value of λ to be small, we need to increase the net load during the valley time. Therefore, part of the wind power will be curtailed during the load valley, and additional electricity needs to be purchased from the main grid, which reduces the peak-to-valley difference and inevitably increase the total operating cost.

TABLE 1 | Average peak-valley difference under different ESS capacities.

Capacity of ESS/MW	1.8	2.2	2.6	2.8	3.2
Mean peak-valley difference/MW	1.37	1.27	1.16	1.11	1.00
Cost/$	25145.35	25029.00	24919.91	24868.68	24778.03

4 CONCLUSION

We have presented a day-ahead co-optimization approach of unban energy systems considering traffic flows and peak shaving. Based on the numerical results obtained, we can draw the following conclusions:

- Optimal charging and discharging dispatch strategies of energy storages can alleviate the peak-valley difference caused by the anti-peak-shaving characteristic of wind power production.
- In addition, multi-energy complement can significantly reduce the peak-valley difference and contribute to the improved energy utilization efficiency. However, increasing the supply of natural gas can reduce the peak load, but the effect on valley filling is not obvious.
- When the ESS capacity is fixed, the higher the peak shaving and valley filling requirements, the greater the operating cost.

Our work, hence, might help the operators of urban energy systems to produce operating decisions of multi-energy production sources and satisfy the requirement from multi-energy demands. Our work might also help the design of a future low-carbon energy system. Meanwhile, in future research, we will consider the optimal dispatch model of the transportation system into the day-ahead dispatch model of the urban energy system to further improve social benefits. Reasonable traffic management strategies can give full play to the initiative of the urban distribution network to achieve peak shaving and valley filling and economic optimization.

DATA AVAILABILITY STATEMENT

The original contributions presented in the study are included in the article/Supplementary Materials, further inquiries can be directed to the corresponding author.

AUTHOR CONTRIBUTIONS

YP: methodology, software, validation, formal analysis, writing—original draft, and visualization. JM: methodology, investigation, and writing—review editing. CL conceptualization, methodology, and writing—review editing. SC conceptualization, resources, and supervision. LP methodology, validation, and writing—review editing.

FUNDING

This work was supported by State Grid Zhejiang Electric Power Company Project "Steady-state models and parameter identification technology of energy storage stations".

REFERENCES

Bakeer, A., and Hossam, S. (2021). Salama and Istvan Vokony. Integration of PV System with SMES Based on Model Predictive Control for Utility Grid Reliability Improvement. *Prot. Control. Mod. Power Syst.* 6 (2), 191–203. doi:10.1186/s41601-021-00191-1

Baran, M. E., and Wu, F. F. (1989). Network Reconfiguration in Distribution Systems for Loss Reduction and Load Balancing. *IEEE Trans. Power Deliv.* 4 (2), 1401–1407. doi:10.1109/61.25627

Bureau of Public Roads (1964). *Traffic Assignment Manual*. Washington, D.C.: U.S. Department of Commerce.

Chen, S., Wei, Z., Sun, G., Cheung, K. W., Wang, D., and Zang, H. (2019). Adaptive Robust Day-Ahead Dispatch for Urban Energy Systems. *IEEE Trans. Ind. Electron.* 66 (2), 1379–1390. doi:10.1109/tie.2017.2787605

Chen, Y., Gribik, P., and Gardner, J. (2014). Incorporating Post Zonal Reserve Deployment Transmission Constraints into Energy and Ancillary Service Co-optimization. *IEEE Trans. Power Syst.* 29 (2), 537–549. doi:10.1109/tpwrs.2013.2284791

Cheng, Yan., Tang, Yi., and Dai, Jianfeng. (2021). Uncertainty Modeling of Wind Power Frequency Regulation Potential Considering Distributed Characteristics of Forecast Errors. *Prot. Control. Mod. Power Syst.* 6 (3), 276–288.

Correa-Posada, C. M., and Sánchez-Martín, P. (2015). Integrated Power and Natural Gas Model for Energy Adequacy in Short-Term Operation. *IEEE Trans. Power Syst.* 30 (6), 3347–3355. doi:10.1109/tpwrs.2014.2372013

Farivar, M., and Low, S. H. (2013). Branch Flow Model: Relaxations and Convexification-Part I. *IEEE Trans. Power Syst.* 28 (3), 2554–2564. doi:10.1109/tpwrs.2013.2255317

Gabash, A., and Li, P. (2012). Active-Reactive Optimal Power Flow in Distribution Networks with Embedded Generation and Battery Storage. *IEEE Trans. Power Syst.* 27 (4), 2026–2035. doi:10.1109/tpwrs.2012.2187315

Gao, H., and Li, Z. (2021). A Benders Decomposition Based Algorithm for Steady-State Dispatch Problem in an Integrated Electricity-Gas System. *IEEE Trans. Power Syst.* 36 (4), 3817–3820. doi:10.1109/tpwrs.2021.3067203

Gao, H., and Li, Z. (2020). "Effect of Power to Gas on Integrated Electricity-Gas System with Uncertain Wind Generation," in IEEE 3rd Student Conference on Electrical Machines and Systems. SCEMS, 164–168. doi:10.1109/scems48876.2020.9352402

Hu, X., Moura, S. J., Murgovski, N., Egardt, B., and Cao, D. (2016). Integrated Optimization of Battery Sizing, Charging, and Power Management in Plug-In Hybrid Electric Vehicles. *IEEE Trans. Contr. Syst. Technol.* 24 (3), 1036–1043. doi:10.1109/tcst.2015.2476799

IEA, Global EV Outlook (2020). *Entering the Decade of Electric Drive?* International Energy Agency.

Jin, X., Mu, Y., Jia, H., Wu, J., Xu, X., and Yu, X. (2016). Optimal Day-Ahead Scheduling of Integrated Urban Energy Systems. *Appl. Energ.* 180, 1–13. doi:10.1016/j.apenergy.2016.07.071

Korpas, M., and Holen, A. T. (2006). Operation Planning of Hydrogen Storage Connected to Wind Power Operating in a Power Market. *IEEE Trans. Energ. Convers.* 21 (3), 742–749. doi:10.1109/tec.2006.878245

Li, Y., Zou, Y., Tan, Y., Cao, Y., Liu, X., Shahidehpour, M., et al. (2018). Optimal Stochastic Operation of Integrated Low-Carbon Electric Power, Natural Gas, and Heat Delivery System. *IEEE Trans. Sustain. Energ.* 9 (1), 273–283. doi:10.1109/tste.2017.2728098

Lu, S., Gu, W., Meng, K., Yao, S., Liu, B., and Dong, Z. Y. (2020). Thermal Inertial Aggregation Model for Integrated Energy Systems. *IEEE Trans. Power Syst.* 35 (3), 2374–2387. doi:10.1109/tpwrs.2019.2951719

Lv, S., Chen, S., Wei, Z., and Zhang, H. (2021). Power Transportation Coordination: toward a Hybrid Economic-Emission Dispatch Model. *IEEE Trans. Power Syst.* doi:10.1109/tpwrs.2021.3131306

Lv, S., Wei, Z., Chen, S., Sun, G., and Wang, D. (2021). Integrated Demand Response for Congestion Alleviation in Coupled Power and Transportation

Networks. *Appl. Energ.* 283, 116206. doi:10.1016/j.apenergy.2020.116206

Mancarella, P. (2014). MES (Multi-energy Systems): An Overview of Concepts and Evaluation Models. *Energy* 65, 1–17. doi:10.1016/j.energy.2013.10.041

Martínez-Mares, A., Fuerte-Esquivel, C. R., and de Ingeniería, I. (2011). *Integrated Energy Flow Analysis in Natural Gas and Electricity Coupled Systems*. North American Power Symposium, 1–7.

Meng, W., and Wang, X. (2017). Distributed Energy Management in Smart Grid with Wind Power and Temporally Coupled Constraints. *IEEE Trans. Ind. Electron.* 64 (8), 6052–6062. doi:10.1109/tie.2017.2682001

Neyestani, N., Yazdani-Damavandi, M., Shafie-khah, M., Chicco, G., and Catalao, J. P. S. (2015). Stochastic Modeling of Multienergy Carriers Dependencies in Smart Local Networks with Distributed Energy Resources. *IEEE Trans. Smart Grid* 6 (4), 1748–1762. doi:10.1109/tsg.2015.2423552

Pan, G., Hu, Q., Gu, W., Ding, S., Qiu, H., and Lu, Y. (2021). Assessment of Plum Rain's Impact on Power System Emissions in Yangtze-Huaihe River basin of China. *Nat. Commun.* 12, 6156. doi:10.1038/s41467-021-26358-w

Rotering, N., and Ilic, M. (2011). Optimal Charge Control of Plug-In Hybrid Electric Vehicles in Deregulated Electricity Markets. *IEEE Trans. Power Syst.* 26 (3), 1021–1029. doi:10.1109/tpwrs.2010.2086083

Saber, A. Y., and Venayagamoorthy, G. K. (2011). Plug-in Vehicles and Renewable Energy Sources for Cost and Emission Reductions. *IEEE Trans. Ind. Electron.* 58 (4), 1229–1238. doi:10.1109/tie.2010.2047828

Shabanpour-Haghighi, A., and Seifi, A. R. (2015). Energy Flow Optimization in Multicarrier Systems. *IEEE Trans. Ind. Inf.* 11 (5), 1067–1077. doi:10.1109/tii.2015.2462316

Sheffi, Y. (1985). *Urban Transportation Networks: Equilibrium Analysis with Mathematical Programming Methods*. Englewood Cliffs, NJ, USA: Prentice-Hall.

Soroudi, A. (2017). *Power System Optimization Modeling in GAMS*.

Strasser, T., Andren, F., Kathan, J., Cecati, C., Buccella, C., Siano, P., et al. (2015). A Review of Architectures and Concepts for Intelligence in Future Electric Energy Systems. *IEEE Trans. Ind. Electron.* 62 (4), 2424–2438. doi:10.1109/tie.2014.2361486

Taylor, J. A., and Hover, F. S. (2012). Convex Models of Distribution System Reconfiguration. *IEEE Trans. Power Syst.* 27 (3), 1407–1413. doi:10.1109/tpwrs.2012.2184307

Teng, W., Wang, Y., and Sun, S. (2021). Robust Stability Control for Electric Vehicles Connected to DC Distribution Systems. *Front. Energ. Res.* 9. doi:10.3389/fenrg.2021.740698

Uddin, M., Romlie, M. F., Abdullah, M. F., Abd Halim, S., Abu Bakar, A. H., and Chia Kwang, T. (2018). A Review on Peak Load Shaving Strategies. *Renew. Sustain. Energ. Rev.* 82, 3323–3332. doi:10.1016/j.rser.2017.10.056

Wei, W., Wu, L., Wang, J., and Mei, S. (2018). Network Equilibrium of Coupled Transportation and Power Distribution Systems. *IEEE Trans. Smart Grid* 9 (6), 6764–6779. doi:10.1109/tsg.2017.2723016

Xu, D., Wu, Q., Zhou, B., Li, C., Bai, L., and Huang, S. (2020). Distributed Multi-Energy Operation of Coupled Electricity, Heating, and Natural Gas Networks. *IEEE Trans. Sustain. Energ.* 11 (4), 2457–2469. doi:10.1109/tste.2019.2961432

Yang, Q., and Fang, X. (2017). Demand Response under Real-time Pricing for Domestic Households with Renewable DGs and Storage. *IET Generation, Transm. Distribution* 11 (8), 1910–1918. doi:10.1049/iet-gtd.2016.1066

Ye, J., Zhao, D., and Zhang, L. (2021). Research on Combined Electricity and Heating System Scheduling Method Considering Multi-Source Ring Heating Network. *Front. Energ. Res.* 9. doi:10.3389/fenrg.2021.800906

Zhao, G. Y., Liu, Z. Y., He, Y., Cao, H. J., and Guo, Y. B. (2017). Energy Consumption in Machining: Classification, Prediction, and Reduction Strategy. *Energy* 133, 142–157. doi:10.1016/j.energy.2017.05.110

Zhao, J., Ma, Y., Liu, Q., Wen, L., Jia, C., and Fang, Y. (2020). A Multi-Source Coordinated Optimal Operation Model Considering the Risk of Nuclear Power Peak Shaving and Wind Power Consumption. *IEEE Access* 8, 189702–189719. doi:10.1109/access.2020.3027705

Conflict of Interest: The authors declare that the research was conducted in the absence of any commercial or financial relationships that could be construed as a potential conflict of interest.

Publisher's Note: All claims expressed in this article are solely those of the authors and do not necessarily represent those of their affiliated organizations or those of the publisher, the editors, and the reviewers. Any product that may be evaluated in this article or claim that may be made by its manufacturer is not guaranteed or endorsed by the publisher.

GLOSSARY

Indices and sets

i, j Subscript indices of nodes in electricity networks

t Subscript indices of time periods

min Superscript index of minimum value

max Superscript index of maximum value

Ω^{node} Set of electrical nodes

Ω^{line} Set of branches

Ω^{sub} Set of root nodes

Ω^{ESS} Set of (energy storage system) ESS nodes

Ω^{DGN} Set of DG nodes

T Operational cycle.

T_A^{rg} Set of regular links in a transportation network.

T_A^{ch} Set of charging links in the transportation network

T_{RS} Set of origin–destination (O-D) pairs

T_R Set of origin nodes

T_S Set of destination nodes.

$\lambda_g^{rs}, \lambda_e^{rs}, \lambda_h^{rs}$ Set of gasoline vehicles/electric vehicles/hydrogen fuel vehicles (GV/EV/HV) paths connecting an O-D pair r-s, where $r \in T_R s \in T_S$ and $rs \in T_{RS}$

Variables

$U_{i,t}$ Voltage of electrical nodes

$I_{ij,t}$ Current magnitude through branch ij

$P_{ij,t}, Q_{ij,t}$ Active and reactive power flow through branch ij

$P_{i,t}^{inj}, Q_{i,t}^{inj}$ The injected active and reactive power of node i

$P_{i,t}^{sub}, Q_{i,t}^{sub}$ Output active and reactive power of the root node

$P_{i,t}^{DG}, Q_{i,t}^{DG}$ Output active and reactive power of the distributed generation

$P_{i,t}^{L}, Q_{i,t}^{L}$ Active and reactive power load

$P_{i,t}^{ch}, P_{i,t}^{dis}$ Active power charge and discharge of ESS

$P_{i,t}^{EH}$ Input power flow of the energy hub (EH)

$P_{i,t}^{GF}$ Input power flow of the gas furnace (GF)

$P_{i,t}^{CHP}$ Input power flow of combined heat and power (CHP)

$P_{i,t}^{P2H}$ Input power flow of power to hydrogen (P2H)

$y_{i,t}^{ch}, y_{i,t}^{dis}$ Binary variable

$E_{i,t}^{ESS}$ Energy level of the ESS

$L_{i,t}^{e}, L_{i,t}^{h}$ Dispatched electricity and heat demand

$F_{i,t}^{EH}$ Input gas flow of the energy hub

v Percentage of gas fed into combined heat and power

$H_{el,t}$ Hydrogen production

$f_{\rho,rs,t}^{g}$ GV flow on path $\rho \in \lambda_g^{rs}$ between O-D pair r-s

$f_{\rho,rs,t}^{e}$ EV flow on path $\rho \in \lambda_e^{rs}$ between O-D pair r-s

$\mathbf{f}_{\rho,rs,t}^{h}$ HV flow on path $\rho \in \lambda_h^{rs}$ between O-D pair r-s

$x_{a,t}^{e}$ Aggregated traffic flow on link $a \in T_A^{ch}$

$x_{a,t}^{g}$ Aggregated traffic flow on link $a \in T_A^{rg}$

$x_{a,t}^{h}$ Aggregated traffic flow on link $a \in T_A^{ch}$

$t_{a,t}^{rg}$ Travel time on link $a \in T_A^{rg}$

$t_{a,t}^{ch,e}$ Average time that EVs spend on link $a \in T_A^{ch}$

$t_{a,t}^{ch,h}$ Average time that HVs spend on link $a \in T_A^{ch}$

$c_{\rho,rs,t}^{g}$ GV travel cost on path $\rho \in \lambda_g^{rs}$ between O-D pair r-s

$c_{\rho,rs,t}^{e}$ EV travel cost on path $\rho \in \lambda_e^{rs}$ between O-D pair r-s

$c_{\rho,rs,t}^{h}$ HV travel cost on path $\rho \in \lambda_h^{rs}$ between O-D pair r-s

$u_{rs,t}^{g}$ Minimal travel cost of GVs between O-D pair r-s

$u_{rs,t}^{e}$ Minimal travel cost of EVs between O-D pair r-s

$u_{rs,t}^{h}$ Minimal travel cost of HVs between O-D pair r-s

$P_{i,t_{peak}}, P_{i,t_{valley}}$ Peak and valley net load

Parameters

$R_{ij,t}$ The resistance of branch ij

$X_{ij,t}$ The reactance of branch ij

$\tan \varphi$ Power factor of DG output

P_{max}^{e} Upper limits of ESS charge and discharge power

α, β Charge and discharge efficiency coefficient of ESS

$\mathbf{E}_{\mathbf{i}}^{\mathbf{max}}$ Maximum storage capacity of ESS

$\boldsymbol{\lambda}_{\mathbf{max}}^{\mathbf{ESS}}$ Maximum charging and discharging times of ESS

η_{ee} Transformer efficiency of the energy hub

$\eta_{CHP,e}$ Electrical efficiency of combined heat and power

$\eta_{CHP,h}$ Thermal efficiency of combined heat and power

η_{gh} Gas furnace efficiency

η_{e2hy} Electrical efficiency of P2H

H_c The higher heating value of hydrogen

π^g, π^e, π^h Ratio of GV/EV/HV traffic demand

$\delta_{a,\rho,rs}^{g}$ If path $\rho \in \lambda_g^{rs}$ passes link $a \in T_A^{rg}$, $\delta_{a,\rho,rs}^{g} = 1$; otherwise, $\delta_{a,\rho,rs}^{g} = 0$.

$\delta_{a,\rho,rs}^{e}$ If path $\rho \in \lambda_e^{rs}$ passes link $a \in T_A^{ch}$, $\delta_{a,\rho,rs}^{e} = 1$; otherwise, $\delta_{a,\rho,rs}^{e} = 0$.

$\delta_{\mathbf{a,\rho,rs}}^{\mathbf{h}}$ If path $\rho \in \lambda_h^{rs}$ passes link $a \in T_A^{ch}$, $\delta_{a,\rho,rs}^{h} = 1$; otherwise, $\delta_{a,\rho,rs}^{h} = 0$.

$\mathbf{t}_{\mathbf{a}}^{\mathbf{0}}$ Free flow travel time on link $a \in T_A^{rg}$

$\mathbf{c}_{\mathbf{a}}^{\mathbf{rg}}$ Traffic flow capacity of link $a \in T_A^{rg}$

$\mathbf{c}_{\mathbf{a}}^{\mathbf{ch,e}}, \mathbf{c}_{\mathbf{a}}^{\mathbf{ch,h}}$ Maximum allowable vehicular flow of charging link $a \in T_A^{ch}$

$p_{ser,e}, p_{ser,h}$ Average service rate at charging stations

E^e, E^h Charging demand of unit traffic flow.

$\mathbf{t}_{\mathbf{a,ch,e}}^{\mathbf{max}}, \mathbf{t}_{\mathbf{a,ch,h}}^{\mathbf{max}}$ Maximum waiting time at charging stations

$q_{rs,t}$ Trip rate (traffic demand) between O-D pair r-s

ω Monetary cost of travel time.

$\boldsymbol{\lambda}_{a,t}^{e}, \boldsymbol{\lambda}_{a,t}^{h}$ Charging price at charging stations

$\mu_{e,t}$ Time of use price

$\mu_{g,t}$ Unit price of natural gas

N_{peak}, N_{valley} Number of peak and valley periods

frontiers | Frontiers in Energy Research

ORIGINAL RESEARCH
published: 10 May 2022
doi: 10.3389/fenrg.2022.877700

Multi-Objective Optimization of Multi-Energy Flow Coupling System With Carbon Emission Target Oriented

Xuanjun Zong[1]*, *Yue Yuan*[1] and *Han Wu*[2]

[1]College of Energy and Electrical Engineering, Hohai University, Nanjing, China, [2]School of Electric Power Engineering, Nanjing Institute of Technology, Nanjing, China

In this paper, aiming to achieve the target of carbon emission orientation, a multi-objective optimization model of the multi-energy flow coupling system is proposed, in which all the environmental protection, system economy, and energy efficiency are comprehensively considered as the addressed objectives. To solve the developed model, by combining the analytic hierarchy process (AHP) and the improved entropy weight method, a so-called AHP-improved entropy weight method is proposed and utilized for weighting the considered objectives, and the model is transformed into a single objective optimization problem, namely, the collaborative optimization model. Then, to expedite the process, a simplified primal dual interior point method is proposed to solve the model. Finally, the results of a case study indicate that the proposed multi-objective collaborative optimization can obtain the optimal solution of the system. In addition, the convergence and global optimization ability of the simplified primal dual interior point method show better characteristics when solving the proposed model.

Keywords: multi-energy flow coupling system, multi-objective collaborative optimization, combined weighting method, simplified primal-dual interior point algorithm, carbon emission

OPEN ACCESS

Edited by:
Qingxin Shi,
North China Electric Power University, China

Reviewed by:
Linquan Bai,
University of North Carolina at Charlotte, United States
Nikolaos Koltsaklis,
Czech Technical University in Prague, Czechia
Zhenkun Li,
Shanghai University of Electric Power, China

***Correspondence:**
Xuanjun Zong
zongxuanjun@163.com

Specialty section:
This article was submitted to Smart Grids, a section of the journal Frontiers in Energy Research

Received: *17 February 2022*
Accepted: *28 March 2022*
Published: *10 May 2022*

Citation:
Zong X, Yuan Y and Wu H (2022) Multi-Objective Optimization of Multi-Energy Flow Coupling System With Carbon Emission Target Oriented. Front. Energy Res. 10:877700. doi: 10.3389/fenrg.2022.877700

1 INTRODUCTION

Energy is the basis and important guarantee for human survival. There are many problems in traditional energy systems, such as independent energy supply, low cascade utilization level, energy waste, and environmental pollution (Zhou et al., 2013; Fan et al., 2021; Hu et al., 2022). The multi-energy flow coupling system (MEFCS) is an energy system form that integrates public cold, heat, electricity, and gas. Its purpose is to integrate multiple energy sources, such as electric energy, natural gas, and thermal energy in a certain area, so as to realize collaborative optimal operation, collaborative management, and complementary mutual assistance among various forms of energy subsystems (Zhao et al., 2018; Klyapovskiy et al., 2019). In addition, under the background of "double carbon", the transformation of clean and low-carbon energy is an inevitable trend of global energy development.

Traditional energy systems are planned and operated independently, and only a single situation needs to be considered in their optimal scheduling. However, for a multi-energy flow coupling system, the correlation among energy subsystems should be considered in planning and operation (Sirvent et al., 2017). In Liu et al. (2019), considering the multi-timescale characteristics, an electrical and thermal energy sharing model of interconnected microgrids with combined heating and power (CHP) and photovoltaic systems was built, in which CHP could operate in a hybrid mode by selecting the operating point flexibly. In Wang et al. (2019), a

multi-objective bi-level optimization model considering the total cost and carbon dioxide emission was built, while the energy efficiency of multi-energy flow coupling system was ignored. In Barati et al. (2015) and Clegg and Mancarella (2016), under the condition of meeting the basic needs of power, gas, and heat loads, the coordinated planning of multi-energy flow coupling system was considered, in order to reduce the construction cost of transmission lines, gas pipelines, and power plants as much as possible. In Koltsaklis and Knápek (2021), the authors presented an optimization framework for the optimal scheduling of a multi-energy microgrid, where a number of aggregated end-users were considered. In Nicolosi et al. (2021), a novel mixed integer linear programming optimization algorithm has been developed to compute the optimal management of a micro-energy grid, where the total cost, the NOx, and the CO_2 emissions of the system were taken into consideration. To meet the safety constraints, in Wang D. et al. (2018), an optimal coordination control strategy (OCCS) for a hybrid energy storage system was developed considering the state-space equation to describe the OCCS, the constraints of the OCCS, and the objective function to express the optimal coordination control performance. In Sun et al. (2020), the authors considered the day ahead optimal scheduling problem of electricity gas interconnected systems, where the two-way energy flow was taken as a non-convex nonlinear mixed integer linear programming problem, and a second-order cone programming (SOCP) method has been proposed. In Luo et al. (2018) and Zhang et al. (2021), the uncertainty caused by renewable energy and multi-energy load was considered, and the robust optimization and stochastic optimization methods were adopted to deal with it respectively, so as to ensure that the system can still maintain stable operation under the worst conditions. In Ghosh and Kamalasadan (2017), a grid-connected two mass DFIG and a grid-supportive single mass squirrel cage induction generator-based flywheel energy storage system model have been considered for controller design and proof-of-concept exploration. In Wang L. et al. (2021), the flexible resources (FRs) on both the energy supply and load sides were introduced into the optimal dispatch of the integrated electricity-heat energy system (IEHES) and further modeled to alleviate the renewable fluctuations, and the solution for FRs participating in IEHES dispatch was given, with goals of maximizing the renewable penetration ratio and lowering operation costs. It can be seen that most of the existing results consider optimization of the economic objectives of the multi-energy flow coupling system, where the index is relatively single, and less consideration is paid on the carbon emission level in the operation of the system. At the same time, the operation strategy is the lack of comprehensive comparison and verification.

In solving the MEFCS collaborative optimization model, when considering multiple optimization objectives including carbon emission, investment and operation cost, and energy utilization, the traditional single objective optimization algorithm may be difficult to ensure that the solution result is the optimal solution of the original problem. In Wang W. et al. (2021), the load characteristics and various constraints of the integrated community energy system were considered, and the operating model with the goal of minimizing operating costs was optimized. In Ma et al. (2018), the energy consumption cost and environmental cost of the multi-energy flow coupling system were considered comprehensively, the optimal scheduling model of multi-energy flow coupling system was proposed, and the optimal scheduling model was transformed into a mixed integer linear programming problem. In Xiao et al. (2018), the method of the probability scenario had been used to model the uncertainties of the distributed renewable energies (DREs) and loads, which could better characterize the impact of uncertainty on the planning and design of the MEFCS. In Yang et al. (2018), a two-stage robust generation scheduling model was proposed for the dynamic safety constraints of the natural gas pipeline network and the uncertainty of wind power, and a new solution method was developed to avoid the nonlinearity of gas flow constraints. In Wu et al. (2021), the multi-objective optimization model was transformed into a single objective optimization model through the multi-objective programming hierarchical solution method, and the primal dual interior point method was used to solve the model. Based on the fast particle swarm optimization algorithm, in Qu et al. (2021), a dual-decomposition-based distributed algorithm was designed to address the problem that the data and information of the EHs during the operation were confidential and should be kept by each owner, where the optimal consensus problem was used for the dual problem to update the multipliers, in Li et al. (2020), the proposed MEFCS planning model, formulated as a two-stage MILP problem, was solved by the Benders decomposition (BD) method to determine the optimal capacity of each component in MEFCS planning.

To be pointed out that, the research on the optimization of multi-energy flow coupling system at home and abroad mainly focuses on the simplification of the optimization model. However, on the one hand, it will lead to the reduction of solution accuracy, at the same time, because the models are more and more complex, which are difficult to be simplified. Therefore, the heuristic algorithm has become an important way to deal with optimization problems. However, the traditional heuristic algorithm has the problems of poor convergence and easy to fall into local optimization, and how to find a simplified and better algorithm is another motivation of this paper. Based on the above discussions, in this paper, the environmental protection goal is taken as the leading factor, the economic and energy efficiency goals are comprehensively considered, the multi-objective collaborative optimization model is developed for the multi-energy flow coupling system, which can be transformed into a single objective optimization model through the linear combination of the analytic hierarchy process and the improved entropy weight method, and then the model can be solved by using the simplified primal dual interior point method. The results avoid falling into local optimization and accelerate convergence. Case studies verify the effectiveness of the proposed algorithm.

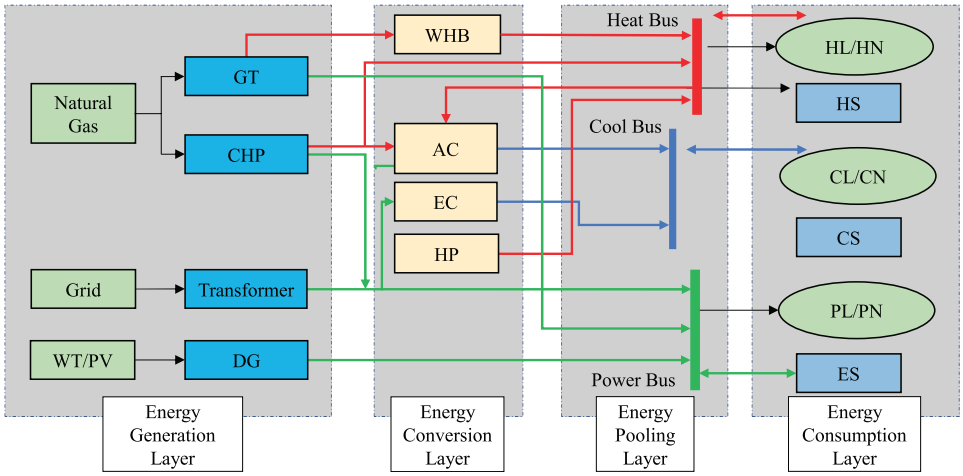

FIGURE 1 | Typical structure of the multi-energy flow coupling system.

2 MODELING OF MULTI-ENERGY FLOW COUPLING SYSTEM

A typical multi-energy flow coupling system structure is shown in **Figure 1**, which is internally connected through the power grid, thermal pipe network, and cooling transmission network. The equipment involved distribution power source includes a wind turbine (WT) and photovoltaic (PV). Cogeneration includes CHP, a gas turbine (GT), a waste heat boiler (WHB), a ground source heat pump (HP), an electric refrigerator (ER), an absorption refrigerator (AR), and other energy conversion equipment, as well as electric energy storage (EES), heat energy storage (HES), and other energy storage equipment.

2.1 Modeling of Distributed Generations

2.1.1 Wind Turbine

$$P_t^{\mathrm{WT}} = \frac{1}{2}\eta_{\mathrm{w}}\pi r^2 \rho v_t^3, \tag{1}$$

where P_t^{WT} indicates the wind turbine generation power (kW) in time period t, η_{w} is the wind energy utilization efficiency of the wind turbine, r represents the blade radius (m), ρ represents the air density (kg/m^3), and v_t is the air velocity (m/s) in time period t.

2.1.2 Photovoltaic

$$\begin{cases} P_t^{\mathrm{PV}} = \dfrac{P_{\mathrm{test}} L_t^{\mathrm{ac}} \left[1 + K\left(\theta_t^{\mathrm{s}} - \theta_t^{\mathrm{r}}\right)\right]}{L_{\mathrm{test}}}, \\ \theta_t^{\mathrm{s}} = \theta_t^{\mathrm{out}} + 30R_t, \end{cases} \tag{2}$$

where P_t^{PV} refers to the output power (kW) of photovoltaic equipment during the period t, P_{test} represents the test power (kW) under standard conditions t, L_t^{ac} refers to the light intensity (W/m^2) in the period t, L_{test} is the test light intensity (W/m^2) under standard conditions, K is the power temperature coefficient, which is taken as −0.0047; θ_t^{s}, θ_t^{r}, and θ_t^{out} represent the solar panel temperature, reference temperature, and external ambient temperature (°C), respectively; normally the reference temperature is taken as 25 °C; and R_t expresses the solar radiation intensity (kW/m^2) in time period t.

2.2 Modeling of Energy Conversion Unit

2.2.1 Cogeneration Unit

The cogeneration unit generates electric energy and heat energy at the same time by consuming natural gas. Its operation mode can be expressed as

$$\begin{cases} P_t^{\mathrm{CHP}} = \eta^{\mathrm{P,CHP}} G_t^{\mathrm{CHP}}, \\ H_t^{\mathrm{CHP}} = \eta^{\mathrm{H,CHP}} G_t^{\mathrm{CHP}}, \end{cases} \tag{3}$$

where P_t^{CHP}, H_t^{CHP}, and G_t^{CHP} are the electric power, thermal power, and gas power consumed by the internal cogeneration unit in scheduling period t, respectively, and $\eta^{\mathrm{P,CHP}}$ and $\eta^{\mathrm{H,CHP}}$ are the power generation efficiency and heating efficiency of cogeneration units, respectively.

2.2.2 Gas Turbine and Waste Heat Boiler

The gas turbine generates electric energy by consuming natural gas, and part of the discharged flue gas can be transformed into available calorific value through a waste heat boiler. Their working characteristics can be expressed as

$$\begin{cases} P_t^{\mathrm{GT}} = \dfrac{\eta_{\mathrm{GT}} L_{\mathrm{gas}} V_t^{\mathrm{gas}}}{t}, \\ H_t^{\mathrm{GT}} = P_t^{\mathrm{GT}} \dfrac{\left(1 - \eta_{\mathrm{GT}} - \eta_{\mathrm{l}}\right)}{\eta_{\mathrm{GT}}}, \\ H_t^{\mathrm{WHB}} = \eta_{\mathrm{WHB}} H_t^{\mathrm{GT}}, \end{cases} \tag{4}$$

where P_t^{GT} and H_t^{GT} indicate the gas turbine generation power and flue gas waste heat power during the period t, respectively; L_{gas} represents

the low calorific value of natural gas, which is set as 9.78 kWh/m^3 in this paper; V_t^{gas} expresses the natural gas consumption during the period t; t is the scheduling period; η_{GT} and η_{l} represent the power generation efficiency and loss rate of gas turbine, respectively; η_{WHB} is the recovery efficiency of the waste heat boiler; and H_t^{WHB} is the heat recovery power of the waste heat boiler in time period.

2.2.3 Ground Source Heat Pump

The heat pump is a high-efficiency and energy-saving equipment in the multi-energy flow coupling system. It can convert low-grade heat energy into high-grade heat energy by consuming electric energy. Its operation mode is given by

$$H_t^{\text{HP}} = \eta_{\text{HP}} P_t^{\text{HP}}, \tag{5}$$

where H_t^{HP} and P_t^{HP} represent the heat energy generated and electric energy consumed of the ground source heat pump during the period t, respectively; and η_{HP} is the conversion efficiency of the heat pump.

2.2.4 Electric Chiller and Absorption Chiller

The electric chiller generates cold power by consuming electric power during operation, and the absorption chiller generates cold power by absorbing thermal power. Its mathematical model is as follows:

$$\begin{cases} C_t^{\text{EC}} = \eta_{\text{EC}} P_t^{\text{EC}}, \\ \eta_{\text{AC}} = \dfrac{\eta_0^{\text{AC}} \beta_{\text{AC}}}{a_{\text{AC}} (\beta_{\text{AC}})^2 + b_{\text{AC}} \beta_{\text{AC}} + c_{\text{AC}}}, \\ C_t^{\text{AC}} = \eta_{\text{AC}} H_t^{\text{AC}}, \end{cases} \tag{6}$$

where C_t^{EC} and C_t^{AC} represent the cool power generated in time period t of the electric chiller and absorption chiller, respectively; η_{EC} and η_{AC} represent the conversion efficiency of the electric chiller and absorption chiller, respectively; P_t^{EC} indicates the electric energy consumed of the electric chiller during the period t; H_t^{AC} represents the heat energy consumed of the absorption chiller during the period t; η_0^{AC} is the rated conversion efficiency of the absorption chiller; a_{AC}, b_{AC}, and c_{AC} are the refrigeration coefficient of the absorption chiller, respectively; and β_{AC} is the load rate when the absorption chiller is working.

2.3 Modeling of Energy Storage Equipment

$$E_{i,t} = E_{i,t-1}(1 - \sigma_i) + P_{i,t}^{\text{c}} \eta_i^{\text{c}} - P_{i,t}^{\text{d}} \big/ \eta_i^{\text{d}}, \tag{7}$$

where $E_{i,t}$ represents the energy storage of energy storage equipment i in time period t, $P_{i,t}^{\text{c}}$ and $P_{i,t}^{\text{d}}$ are the charging power and discharging power of energy storage equipment i in time period t, η_i^{c} and η_i^{d} represent the charging efficiency and discharging efficiency of energy storage equipment i, and σ_i is the consumption rate of energy storage equipment i.

3 MODELING OF MULTI-OBJECTIVE COLLABORATIVE OPTIMIZATION

In the multi-objective collaborative optimization of MEFCS considering carbon emissions, the optimization objectives considered in this paper include the environmental protection objective, economic objective, and energy efficiency objective.

3.1 Each Optimization Objective Function

3.1.1 Environmental Protection Objective

Aiming at minimizing the CO_2 emission of MEFCS in 1 day, the optimization model can be established as follows:

$$\min \quad F_1 = \sum_{t=1}^{24} \left[\alpha_{\text{gas}} \cdot \left(P_t^{\text{GT}} + G_t^{\text{CHP}} \right) + \alpha_{\text{grid}} \cdot \left(P_t^{\text{HP}} + P_t^{\text{EC}} \right) \right], \tag{8}$$

where α_{gas} and α_{grid} represent the CO_2 emission coefficient corresponding to the combustion of natural gas and the consumption of electric energy; in this paper, they are taken as 184 g/kWh and 877 g/kWh, respectively.

3.1.2 Economic Objective

In order to minimize the operation cost of MEFCS in 1 day, the optimization model can be formulated as

$$\begin{cases} \min \quad F_2 = \sum_{t=1}^{24} \left(c_{\text{grid}} P_t^{\text{grid}} + c_{\text{gas}} G_t^{\text{gas}} \right) + \sum_{i=1}^{N} c_i^{\text{ma}} P_i, \\ P_t^{\text{grid}} = P_t^{\text{HP}} + P_t^{\text{EC}}, \\ G_t^{\text{gas}} = P_t^{\text{GT}} + G_t^{\text{CHP}}, \end{cases} \tag{9}$$

where c_{grid} and c_{gas} are the cost coefficients corresponding to the electric energy and natural gas consumed by the system, respectively; c_i^{ma} is the maintenance cost of equipment i; P_i is the rated capacity of equipment i; and N represents the total amount of equipment.

3.1.3 Energy Efficiency Objective

Primary energy utilization is defined as the ratio of MEFCS load to MEFCS primary energy input in a day. Aiming at the maximum utilization of primary energy, the optimization model can be formulated as

$$\begin{cases} \max \quad F_3 = \dfrac{W_{PL} + W_{HL} + W_{CL}}{\sum_{t=1}^{24} \left(\dfrac{P_t^{\text{grid}}}{1 - \zeta} + G_t^{\text{gas}} \right)}, \\ W_{PL} = \sum_{t=1}^{24} P_t^{\text{L}}, \\ W_{HL} = \sum_{t=1}^{24} H_t^{\text{L}}, \\ W_{CL} = \sum_{t=1}^{24} C_t^{\text{L}}, \end{cases} \tag{10}$$

where W_{PL}, W_{HL}, and W_{CL} represent the total load of the system in a day, respectively, and ζ represents the network loss rate of transmission line, which is usually chosen as 5%.

3.2 Constraint Condition

3.2.1 Energy Balance Constraints

1) Power balance constraint

$$\begin{aligned} &P_t^{\text{grid}} + P_t^{\text{CHP}} + P_t^{\text{GT}} + P_t^{\text{WT}} + P_t^{\text{PV}} + P_t^{\text{ES,d}} \\ &= P_t^{\text{L}} + P_t^{\text{HP}} + P_t^{\text{ES,c}} + P_t^{\text{EC}}. \end{aligned} \tag{11}$$

2) Heat energy balance constraint

$$H_t^{\mathrm{CHP}} + H_t^{\mathrm{HP}} + H_t^{\mathrm{WHB}} + H_t^{\mathrm{HS,d}} = H_t^{\mathrm{L}} + H_t^{\mathrm{HS,c}} + H_t^{\mathrm{AC}}. \tag{12}$$

3) Cool energy balance constraint

$$C_t^{\mathrm{EC}} + C_t^{\mathrm{AC}} = C_t^{\mathrm{L}}. \tag{13}$$

3.2.2 Upper and Lower Limits of Equipment Output

$$0 \le O_{i,t} \le P_i, \tag{14}$$

where $O_{i,t}$ represents the output power of equipment i in period t.

3.2.3 Energy Storage Constraints

$$\begin{cases} P_{i,t}^{\mathrm{c}} \le \upsilon \bar{P}_i^{\mathrm{c}}, \\ P_{i,t}^{\mathrm{d}} \le (1-\upsilon)\bar{P}_i^{\mathrm{d}}, \\ \upsilon \in \{0,1\}, \\ E_{i,1} = E_{i,24}, \\ \underline{\mu_i}\, P_i \le E_{i,t} \le \bar{\mu}_i P_i, \end{cases} \tag{15}$$

where $\bar{P}_i^{\mathrm{c}}$ and $\bar{P}_i^{\mathrm{d}}$ represent the upper limit of charging and discharging power of energy storage equipment i, respectively; υ represents 0–1 variable; $E_{i,t}$ is the energy storage of equipment i in period t; and $\bar{\mu}_i$ and $\underline{\mu_i}$ represent the upper and lower limits of the charging and discharging state of the energy storage equipment i, respectively.

3.3 Collaborative Optimization Objective

The developed optimization model is a multi-objective optimization problem. First, the optimal solution of each objective is obtained through single objective optimization, and then the optimization results of each objective are standardized, so the multi-objective optimization is transformed into single objective optimization with the help of the linear weighting method. Finally, the single objective optimization algorithm can be solved.

3.3.1 Normalization and Standardization

As the environmental protection goal and economic goal belong to very small goals, that is, the smaller the final result, the better, while the energy efficiency goal belongs to maximum goals, the larger the final result, the better. Therefore, before establishing the collaborative optimization objectives, each single objective should be normalized and standardized, which can be expressed as follows:

$$S_1(F_i) = \begin{cases} 1, \ F_i \le F_{i,\min}, \\ \dfrac{F_{i,\max} - F_i}{F_{i,\max} - F_{i,\min}}, \ F_{i,\min} < F_i \le F_{i,\max}, \\ 0, \ F_i > F_{i,\max}, \end{cases} \tag{16}$$

$$S_2(F_i) = \begin{cases} 0, \ F_i \le F_{i,\min}, \\ \dfrac{F_i - F_{i,\min}}{F_{i,\max} - F_{i,\min}}, \ F_{i,\min} < F_i \le F_{i,\max}, \\ 1, \ F_i > F_{i,\max}, \end{cases} \tag{17}$$

where S_1 and S_2 represent the membership function of very small target and maximum target, respectively, F_i is the ith objective function, and $F_{i,\min}$ and $F_{i,\max}$ are the minimum and maximum of the ith objective function, respectively.

3.3.2 Index Weighting

Generally, the methods of weighting indicators can be divided into subjective method, objective method, and the combination of subjective and objective methods. The subjective weighting method is simple to operate and does not need the support of original data, but the subjectivity of weighting results is often too large. The objective weighting method can show the relationship between indicators well, but it has high requirements for the original data. Therefore, in this paper, a new combination method based on the analytic hierarchy process (AHP) and the improved entropy weight method is adopted.

The analytic hierarchy process first judges the relative importance of each index through decision-making experts and scores each index with an integer between 1 and 9, and then the judgment matrix is obtained,

$$\mathrm{A} = \begin{bmatrix} a_{11} & a_{12} & \cdots & a_{1n} \\ a_{21} & a_{22} & \cdots & a_{2n} \\ \vdots & \vdots & \ddots & \vdots \\ a_{n1} & a_{n2} & \cdots & a_{nn} \end{bmatrix}, \tag{18}$$

where n denotes the number of indicators. **A** is a positive reciprocal matrix, which satisfies $a_{ij} = 1/a_{ji}$.

To be noted that, due to the environmental protection goal is taken as the leading factor in this paper, when forming the judgment matrix, the score of the environmental protection index is relatively high so that the final weight is relatively maximum.

Then check the consistency of the judgment matrix,

$$\begin{cases} CR = \dfrac{CI}{RI}, \\ CI = \dfrac{\lambda_{\max} - n}{n-1}, \end{cases} \tag{19}$$

where CR represents the consistency proportion. If $CR < 0.1$, the consistency verification passes, otherwise the judgment matrix needs to be modified. CI and RI represent the consistency index and average random consistency index, respectively. $\lambda_{\max}$ is the maximum eigenvalue of judgment matrix **A**.

When the judgment matrix **A** passes the consistency check, the eigenvector corresponding to its maximum eigenvalue $\lambda_{\max}$ is obtained and normalized, that is, the weight vector is obtained by the analytic hierarchy process,

$$\omega^1 = \left[\omega_1^1, \omega_2^1, \cdots, \omega_n^1\right]^{\mathrm{T}}. \tag{20}$$

The entropy weight method reflects the amount of information contained in each index through the entropy value of each index. Generally speaking, the smaller the entropy value, the greater the amount of index information and the greater the weight should be set. Since the standard entropy weight method is mainly applied to multiple schemes, the entropy weight method can be improved by

$$\begin{cases} p_i = \dfrac{1+S_i}{(1+S_{i,\min})+(1+S_i)+(1+S_{i,\max})}, \\ H_i = \dfrac{p_{i,\min}\ln p_{i,\min} + p_i \ln p_i + p_{i,\max}\ln p_{i,\max}}{\ln 3}, \end{cases} \tag{21}$$

where p_i represents the characteristic specific gravity of the ith target, H_i is the entropy of the ith target, and S_i is the membership function of the ith objective.

To be noted that, this improvement is mainly to adapt to the optimization model. The objective functions have been processed and converted into the form of membership function. Therefore, in order to adapt to this form, the index value is replaced by membership S_i. Because this is not an evaluation problem, there are no multiple schemes to be evaluated. Therefore, the possible maximum and minimum values of each membership degree are substituted into the formula to reduce the individual deviation. In this way, there are three evaluation schemes in terms of quantity, that is, $m = 3$. Therefore, the above formula is obtained.

According to the calculation results of entropy value of each index, the weight of each index can be obtained by

$$\omega_i^2 = \frac{1-H_i}{n-\sum_{i=1}^{n} H_i}. \tag{22}$$

Therefore, the weight vector is obtained by the improved entropy weight method,

$$\boldsymbol{\omega}^2 = \left[\omega_1^2, \omega_2^2, \cdots, \omega_n^2\right]^{\mathrm{T}}. \tag{23}$$

In order to obtain the combined weight of AHP and improved entropy weight method, the coupling vector is taken as follows:

$$\left[\theta^1, \theta^2\right] = \left[\theta_1^1, \theta_2^1, \cdots, \theta_n^1, \theta_1^2, \theta_2^2, \cdots, \theta_n^2\right], \tag{24}$$

where θ_i^1 and θ_i^2 represent the coupling weight of index I for weight coefficients ω_i^1 and ω_i^2, respectively, which can be expressed as

$$\begin{cases} \theta_i^1 = \dfrac{\omega_i^1}{\omega_i^1+\omega_i^2}, \\ \theta_i^2 = \dfrac{\omega_i^2}{\omega_i^1+\omega_i^2}. \end{cases} \tag{25}$$

Therefore, the weight after coupling is

$$\omega_i^* = \theta_i^1\omega_i^1 + \theta_i^2\omega_i^2. \tag{26}$$

Normalize it, one has

$$\omega_i = \frac{\theta_i^1\omega_i^1 + \theta_i^2\omega_i^2}{\sum_{i=1}^{n}\left(\theta_i^1\omega_i^1 + \theta_i^2\omega_i^2\right)}. \tag{27}$$

Then, the combined weight of the AHP improved entropy weight method can be finally expressed as

$$\omega = [\omega_1, \omega_2, \cdots, \omega_n]^{\mathrm{T}}. \tag{28}$$

3.3.3 Collaborative Optimization Objective

After obtaining the index weight, combined with the standardized objective function in the above sections, we can obtain the comprehensive satisfaction goal, that is, the collaborative optimization objective is given as

$$\max \ F = \omega_1 S_1(F_1) + \omega_2 S_1(F_2) + \omega_3 S_2(F_3). \tag{29}$$

4 OPTIMIZATION ALGORITHM

Based on the above analysis, it can be found that the multi-objective collaborative optimization of the multi-energy flow coupling system considered in this paper is a complex nonlinear programming problem. In order to make the solution speed and convergence meet the requirements of practical problems, the simplified primal dual interior point algorithm is used in this paper. For the sake of brevity, first, the optimization model described above is transformed into the following general form:

$$\begin{cases} \max \ F(x), \\ \text{s.t.} \quad h(x) = 0, \\ g_{\min} \le g(x) \le g_{\max}, \end{cases} \tag{30}$$

where x is the state variable, including the output power, external power purchase, gas purchase, etc., of each equipment, $h(x)$ is the equality constraint, including the power balance constraint of the system, the energy balance constraint at the beginning and end of the scheduling cycle of energy storage equipment, etc.; $g(x)$ is the inequality constraint, including the upper and lower limits of equipment output, energy storage charge and discharge constraints, etc.; and $g_{\max}$ and $g_{\min}$ represent the upper and lower bounds of the inequality, respectively.

When dealing with this optimization model with the traditional interior point algorithm, relaxation variables $u = [u_1, \cdots, u_r]^{\mathrm{T}}$ and $l = [l_1, \cdots, l_r]^{\mathrm{T}}$ are introduced first, where r represents the number of inequality constraints; thus, the original inequality constraints are transformed into the equality constraints. The resulting optimization model is formulated as

$$\begin{cases} \min \ -F(x), \\ \text{s.t.} \quad h(x) = 0, \\ \qquad g(x) + u = g_{\max}, \\ \qquad gx - l = g_{\min}, \\ \qquad u > 0, l > 0. \end{cases} \tag{31}$$

At the same time, the size of relaxation variables u and l should be restricted to ensure that the objective function $F(x)$ is always far away from the solution boundary so that it can be solved in the feasible domain as follows:

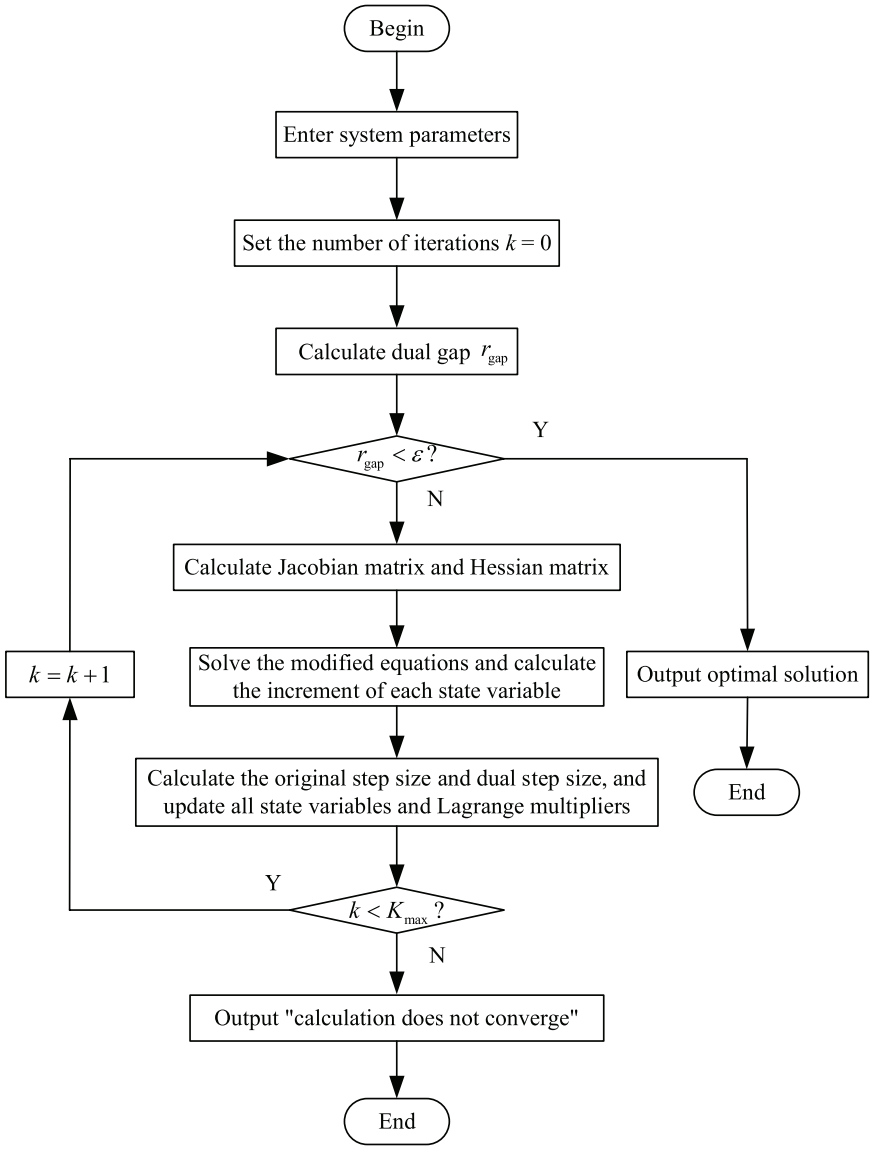

FIGURE 2 | Calculation flow of multi-objective collaborative optimization.

$$\begin{cases} \min & -F(x) - \mu\sum_{i=1}^{r}\log(l_i) - \mu\sum_{i=1}^{r}\log(u_i), \\ \text{s.t.} & h(x) = 0, \\ & g(x) + u = g_{\max}, \\ & g(x) - l = g_{\min}, \end{cases} \tag{32}$$

where μ represents the introduced disturbance factor.

At this point, the inequality constraints contained in the optimization model described in this paper have all been converted into the equality constraints, and the Lagrange function for this optimization problem can be expressed as

$$\begin{aligned} L = & -F(x) - y^T h(x) \\ & -z^T\left[g(x) - l - g_{\min}\right] \\ & -w^T\left[g(x) + u - g_{\max}\right] \\ & -\mu\sum_{i=1}^{r}\log(l_i) - \mu\sum_{i=1}^{r}\log(u_i), \end{aligned} \tag{33}$$

where y, z, and w all represent the Lagrange operators, also known as the dual variables. By deriving this Lagrange function, the optimal solution to this optimization problem can be obtained.

In this paper, by simplifying the original dual interior point algorithm, the simplified original dual interior point method can

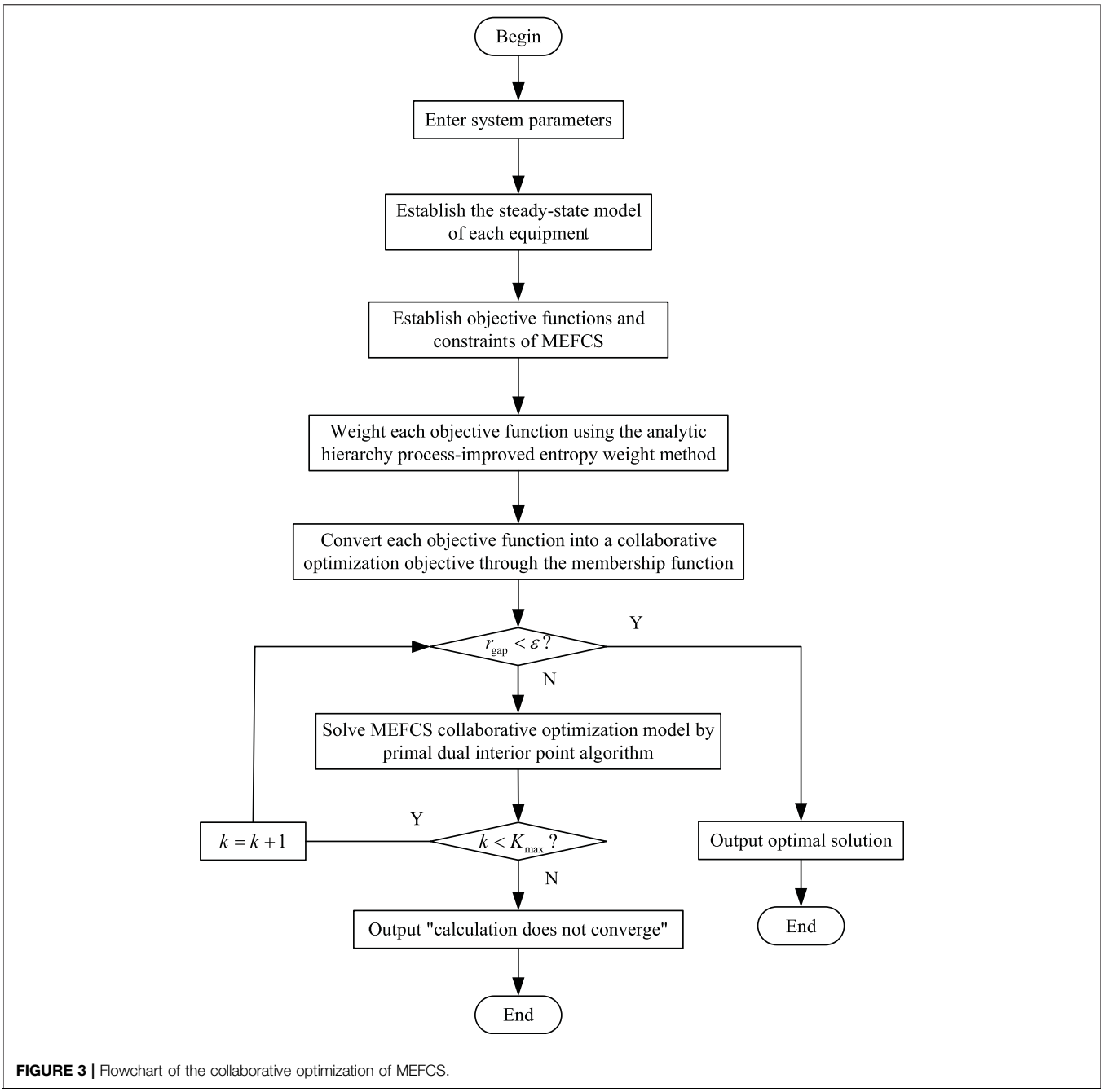

FIGURE 3 | Flowchart of the collaborative optimization of MEFCS.

be utilized to solve the optimization model, and the simplified process is to rewrite the inequality constraint to

$$\begin{cases} \hat{g}(x) \le \hat{g}_{\max}, \\ \hat{g}(x) = \left[g(x), -g(x)\right]^{\mathrm{T}}, \\ \hat{g}_{\max} = \left[g_{\max}, -g_{\max}\right]^{\mathrm{T}}, \end{cases} \tag{34}$$

where $\hat{g}(x)$ and $\hat{g}_{\max}$ represent the generalized inequality constraints and generalized upper bounds, respectively.

It can be found from the traditional interior point algorithm that in the process of dealing with inequality constraints, the upper and lower bounds of inequality constraints need to be relaxed, and then converted into equality constraints, respectively. At the same time, Lagrange operators are also introduced for equality constraints converted from upper-bound inequality constraints and lower-bound inequality constraints, respectively, which introduce more variables in the Lagrange function. This simplification algorithm greatly reduces the relaxation variables and corresponding Lagrange operators introduced in the optimization model, improves the convergence speed of the algorithm while guaranteeing the

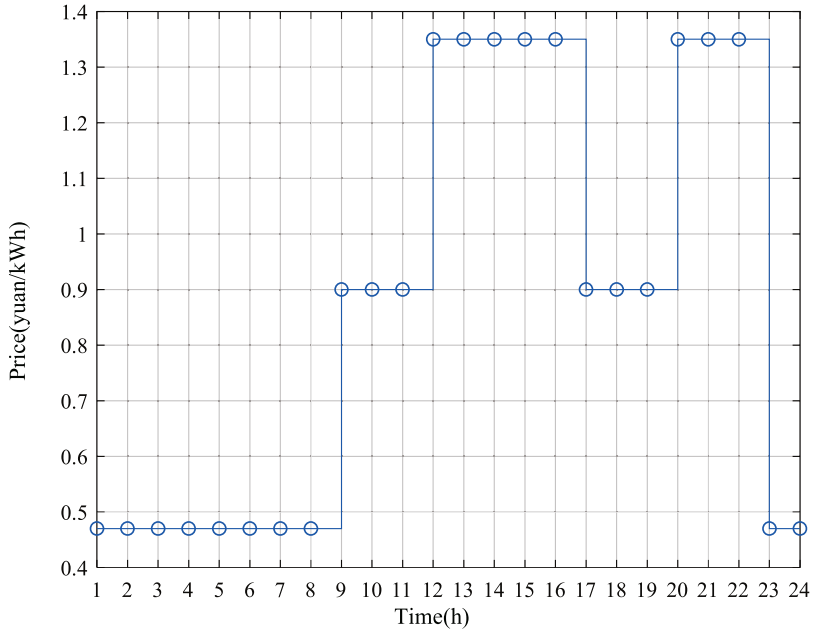

FIGURE 4 | Power purchase price of MEFCS.

calculation accuracy, and reduces the amount of programming to a certain extent. The rest of the algorithm is handled similarly to the traditional algorithm, which are not discussed here. For ease of understanding, the multi-objective collaborative optimization calculation flow of the multi-energy flow coupling system based on the simplified primal dual interior point algorithm is shown in **Figure 2**, where r_{gap} is the dual gap, ε represents the convergence accuracy, which is taken as 10–6 in this paper, and K_{max} represents the maximum number of iterations, normally is set as 300.

Based on the above analysis, the collaborative optimization of MEFCS dominated by the carbon emission targets in this paper can be summarized as the following steps:

Step 1. Enter parameter information of the multi-energy flow coupling system, such as system load, rated capacity of each unit, equipment parameters, and time-of-use electricity price.

Step 2. Establish the steady-state operation model of each equipment, as shown in **Eqs 1**–**7**.

Step 3. Establish the objective functions and constraints of the MEFCS, as shown in **Eqs 8**–**15**.

Step 4. Weight each objective function using the analytic hierarchy process-improved entropy weight method, as shown in **Eqs 18**–**28**.

Step 5. Convert each objective function into a collaborative optimization objective through the membership function and the obtained weight information, as shown in **Eqs 16**, **17**, **29**.

Step 6. Solve the MEFCS collaborative optimization model by the primal dual interior point algorithm until the optimal solution is obtained or the algorithm does not converge.

The above steps can be clearly represented by the flowchart shown in **Figure 3**.

5 CASE STUDY

5.1 Case Description

In this paper, the typical multi-energy flow coupling system shown in **Figure 1** is selected as an example. The capacity of each equipment is as follows: one photovoltaic generator unit with a rated output of 700 kW and one wind turbine generator unit with a rated output of 500 kW, one cogeneration unit with a rated output of 3 MW, one gas turbine with a rated output of 2 MW, one waste heat boiler with a rated output of 1 MW, four heat pumps with a rated output of 500 kW, four electric refrigerators and four absorption refrigerators with a rated output of 200 kW, and four batteries and heat storage equipment with a rated capacity of 500 kwh. Other economic and technical parameters of the equipment can be found in Wang Y. et al. (2018) and Huang et al. (2019). The time of use electricity price information of the multi-energy flow coupling system is shown in **Figure 4**, and the price of natural gas is 2.71 yuan/m^3 (Shen et al., 2020). The load data of the system are shown in **Figure 5**.

5.2 Results Analysis

The output curve of each equipment is shown in **Figure 6**. It can be seen that the supply of electric energy and heat energy of the system is mainly guaranteed by a gas turbine and heat pump, but only the output of each equipment is not enough to meet the load demand during the peak load period of the system. At this time, the system

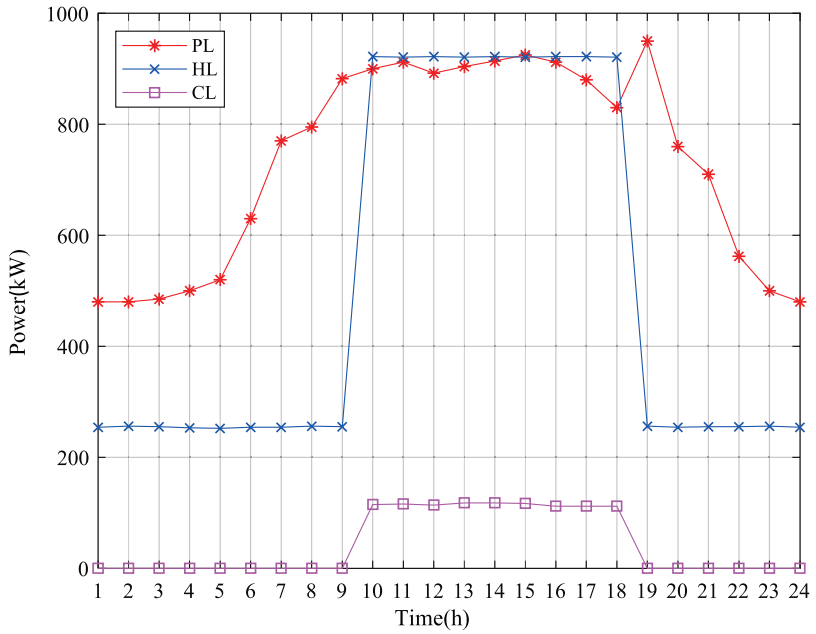

FIGURE 5 | Load of MEFCS

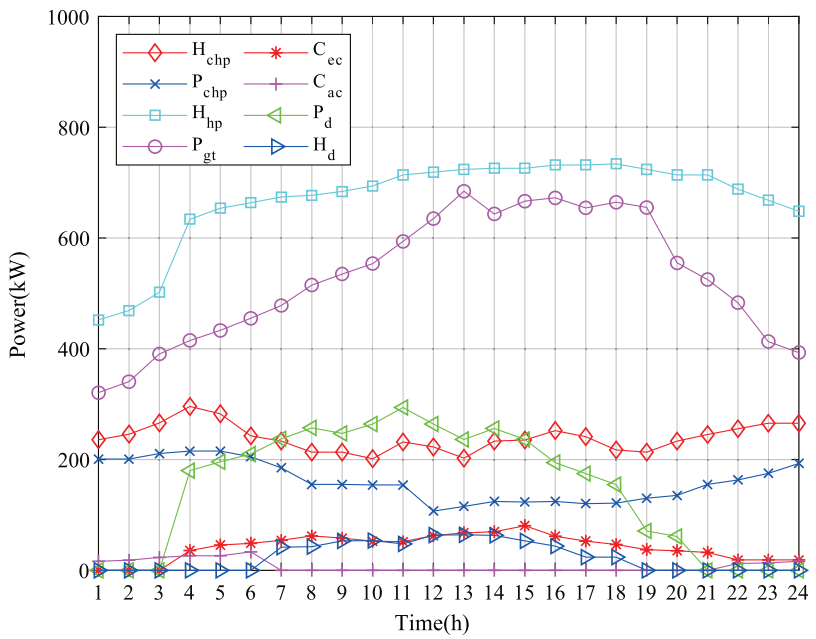

FIGURE 6 | Output of each equipment of MEFCS.

needs to purchase electricity from the external power grid to jointly supply energy to the load. In addition, it can be seen from the figure that the discharge time of the power storage equipment is 03:00–21:00, and the heat release time of the heat storage equipment is 06:00–19:00. In other periods, that energy storage equipment is in the charged states.

While using the multi-objective collaborative optimization model proposed in this paper to solve the multi-energy flow coupling system, three separate objectives are solved respectively. After finding the individual optimization of each objective, its state variables are substituted into the other two objectives to obtain the respective results of the three objectives in this case.

TABLE 1 | Comparison between multi-objective collaborative optimization and single-objective optimization.

Operation form	Multi-objective collaborative optimization	Single objective optimization		
		F_1 optimal	F_2 optimal	F_3 optimal
F	0.9685	0.8943	0.8304	0.8612
F_1 (kg)	10,403.5	10,022.2	15,113.3	10,543.7
F_2 (yuan)	14,568.8	16,205.2	13,727.1	14,037.3
F_3 (%)	79.04	81.67	67.94	86.33

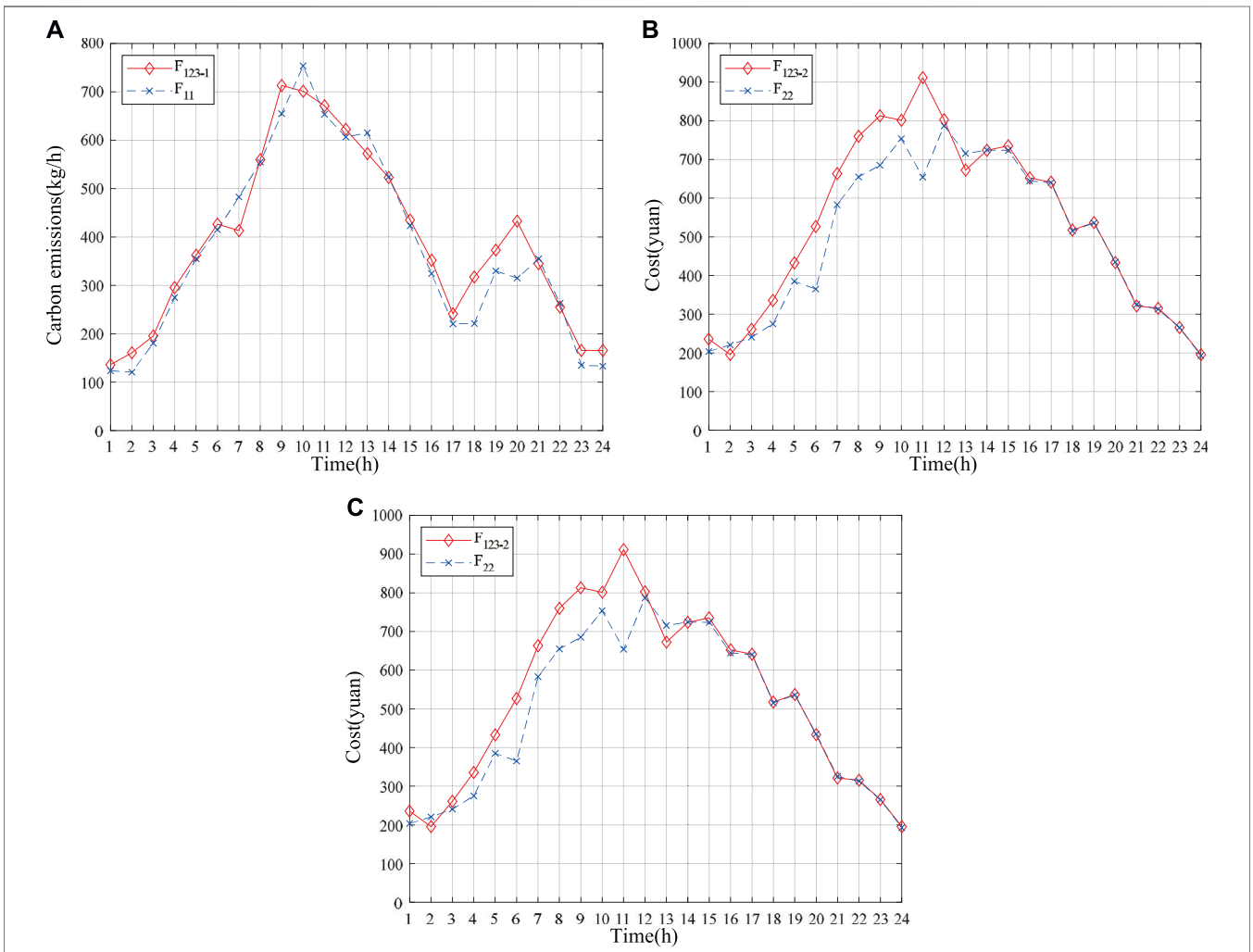

FIGURE 7 | Period by period analysis of single objective and multi-objective optimization results. **(A)** Comparison of environmental protection objectives by period. **(B)** Period by period comparison of economic objectives. **(C)** Period by period comparison of energy efficiency objectives.

The comparison between the operation results of each scheme and the operation results of multi-objective collaborative optimization is shown in **Table 1**. It can be found from **Table 1** that the CO2 emission under multi-objective collaborative optimization increases by 3.8% compared with that under single objective *F*1 optimization, the system operation cost increases by 6.1% compared with that under single objective *F*2 optimization, and the primary energy utilization rate decreases by 7.2% compared with that under single objective *F*3 optimization. Although each objective under multi-objective collaborative optimization is not the optimal solution, the contradiction and conflict between each single objective are balanced in the optimization process. On the premise of taking the minimum carbon emission of the system as the leading objective, the comprehensive satisfaction of the system is significantly higher than the solution results of each

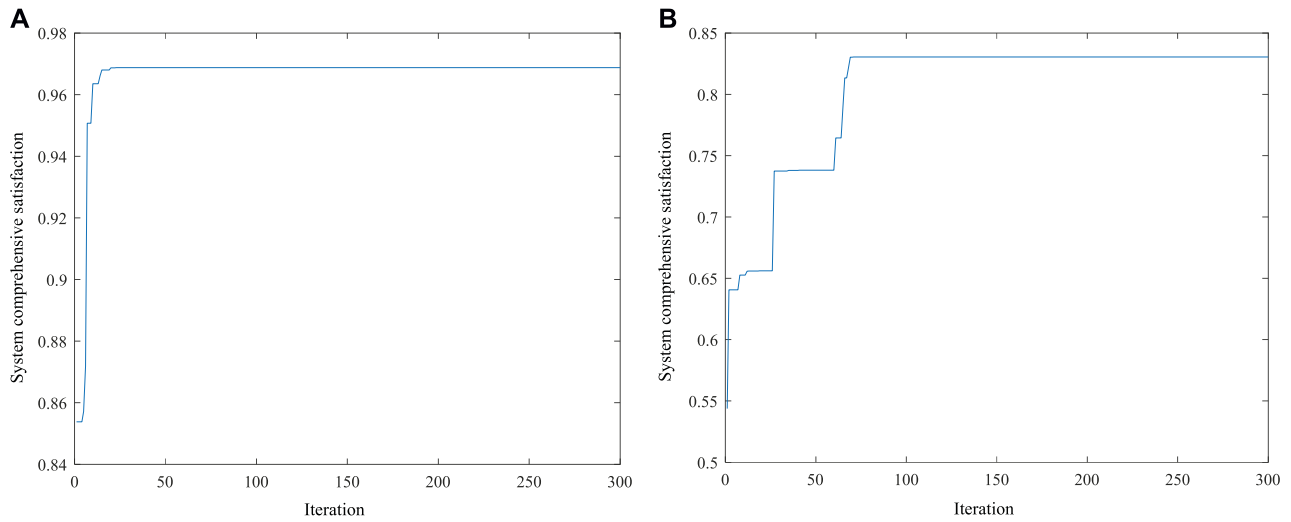

FIGURE 8 | Solving process of the comprehensive satisfaction objective for MEFCS. **(A)** Simplified primal dual interior point method. **(B)** Particle swarm optimization algorithm.

single objective, and a relatively satisfactory optimal scheduling scheme is given.

In order to further compare the differences between the multi-objective collaborative optimization proposed in this paper and the traditional single objective optimization, the optimization results of each single objective and the multi-objective collaborative optimization results are analyzed period by period, as shown in **Figure 7**. In the figure, F_{123-1}, F_{123-2}, and F_{123-3} represent the environmental protection objective, economic objective, and energy efficiency objective under collaborative optimization, while F_{11}, F_{22}, and F_{33} represent the environmental protection objective, economic objective, and energy efficiency objective under single objective optimization. **Figure 7A** shows the carbon emissions in each period of the two optimization methods. It can be seen from the figure that the two carbon emission curves cross each other. Except that the carbon emissions during collaborative optimization in 17:00–21:00 are significantly higher than those in single objective optimization, they are very close in other times. It shows that when taking the minimum carbon emission as the leading objective, the effect of collaborative optimization is not different from the single objective optimization with the minimum carbon emission, and the working state of each equipment is also relatively stable. **Figure 7B** shows the cost curves of the two optimization methods. During 3:00–12:00, the cost of multi-objective collaborative optimization is about 100 yuan/h higher than that of single objective optimization, and the two curves almost coincide after 12:00. It can be seen from **Table 1** that the comprehensive satisfaction of multi-objective collaborative optimization is obviously higher than that of single objective optimization. On this basis, it ensures that the operation cost of the system is not too high, and it is almost the same as that of single objective optimization in most periods, indicating that the result of multi-objective collaborative optimization is ideal. **Figure 7C** shows the comparison of energy efficiency of the two methods in each period. Although the operation energy efficiency of multi-objective optimization in each period is not as good as that of single objective energy efficiency optimization, the overall operation result is relatively stable, indicating that each equipment can achieve stable energy supply and continuous output during the operation of the system, and the working state is not easy to fluctuate violently.

In order to highlight the effectiveness of the simplified primal dual interior point method proposed in this paper, the particle swarm optimization (PSO) algorithm is selected to compare with the algorithm proposed in this paper. The solution process curves of the simplified primal dual interior point method and particle swarm optimization algorithm for the system comprehensive satisfaction objective are shown in **Figures 8A,B**, respectively. They tend to converge at the 25th and 65th iterations, respectively. It can be seen that the convergence of the simplified primal dual interior point method is better than that of the particle swarm optimization algorithm. In addition, from the solution results of the two algorithms, it can be seen that the simplified primal dual interior point method finally converges near 0.9685, while the particle swarm optimization algorithm finally converges only near 0.8352, which still has a certain deviation from the global optimal solution. Therefore, the global optimization ability of the simplified primal dual interior point method proposed in this paper is also stronger than that of the particle swarm optimization algorithm.

6 CONCLUSION

In this paper, the multi-objective collaborative optimization model of MEFCS has been developed considering each of the environmental protection, system economy, and energy efficiency

as the objectives of this study, in which the carbon emission orientation goal could be achieved. Moreover, the simplified primal dual interior point method has been used to solve the constructed model. According to the obtained results, the following findings have been concluded: 1) The contradiction and conflict between the three objectives (CO2 emission, system operation cost, and primary energy utilization rate) were relatively balanced under the proposed collaborative optimization operation, which have clearly demonstrated that the satisfaction of collaborative optimization operation considering multiple objectives could be higher than that considering a single objective of the system. 2) Each equipment of the system could achieve stable energy supply as well as continuous output throughout the whole operation process, whereas the working state was difficult to fluctuate sorely. 3) At the same time, the operator could adjust the weight of the three objectives through his own will, so as to get the best operation results that meet his requirements. 4) In addition, the simulation results have illustrated that the simplified primal dual interior point method being adopted in this paper has better convergence and global optimization ability in multi-objective collaborative optimization. However, more investigations are needed regarding the sensitivity analysis on the critical parameters of the multi-energy flow coupling system, which will be considered in our future research work.

DATA AVAILABILITY STATEMENT

The original contributions presented in the study are included in the article/Supplementary Material, further inquiries can be directed to the corresponding author.

AUTHOR CONTRIBUTIONS

XZ: Methodology, software, writing—original draft, data curation. YY: Conceptualization of this study, supervision, review and editing. HW: Review and editing.

FUNDING

This work was supported by the National Natural Science Foundation of China (No. 51477041).

REFERENCES

Barati, F., Seifi, H., Sepasian, M. S., Nateghi, A., Shafie-khah, M., and Catalao, J. P. S. (2015). Multi-period Integrated Framework of Generation, Transmission, and Natural Gas Grid Expansion Planning for Large-Scale Systems. *IEEE Trans. Power Syst.* 30 (5), 2527–2537. doi:10.1109/TPWRS.2014.2365705

Clegg, S., and Mancarella, P. (2016). Integrated Electrical and Gas Network Flexibility Assessment in Low-Carbon Multi-Energy Systems. *IEEE Trans. Sustain. Energ.* 7 (2), 718–731. doi:10.1109/TSTE.2015.2497329

Fan, D., Dou, X., Xu, Y., Wu, C., Xue, G., and Shao, Y. (2021). A Dynamic Multi-Stage Planning Method for Integrated Energy Systems Considering Development Stages. *Front. Energ. Res.* 9, 723702. doi:10.3389/fenrg.2021.723702

Ghosh, S., and Kamalasadan, S. (2017). An Energy Function-Based Optimal Control Strategy for Output Stabilization of Integrated DFIG-Flywheel Energy Storage System. *IEEE Trans. Smart Grid.* 8 (4), 1922–1931. doi:10.1109/TSG.2015.2510866

Hu, Q., Liang, Y., Ding, H., Quan, X., Wang, Q., and Bai, L. (2022). Topological Partition Based Multi-Energy Flow Calculation Method for Complex Integrated Energy Systems. *Energy.* 244, 123152. doi:10.1016/j.energy.2022.123152

Huang, W., Zhang, N., Yang, J., Wang, Y., and Kang, C. (2019). Optimal Configuration Planning of Multi-Energy Systems Considering Distributed Renewable Energy. *IEEE Trans. Smart Grid.* 10 (2), 1452–1464. doi:10.1109/TSG.2017.2767860

Klyapovskiy, S., You, S., Cai, H., and Bindner, H. W. (2019). Integrated Planning of a Large-Scale Heat Pump in View of Heat and Power Networks. *IEEE Trans. Ind. Applicat.* 55 (1), 5–15. doi:10.1109/TIA.2018.2864114

Koltsaklis, N. E., and Knápek, J. (2021). Optimal Scheduling of a Multi-Energy Microgrid. *Chem. Eng. Trans.* 88, 901–906. doi:10.3303/CET2188150

Li, C., Yang, H., Shahidehpour, M., Xu, Z., Zhou, B., Cao, Y., et al. (2020). Optimal Planning of Islanded Integrated Energy System with Solar-Biogas Energy Supply. *IEEE Trans. Sustain. Energ.* 11 (4), 2437–2448. doi:10.1109/TSTE.2019.2958562

Liu, N., Wang, J., and Wang, L. (2019). Hybrid Energy Sharing for Multiple Microgrids in an Integrated Heat-Electricity Energy System. *IEEE Trans. Sustain. Energ.* 10 (3), 1139–1151. doi:10.1109/TSTE.2018.2861986

Luo, Z., Gu, W., Wu, Z., Wang, Z., and Tang, Y. (2018). A Robust Optimization Method for Energy Management of CCHP Microgrid. *J. Mod. Power Syst. Clean. Energ.* 6 (1), 132–144. doi:10.1007/s40565-017-0290-3

Ma, T., Wu, J., Hao, L., Lee, W.-J., Yan, H., and Li, D. (2018). The Optimal Structure Planning and Energy Management Strategies of Smart Multi Energy Systems. *Energy.* 160, 122–141. doi:10.1016/j.energy.2018.06.198

Nicolosi, F. F., Alberizzi, J. C., Caligiuri, C., and Renzi, M. (2021). Unit Commitment Optimization of a Micro-grid with a MILP Algorithm: Role of the Emissions, Bio-Fuels and Power Generation Technology. *Energ. Rep.* 7, 8639–8651. doi:10.1016/j.egyr.2021.04.020

Qu, M., Ding, T., Jia, W., Zhu, S., Yang, Y., and Blaabjerg, F. (2021). Distributed Optimal Control of Energy Hubs for Micro-integrated Energy Systems. *IEEE Trans. Syst. Man. Cybern, Syst.* 51 (4), 2145–2158. doi:10.1109/TSMC.2020.3012113

Shen, F., Zhao, L., Du, W., Zhong, W., and Qian, F. (2020). Large-scale Industrial Energy Systems Optimization under Uncertainty: A Data-Driven Robust Optimization Approach. *Appl. Energ.* 259, 114199. doi:10.1016/j.apenergy.2019.114199

Sirvent, M., Kanelakis, N., Geissler, B., and Biskas, P. (2017). Linearized Model for Optimization of Coupled Electricity and Natural Gas Systems. *J. Mod. Power Syst. Clean. Energ.* 5 (3), 364–374. doi:10.1007/s40565-017-0275-2

Sun, Y., Zhang, B., Ge, L., Sidrov, D., Wang, J., and Xu, Z. (2020). Day-ahead Optimization Schedule for Gas-Electric Integrated Energy System Based on Second-Order Cone Programming. *Csee Jpes.* 6 (1), 142–151. doi:10.17775/CSEEJPES.2019.00860

Wang, D., Zhi, Y., Zhi, Y., Yu, B., Chen, Z., An, Q., et al. (2018). Optimal Coordination Control Strategy of Hybrid Energy Storage Systems for Tie-Line Smoothing Services in Integrated Community Energy Systems. *Csee Jpes.* 4 (4), 408–416. doi:10.17775/CSEEJPES.2017.01050

Wang, Y., Zhang, N., Zhuo, Z., Kang, C., and Kirschen, D. (2018). Mixed-integer Linear Programming-Based Optimal Configuration Planning for Energy Hub: Starting from Scratch. *Appl. Energ.* 210, 1141–1150. doi:10.1016/j.apenergy.2017.08.114

Wang, L., Hou, C., Ye, B., Wang, X., Yin, C., and Cong, H. (2021). Optimal Operation Analysis of Integrated Community Energy System Considering the Uncertainty of Demand Response. *IEEE Trans. Power Syst.* 36 (4), 3681–3691. doi:10.1109/TPWRS.2021.3051720

Wang, W., Huang, S., Zhang, G., Liu, J., and Chen, Z. (2021). Optimal Operation of an Integrated Electricity-Heat Energy System Considering Flexible Resources Dispatch for Renewable Integration. *J. Mod. Power Syst. Cle.* 9 (4), 699–710. doi:10.35833/MPCE.2020.000917

Wang, Y., Li, R., Dong, H., Ma, Y., Yang, J., Zhang, F., et al. (2019). Capacity Planning and Optimization of Business Park-Level Integrated Energy System

Based on Investment Constraints. *Energy*. 189, 116345. doi:10.1016/j.energy.2019.116345

Wu, J., Li, B., Chen, J., Ding, Y., Lou, Q., Xing, X., et al. (2021). Multi-objective Optimal Scheduling of Offshore Micro Integrated Energy System Considering Natural Gas Emission. *Int. J. Electr. Power Energ. Syst.* 125, 106535. doi:10.1016/j.ijepes.2020.106535

Xiao, H., Pei, W., Pei, W., Dong, Z., and Kong, L. (2018). Bi-level Planning for Integrated Energy Systems Incorporating Demand Response and Energy Storage under Uncertain Environments Using Novel Metamodel. *Csee Jpes*. 4 (2), 155–167. doi:10.17775/CSEEJPES.2017.01260

Yang, J., Zhang, N., Kang, C., and Xia, Q. (2018). Effect of Natural Gas Flow Dynamics in Robust Generation Scheduling under Wind Uncertainty. *IEEE Trans. Power Syst.* 33 (2), 2087–2097. doi:10.1109/TPWRS.2017.2733222

Zhang, S., Gu, W., Yao, S., Lu, S., Zhou, S., and Wu, Z. (2021). Partitional Decoupling Method for Fast Calculation of Energy Flow in a Large-Scale Heat and Electricity Integrated Energy System. *IEEE Trans. Sustain. Energ.* 12 (1), 501–513. doi:10.1109/TSTE.2020.3008189

Zhao, B., Conejo, A. J., and Sioshansi, R. (2018). Coordinated Expansion Planning of Natural Gas and Electric Power Systems. *IEEE Trans. Power Syst.* 33 (3), 3064–3075. doi:10.1109/TPWRS.2017.2759198

Zhou, Z., Liu, P., Li, Z., and Ni, W. (2013). An Engineering Approach to the Optimal Design of Distributed Energy Systems in China. *Appl. Therm. Eng.* 53 (2), 387–396. doi:10.1016/j.applthermaleng.2012.01.067

Conflict of Interest: The authors declare that the research was conducted in the absence of any commercial or financial relationships that could be construed as a potential conflict of interest.

Publisher's Note: All claims expressed in this article are solely those of the authors and do not necessarily represent those of their affiliated organizations, or those of the publisher, the editors, and the reviewers. Any product that may be evaluated in this article, or claim that may be made by its manufacturer, is not guaranteed or endorsed by the publisher.

GLOSSARY

Acronyms

AHP Analytic hierarchy process

AR Absorption refrigerator

BD Benders decomposition

CHP Combined heating and power

DRE Distributed renewable energy

EES Electric energy storage

ER Electric refrigerator

FRs Flexible resources

GT Gas turbine

HP Heat pump

HES Heat energy storage

IEHES Integrated electricity-heat energy system

MEFCS Multi-energy flow coupling system

OCCS Optimal coordination control strategy

PV Photovoltaic

SOCP Second-order cone programming

WHB Waste heat boiler

WT Wind turbine

Parameters

$\eta_{\mathbf{w}}$ Wind energy utilization efficiency

r Blade radius

ρ Air density

$P_{\mathbf{test}}$ Test power under standard conditions

$L_{\mathbf{test}}$ Test light intensity under standard conditions

$\boldsymbol{K}$ Power temperature coefficient

$\eta^{\mathbf{P,CHP}}$ Power generation efficiency

$\eta^{\mathbf{H,CHP}}$ Heating efficiency of cogeneration units

$L_{\mathbf{gas}}$ Low calorific value of natural gas

$\eta_{\mathbf{GT}}$ Power generation efficiency

$\eta_{\mathbf{l}}$ Loss rate of gas turbine

$\eta_{\mathbf{WHB}}$ Recovery efficiency of waste heat boiler

$\eta_{\mathbf{HP}}$ Conversion efficiency of the heat pump

$\eta_{\mathbf{EC}}$ η_{AC} Conversion efficiency of electric chiller and absorption chiller

$\eta_0^{\mathbf{AC}}$ Conversion efficiency of absorption chiller

$a_{\mathbf{AC}}$ b_{AC} c_{AC} Refrigeration coefficients of absorption chiller

$\beta_{\mathbf{AC}}$ Load rate

$\alpha_{\mathbf{gas}}$ α_{grid} CO_2 emission coefficient corresponding to the combustion of natural gas and the consumption of electric energy

$c_{\mathbf{grid}}$ c_{gas} Cost coefficients corresponding to the electric energy and natural gas consumed by the system

$\boldsymbol{N}$ Total amount of equipment

W_{PL} W_{HL} W_{CL} Total load of the system in a day

ζ Network loss rate of transmission line

CR Consistency proportion

CI Consistency index

RI Average random consistency index

Variables

$P_t^{\mathbf{WT}}$ Wind turbine generation power in period t

v_t Air velocity in period t

$P_t^{\mathbf{PV}}$ Output power of photovoltaic equipment in period t

$L_t^{\mathbf{ac}}$ Light intensity in period t

$\theta_t^{\mathbf{s}}$ Solar panel temperature in period t

$\theta_t^{\mathbf{r}}$ Reference temperature in period t

$\theta_t^{\mathbf{out}}$ External ambient temperature in period t

R_t Solar radiation intensity in period t

$P_t^{\mathbf{CHP}}$ Electric power consumed by internal cogeneration unit in period t

$H_t^{\mathbf{CHP}}$ Thermal power consumed by the internal cogeneration unit in period t

$G_t^{\mathbf{CHP}}$ Gas power consumed by the internal cogeneration unit in period t

$P_t^{\mathbf{GT}}$ Gas turbine generation power in period t

$H_t^{\mathbf{GT}}$ Flue gas waste heat power in period t

$V_t^{\mathbf{gas}}$ Natural gas consumption during in period t

$H_t^{\mathbf{WHB}}$ Heat recovery power of the waste heat boiler in period t

$H_t^{\mathbf{HP}}$ Heat energy generated of the ground source heat pump in period t

$P_t^{\mathbf{HP}}$ Electric energy consumed of the ground source heat pump in period t

$C_t^{\mathbf{EC}}$ Cool power generated of EC in period t

$C_t^{\mathbf{AC}}$ Cool power generated of AC in period t

$P_t^{\mathbf{EC}}$ Electric energy consumed of the electric chiller in period t

$H_t^{\mathbf{AC}}$ Heat energy consumed of the absorption chiller in period t

$E_{i,t}$ Energy storage of energy storage equipment i in period tEnergy storage of equipment i in period t

$P_{i,t}^{\mathbf{c}}$ $P_{i,t}^{\mathrm{d}}$ Charging power and discharging power of energy storage equipment i in period t

$O_{i,t}$ Output power of equipment i in period t

$\bar{P}_i^{\mathbf{c}}$ $\bar{P}_i^{\mathrm{d}}$ Upper limit of the charging and discharging power of energy storage equipment i

$E_{i,t}$ Energy storage of energy storage equipment i in period tEnergy storage of equipment i in period t

σ_i Consumption rate of energy storage equipment i

$c_i^{\mathbf{ma}}$ Maintenance cost of equipment i

P_i Rated capacity of equipment i

$\bar{\mu}_i$ $\underline{\mu_i}$ Upper and lower limits of the charging and discharging state of the energy storage equipment i

S_1 S_2 Membership function of a very small target and maximum target

F_i ith objective function

$F_{i,\min}$ $F_{i,\max}$ Minimum and maximum of the *i*th objective function

η_i^c η_i^d Charging efficiency and discharging efficiency of energy storage equipment *i*

$\lambda_{\max}$ Maximum eigenvalue

p_i Characteristic specific gravity of the *i*th target

H_i Entropy of the *i*th target

S_i Membership function of the *i*th objective

x State variable

$h(x)$ Equality constraint

$g(x)$ Inequality constraint

$g_{\max}$ $g_{\min}$ Upper and lower bounds of inequality

$\hat{g}(x)$ Generalized inequality constraints

$\hat{g}_{\max}$ Generalized upper bounds

frontiers | Frontiers in Energy Research

ORIGINAL RESEARCH
published: 19 May 2022
doi: 10.3389/fenrg.2022.920441

An Optimal Scheduling Strategy for Integrated Energy Systems Using Demand Response

Shunfu Lin, Mengchen Lin, Yunwei Shen and Dongdong Li*

School of Electrical Engineering, Shanghai University of Electric Power, Shanghai, China

With the development of power-to-gas (P2G) technology and demand-response (DR) technology, new ideas have been proposed for research into the scheduling strategy for integrated energy systems (IER). Focusing on wind power consumption, this paper proposes a day-ahead scheduling strategy for IER with P2G equipment, taking into consideration DR. On the energy consumption side, a demand elasticity matrix is introduced to describe the user's participation in DR. On the energy supply side, P2G equipment is introduced to improve the coupling of electricity and natural gas, and scenario generation and reduction techniques are introduced to describe the uncertainty of renewable energy output. The maximum net income of the IER is set as the objective function. The optimal scheduling scheme of the system was obtained by solving the scheduling model. The results indicate that the proposed strategy outperforms the traditional operation and can achieve peak cutting and valley filling, maximize the net income of the IER operators, promote the consumption of renewable energy and improve the energy utilization rate of the system.

Keywords: integrated energy system, optimal scheduling strategy, demand response, wind power consumption, scenario generation and reduction

OPEN ACCESS

Edited by:
Qingxin Shi,
North China Electric Power University, China

Reviewed by:
Buxin She,
The University of Tennessee, United States
Xiaofei Wang,
The University of Tennessee, United States

****Correspondence:***
Yunwei Shen
ywshen@shiep.edu.cn

Specialty section:
This article was submitted to Smart Grids, a section of the journal Frontiers in Energy Research

Received: *14 April 2022*
Accepted: *29 April 2022*
Published: *19 May 2022*

Citation:
Lin S, Lin M, Shen Y and Li D (2022) An Optimal Scheduling Strategy for Integrated Energy Systems Using Demand Response. Front. Energy Res. 10:920441. doi: 10.3389/fenrg.2022.920441

1 INTRODUCTION

According to the latest report of the National Energy Administration, the proportion of renewable energy in China has increased significantly, but the accompanying problem of renewable energy consumption has not been solved. The main goal of the new integrated energy system (IES) is to improve energy utilization (Yang et al., 2019). At present, it is important to achieve multi-energy complementarity and improve system flexibility and energy utilization. Determining the optimal scheduling strategy of the IES has become crucial. The IES involves many devices, and the operation of different subsystems varies greatly. The high penetration of renewable energy increases the difficulty of optimizing system scheduling. Taking into account as many factors as possible to develop an economic, efficient and environmentally friendly scheduling scheme has been a popular line of research in recent years. Power-to-gas (P2G) and demand-response (DR) technology is becoming increasingly mature, which brings new ideas for the research into scheduling strategies for the IES.

At present, most of the research on the optimal scheduling of the IES assumes an economic perspective. The system scheduling strategy model is established with the goal of minimum cost or maximum benefit, and the output of each unit under this goal is obtained by solving the model. A large number of achievements have been made in the research into optimal dispatching of the IES (Gu et al., 2017a; Ran et al., 2017). The researchers in (Hongjie et al., 2015) describe the

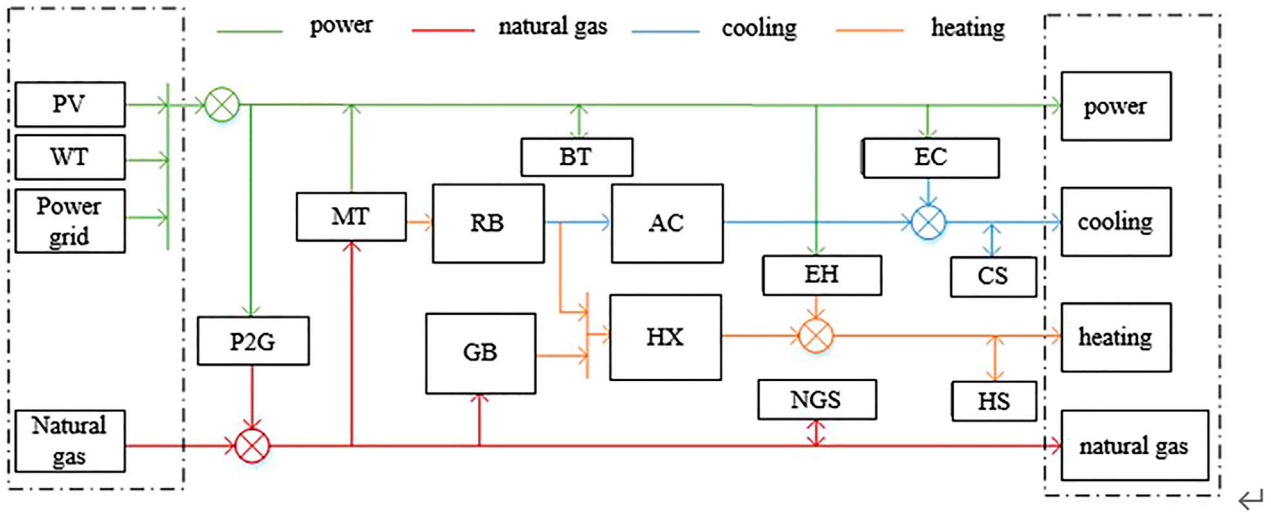

FIGURE 1 | The integrated energy system framework.

effect of peak cutting and valley filling by the square of the net load change rate in adjacent periods. The economic conversion coefficient is introduced into the economic objective function of comprehensive cost. This strategy was shown to be effective in stabilizing net load fluctuation and improving consumption capacity. Studies (Zhinong et al., 2017; Lin et al., 2019; Khani and Farag, 2018), respectively, introduce the penalty mechanism into the objective function and constraint condition to coordinate the maximum wind power consumption and the minimum low-carbon economic cost. In (Zhinong et al., 2017), an improved successive linearization method is proposed, which speeds up the convergence effect and improves the solution efficiency. In (Khani and Farag, 2018), the utilization rate of energy is improved. Studies (Liu et al., 2020; Ran et al., 2017) introduce the concept of an energy hub and establish an optimization model taking into account the characteristics of the conversion between electricity, gas and thermal energy. In (Liu et al., 2020), a day-to-day optimal economic dispatching model is established to minimize the operation cost of the micro-energy network. In (Ran et al., 2017) a two-tier optimization model is established that not only considers the comprehensive energy cost, but also takes into account the energy efficiency, which plays a positive role in the economic operation and renewable energy consumption.

The studies mentioned above, however, do not consider the impact of DR on the scheduling. In the scheduling of the IES, DR technology has been vigorously promoted (Gu et al., 2017b; Nolan and Malley, 2015). Many scholars have taken into account DR in their research into the scheduling strategy of the IES (Wang et al., 2018; YangBotterud et al., 2020; Zhang et al., 2021). The scheduling model in (Wang et al., 2018; Huang et al., 2022) takes into account the dynamic characteristics of the water temperature of the heating pipeline, transmission delay and loss, and the conversion characteristics of electric heating demand, which can achieve the time translation of the power and heat supply-and-demand curve and the optimal substitution between power and heat energy. In (Cui et al., 2020) a ground-source heat pump is introduced and a double-layer optimization model of source-load coordination is proposed. The upper model adopts price-based DR to adjust electricity load, and introduces user satisfaction factor. The lower model adopts incentive DR to adjust heat load. The researchers in (HongZhong et al., 2019) proposed the concept of generalized energy storage resources in the system, making full use of energy coupling and complementarity. By integrating and using generalized energy storage resources, the operation cost can be reduced and the consumption level can be improved while ensuring the safe operation of the system. Studies (Ding et al., 2021; Zhang et al., 2021) propose a comprehensive DR model for electricity, gas and heat loads to strengthen the coupling relationship between the three, and realize the horizontal time transfer and vertical substitution of the three loads. The studies described here, however, do not take into account the impact of the uncertainty of renewable energy output on dispatching.

To overcome these problems, this paper proposes a day-ahead scheduling strategy for IES that takes into account DR. Based on the traditional scheduling model, it makes the following additions:

(1) On the energy consumption side, a demand elasticity matrix is introduced to describe the user's participation in the DR;
(2) On the energy supply side, P2G equipment is introduced to improve the electrical pneumatic coupling of the IES;
(3) Scenario generation and reduction techniques are introduced to describe the uncertainty of renewable energy output.

The maximum net income of the IES operators is set as the objective function. The optimal scheduling scheme of the system

TABLE 1 | Description of the four cases.

	P2G	Demand response	Uncertainty of new power output
Case 1	Not considered	Not considered	Not considered
Case 2	Considered	Not considered	Not considered
Case 3	Considered	Considered	Not considered
Case 4	Considered	Considered	Considered

TABLE 2 | The economic parameters of the IER and power grid.

Parameter/(¥/kWh)	Value	Parameter/(¥/kWh)	Value
R_{P2G}	0.28	c_{mt}	0.025
c_{pv}	0.025	c_{wt}	0.029
c_{bt}	0.4	c_{ng}	1.1
c_{hs}	0.4	c_{cs}	1.1

TABLE 3 | The operating parameters of the equipment in the IER.

Parameter/kW	Value	Parameter	Value
Gas boiler capacity	500	COP_{AC}	1.2
Micro-turbine capacity	500	COP_{MT}	0.35
Heat recovery unit capacity	90	COP_{REC}	0.35
Electrical chiller capacity	200	COP_{GB}	0.9
Electrical heater capacity	200	COP_{EC}	3
Absorption chiller capacity	90	COP_{EH}	3
Power to gas capacity	300	COP_{P2G}	0.6

is obtained by solving the scheduling model. The results indicate that the proposed strategy outperforms the traditional operation and can achieve peak cutting and valley filling, maximize the net income of the system operators, promote the consumption of renewable energy and improve the energy utilization rate of the system.

2 INTEGRATED ENERGY SYSTEM ARCHITECTURE

In this paper, the IES includes the following units: wind turbine (WT), photovoltaic (PV) unit, micro-turbine (MT), heat recovery unit (REC), gas boiler (GB), electric refrigeration (EC) unit, electrical boiler (EH), absorption refrigerator (AC), P2G equipment, heat exchanger (HX), battery (BT), natural gas storage tank (NGS), cold storage tank (CS) and heat storage tank (HS).

The IES framework is shown in **Figure 1**. The green line represents the flow direction of electric energy; the red lines represent the direction of natural gas transmission; and the blue and yellow lines represent the direction of cold and heat transfer, respectively. The left virtual box represents the energy source of the system, including distributed renewable energy, an external power grid and a natural gas network. The right virtual box represents the user's load, including electricity load, natural gas load, cold load and heat load. Electricity can be converted into natural gas through P2G equipment. The electric refrigeration unit and electrical boiler convert electric energy into cold energy and heat energy, respectively. The micro-turbine consumes natural gas to generate electricity. Heat energy produced in the process is recovered by the heat recovery unit and part of the heat is supplied to the heat exchanger. The remaining heat is supplied to the absorption refrigerator to convert into cold energy. The gas boiler consumes natural gas to produce heat. When energy is abundant, energy storage devices are used to store energy for occasional needs.

3 SCHEDULING MODEL OF THE INTEGRATED ENERGY SYSTEM

3.1 Demand Response

The price-based DR uses time-of-use electricity price to guide users to adjust load demand to achieve peak cutting and valley filling, thereby improving the electricity load characteristic. In the case of time-of-use electricity price, the change of load is expressed by the price elasticity matrix, which is based on the price elasticity coefficient of electricity. The elasticity coefficient is the ratio of the rate of change in demand to the rate of price change:

$$\varepsilon_{ij} = \frac{\Delta Q_j}{Q_j} \Big/ \frac{\Delta P_j}{P_j} \tag{1}$$

where Q_j and ΔQ_j represent electricity demand and its adjustment, respectively; and P_j and ΔP_j represent electricity price and its adjustment, respectively. If $i = j$, ε_{ij} denotes the coefficient of self-elasticity, otherwise the cross-elastic coefficient.

According to the price elasticity coefficient, the change of electricity load expressed by the price elasticity matrix can be obtained as follows:

$$\begin{bmatrix} \Delta Q_1/Q_1 \\ \Delta Q_2/Q_2 \\ \vdots \\ \Delta Q_n/Q_n \end{bmatrix} = \begin{bmatrix} \varepsilon_{11} & \varepsilon_{12} & \dots & \varepsilon_{1n} \\ \varepsilon_{21} & \varepsilon_{22} & \dots & \varepsilon_{2n} \\ \vdots & \vdots & & \vdots \\ \varepsilon_{n1} & \varepsilon_{n2} & \dots & \varepsilon_{nn} \end{bmatrix} \bullet \begin{bmatrix} \Delta P_1/P_1 \\ \Delta P_2/P_2 \\ \vdots \\ \Delta P_n/P_n \end{bmatrix} \tag{2}$$

3.2 Uncertainty of Renewable Energy Output

Renewable energy output is affected by many factors and presents uncertainty. To reduce the impact of uncertainty on the scheduling of the IES, this paper uses an autoregressive moving average model to generate scenarios of renewable energy output. The autoregressive moving average model is as follows:

$$P_t = \sum_{i=1}^{R} a_i P_{t-1} + e_i - \sum_{i=1}^{M} b_i P_{t-1} \tag{3}$$

where a_i and b_i represent the autoregressive coefficient and moving average coefficient, respectively; R and M represent

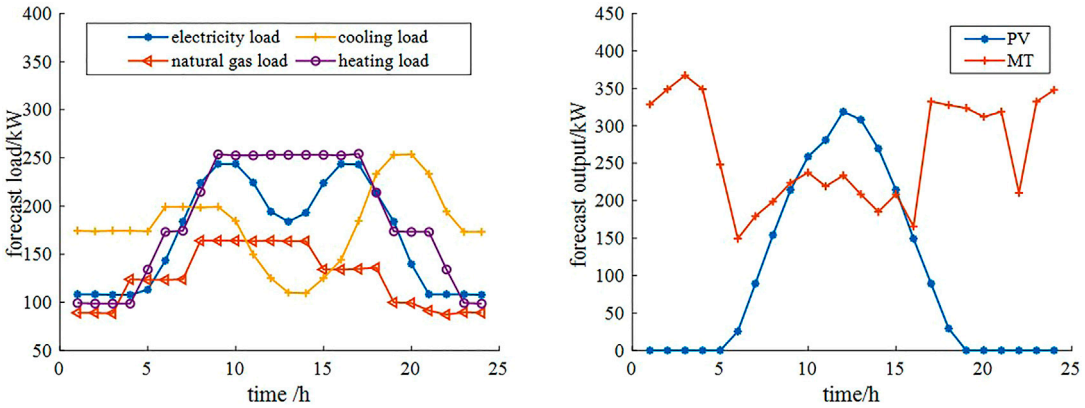

FIGURE 2 | The load curves (left) and the wind turbine and photovoltaic output curves (right).

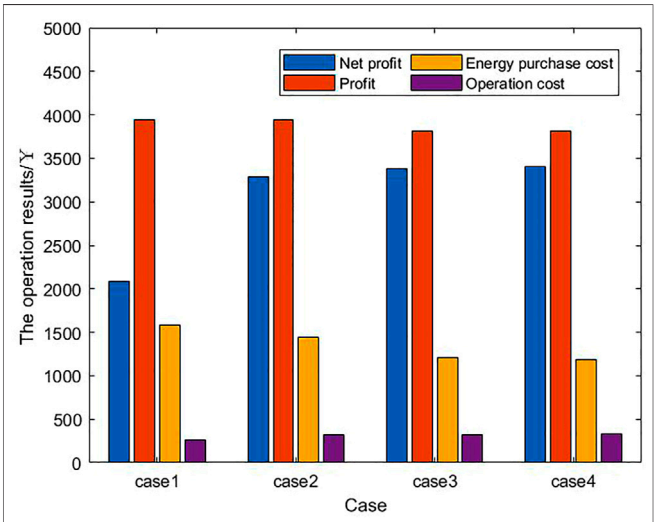

FIGURE 3 | Operation results of the four cases.

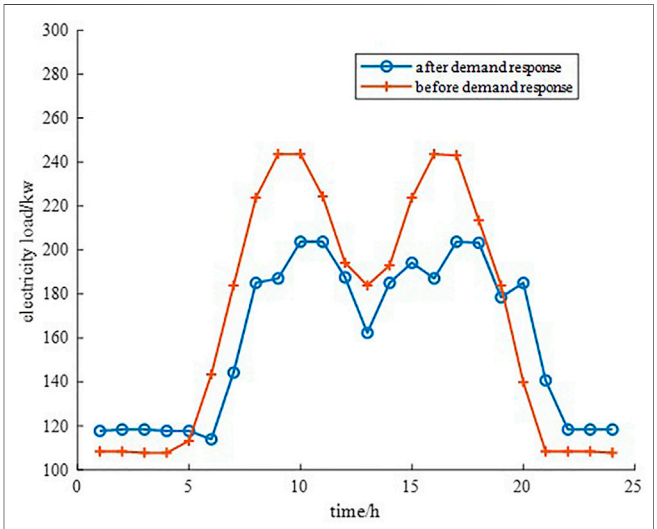

FIGURE 4 | Load curves after the demand response in Case 4.

the autoregressive order and moving average order, respectively; and e_i represents independent white noise and follows the normal distribution.

The steps of scenario reduction are as follows：

Step 1: Calculate the geometric distance between each pair of scenes in the scene set S1; Step 2: Calculate the sum of the distances between each scene and other scenes, find the scene with the smallest value and record it as C1; Step 3: Merge the scenes C1 and C2, which is closest to C1 by geometric distance, into a new scene and record it as scene C3. The probability of scene C3 is the sum of the probabilities of scenes C1 and C2; Step 4: Delete scenes C1 and C2, then add scene C3 to the scene set S1 to generate a new scene set and record it as S2.

The new scene set S2 has one fewer scene than S1. The operations above are repeated until the number of scenes meets the requirement, and then the scene reduction can be realized.

3.3 Objective Function

The net income of the operator of the IES includes the revenue from the sale of energy, the cost of purchasing energy and the operation cost of the equipment. The formula is as follows:

$$F_{\mathrm{UP}} = \max\left(R_{\mathrm{E}} - C_{\mathrm{BUY}} - C_{\mathrm{OP}}\right) \tag{4}$$

where R_{E} represents the revenue from the sale of energy to users; C_{BUY} represents the cost to the operator of purchasing energy; and C_{OP} represents the operation cost of the equipment. **Eqs 5–7** provide more details:

$$R_{\mathrm{E}} = \sum_{t=1}^{T}\left[R_{\mathrm{DL}}^{t}P_{\mathrm{DL}}^{t} + R_{\mathrm{GL}}^{t}Q_{\mathrm{GL}}^{t} + R_{\mathrm{p2g}}Q_{\mathrm{P2G}}^{t}\right] \tag{5}$$

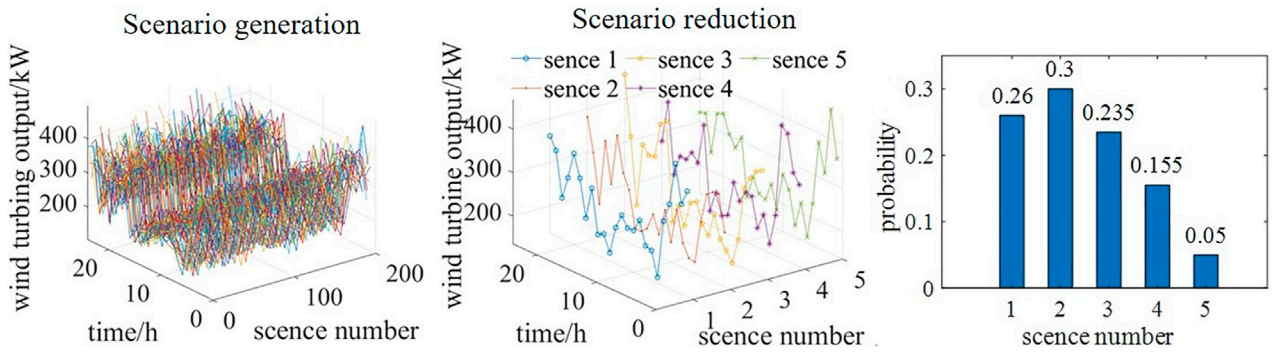

FIGURE 5 | Scenario generation and reduction of the wind turbine output curve in Case 4.

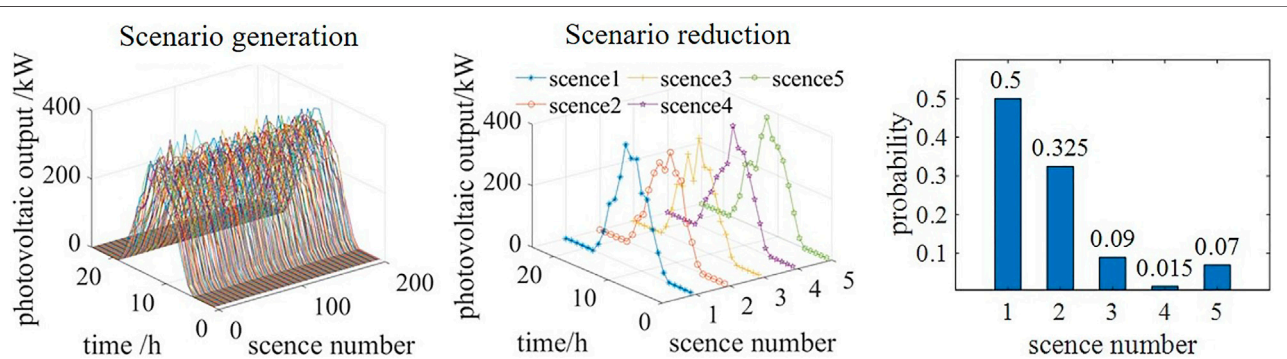

FIGURE 6 | Scenario generation and reduction of the photovoltaic unit output curve in Case 4.

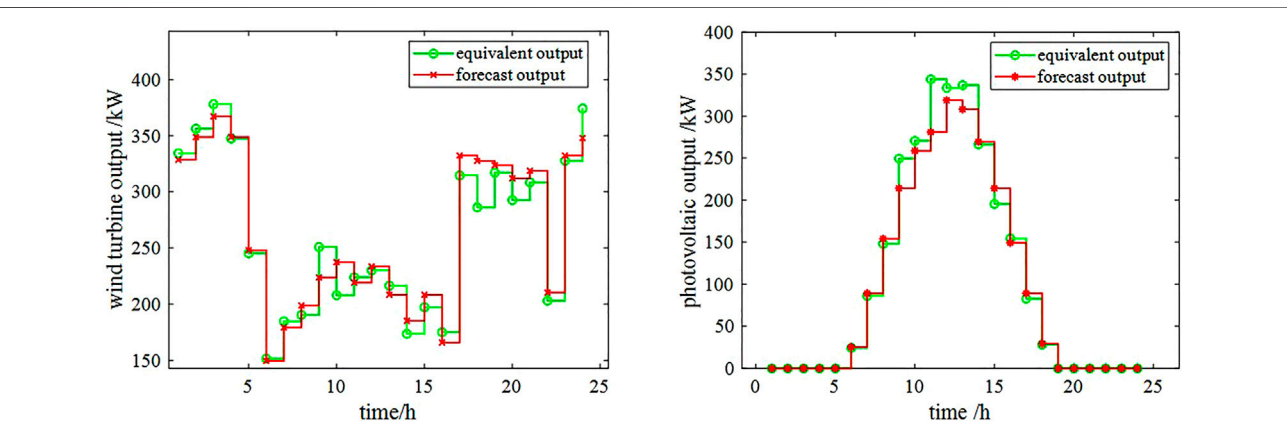

FIGURE 7 | Equivalent wind turbine (left) and photovoltaic unit (right) output curves in Case 4.

where R_{DL} and R_{GL} represent the coefficients of return on electricity and gas sales, respectively; P^t_{DL} and Q^t_{GL} represent the amount of electricity and gas purchased by consumers at time t, respectively; R_{p2g} represents the coefficients of P2G equipment; and Q^t_{P2G} represents the amount of gas converted by the P2G equipment.

$$C_{BUY} = \sum_{t=1}^{T} \left[c^t_{buy,dl} P^t_{PBUY} + c^t_{buy,gl} Q^t_{NGBUY} \right] \tag{6}$$

where $c^t_{buy,dl}$ and $c^t_{buy,gl}$ represent the unit price of electricity and gas purchased by the system operator at time t, respectively; and

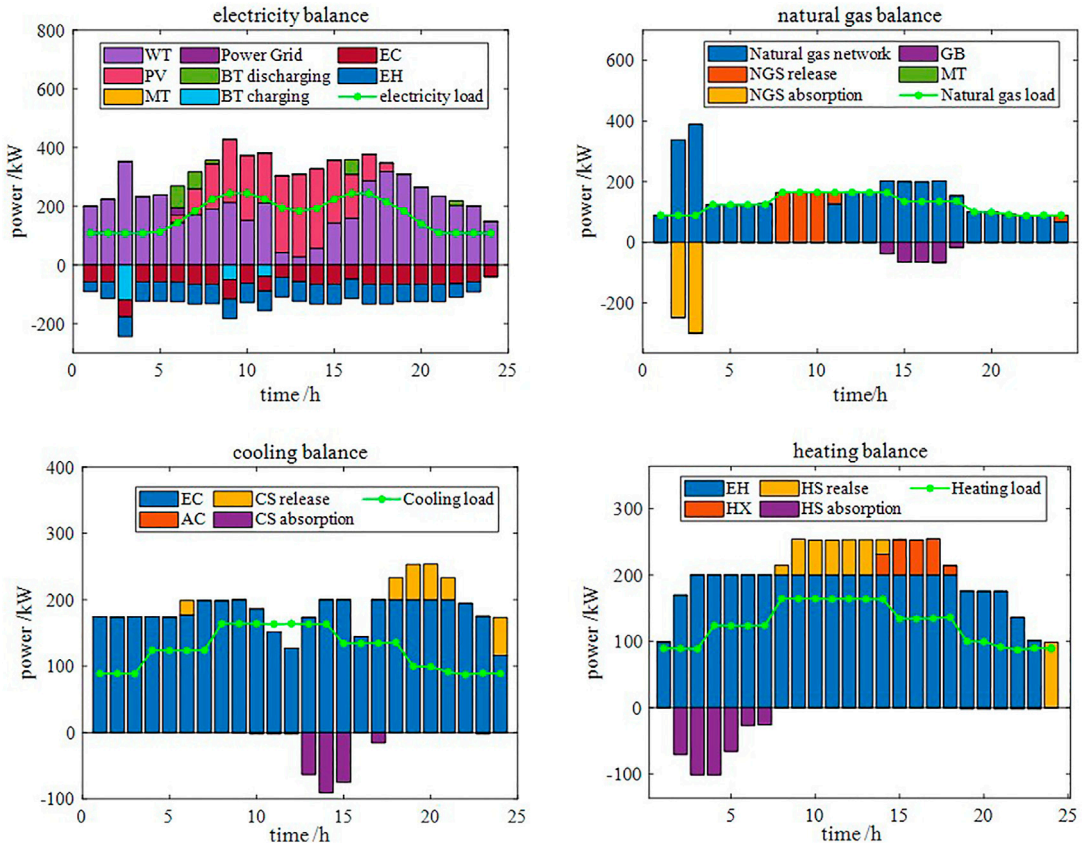

FIGURE 8 | Power balance in Case 1.

P^t_{PBUY} and Q^t_{NGBUY} represent the amount of electricity and gas purchased by system operators at time t, respectively.

$$C_{\mathrm{OP}} = \sum_{t=1}^{T} \begin{bmatrix} c_{\mathrm{pv}} P^t_{\mathrm{PV}} + c_{\mathrm{wt}} P^t_{\mathrm{WT}} + c_{\mathrm{mt}} P^t_{\mathrm{MT}} \\ + c_{\mathrm{bt}} \left(P^t_{\mathrm{BT\_D}} + \left| P^t_{\mathrm{BT\_C}} \right| \right) \\ + c_{\mathrm{ng}} \left(Q^t_{\mathrm{NG\_D}} + \left| Q^t_{\mathrm{NG\_C}} \right| \right) \\ + c_{\mathrm{cs}} \left(H^t_{\mathrm{CS\_D}} + \left| H^t_{\mathrm{CS\_C}} \right| \right) \\ + c_{\mathrm{hs}} \left(H^t_{\mathrm{HS\_D}} + \left| H^t_{\mathrm{HS\_C}} \right| \right) \end{bmatrix} \tag{7}$$

where $c_{\mathrm{pv/wt/mt/bt/ng/cs/hs}}$ represent the coefficients of the operating costs of the equipment corresponding to the subscript; P^t_{MT} represents the micro-turbine output at time t; P^t_{PV} and P^t_{WT} represent the photovoltaic and wind turbine output at time t, respectively; and $P^t_{\mathrm{BT/NG/CS/HS\_C}}$ represent the charging power of energy storage equipment corresponding to the subscript; and $P^t_{\mathrm{BT/NG/CS/HS\_D}}$ represent the discharging power of energy storage equipment corresponding to the subscript.

3.4 Constraint Conditions

3.4.1 Constraints on Energy Supply Equipment

The energy supply equipment includes a gas boiler and cogeneration device. The operation of the energy supply equipment must meet certain equation constraints and inequality constraints:

$$\begin{cases} H_{\mathrm{GB\_EX}} = COP_{\mathrm{GB}} Q_{\mathrm{GB\_EN}} \\ P_{\mathrm{MT}} = \omega_{\mathrm{MT}} H_{\mathrm{REC\_EX}} \\ H_{\mathrm{REC\_EX}} = COP_{\mathrm{REC}} H_{\mathrm{REC\_EN}} \\ P_{\mathrm{MT}} + H_{\mathrm{REC\_EN}} = COP_{\mathrm{MT}} Q_{\mathrm{MT\_EN}} \end{cases} \tag{8}$$

$$\begin{cases} P_{\mathrm{MT\_MIN}} \le P_{\mathrm{MT}} \le P_{\mathrm{MT\_MAX}} \\ -P_{\mathrm{MT\_D}} \le P^{t+1}_{\mathrm{MT}} - P^t_{\mathrm{MT}} \le P_{\mathrm{MT\_U}} \\ Q_{\mathrm{REC\_MIN}} \le Q_{\mathrm{REC\_EX}} \le Q_{\mathrm{REC\_MAX}} \\ Q_{\mathrm{GB\_MIN}} \le Q_{\mathrm{GB\_EX}} \le Q_{\mathrm{GB\_MAX}} \\ -P_{\mathrm{GB\_D}} \le P^{t+1}_{\mathrm{GB}} - P^t_{\mathrm{GB}} \le P_{\mathrm{GB\_U}} \end{cases} \tag{9}$$

where COP_{GB} represents the conversion efficiency of the gas boiler; ω_{MT} represents the ratio of the generating power and the heating power of the cogeneration device; COP_{REC} represents the conversion efficiency of the heat recovery unit; and COP_{MT} represents the conversion efficiency of the micro-turbine. As shown in **Eq. 9**, the output power of the micro-turbine and gas turbine meets the upper and lower limit constraints and climbing constraints. The output power of the heat recovery unit meets the upper and lower limit constraints.

3.4.2 Constraints on Energy Conversion Equipment

The energy conversion equipment includes an electrical chiller, an absorption chiller, an electrical heater and a P2G device. The operation of the energy conversion equipment must meet certain equation constraints and inequality constraints.

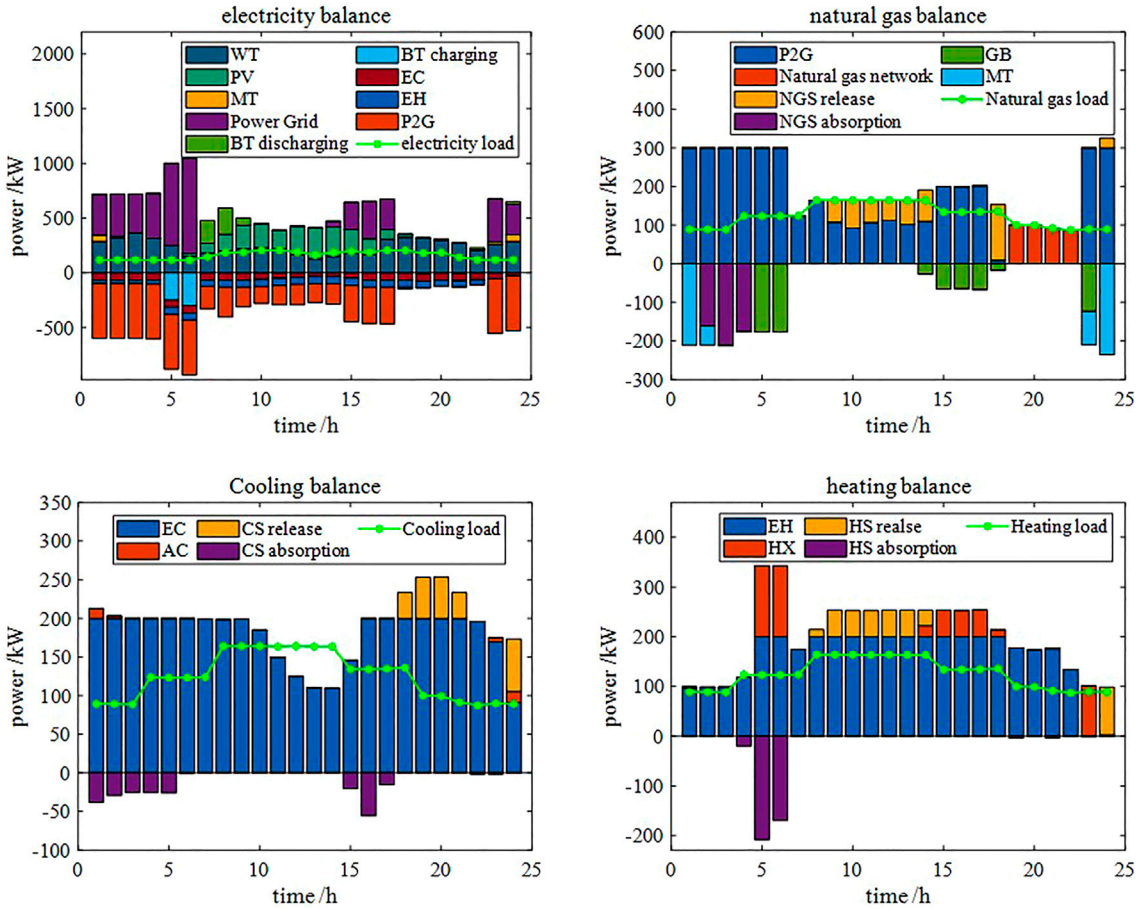

FIGURE 9 | Power balance in Case 4.

$$\begin{cases} H_{\mathrm{EC\_EX}} = COP_{\mathrm{EC}} P_{\mathrm{EC\_EN}} \\ H_{\mathrm{AC\_EX}} = COP_{\mathrm{AC}} H_{\mathrm{AC\_EN}} \\ H_{\mathrm{EH\_EX}} = COP_{\mathrm{EH}} P_{\mathrm{EH\_EN}} \\ Q_{\mathrm{P2G\_EX}} = COP_{\mathrm{P2G}} P_{\mathrm{P2G\_EN}} \end{cases} \tag{10}$$

$$\begin{cases} H_{\mathrm{EC\_MIN}} \le H_{\mathrm{EC\_EX}} \le H_{\mathrm{EC\_MAX}} \\ H_{\mathrm{EH\_MIN}} \le H_{\mathrm{EH\_EX}} \le H_{\mathrm{EH\_MAX}} \\ H_{\mathrm{AC\_MIN}} \le H_{\mathrm{AC\_EX}} \le H_{\mathrm{AC\_MAX}} \\ Q_{\mathrm{P2G\_MIN}} \le Q_{\mathrm{P2G\_EX}} \le Q_{\mathrm{P2G\_MAX}} \end{cases} \tag{11}$$

where $COP_{\mathrm{EC/EH/AC/P2G}}$ represents the conversion efficiency of the equipment corresponding to the subscript. As shown in **Eq. 11**, the output power of the electrical chiller, electrical heater, absorption chiller and P2G device meet the upper and lower limit constraints.

3.4.3 Constraints on the Battery

The operating condition of battery can be expressed by the stored energy state. The mathematical model of the battery is as follows:

$$SOC_{\mathrm{BT}}^{t} = SOC_{\mathrm{BT}}^{t-1} + \left[\eta_{\mathrm{bt,c}} P_{\mathrm{BT\_C}}^{t} - P_{\mathrm{BT\_D}}^{t} / \eta_{\mathrm{bt,d}}\right] \Delta t \tag{12}$$

where η_{hs} represents the self-discharge rate of the battery; $\eta_{\mathrm{bt,c}}$ and $\eta_{\mathrm{bt,c}}$ represent the battery charging and discharging efficiency, respectively; $P_{\mathrm{BT\_C}}$ and $P_{\mathrm{BT\_D}}$ represent the battery charging and discharging power, respectively; and SOC_{BT} represents the stored energy state of the battery.

To avoid overcharging and discharging and thus shortening the service life of the battery, the following constraints are met during operation:

$$\begin{cases} X_{\mathrm{bt\_c}} \cdot P_{\mathrm{BT\_C,MIN}} \le P_{\mathrm{BT\_C}} \le X_{\mathrm{bt\_c}} \cdot P_{\mathrm{BT\_C,MAX}} \\ X_{\mathrm{bt\_d}} \cdot P_{\mathrm{BT\_D,MIN}} \le P_{\mathrm{BT\_D}} \le X_{\mathrm{bt\_d}} \cdot P_{\mathrm{BT\_D,MAX}} \\ SOC_{\mathrm{BT\_MIN}} \le SOC_{\mathrm{BT}}^{t} \le SOC_{\mathrm{BT\_MAX}} \\ 0 \le X_{\mathrm{bt\_c}} + X_{\mathrm{bt\_d}} \le 1 \\ \sum_{t=1}^{T} \left(X_{\mathrm{bt\_c}} + X_{\mathrm{bt\_d}}\right) \le N \end{cases} \tag{13}$$

where $X_{\mathrm{bt,c}}$ and $X_{\mathrm{bt,c}}$ are binary variables representing states of charge and discharge, respectively. The output power and the stored energy state of the battery meet the upper and lower limit constraints, respectively. N represents the maximum number of times the battery can be charged and discharged.

3.4.4 Constraints on the Heat Storage Tank

The mathematical model of the heat storage equipment is as follows:

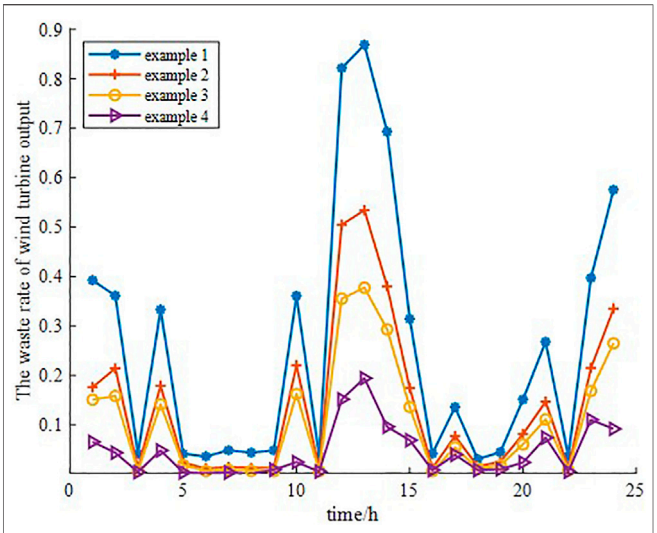

FIGURE 10 | Waste rate of wind turbine output in the four cases.

$$W_{HS}^{t} = W_{HS}^{t-1}\left(1-\eta_{hs}\right) + \left(\eta_{hs,c}Q_{HS\_C}^{t} - Q_{HS\_D}^{t}/\eta_{hs,d}\right)\Delta t \quad (14)$$

where η_{hs} represents the self-discharge rate of the heat storage equipment; $\eta_{hs,c}$ and $\eta_{hs,c}$ represent the efficiency of the heat storage equipment to absorb and release heat energy, respectively; Q_{HS_C} and Q_{HS_D} represent the endothermic and exothermic power of the heat storage equipment, respectively; and W_{HS} represents the state of stored energy in the heat storage equipment.

To avoid excessive absorbing and releasing and thus shortening the service life of the heat storage equipment, the following constraints are met during operation:

$$\begin{cases} X_{hs\_c} \cdot Q_{HS\_C,MIN} \le Q_{HS\_C} \le X_{hs\_c} \cdot Q_{HS\_C,MAX} \\ X_{hs\_d} \cdot Q_{HS\_D,MIN} \le Q_{HS\_D} \le X_{hs\_d} \cdot Q_{HS\_D,MAX} \\ W_{HS,MIN} \le W_{HS} \le W_{HS,MAX} \\ 0 \le X_{hs\_c} + X_{hs\_d} \le 1 \end{cases} \quad (15)$$

where $X_{hs,c}$ and $X_{hs,c}$ are binary variables representing the endothermic and exothermic state of the heat storage equipment, respectively. The output power and the stored energy state of the heat storage equipment meet the upper and lower limit constraints, respectively.

Since the mathematical model and the constraints of the natural gas storage tank and cold storage tank in this paper are the same as those of the equipment heat storage tank, the explanation and description are not repeated here.

3.4.5 Power Balance Constraint Conditions

Power balance of four kinds of energy should always be satisfied during equipment operation. As shown in the following formula:

$$\begin{cases} P_{WT} + P_{PV} + P_{MT} + P_{BT\_D} + P_{DBUY} = P_{BT\_C} + P_{EC\_EN} + P_{EH\_EN} + P_{P2G\_EN} + P_{DL} \\ Q_{P2G\_EX} + Q_{NG\_D} + Q_{GBUY} = Q_{NG\_C} + Q_{MT\_EN} + Q_{GB\_EN} + Q_{GL} \\ H_{EC\_EX} + H_{AC\_EX} + H_{CS\_D} = H_{CS\_C} + H_{CL} \\ H_{EH\_EX} + H_{REC\_EX} + H_{GB\_EX} + H_{HS\_D} = H_{HS\_C} + H_{HL} \end{cases} \quad (16)$$

where $P_{P2G/EC/EH}$ represents the power consumption of the equipment corresponding to the subscript; Q_{MT/GB_EN} represents the natural gas consumption of the equipment corresponding to the subscript; Q_{P2G_EX} represents the natural gas supply of the P2G equipment; $H_{REC/EH/GB\_EX}$ represents the heating power of the equipment corresponding to the subscript; H_{EC/AC_EX} represents the refrigeration power of the equipment corresponding to the subscript; and $H_{CL/HL}$ represents the cooling and heating load.

4 CASE STUDY

For this study, a park-level IES as an example, four cases were set up, as shown in **Table 1**. Case 1 does not take into account any factors. Case 2 takes into account the introduction of P2G equipment. In Case 3, the influence of DR is considered as well as the P2G equipment. Based on Case 3, Case 4 introduces scenario generation and reduction to describe the uncertainty of renewable energy output.

4.1 Basic Data

The economic parameters of the IER and power grid involved in this study are shown in **Table 2**, and the operating parameters of the equipment in the IER are shown in **Table 3** (Gu et al., 2020).

The electricity, natural gas, cooling and heating load curves are shown on the left of **Figure 2**, and the wind turbine and photovoltaic outputs are shown on the right.

4.2 Economic Analysis

The CPLEX solver in GAMS is used to solve the optimal scheduling model. **Figure 3** shows the income and cost details of the IER operators in the four cases.

After the introduction of the P2G equipment (Case 2), the operation cost increased by ¥50.40, the energy purchase cost of the system decreased by ¥139.57 and the net income increased by ¥1,197.13. These changes occurred because the surplus wind turbine and photovoltaic output can be converted into natural gas through the P2G equipment. It can not only solve the problem of renewable energy consumption, but also reduce the cost of natural gas purchased by the system from the natural gas network and increase the net income of the system.

Compared with Case 2, the system revenue of Case 3 decreased by ¥129.72, because the user transferred the load during the period of high electricity price to the period of low electricity price after participating in the DR. The energy purchase cost was reduced by ¥235.58, because after the user participated in the DR, the system achieved peak cutting and valley filling, and the energy supply pressure was reduced. The cost of purchasing electricity and natural gas from the external power grid and the natural gas network was therefore reduced. The operating cost increased by ¥7.56, and the net income increased by ¥89.26. Compared with Case 1, the net income of Case 3 increased by ¥1,286.39.

Compared with Case 3, the energy purchase cost of Case 4 decreased by ¥26.37, the operating cost increased by ¥2 and the net income increased by ¥24.39. These changes occurred because Case 4 takes into consideration the uncertainty of renewable energy output. It can further improve the utilization of renewable

energy and reduce the purchase cost of external energy. Compared with Case 1, the net income of case 4 increased by ¥1,310.78.

The results presented above show that Case 4 (i.e., the proposed strategy), which introduces P2G equipment and takes into account the user's participation in the DR and the uncertainty of wind turbine and photovoltaic output, is economical and greatly improves the net income of the system.

4.3 Scheduling Plan Analysis

Figure 4 shows the load curves after users participate in the DR in Case 4. Affected by the energy price, users transfer part of the load during the period of high electricity prices to the period of electricity prices, which has a positive effect on peak cutting and valley filling.

Figure 5 shows 200 output curves of the wind turbine, five output curves after scenario reduction, and the corresponding probability of five scenes. **Figure 6** shows 200 output curves of the photovoltaic units, five output curves after scenario reduction, and the corresponding probability of the five scenes. The output of the five scenes after scenario reduction is multiplied by their corresponding probabilities, and the equivalent output curve can be obtained by summing the five products. **Figure 7** shows the equivalent wind turbine output curve and the equivalent photovoltaic unit output curve.

By comparing the equivalent output curves with the originally predicted output curves, one can see that there is a certain gap in the output. If the dispatching is carried out according to the original data, there will be an imbalance between supply and demand.

Figure 8 shows the balance of electric power, natural gas power, cold power and thermal power in Case 1, and **Figure 9** shows the same balance in Case 4. By comparing **Figures 8**, **9**, one can see that, in Case 4 (P2G equipment added), the amount of power purchased from the power grid increases during the period of low electricity prices. The electric energy is converted into natural gas to supply gas load through the P2G equipment, and the rest is stored by energy storage equipment for standby. The amount of natural gas purchased from the natural gas network is reduced, and the natural gas load changes from relying only on the natural gas network to mainly on the P2G equipment. Since the natural gas supply is sufficient, the output of the gas boiler and micro-turbine increases. Accordingly, the output of the absorption refrigerator and heat exchanger is also increased.

As the cost coefficient of the photovoltaic unit in this study is lower than that of the wind turbine, all the output of the photovoltaic unit has been preferentially consumed, and only the wind energy is wasted. **Figure 10** shows the waste rate of wind turbine output in the four cases. From Case 1 to Case 4 (i.e., with the introduction of the P2G equipment, DR technology and scenario generation and reduction technology), the waste rate gradually decreases. Case 4, the proposed strategy, has the optimal consumption ability.

5 CONCLUSION

Based on economic principles, this paper introduces a demand elasticity matrix in the price-based DR. According to the predicted wind turbine and photovoltaic unit outputs in the next 24 h, the scenario generation and reduction technology are used to obtain the equivalent wind turbine and photovoltaic unit output curves. P2G equipment is introduced to enhance the electro-pneumatic coupling of the system. The GAMS solver is used to solve the model and obtain the optimal energy purchase plan and scheduling scheme of the energy equipment, the energy conversion equipment and the energy storage equipment. Taking a park-level IES as an example, four cases were set up. Analysis and comparison of the results show that the proposed strategy performs well in achieving peak cutting and valley filling, maximizing the net income of the system operators, promoting the consumption of renewable energy and improving the energy utilization rate of the system.

DATA AVAILABILITY STATEMENT

The original contributions presented in the study are included in the article/Supplementary Material, further inquiries can be directed to the corresponding author.

AUTHOR CONTRIBUTIONS

SL, ML, YS, and DL contributed to conception and design of the study. SL and YS organized the database. ML performed the statistical analysis and wrote the first draft of the manuscript. All authors contributed to manuscript revision, read, and approved the submitted version.

FUNDING

This work was supported in part by the National Natural Science Foundation of China (51977127), in part by the project supported by the Science and Technology Commission of Shanghai Municipality (19020500800), "Shuguang Program" (20SG52) supported by Shanghai Education Development Foundation and Shanghai Municipal Education Commission, "Chen Guang" project supported by Shanghai Municipal Education Commission and Shanghai Education Development Foundation (21CGA64) and Shanghai Sailing Program (No. 21YF1414700) supported by Shanghai Municipal Science and Technology Commission.

REFERENCES

Cui, Y., Jiang, T., and Wuzhi, Z. (2020). Source Load Coordinated Economic Dispatch of Regional Integrated Energy System Considering Wind Power Consumption[J]. *Power Syst. Technol.* 44 (07), 2474–2483.

Ding, Y., Chen, H., and Wu, J. (2021). Multi Objective Optimal Scheduling of Electricity Gas Heat Integrated Energy System Considering Comprehensive Energy Efficiency [J]. *Automation Electr. Power Syst.* 45 (02), 64–73.

Gu, H., Li, Y., and Yu, J. (2020). Bi-level Optimal Low-Carbon Economic Dispatch for an Industrial Park with Consideration of Multi-Energy Price Incentives[J]. *Appl. Energy* 262, 11427. doi:10.1016/j.apenergy.2019.114276

Gu, W., Lu, S., Wu, Z., Zhang, X., Zhou, J., Zhao, B., et al. (2017). Residential CCHP Microgrid with Load Aggregator: Operation Mode, Pricing Strategy and Optimal Dispatch[J]. *Appl. Energy* 205, 173–186. doi:10.1016/j.apenergy.2017.07.045

Gu, W., Wang, J., Lu, S., Loo, Z., and Wu, C. (2017). Optimal Operation for Integrated Energy System Considering Thermal Inertia of District Heating Network and Buildings[J]. *Appl. Energy* 199, 234–246. doi:10.1016/j.apenergy.2017.05.004

Hongjie, J., Wang, D., and Xu, X. (2015). Study on Some Problems of Regional Integrated Energy System [J]. *Automation Electr. Power Syst.* 39 (07), 198–207. doi:10.7500/AEPS20141009011

HongZhong, L., Yujiao, F., and Xiao, B. (2019). Study on Optimal Operation of Regional Integrated Energy System Considering Generalized Energy Storage [J]. *Power Syst. Technol.* 43 (09), 3130–3138.

Huang, Y., Dan, L., and Yan, G. (2022). Day Ahead Optimal Scheduling Strategy of Electric Thermal Integrated Energy System Considering Heat Network Transmission Delay and Heat Storage [J/OL]. *Electr. Meas. Instrum.* 1, 1–9.

Khani, H., and Farag, H. E. Z. (2018). Optimal Day-Ahead Scheduling of Power-To-Gas Energy Storage and Gas Load Management in Wholesale Electricity and Gas Markets. *IEEE Trans. Sustain. Energy* 9 (2), 940–951. doi:10.1109/tste.2017.2767064

Lin, K., Chen, Z., and Zhang, Y. (2019). Wind Power Consumption and Successive Linear Low-Carbon Economic Dispatching of Power Gas Interconnection Network with Power-Gas [J]. *Automation Electr. Power Syst.* 43 (21), 23–33.

Liu, Z., Liu, R., and Ning, L. (2020). Day Ahead Economic Optimal Dispatching Strategy of Micro Energy Network from Power to Gas [J]. *Trans. China Electrotech. Soc.* 35 (S2), 535–543.

Nolan, S., and Malley, M. (2015). Challenges and Barriers to Demand Response Deployment and Evaluation[J]. *Appl. Energy* 152, 1–10. doi:10.1016/j.apenergy.2015.04.083

Ran, H., Qian, A., and Zhu, Y. (2017). Hierarchical Optimal Scheduling of Regional Integrated Energy System Based on Energy Hub [J]. *Electr. Power Autom. Equip.* 37 (06), 171–178.

Wang, W., Yang, L., and Wang, L. (2018). Optimal Dispatching of Electric Thermal Integrated Energy System Considering the Heat Storage Characteristics of Heating Network [J]. *Automation Electr. Power Syst.* 42 (21), 45–52.

Yang, N., Huang, Y., and Dong, B. (2019). Research on Joint Planning Method of Power Natural Gas Integrated Energy System Based on Multi-Agent Game[J]. *Proc. CSEE* 39 (22), 6521–6533.

YangBotterud, J., Zhang, N., Botterud, A., and Kang, C. (2020). On an Equivalent Representation of the Dynamics in District Heating Networks for Combined Electricity-Heat Operation. *IEEE Trans. Power Syst.* 35 (1), 560–570. doi:10.1109/tpwrs.2019.2935748

Zhang, T., Guo, Y., and Li, Y. (2021). Optimal Dispatching of Regional Integrated Energy System Considering the Response of Electrical and Thermal Comprehensive Demand [J]. *Power Syst. Prot. Control* 49 (01), 52–61.

Zhinong, W., Zhang, S., and Sun, G. (2017). Study on Peak Shaving and Valley Filling of Electricity Gas Interconnected Integrated Energy System Considering Electricity to Gas [J]. *Proc. CSEE* 37 (16), 4601–4609+4885.

Conflict of Interest: The authors declare that the research was conducted in the absence of any commercial or financial relationships that could be construed as a potential conflict of interest.

frontiers | Frontiers in Energy Research

ORIGINAL RESEARCH
published: 24 May 2022
doi: 10.3389/fenrg.2022.916996

Multi-Agent Schedule Optimization Method for Regional Energy Internet Considering the Improved Tiered Reward and Punishment Carbon Trading Model

Tianxiang Li[1], *Qian Xiao*[1]*, *Hongjie Jia*[1], *Yunfei Mu*[1], *Xinying Wang*[2], *Wenbiao Lu*[1] and *Tianjiao Pu*[2]

[1]Key Laboratory of Smart Grid of Ministry of Education, Tianjin University, Tianjin, China, [2]China Electric Power Research Institute, Beijing, China

Regional energy internet (REI) contains massive market agents, whose interests and objectives vary from each other. In consequence, it is challenging to stimulate the energy conservation and emissions reduction participation of each agent by the conventional schedule optimization method. This paper proposes a multi-agent schedule optimization method for REI considering the improved tiered reward and punishment carbon trading model. Firstly, the energy flow constraints and device constraints of REI are established. Secondly, to tighten restrictions on carbon emissions, the relative carbon emission is used as the criterion to establish the improved tied reward and punishment carbon trading model. Next, to analyze the real multi-agent game situation in the market, different agents are classified, and the objective functions are defined based on their revenue. Finally, a two-layer algorithm is used to solve the above multi-agent model. Simulation results verify that the proposed method can effectively reduce carbon emissions and significantly enhance the revenue of the region.

Keywords: carbon trading, multi-agent game, regional energy internet, schedule optimization, reward and punishment mechanism

OPEN ACCESS

Edited by:
Qinran Hu,
Southeast University, China

Reviewed by:
Sheng Chen,
Hohai University, China
Jian Chen,
Shandong University, China

***Correspondence:**
Qian Xiao
xiaoqian@tju.edu.cn

Specialty section:
This article was submitted to Smart Grids, a section of the journal Frontiers in Energy Research

Received: *10 April 2022*
Accepted: *25 April 2022*
Published: *24 May 2022*

Citation:
Li T, Xiao Q, Jia H, Mu Y, Wang X, Lu W and Pu T (2022) Multi-Agent Schedule Optimization Method for Regional Energy Internet Considering the Improved Tiered Reward and Punishment Carbon Trading Model. Front. Energy Res. 10:916996. doi: 10.3389/fenrg.2022.916996

1 INTRODUCTION

Low-carbon and environmentally friendly energy production is the foundation of sustainable development in the world. Therefore, reducing the carbon emissions of energy systems gradually become a key research work. At present, with the gradual integration of energy systems, the research in this area mainly focuses on the following two aspects. The first is establishing a detailed carbon trading system to limit carbon emissions (Zhang et al., 2020), and the second is establishing an energy internet optimization system to improve energy efficiency (Yu et al., 2016).

Many scholars have made outstanding contributions to the energy internet carbon trading model. Huang et al. (2021) summarized the research status and application prospect of low carbonization technology, and respectively refined the carbon emissions reduction removal technologies of energy supply side and consumption measurement. Li et al. (2021) established a multi-layer key index system of source-net-network-load, and set a carbon index membership function suitable for central cities on the premise that the subjective and objective weight deviations were the smallest sum of

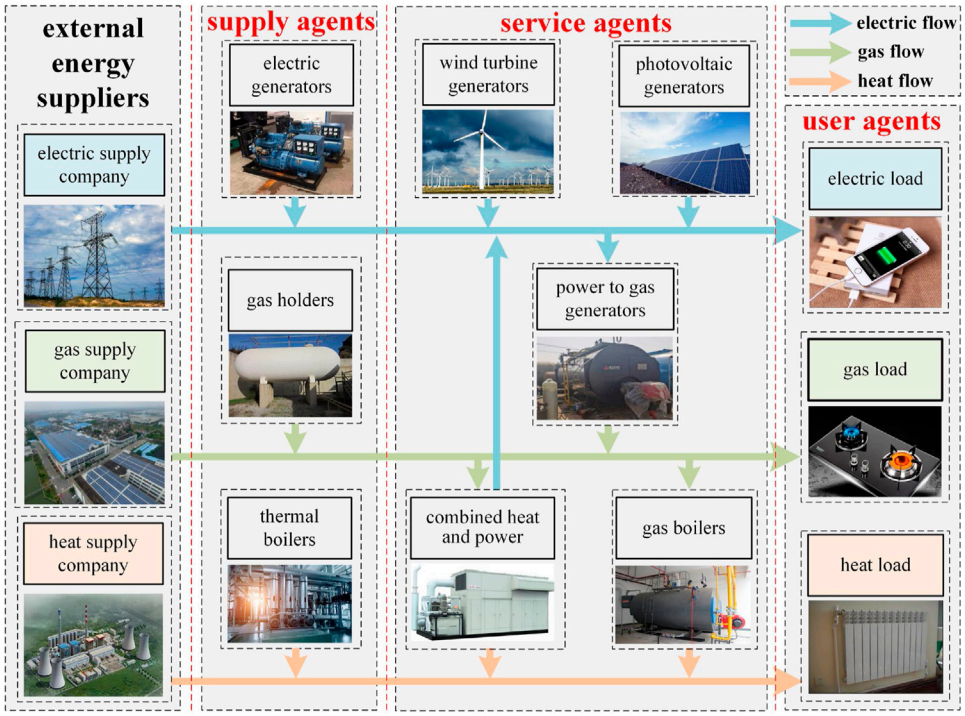

FIGURE 1 | Regional energy internet.

squares. Yuan et al. (2022) introduced carbon capture power plants, which improved peak regulation capabilities and system economic benefits for cogeneration units, while the carbon emissions were reduced. Cui et al. (2021) introduced a comprehensive and flexible operation mode of carbon capture power plants on the source site, which was considered on the load side demand response. This mode explored the dispatching advantages of the complementary low-carbon characteristics of the two means, achieving a high degree of wind power consumption. Li and Niu (2021) summarized the current technical characteristics of the power system and believed that the expansion of renewable energy, the early withdrawal of coal power, the application of carbon capture technology, and the guarantee of transformation investment need to be handled in the future energy transition. Cui et al. (2022) proposed a multi-time scale source-load dispatch method of power system with wind power considering low-carbon characteristics of carbon capture power plant, which was able to take advantage of the dispatch of source-load adjustable resources to achieve low power systems the goal of carbon economy schedule. However, the above literature did not put strong restrictions on ultra-high carbon emissions enterprises, which was not conducive to significant control of carbon emissions.

Optimizing energy internet operation and reducing energy consumption is one of the current research priorities. Zhang et al. (2016) fully considered the characteristics of renewable energy and the characteristics of user demand response. He proposed a renewable energy day dispatch method to improve the revenue of the energy system. Based on the current energy internet operation model, Zhang et al. (2015) proposed a new energy Internet optimization model that considered electricity, heat, and gas. Because of the distribution characteristics of the energy internet, Xiao et al. (2022) proposed a side-cloud collaborative architecture. Under this architecture, the system optimization scheduling was realized by using multi-server layering, and the rapid scheduling of the energy internet was realized. Bahrami et al. (2015) and Zhang et al. (2019) extended the demand response of the traditional power system to the heat and gas system and proposed an optimal dispatching method that considered multi-dimensional demand response. Mohammadian et al. (2021) proposed a data-driven classifier for extreme outage prediction based on Bayes decision theory, which can guarantee the optimization effect and significantly improve the optimization rate of the energy system. Kamruzzaman et al. (2021) used deep reinforcement learning to improve the elasticity of the power system and then laid the foundations for improved energy efficiency and a low-carbon economy. In the microgrid scenario, Zeng et al. (2019) proposed a grid optimization and energy management method based on a deep neural network. Mohsenian-Rad et al. (2010) proposed an autonomous demand-side management based on game-theoretic energy consumption scheduling, which provided direction for the low-carbon transformation of smart grids in the future. Peng et al. (2021), Wang et al. (2020), and Chen et al. (2019) used the edge computing method to realize the hierarchical optimization of energy internet. However, the above literature did not consider the game relationship between different agents of energy internet adequately. It is difficult to mobilize the enthusiasm of the energy

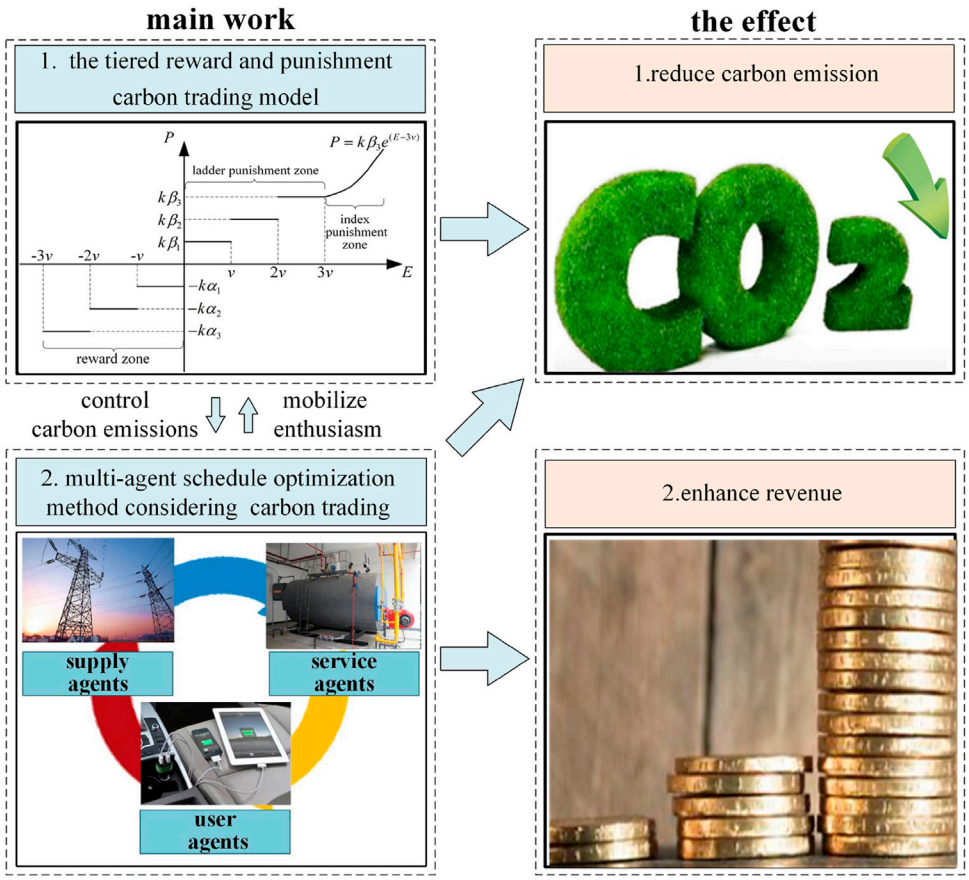

FIGURE 2 | The main work of this paper and the effects.

internet to participate in energy conservation and emissions reduction only by general overall optimization.

To reduce REI's carbon emissions and enhance the different agents' revenue, this paper proposes a multi-agent schedule optimization method for REI considering the improved tiered reward and punishment carbon trading model.

Compared with other works, the main contributions of the paper are summarized as follows.

1) This paper establishes a tiered reward and punishment carbon trading model for REI, which includes reward zone, ladder punishment zone, and index punishment zone. The model can reward enterprises that actively participate in reducing carbon emissions, and gradually raises the price of carbon to limit those enterprises that exceed carbon emissions standards.
2) This paper establishes a multi-agent schedule optimization method considering carbon trading for REI, which considers the interest demands of different agents in REI. This method divides all kinds of agents into supply agents, service agents and user agents. Then it sets up the objective function according to its actual revenue, which can stimulate the vitality of agents to participate in emissions reduction and market competition.

The rest of this paper is organized as follows. **Section 2** establishes the REI mathematical model. The proposed tied reward and punishment carbon trading model is detailed in **Section 3**, and the proposed multi-agent schedule optimization method considering carbon trading is detailed in **Section 4**. In **Section 5**, this paper uses two sets of contrasting scenes to support the advantages of the proposed model and method. Finally, some conclusions are given in **Section 6**.

2 REGIONAL ENERGY INTERNET MODEL AND MAIN WORK OF THIS PAPER

2.1 Regional Energy Internet Model

The REI model is shown in **Figure 1**.

There are three external energy suppliers, namely electric supply company, heat supply company and gas supply company. In the REI, there are supply agents, service agents and user agents. Supply agents have gas generators, thermal boilers and gas holders to supply this region. Service agents have wind turbine generators, photovoltaic generators, power to gas generators, combined heat and power generators and gas boilers. Service agents can use these devices to optimize regional operations. User agents have three kinds

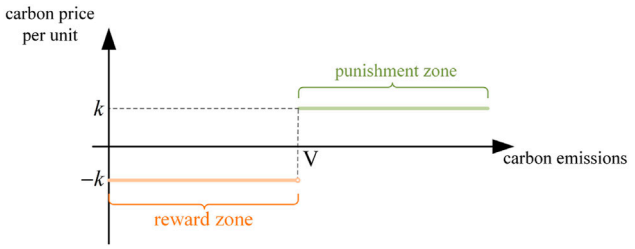

FIGURE 3 | Traditional carbon trading model.

of load, there are electric load, heat load and gas load. In this model, service agents are responsible for optimizing area operation.

2.1.1 Energy Flow Constraints

1) Electric flow constraints can be expressed as follows.

$$p_{e,t}^{UB} = p_{e,t}^{ESC} + p_{e,t}^{SS} + p_{e,t}^{VS} \tag{1}$$

$$p_{e,t}^{VS} = p_t^{WTG} + p_t^{PG} + p_{e,t}^{CHP} - p_{e,t}^{PTG} \tag{2}$$

Where $p_{e,t}^{UB}$ is the electric power of load after demand response at the time t, $p_{e,t}^{ESC}$ is electric power purchased from the electric supply company at the time t, $p_{e,t}^{SS}$ is electric power purchased from supply agents at the time t, $p_{e,t}^{VS}$ is electric power offered by service agents at the time t, p_t^{WTG} is electric power offered by wind turbine generators at the time t, p_t^{PG} is electric power offered by photovoltaic generators at the time t, $p_{e,t}^{CHP}$ is electric power offered by combined heat and power generators at the time t, $p_{e,t}^{PTG}$ is electric power consumed by power to gas generators at the time t.

2) Heat flow constraints can be expressed as follows.

$$p_{h,t}^{UB} = p_{h,t}^{HSC} + p_{h,t}^{SS} + p_{h,t}^{VS} \tag{3}$$

$$p_{h,t}^{VS} = p_{h,t}^{CHP} + p_{h,t}^{GB} \tag{4}$$

Where $p_{h,t}^{UB}$ is the heat power of load after demand response at the time t, $p_{h,t}^{HSC}$ is heat power purchased from heat supply company at the time t, $p_{h,t}^{SS}$ is heat power purchased from supply agents at the time t, $p_{h,t}^{VS}$ is heat power offered by service agents at the time t, $p_{h,t}^{CHP}$ is heat power offered by combined heat and power generators at the time t, $p_{h,t}^{GB}$ is heat power offered by the gas boiler at the time t.

3) Gas flow constraints can be expressed as follows.

$$p_{s,t}^{UB} = p_{s,t}^{PSC} + p_{s,t}^{SS} + p_{s,t}^{VS} \tag{5}$$

$$p_{s,t}^{VS} = p_{s,t}^{PTG} - p_{s,t}^{CHP} - p_{s,t}^{GB} \tag{6}$$

Where $p_{s,t}^{UB}$ is the gas power of load after demand response at the time t, $p_{s,t}^{PSC}$ is gas power purchased from gas supply company at the time t, $p_{s,t}^{SS}$ is gas power purchased from supply agents at the time t, $p_{s,t}^{VS}$ is gas power offered by service agents at the time t, $p_{s,t}^{PTG}$ is gas power offered by the power to gas generators at the time t, $p_{s,t}^{CHP}$ is gas power consumed by combined heat and power generators at the time t, $p_{s,t}^{GB}$ is gas power consumed by the gas boiler at the time t.

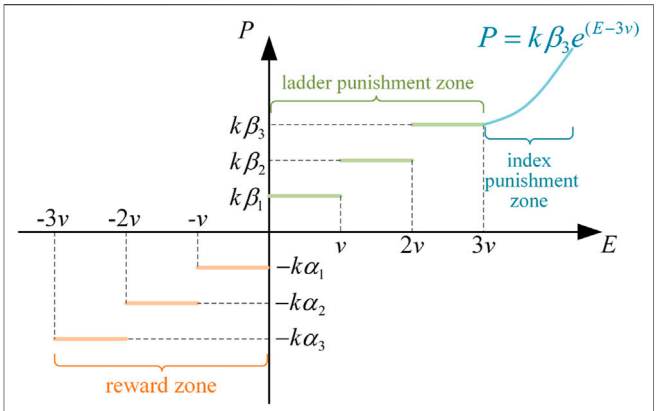

FIGURE 4 | The proposed tiered reward and punishment carbon trading model.

2.1.2 Device Constraints

1) Power to gas generators constraints can be expressed as follows.

$$p_{s,t}^{PTG} = \eta^{PTG} p_{e,t}^{PTG} \tag{7}$$

$$0 \le p_{e,t}^{PTG} \le p_{max}^{PTG} \tag{8}$$

Where η^{PTG} is the efficiency of the power to the gas generators, p_{max}^{PTG} is the maximum input power of the power to gas generators.

2) Combined heat and power generators constraints can be expressed as follows.

$$p_{e,t}^{CHP} = \eta_e^{CHP} p_{s,t}^{CHP} \tag{9}$$

$$p_{h,t}^{CHP} = \eta_h^{CHP} p_{s,t}^{CHP} \tag{10}$$

$$0 \le p_{s,t}^{CHP} \le p_{max}^{CHP} \tag{11}$$

Where η_e^{CHP} is the electric efficiency of the combined heat and power generators, η_h^{CHP} is the heat efficiency of the combined heat and power generators, p_{max}^{CHP} is the maximum input power of the combined heat and power generators.

3) Gas boiler constraints can be expressed as follows.

$$p_{h,t}^{GB} = \eta^{GB} p_{s,t}^{GB} \tag{12}$$

$$0 \le p_{s,t}^{GB} \le p_{max}^{GB} \tag{13}$$

Where η^{GB} is the efficiency of the gas boiler, p_{max}^{GB} is the maximum input power of the gas boiler.

4) Wind turbine generators constraints can be expressed as follows.

$$0 \le p_t^{WTG} \le p_{fore,t}^{WTG} \tag{14}$$

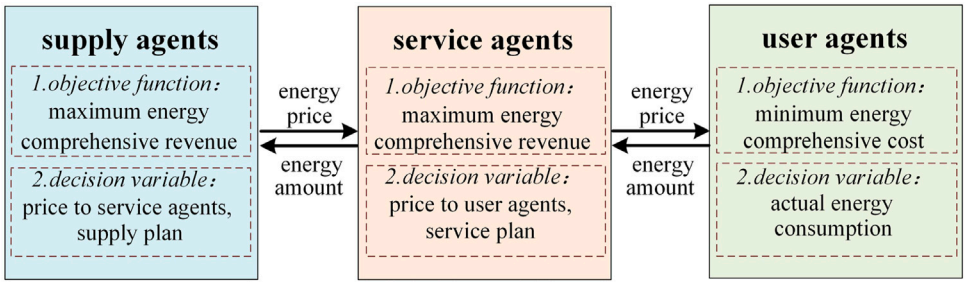

FIGURE 5 | Multi-agent game relationship diagram.

Where $p_{fore,t}^{WTG}$ is current wind turbine generators forecast power at the time t.

5) Photovoltaic generators constraints can be expressed as follows.

$$0 \le p_t^{PG} \le p_{fore,t}^{PG} \tag{15}$$

Where $p_{fore,t}^{PG}$ is current photovoltaic generators forecast power at the time t.

2.2 Main Work of This Paper

To solve the problems of high carbon emissions and insufficient enthusiasm of all agents in the REI, this paper proposes the improved tiered reward and punishment carbon trading model and the multi-agent schedule optimization method considering carbon trading. As shown in **Figure 2**, the carbon trading model rewards and punishes counterpart enterprises, which achieves the goal of reducing carbon emissions. The multi-agent game method can consider the subjectivity of different agents participating in energy conservation and emissions reduction, which achieves the goal of reducing carbon emissions and enhancing revenue. The connection between the two parts is as follows. The carbon trading model helps the multi-agent method control carbon emissions, and the multi-agent game method helps the carbon trading model mobilize the enthusiasm of different subjects to participate in energy conservation and emission reduction.

3 THE TIED REWARD AND PUNISHMENT CARBON TRADING MODEL

The traditional carbon trading model often punishes and rewards carbon trading in a single-priced monopoly, which is not conducive to mobilizing the enthusiasm of all kinds of agents in the market to participate in energy conservation and emissions reduction. The traditional carbon trading model is shown in **Figure 3**.

This traditional model will enable some enterprises to arbitrage revenue from it. For example, if the revenue of one enterprise emitting a unit of carbon dioxide is greater than the benchmark price of carbon emissions per unit k, this model does nothing to limit the enterprise's carbon emissions!

Therefore, to stimulate the enthusiasm of stakeholders in the energy market to participate in energy conservation and emissions reduction, the improved tiered reward and punishment carbon trading model is proposed in this paper, which is shown in **Figure 4**.

$$E = E_r - E_g \tag{16}$$

In **Figure 4**, the horizontal axis E is the relative carbon emission for the entire simulation period, which can be calculated by the formula (Zeng et al., 2019), and the vertical axis P is the carbon price per unit given by the government. In formula (Zeng et al., 2019), E_r is the actual carbon emissions of the enterprise, E_g is the free carbon emissions of the enterprise. The reward and punishment carbon trading model include reward zone, ladder punishment zone and index punishment zone. The reward zone can reward enterprises with lower carbon emissions on a tiered basis. In the same way, the ladder punishment zone can punish enterprises with higher carbon emissions at different levels. And the index punishment zone can limit enterprises with extremely high carbon emissions.

Compared with the traditional carbon trading model, the improved tiered reward and punishment carbon trading model has the following advantages:

1) It can reward or punish enterprises with different carbon emissions at different levels, which can mobilize the enthusiasm of enterprises to participate in energy conservation and emissions reduction.
2) It can eliminate the possibility of some high-carbon emissions enterprises profiting from it.

3.1 Reward Zone

When an enterprise's relative carbon emission E is less than zero, it means this enterprise's actual carbon emissions E_r under the free carbon emissions of the enterprise E_g. On this occasion, this enterprise should be rewarded. The reward amount should be determined by the enterprise's relative carbon emission E. This paper divides the reward zone into three levels. The carbon price per unit P can be calculated as follows.

TABLE 1 | Supply agents' price limit.

Types of energy	Maximum (USD/MW)	Minimum (USD/MW)
Electricity	115	0
Heat	110	0
Gas	110	0

TABLE 2 | Service agents' price limit.

Types of energy	Maximum (USD/MW)	Minimum (USD/MW)
Electricity	90	85
Heat	90	85
Gas	90	85

$$P = \begin{cases} -k\alpha_1 & -v \le E < 0; \\ -k\alpha_2 & -2v \le E < -v; \\ -k\alpha_3 & -3v \le E < -2v. \end{cases} \tag{17}$$

Where k is the benchmark price of carbon emissions per unit, α_k (k =1, 2, 3) is the carbon emissions incentive factor, v is the carbon emissions classification unit.

The cost of carbon emissions C^{co_2} can be calculated as follows.

$$C^{co_2} = \begin{cases} -k[\alpha_1(-E)] & -v \le E < 0; \\ -k[\alpha_1 v + \alpha_2(-E - v)] & -2v \le E < -v; \\ -k[\alpha_1 v + \alpha_2 v + \alpha_3(-E - 2v)] & -3v \le E < -2v. \end{cases} \tag{18}$$

In the reward zone, the carbon price per unit given by the government and the cost of carbon emissions is negative. That means this enterprise is rewarded for reducing carbon emissions.

3.2 Ladder Punishment Zone

When an enterprise's relative carbon emission E is more than zero, it means this enterprise should be punished for its carbon emissions. If the enterprise's carbon emissions are less than the set standard $3v$ in the meantime, its carbon price will fall into the ladder punishment zone. This paper divides the ladder punishment zone into three levels. The carbon price per unit P can be calculated as follows.

$$P = \begin{cases} k\beta_1 & 0 \le E < v; \\ k\beta_2 & v \le E < 2v; \\ k\beta_3 & 2v \le E < 3v. \end{cases} \tag{19}$$

Where β_k (k = 1, 2, 3) is the carbon emissions punishment factor.

The cost of carbon emissions C^{co_2} can be calculated as follows.

$$C^{co_2} = \begin{cases} k\beta_1 E & 0 \le E < v; \\ k[\beta_1 v + \beta_2(E - v)] & v \le E < 2v; \\ k[\beta_1 v + \beta_2 v + \beta_3(E - 2v)] & 2v \le E < 3v. \end{cases} \tag{20}$$

In the ladder punishment zone, the carbon price per unit presents a ladder distribution. That means this enterprise is punished for carbon emissions, and the price of the punishment varies with the amount of carbon emitted.

3.3 Index Punishment Zone

When an enterprise's relative carbon emission E is more than $3v$, it means that the enterprise's carbon emissions seriously exceeded the standard. In this case, the punishment must be increased to ensure the environmental protection of the energy system. Therefore, this paper sets up an index punishment zone. In this zone, the carbon price per unit P can be calculated as follows.

$$P = k\beta_3 e^{(E-3v)} \tag{21}$$

The cost of carbon emissions C^{co_2} can be calculated as follows.

$$C^{co_2} = k\left[\beta_1 v + \beta_2 v + \beta_3 v + \int_{3v}^{E-3v} \beta_3 e^{(E-3v)} dE\right] \tag{22}$$

In the index punishment zone, the carbon price per unit presents exponential growth.

4 THE MULTI-AGENT SCHEDULE OPTIMIZATION METHOD CONSIDERING CARBON TRADING

There are many different types of agents in REI, and the general optimization of REI operation is not conducive to mobilizing the enthusiasm of all agents to participate in energy conservation and emissions reduction. According to the characteristics of different agents in REI, various agents are divided into supply agents, service agents and user agents. Then the objective function is set according to their actual interests, and an optimization scheduling method considering multi-agent carbon trading is proposed. The interests of each agent are affected by the policies of other agents. The game relationship of the three types of agents is shown in **Figure 5**.

4.1 Supply Agents

Supply agents refer to all market agents who profit by producing and selling energy. Their main feature is that they have energy production facilities. Their revenue is mainly influenced by the number of purchases by lower-level buyers and the cost of energy production. When such supply agents are optimized, their energy comprehensive revenue can be maximized by adjusting their price to service agents and their energy supply project. Supply agents' objective function I^S can be calculated as follows.

$$I^S = max\left(I^{SSale} - C^{SS} - C^{SC} - C^{CO_2}\right) \tag{23}$$

Where I^{SSale} is the supply agents' revenue of energy sales, C^{SS} is the supply agents' cost of energy production, C^{SC} is the comfort cost of supply agents. They can be calculated as follows.

$$I^{SSale} = \sum_{t=1}^{T} \delta_t^{SS} p_t^{SS} \Delta t \tag{24}$$

Where t is current simulation time, T is total simulation time, δ_t^{SS} is energy sale price from supply agents at the time t, p_t^{SS} is the amount of energy sale power from supply agents at the time t, Δt is the length of simulation time.

TABLE 3 | Device parameters.

Types of devices	Efficiency	Service cost (USD/MW)	Maximum power (MW)
Power to gas	0.80	4	1.50
Combined heat and power (heat efficiency)	0.65	3	1.05
Combined heat and power (electric efficiency)	0.25	3	0.30
Gas boiler	0.90	6	3.00

TABLE 4 | Carbon trading scenes.

Scene number	Scene description
1	No carbon trading model
2	The traditional carbon trading model (**Figure 3**)
3	The improved tiered reward and punishment carbon trading model (**Figure 4**)

$$C^{SS} = \sum_{t=1}^{T}\left[\sum_{m\in M}\left(\gamma_m^{SS} p_{m,t}^{SS}\Delta t + \varepsilon_m^{SS} p_{m,t}^{SS}\Delta t\right)\right] \tag{25}$$

Where m is the current device number, M is the gathering of all supply agents' devices. γ_m^{SS} is the service cost per unit of device m, which usually includes equipment maintenance, sewage treatment and so on. ε_m^{SS} is the product cost per unit of device m. $p_{m,t}^{SS}$ is the power of device m at the time t.

$$C^{SC} = \sum_{t=1}^{T} k_1\left[\left(\frac{\delta_t^{SS}}{\delta}\right)^{k_2} - 1\right] \tag{26}$$

Where k_1 is the product coefficient of comfort for supply agents, k_2 is the index coefficient of comfort for supply agents, δ is the average market energy price.

Supply agents' revenue is affected by various market factors. Supply agents can change their price to service agents δ_t^{SS} and supply project $p_{m,t}^{SS}$ to enhance their revenue.

4.2 Service Agents

Service agents refer to all market agents who profit from energy conversion and dispatching. Their main feature is that they have power to gas, gas boiler and other energy conversion equipment. Their revenue is influenced by market conditions, equipment performance and other agents' policies. When service agents are optimized, their energy comprehensive revenue can be maximized by adjusting their energy purchasing power, energy selling price and conversion strategy. Service agents' objective function I^V can be calculated as follows.

$$I^V = max\left(I^{VSale} - C^{VS} - C^{VC} - C^{VB} - C^{CO_2}\right) \tag{27}$$

Where I^{VSale} is the service agents' revenue of energy sales, C^{VS} is the service agents' cost of equipment maintenance, C^{VC} is the service agents' comfort cost, C^{VB} is the service agents' cost for purchasing energy. They can be calculated as follows.

$$I^{VSale} = \sum_{t=1}^{T}\delta_t^{VS} p_t^{VS}\Delta t \tag{28}$$

Where δ_t^{VS} is energy sale price from service agents at the time t, p_t^{VS} is the amount of energy sold power from service agents at the time t.

$$C^{VS} = \sum_{t=1}^{T}\left(\sum_{u\in U}\gamma_u^{VS} p_{u,t}^{VS}\Delta t\right) \tag{29}$$

Where u is the current device number, U is the gathering of all service agents' devices. γ_u^{VS} is the service cost per unit of device u, which usually includes equipment maintenance, energy efficiency conversion and so on. $p_{u,t}^{VS}$ is the power of device u at the time t.

$$C^{VC} = \sum_{t=1}^{T} k_3\left[\left(\frac{\delta_t^{VS}}{\delta}\right)^{k_4} - 1\right] \tag{30}$$

Where k_3 is the product coefficient of comfort for service agents, k_4 is the index coefficient of comfort for service agents, δ is the average market energy price.

$$C^{VB} = \sum_{t=1}^{T}\delta_t^{SS} p_t^{VB}\Delta t \tag{31}$$

Where p_t^{VB} is the amount of energy buying power from supply agents at the time t.

Service agents can change their price to user agents δ_t^{VS}, service project $p_{u,t}^{VS}$ and the amount of energy buying power from supply agents p_t^{VB} to enhance their revenue.

4.3 User Agents

User agents refer to all market agents who benefit in other ways. They usually act as a user of energy rather than participating in energy production and transmission activities. In the process of energy optimization, the minimum energy purchase cost of the user agents is considered. User agents' objective function I^{US} can be calculated as follows.

$$I^{US} = min\left(C^{UB} + C^{UC} + C^{UCT}\right) \tag{32}$$

Where C^{UB} is the user agents' cost of buying energy, C^{UC} is the user agents' comfort cost, C^{UCT} is the carbon limits cost of user agents. They can be calculated as follows.

$$C^{UB} = \sum_{t=1}^{T}\delta_t^{VS} p_t^{UB}\Delta t \tag{33}$$

Where p_t^{UB} is the amount of energy buying power from service agents at the time t. In this paper the user agents can only purchase energy from the service agents, so p_t^{UB} is the same as the actual load after the demand response.

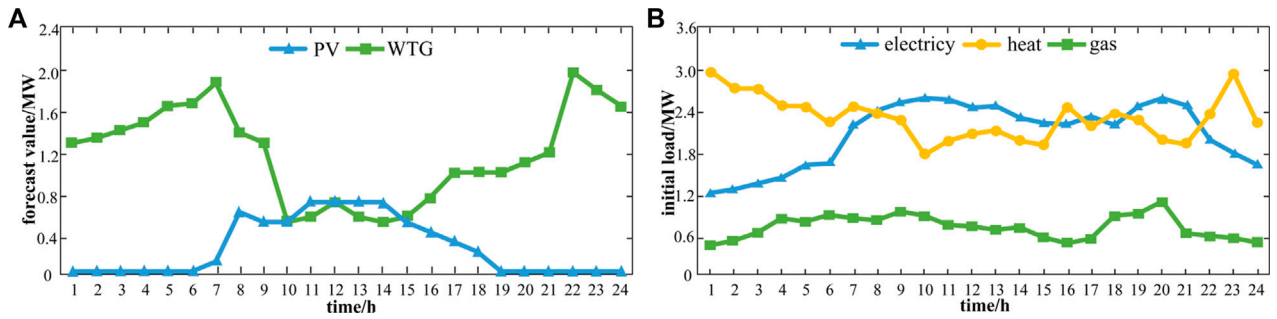

FIGURE 6 | Renewable energy and load data.

TABLE 5 | Carbon trading results.

Scene number	Carbon emissions (t)	Cost of carbon emissions (USD)	Comprehensive revenue (USD)
1	12.29	0	5,246.64
2	12.21	347.25	4,905.01
3	12.05	498.21	4,776.63

TABLE 6 | Game scenes.

Scene number	Consider electric game	Consider heat game	Consider gas game
1	×	×	×
2	×	√	×
3	×	√	√
4	√	√	√

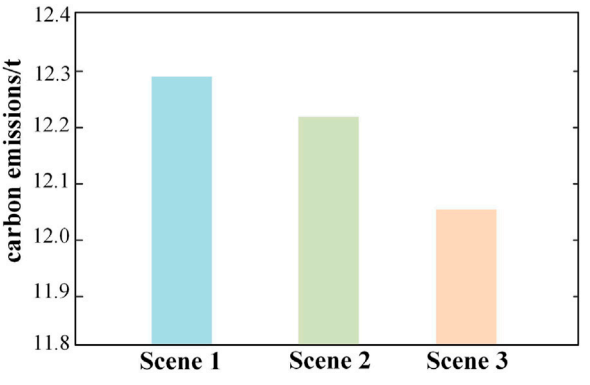

FIGURE 7 | Comparison of carbon emissions.

$$C^{UC} = \sum_{t=1}^{T}\left[\frac{y}{2L_t}\left(p_t^{UB}\right)^2 - yp_t^{UB} + \frac{y}{2}L_t\right] \tag{34}$$

Where y is the comfort coefficient of user agents, L_t is the initial load before the demand response.

$$C^{UCT} = \sum_{t=1}^{T} k_5\left(C^{CO_2}\right)^{k_6} \tag{35}$$

Where k_5 is the product coefficient of carbon limits for user agents, k_6 is the index coefficient of carbon limits for user agents. Although carbon emissions are not directly emitted by users, the energy consumption of users has a great influence on the carbon emissions of the park. Therefore, this paper uses C^{UCT} to limit user agents' energy consumption.

User agents can change their amount of energy buying power from service agents p_t^{UB} to reduce its' cost.

4.4 Optimization Calculation Method

Multi-agent game is different from multi-objective optimization. It is not simply to pursue maximum comprehensive revenue. It is trying to find a stable operating point where no one can enhance his revenue by chance himself. This feature can be expected as follows.

$$i \in O, a_j^i \in A^i, s \in S \tag{36}$$

Where i is the current agent, O is the gathering of agents in the REI, a_j^i is agent i 's action j, A^i is the gathering of agent i 's

TABLE 7 | Game results.

Scene number	Energy sales revenue (USD)	Carbon emissions (t)	Comprehensive revenue (USD)
1	997.72	12.66	434.22
2	1,053.16	12.40	504.29
3	5,056.96	12.38	4,509.06
4	5,274.84	12.05	4,776.63

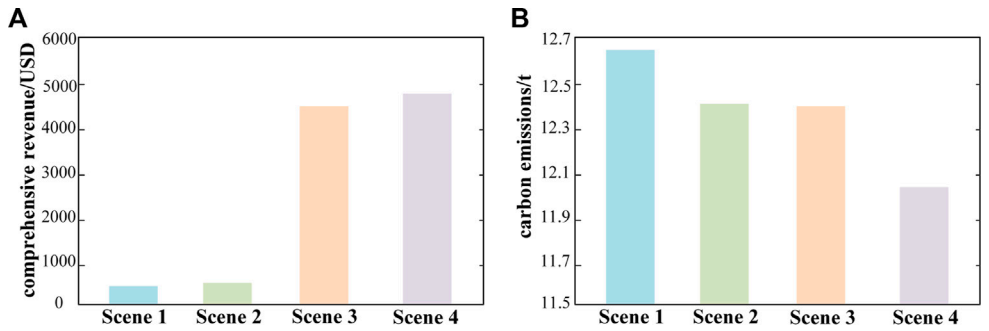

FIGURE 8 | Comparison results.

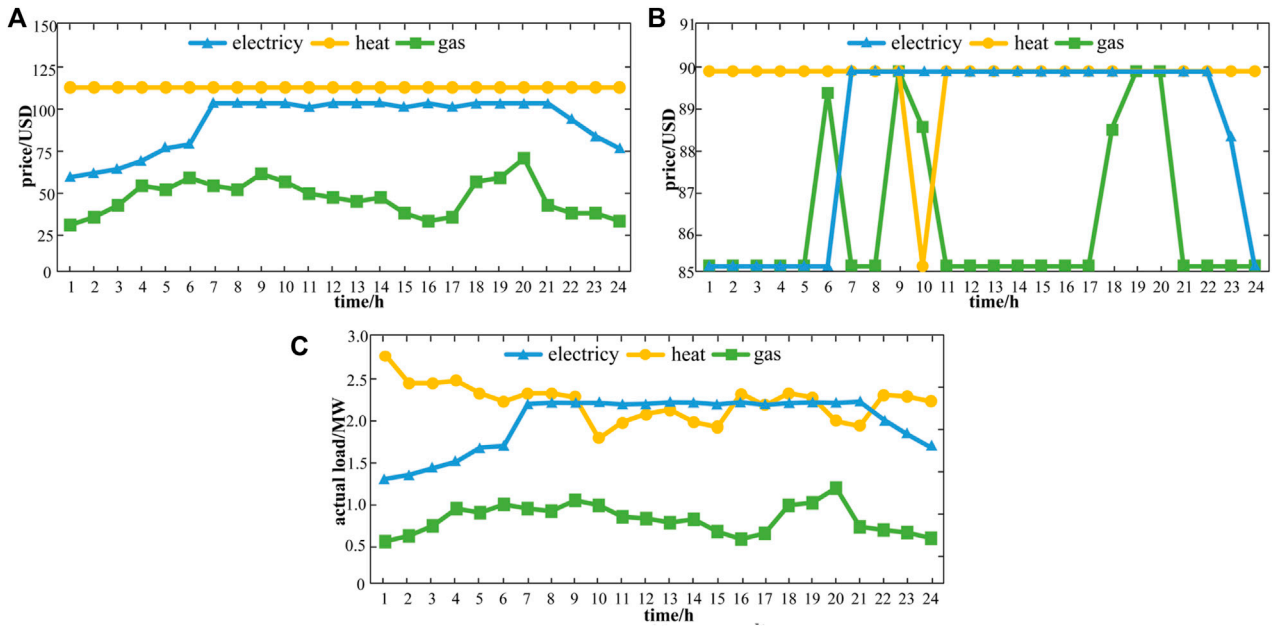

FIGURE 9 | Multi-agent results.

actions, s is a current station, S is the gathering of stations in the REI.

At Station s, if Satisfies

$$\forall i \in O, \forall a_j^i \in A^i \tag{37}$$

$$I_i^{a_*^i} \geq I_i^{a_j^i} \tag{38}$$

Then $(a_*^1, a_*^2, \ldots, a_*^i, \ldots)$ is the equilibrium solution at station s. Where $I_i^{a_*^i}$ is agent i's revenue at actor a_*^i, $I_i^{a_j^i}$ is agent i's revenue at actor a_j^i.

Considering that the multi-agent game process of REI is complex, this paper divides the whole operation optimization process into the following two parts: the upper price game and the bottom device game. The algorithm can be expressed as follows.

1: **Initialize**: $i_{\max}$, $\delta_t^{SS}(0)$, $p_{m,t}^{SS}(0)$, $\delta_t^{VS}(0)$, $p_{u,t}^{VS}(0)$, $p_t^{VB}(0)$, $p_t^{UB}(0)$.
2: **for** i=0
3: **if** satisfies (37) and (38)
4: break;
5: **else**
6: Run the algorithm 2;
7: Run the algorithm 3;
8: i=i+1;
9: **if** i= $i_{\max}$
10: break;
11: **end**

1: **Let** $p_{m,t}^{SS}(i)$, $p_{u,t}^{VS}(i)$ invariant.
2: **Change** $\delta_t^{SS}(i)$, $\delta_t^{VS}(i)$, $p_t^{VB}(i)$, $p_t^{UB}(i)$ to change (23), (27), (32) until satisfies (37) and (38).

1: **Let** $\delta_t^{SS}(i)$, $\delta_t^{VS}(i)$, $p_t^{VB}(i)$, $p_t^{UB}(i)$ invariant.
2: **Change** $p_{m,t}^{SS}(i)$, $p_{u,t}^{VS}(i)$ to change (23), (27), (32) until satisfies (37) and (38).

5 SIMULATION RESULT

To verify the superiority of the proposed method, this paper establishes an REI for simulation which includes supply, service and user agents. Supply agents possess electric generators, gas holders and thermal boilers. Service agents possess wind turbine generators, photovoltaic generators, combined heat and power generators, power to gas generators and gas boilers. User agents include electric, gas and heat load. The energy flow model and device model are shown in **Section 2**. This paper sets the simulation time as 24 h, and the time interval as 1 h. To ensure the rationality of the simulation results, the price needs to be limited. Supply agents' price limit is shown in **Table 1**, and service agents' price limit is shown in **Table 2**. At the same time, the efficiency should be set, unit service cost, and maximum output power constraints of the various device according to the situation of the region. Device parameters are shown in **Table 3**. Parameters in the carbon trading model are shown in **Table 4**.

The renewable energy forecast value and initial load value are shown in **Figure 6**. This paper sets that the output power of renewable energy in the REI cannot exceed its predicted value. At the same time, the demand response in this paper is in the form of an interruptible load, so the actual user load value cannot exceed the initial value.

To fully explain that the proposed improved tiered reward and punishment carbon trading model and the proposed multi-agent game method in this paper are beneficial to the REI, this paper sets up a simulation scenario under the principle of control variables. In **section 5.1**, considering three kinds of energy games, only the carbon trading model for simulation is changed; in **section 5.2**, considering the proposed tiered reward and punishment carbon trading model, only the game energy types for simulation are changed. The other parameter settings of the two sets of scenes are the same.

5.1 Carbon Trading Scenes Analysis

To verify the advantages of the proposed tiered reward and punishment carbon trading model, this paper sets up three scenes which are shown in **Table 4** for comparison.

In **Table 4**, there are 3 scenes to simulate. In scene 1, the carbon trading model is not considered, which means the revenue of the whole region will not be affected by carbon emissions; in scene 2, the traditional carbon trading model in **Figure 3** is considered; in scene 3, the improved tiered reward and punishment carbon trading model in **Figure 4** is considered.

The simulation results are shown in **Table 5**.

The comparison of carbon emissions is shown in **Figure 7**.

In **Table 5** and **Figure 7**, the results indicate that: from scene 1 to scene 3, carbon emissions significantly decrease by about 2.2%, which illustrates the method proposed in this paper is useful to control carbon emissions. But the cost of carbon emissions rises, which makes the comprehensive revenue decrease. This is an accepted thing. Controlling carbon emissions will reduce revenue.

5.2 Game Scenes Analysis

To verify the advantages of the proposed multi-agent game method, this paper sets up 4 scenes which are shown in **Table 6** for simulation. In **Table 6**, there are 4 scenes to simulate: in scene 1, supply agents, service agents and user agents only focus on immediate revenue, do not consider the impact of other market players; in scene 2, each agent only considers heat game; in scene 3, consider heat and gas game; in scene 4, consider electric, heat and gas game.

The simulation results are shown in **Table 7**.

The comprehensive revenue and carbon emissions are shown in **Figure 8**.

In **Table 7** and **Figure 8**, the results indicate that as more types of energy games are considered, the higher the energy sales revenue. That's because when taking the energy game out of the equation, supply agents and service agents only consider immediate revenue. At this moment, these agents do not analyze market conditions for an inflated price, which makes the region's energy sales revenue fall instead. When considering fewer types of energy games, the carbon emissions go up, this is because users do not consider the market game, blindly reducing the demand response, increasing the total energy consumption, thus making carbon emissions up. Compared

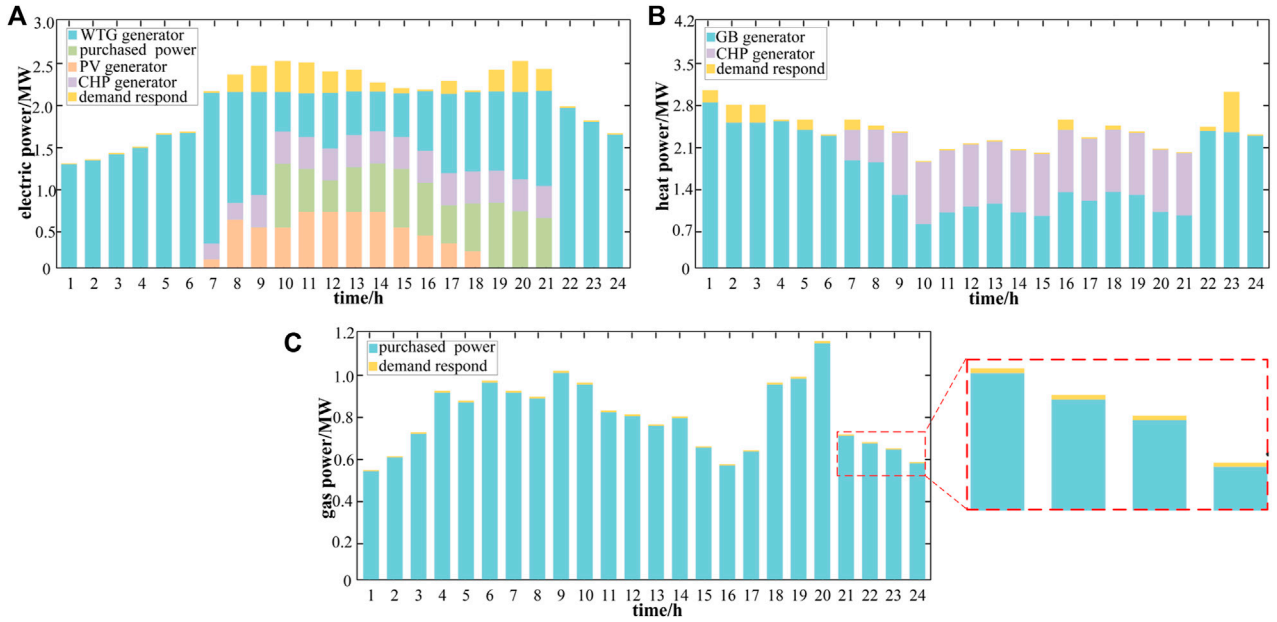

FIGURE 10 | Device optimization results.

with scene 1, in scene 4, carbon emissions significantly decrease by about 5.1%.

More carbon emissions make the cost of carbon emissions rise, plus with the influence of energy sales revenue, both of them make comprehensive revenue decline.

5.3 Game and Device Results Analysis

Multi-agent game results are shown in the **Figure 9**.

In **Figure 9**, the changing user loads make supply agents' and service agents' prices change with time. Heat price is always very high (the upper limit is often reached), this is because the heat demand in this paper is large. For service agents, the revenue of increasing the price is higher than the losses of the comfort function. In contrast, natural gas demand in this REI is low, reducing the price to increase the comfort function brings more revenue.

Device optimization results are shown in **Figure 10**.

In **Figure 10**, the results indicate that: WTG generators' power and PV generators' power are almost the same as predicted, this is because renewable energy is given priority in this paper. CHP generators are used when renewable energy cannot meet system requirements and there is a simultaneous thermoelectric demand. As for service agents, it is cheaper to supply heat through GB generators than buy it from supply agents. As opposed to this, P2G generators are not being used because it is inefficient. Demand response exists for all three energy sources at any one time, the demand response is affected by load type, energy price and renewable energy power. When the initial load is high, user agents need to bear higher energy costs, so they will increase demand response. The gas load at each time is low, that is, why gas demand response is low.

6 CONCLUSION

To reduce REI's carbon emissions and enhance the different agents' revenue, this paper proposes a multi-agent schedule optimization method considering the improved tiered reward and punishment carbon trading model. The advantages of this method are as follows.

1) The proposed improved tiered reward and punishment carbon trading model can reward or punish enterprises at different levels to reduce carbon emissions. Considering the game, this paper only changes the carbon trading model for simulation, and the results show that compared with the traditional model, the proposed model can reduce carbon emissions by about 1.3% in the REI.
2) The proposed multi-agent schedule optimization method can stimulate the energy conservation and emissions reduction participation of each agent to reduce carbon emissions and enhance revenue. Considering the improved tiered reward and punishment carbon trading model, this paper only changes the game energy types for simulation, and the results show that compared with the non-game method, this method can reduce carbon emissions

by about 5.1% and significantly enhance the revenue of the REI.

Nevertheless, the different carbon emissions of the different devices are not considered in this paper. This will be the focus of future work.

DATA AVAILABILITY STATEMENT

The original contributions presented in the study are included in the article/Supplementary Material, further inquiries can be directed to the corresponding author.

REFERENCE

Bahrami, S., and Sheikhi, A. (2015). From Demand Response in Smart Grid toward Integrated Demand Response in Smart Energy Hub. *IEEE Trans. Smart Grid* 7 (2), 1. doi:10.1109/TSG.2015.2464374

Chen, S., Wen, H., Wu, J., Lei, W., Hou, W., Liu, W., et al. (2019). Internet of Things Based Smart Grids Supported by Intelligent Edge Computing. *IEEE Access* 7, 74089–74102. doi:10.1109/ACCESS.2019.2920488

Cui, Y., Deng, G., and Zhao, Y. (2021). Economic Dispatch of Power System with Wind Power Considering the Complementarity of Low-Carbon Characteristics of Source Side and Load Side. *Proceeding CSEE* 41 (14), 4799–4815. doi:10.13334/j.0258-8013.pcsee.202533

Cui, Y., Deng, G., and Zhao, Y. (2022). Multi-time Scale Source-Load Dispatch Method of Power System with Wind Power Considering Low-Carbon Characteristics of Carbon Capture Power Plant. *Proceeding CSEE*. doi:10.13334/j.0258-8013.pcsee.210697

Huang, Y., Ding, T., and Li, Y. (2021). Decarbonization Technologies and Inspirations for the Development of Novel Power Systems in the Context of Carbon Neutrality. *Proceeding CSEE* 41, 28–51. doi:10.13334/j.0258-8013.pcsee.211016

Kamruzzaman, M., Duan, J., Shi, D., and Benidris, M. (2021). A Deep Reinforcement Learning-Based Multi-Agent Framework to Enhance Power System Resilience Using Shunt Resources. *IEEE Trans. Power Syst.* 36 (6), 5525–5536. doi:10.1109/TPWRS.2021.3078446

Li, X., and Niu, S. (2021). Study on Multi-Layer Evaluation System of Source-Grid-Load under Carbon-Neutral Goal. *Proceeding CSEE* 41, 178–184. doi:10.13334/j.0258-8013.pcsee.211576

Li, Z., Chen, S., and Dong, W. (2021). Low Carbon Transition Pathway of Power Sector under Carbon Emission Constraints. *Proceeding CSEE* 41 (12), 3987–4000. doi:10.13334/j.0258-8013.pcsee.210671

Mohammadian, M., Aminifar, F., Amjady, N., and Shahidehpour, M. (2021). Data-driven Classifier for Extreme Outage Prediction Based on Bayes Decision Theory. *IEEE Trans. Power Syst.* 36 (6), 4906–4914. doi:10.1109/TPWRS.2021.3086031

Mohsenian-Rad, A.-H., Wong, V. W. S., Jatskevich, J., Schober, R., and Leon-Garcia, A. (2010). Autonomous Demand-Side Management Based on Game-Theoretic Energy Consumption Scheduling for the Future Smart Grid. *IEEE Trans. Smart Grid* 1 (6), 320–331. doi:10.1109/TSG.2010.2089069

Peng, N., Liang, R., Wang, G., Sun, P., Chen, C., and Hou, T. (2021). Edge Computing-Based Fault Location in Distribution Networks by Using Asynchronous Transient Amplitudes at Limited Nodes. *IEEE Trans. Smart Grid* 12 (1), 574–588. doi:10.1109/TSG.2020.3009005

Wang, S., Wang, X., and Wu, W. (2020). Cloud Computing and Local Chip-Based Dynamic Economic Dispatch for Microgrids. *IEEE Trans. Smart Grid* 11 (5), 3774–3784. doi:10.1109/TSG.2020.2983556

Xiao, Q., Li, T., and Jia, H. (2022). Research on Edge Cloud Collaboration Architecture and Optimization Strategy for Regional Energy Internet. *Proceeding CSEE*. doi:10.13334/j.0258-8013.pcsee.212931

AUTHOR CONTRIBUTIONS

TL and QX constructed the model and method of this paper. HJ and YM collected data. XW, WL, and TP worked together to design scenes.

FUNDING

The paper is supported by the National Natural Science Foundation of China (U2066213) from the Chinese Government. The author QX is the Subject Investigator of this project and the author TP is the Project Investigator of this project.

Yu, M., and Hong, S. H. (2016). Supply-demand Balancing for Power Management in Smart Grid: A Stackelberg Game Approach. *Appl. Energy* 164 (15), 702–710. doi:10.1016/j.apenergy.2015.12.03910.1016/j.apenergy.2015.12.039

Yuan, G., Liu, H., and Yu, J. (2022). Combined Heat and Power Optimal Dispatching in Virtual Power Plant with Carbon Capture Cogeneration Unit. *Proceeding CSEE*. doi:10.2107/TM.20211104.2019.005

Zeng, P., Li, H., He, H., and Li, S. (2019). Dynamic Energy Management of a Microgrid Using Approximate Dynamic Programming and Deep Recurrent Neural Network Learning. *IEEE Trans. Smart Grid* 10 (4), 4435–4445. doi:10.1109/TSG.2018.2859821

Zhang, W., and Xu, Y. (2019). Distributed Optimal Control for Multiple Microgrids in a Distribution Network. *IEEE Trans. Smart Grid* 10 (4), 3765–3779. doi:10.1109/TSG.2018.2834921

Zhang, X., Liu, X., and Zhong, J. (2020). Integrated Energy System Planning Considering a Reward and Punishment Ladder-type Carbon Trading and Electric-Thermal Transfer Load Uncertainty. *Proceeding CSEE* 40 (9), 6132–6141. doi:10.13334/j.0258-8013.pcsee.191302

Zhang, X., Shahidehpour, M., Alabdulwahab, A., and Abusorrah, A. (2016). Hourly Electricity Demand Response in the Stochastic Day-Ahead Scheduling of Coordinated Electricity and Natural Gas Networks. *IEEE Trans. Power Syst.* 31 (1), 592–601. doi:10.1109/TPWRS.2015.2390632

Zhang, X., Shahidehpour, M., Alabdulwahab, A., and Abusorrah, A. (2015). Optimal Expansion Planning of Energy Hub with Multiple Energy Infrastructures. *IEEE Trans. Smart Grid* 6 (5), 2302–2311. doi:10.1109/TSG.2015.2390640

Conflict of Interest: Authors XW and TP were employed by the company China Electric Power Research Institute.

The remaining authors declare that the research was conducted in the absence of any commercial or financial relationships that could be construed as a potential conflict of interest.

Publisher's Note: All claims expressed in this article are solely those of the authors and do not necessarily represent those of their affiliated organizations, or those of the publisher, the editors and the reviewers. Any product that may be evaluated in this article, or claim that may be made by its manufacturer, is not guaranteed or endorsed by the publisher.

frontiers | Frontiers in Energy Research

ORIGINAL RESEARCH
published: 01 July 2022
doi: 10.3389/fenrg.2022.921335

Improving Power Grid Resilience Under Extreme Weather Conditions With Proper Regulation and Management of DERs—Experiences Learned From the 2021 Texas Power Crisis

*Weiqi Pan and Yang Li**

Department of Electrical Engineering, Southeast University, Nanjing, China

Due to climate change in the past few decades, extreme weather conditions have become more frequent and caused power outages with enormous damage to the well-being and the economy. Affected by extremely cold weather, the 2021 Texas power crisis deployed the most significant firm load shedding in US history, costing the economy $10 billion to $20 billion *via* direct and indirect loss. The North American Electric Reliability Organization (NERC), Federal Energy Commission (FERC), and other literature studies conducted post-event analysis from the perspective of conventional power systems' planning and operation, and little discussion was made on the distributed energy resources (DERs). Based on the actual data on the 2021 Texas power crisis, this study analyzed the role of DERs in this event and showed the importance of effective regulation and management in improving power grid resilience under such extreme weather conditions.

Keywords: grid resilience, extreme weather, power crisis, DERs, regulation and management

OPEN ACCESS

Edited by:
Qingxin Shi,
North China Electric Power University, China

Reviewed by:
Pudong Ge,
Imperial College London, United Kingdom
Sheng Chen,
Hohai University, China

****Correspondence:***
Yang Li
li_yang@seu.edu.cn

Specialty section:
This article was submitted to Smart Grids, a section of the journal Frontiers in Energy Research

Received: *15 April 2022*
Accepted: *19 May 2022*
Published: *01 July 2022*

Citation:
Pan W and Li Y (2022) Improving Power Grid Resilience Under Extreme Weather Conditions With Proper Regulation and Management of DERs—Experiences Learned From the 2021 Texas Power Crisis. Front. Energy Res. 10:921335. doi: 10.3389/fenrg.2022.921335

1 INTRODUCTION

In the past few decades, extreme weather conditions have occurred frequently due to climate change. Such weather conditions pose challenges to the power system reliability and have become the leading causes of large-scale power outages, causing enormous damage to the well-being and the economy (Jufri et al., 2019). From February 8th to 20th, 2021, the severe winter storm Uri swept across Texas and the south-central areas in the US and caused the 2021 Texas power crisis in the bulk electric system (BES) operated by the three independent system operators and regional transmission organizations (ISO/RTOs), namely, the Electric Reliability Commission of Texas (ERCOT), the Southwest Power Pool (SPP), and the Midcontinent Independent System Operator (MISO) (Federal Communications Commission, 2021).

In the south-central US, this event is the fourth major power system event caused by extreme weather conditions over the past 10 years, following the event in February 2011, January 2014, and January 2018. As shown in **Figure 1**, the 2021 Texas power crisis is more destructive and long-lasting than the previous cold weather events (Sperstad et al., 2020). **Figure 1A** shows the lowest temperature is 28°C below the average daily local temperature, and the largest unavailable generation due to cold weather is over 60 GW during the event in the affected area. Meanwhile,

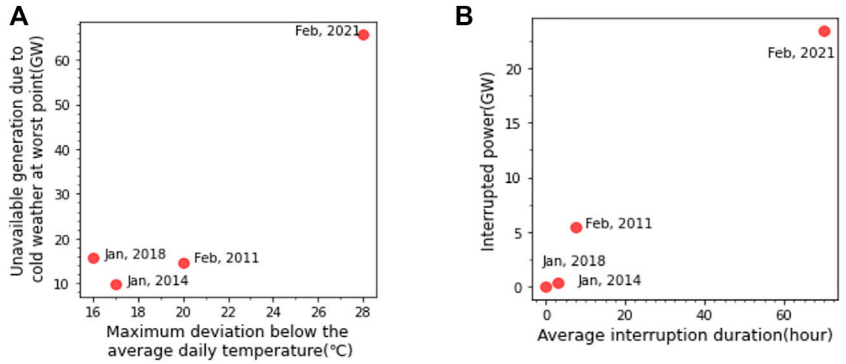

FIGURE 1 | Consequence diagrams comparing the four power outages in the previous 10 years in south-central US by unavailable generation VS tempearture **(A)**, and interrupted power VS interruption duration **(B)**.

Figure 1B shows the high magnitude and the long-lasted time of the power interruption in the 2021 event as compared to the previous events. It needs to be noted that the manual firm load shed is the largest in US history over 24 GW, and a few areas were without power for 4 days (Federal Energy Regulatory Commission, 2021).

Regarding the unprecedented damaging results and negative cascading impacts, the 2021 Texas power crisis has drawn significant attention from the both power industry and academia. The North American Electric Reliability Organization (NERC) and the affected ISO/RTOs have already published the official reports revealing the event's details. In addition, the Federal Energy Commission (FERC) has investigated and released an official report (Midcontinent Independent System Operator, 2021a; Southwest Power Pool, 2021a; the University of Texas at Austin and Energy Institute, 2021). The official reports attribute the direct reasons for massive generation outages to the inadequate winter operation preparedness of generation units and natural gas production infrastructure. Meanwhile, in academia, researchers have examined this event from multiple aspects. Busby et al. (2021) analyzed the subsequent cascading effects after load shedding on Texas' economy and politics. Yan et al. (2021) showed the importance of power grid safety management, emergency response, power grid differentiation planning, and emergency material reserves in preventing such power system outages under extreme weather conditions. Wu et al. (2021) quantitatively provided access to the impact of generator weatherization, demand response, and energy storage on mitigating this power outage. Zhang et al. (2022) identified this event as the energy insufficiency-caused power outages which are primarily caused by the insufficient fuel supply of natural gas. Hence, official reports and the literature analysis of this event are provided from the perspective of conventional power systems' planning and operation.

Meanwhile, in south-central US systems which had a high penetration of renewables, natural gas generators take major responsibilities in maintaining the real-time balance between power supply and demand. However, as those generators are

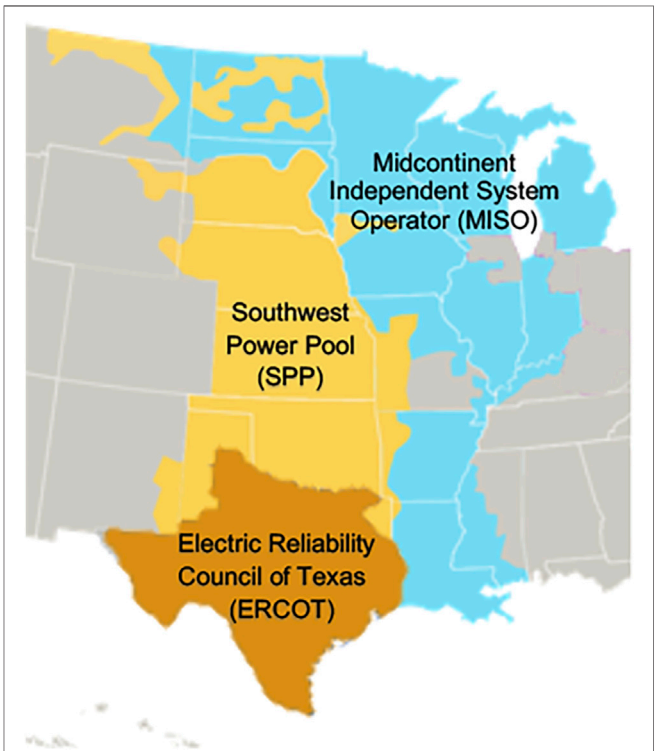

FIGURE 2 | Areas affected by this event.

expensive, their limited capacity can hardly cope with the increased uncertainties from both supply and demand sides in the near future. In addition, for long-lasting extreme weather conditions such as in February 2021, natural gas generators may suffer from the issue of gas supply as what has happened in the 2021 Texas power crisis. It should be noted that the coordinated control of flexible distributed energy resources (DERs) can help maintain the supply and demand balance; the long-term regulations and management of DERs can also be useful in facilitating the system operation in long-lasting extreme weather conditions. However, little discussion was made on

TABLE 1 | Comparison of the affected ISO/RTOs in the 2021 Texas power crisis.

Region	Installed capacity (MW)	Peak load in winter 2021 (MW)	Maximum load shed capacity (MW)	Duration (h)
ERCOT	104,500	69,871	20,000	70
SPP	94,648	43,661	2,718	5.3
MISO South	41,865	29,946	700	14.3

the regulation and management of DERs under extreme weather conditions.

Hence, based on the actual data on the 2021 Texas power crisis, this study analyzes the importance of effective regulation and management of DERs in improving power grid resilience under such extreme weather conditions. The rest of this article is organized as follows: **Section 2** describes the event timeline and detailed facts. **Section 3** analyzes the problem and potential effects from the perspective of regulation and management of DERs. **Section 4** concludes this article.

2 EVENT SUMMARY

2.1 Basic Information of the Affected Region

In the US, three main interconnections, the Eastern Interconnection, the Western Interconnection, and ERCOT, connect the regional grids in a physical network structure and conduct the cross-regional transmission for reliability and commercial purposes. The interconnections operate independently with limited electricity transmission capacity between them. The power systems affected in this event include the areas operated by ERCOT, SPP, and MISO. Their regions are as shown in **Figure 2**, and the event-related data are shown in **Table 1**.

The ERCOT serves 90% load in Texas. As shown in **Table 1**, the installed generation capacity in the ERCOT is over 100 GW (Climate Central, 2014). SPP serves 14 states in the central US with over 94 GW generation capacity (Midcontinent Independent System Operator, 2021b). MISO serves 15 states across the central US with over 198 GW generation capacity (Electric Reliability Council of Texas, 2020). However, only the south part of MISO with 42 GW installed generation capacity was affected in the event. Meanwhile, the ERCOT has limited interstate transmission capacity and operates independently from the US Eastern Interconnection and US Western Interconnection. The total transmission capacity was 1220 MW, which only accounts for 1.8% of the system peak load (Electric Reliability Council of Texas, 2022a). Thus, its maximum load shed reaches 20,000 MW and lasts 70 h. Different from ERCOT, SPP and MISO are connected by the 193 transmission lines and are jointly connected to the Eastern Interconnection, which provides sufficient transmission availability (Southwest Power Pool, 2021b). Thus, their maximum load shed and duration are significantly lower.

As for the regulation, the independent agency FERC is responsible for regulating the interstate transmission and wholesale of the electricity market and the interstate commerce and transportation of the oil and gas market. Oversight by FERC, the NERC is responsible for improving the reliability and security of the power systems over the nation. The specific duties include developing and enforcing the reliability standards, monitoring BES, and assessing the system adequacy annually. The regional electricity, gas, and oil retail services are regulated through the public utility commissions or equivalent. For instance, within Texas, the electricity market is mainly regulated by the Public Utility Commission of Texas (PUCT), and the intrastate oil and gas industry is regulated by the Railroad Commission. It is noticeable that because of the relative independence of ERCOT, the electricity market is largely unregulated by FERC rules.

2.2 Timeline of the Event

The cold weather-related power outage (the 2021 Texas power crisis) caused cascading damages to over 4.5 million people, and at least 210 people were dead due to power shortage-related reasons (Federal Energy Regulatory Commission, 2021). According to the Federal Reserve Bank of Dallas (FRBD), this event costed the economy $10 billion to $20 billion *via* direct and indirect loss (Federal Reserve Bank of Dallas, 2021). For the BES reliability, 1045 individual BES generating units, with a combined nameplate capacity of over 192 GW in ERCOT, SPP, and MISO, experienced over 4000 times of outages, derates, and failures to start; several transmission lines tripped or had congestion problems; the curtailed load was not fully restored until the temperature rose after February 19th.

The worsening situation of the power grid operation was related to the dropping temperature (Eskandarpour et al., 2017). In this event, the extreme weather condition has two distinct characteristics. First, the below-average freezing temperature lasted relatively long, from February 8th to February 18th. Second, the temperature was much lower than the historical average daily temperature. Specifically, the climate was mild in early February with an average temperature of 15°C in the south-central US. From February 8th to 14th, the average temperature dropped to 0°C, and some regions experienced extreme weather conditions such as freezing rains or snowstorms. The severe cold weather lasted until the 18th, when the average temperature dropped as low as −20°C (Wundergroud, 2022).

With the clear deviation of weather conditions along with the event process, this study examines the performance of the power grid under different phases based on weather conditions.

2.2.1 Phase 1 (Early February to February 8th)

By early February, ERCOT, SPP, and MISO were already aware of the upcoming extreme weather conditions in the mid-February

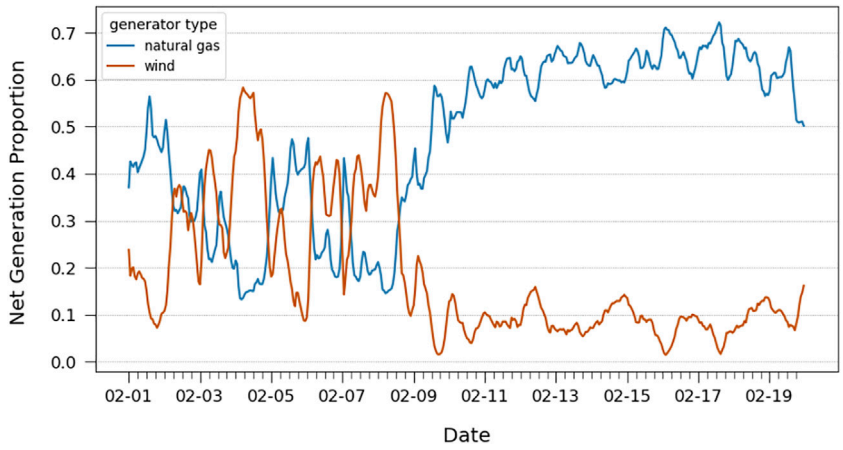

FIGURE 3 | Net generation proportion.

and had issued winterization preparation notices to the system generator owners (GOs), generator operators (GOPs), transmission owners (TOs), and transmission operators (TOPs), suggesting a series of preparation actions, including updating the information of the generation capacity, checking the fuel supply, and implementing the winterization preparation process based on the generation type (Electric Reliability Council of Texas, 2021a).

In response to the alert, all types of generators declared a series of winter operation preparedness actions. According to the record, the response actions of the wind generators included performing annual service and winterization checks, canceling planned maintenance, and ordering additional nitrogen for maintaining the hydraulic braking system; the response actions of the solar units included preparing inverters by checking the functionality of heaters and ensuring adequate temperature settings and functioning alarms; the response actions of natural gas-fired units included checking freeze protection, checking natural gas inventories and placing natural gas commodity order in advance, and testing heating supplies and protective equipment (Federal Energy Regulatory Commission, 2021).

Meanwhile, the natural gas production infrastructures, closely coupled with the natural gas-fired generation units, also declared the winterization preparations. The preparations mainly focused on freezing protection, fluid management, and staffing communications for the natural gas production side. A few gas production facilities shut down before the event in the case of potential freezing issues. The preparations focused on the electric power supply, equipment maintenance, and personnel deployment for the natural gas-processing side. The pipeline facilities focused on the storage activity reports and arranging staffing at critical field operations.

2.2.2 Phase 2 (February 8th to February 14th)

As the temperature decreased, the load demand for heating increased sharply. With an average daily electricity demand increase of 18% from February 9th to February 14th, the electricity demands in affected areas were approaching the historical peak of wintertime by the end of *Phase 2* (Electric Reliability Council of Texas, 2021c). Meanwhile, affected by the extreme weather conditions, the generation capacity on the supply side began declining. Although most generation units had declared the preparations for cold weather in *Phase 1*, most of the units still experienced freezing, transmission system issues, or failure to operate under low ambient temperature. Among the affected generation units, the generation capacity of the wind turbines is mostly reduced due to freezing issues. Under cold weather, the precipitation and condensation caused icy layers on turbine blades, further leading to the balancing, bearing, and other problems for wind turbines. In the event, wind turbine outages and derates caused by freezing issues accounted for 23% of the total outages (Federal Communications Commission, 2021; Southwest Power Pool, 2021b; Eskandarpour et al., 2017). Thus, the operators utilized natural gas generation to compensate for the deficit caused by wind turbines. As shown in **Figure 3**, compared to the net generation proportions at the beginning of February, the proportion of wind generation declined steadily since February 9th, while the natural gas generation proportion has been increasing to compensate for the loss in wind generation (Energy Information Administration, 2021a). At this phase, the BES reliability was still maintained.

2.2.3 Phase 3 (February 15th to February 20th)

Along with the deteriorating weather condition, the large-scale and long-lasted decline in the generation capacity occurred in all the affected power systems. With a total of 95 GW, the unavailable generation reached its peak on February 17th, accounting for 37% of the total installed capacity in the affected areas (Federal Energy Regulatory Commission, 2021). All the system operators deployed the multi-stage emergency energy actions (EEA) to utilize the demand resources to maintain the system's reliability. The load shed in ERCOT, SPP, and MISO is shown in **Figure 4** (Electric Reliability Council of Texas, 2021b). Specifically, the following actions were taken:

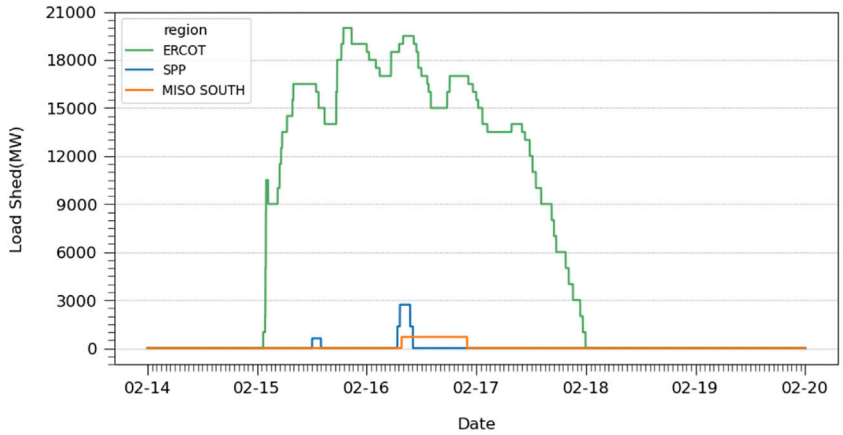

FIGURE 4 | Load shed in ERCOT, SPP, and MISO South during the event.

The ERCOT initiated the EEA procedures to maintain the dropping system frequency from the night on the 14th to the morning on the 19th. At 0:15 a.m. on February 15th, EEA 1 was declared when the reserve dropped below the minimum responsive reserve requirement of 2300 MW. The demand resource 30-min Emergency Response Service (ERS-30) was deployed for 847.15 MW (Electric Reliability Council of Texas, 2022b). At 1:07 a.m. on February 15th, EEA 2 was declared. The demand resources 10-min Emergency Response Service (ERS-10) and the responsive reserve service (RRS) were declared successively for 51.6 and 423 MW load reduction (Electric Reliability Council of Texas, 2022c). At 1:20 a.m., when the frequency dropped to 59.938 Hz, ERCOT announced EEA 3 and instructed the immediate firm load reduction. The load shedding lasted from the 15th to the 18th, and the reduction peak was at 19:00 on February 15th with up to 200,000 MW, which accounts for approximately 37.7% of ERCOT's peak demand. At 10:00 a.m. on February 19th, ERCOT lowered the emergency level to EEA 2. At 11:00 a.m. on the same day, ERCOT lowered the level to EEA 1, which indicates that ERCOT has been restored from the system emergency states (University of Texas at Austin and Energy Institute, 2021).

SPP is connected with the Eastern Interconnection through MISO, having more power transmission capacity than ERCOT. However, due to the transfer limit during the event, when the importable power supply decreased, SPP could not maintain system balance and declared EEA from February 15th. At 5:00 a.m. on February 15th, at the risk of not meeting the required operating reserves, SPP began EEA 1 and made public appealing to the customers to reduce power consumption. At 7:22 a.m. on February 15th, as the unplanned generation outages exceeded 3300 MW, SPP declared EEA 2 and began interrupting interruptible, curtailable load and utilizing demand resources. At 10:08 a.m., because of the reduced imports and insufficient reserves, SPP stated EEA 3, under which could terminate the load export and request firm load shedding (Southwest Power Pool, 2021a).

MISO is directly connected with the Eastern Interconnection. In this event, MISO imported large amounts of power flows to maintain system stability. However, the inadequate generation forced MISO to declare EEA on the 16th. At 4:59 p.m. on February 16th, MISO declared EEA 2. At 6:40 p.m. on February 16th, MISO declared EEA3. At 8:41 p.m.; all the curtailed loads were restored (Midcontinent Independent System Operator, 2021a).

3 EVENT ANALYSIS

At the worst point, the total unavailable generation accounted for 38.8, 33.2, and 40.2% of the installed capacity in ERCOT, SPP, and MISO South, respectively, due to freezing issues and fuel supply shortage (Federal Energy Regulatory Commission, 2021). However, the scale of load shedding in ERCOT is remarkably higher and lasted for the longest time. The underlying reasons for this difference are complex and could be partly explained by the varying interconnection transmission capabilities among the three regions. During this event, SPP conducted the power inflows, ranging from 4000 to 6000 MW, and MISO South imported 3000 MW. Compared to SPP and MISO, which have abundant transmission capability with the Eastern Interconnection, ERCOT is restrained by the limited transmission capability to conduct power import to alleviate system imbalance. Hence, this section targets ERCOT and analyzes the impact of regulatory and management on DERs.

3.1 Winter Assessment of Distributed Generation

3.1.1 Inaccurate Assessment of Winter Generation Capability

After the power outage event in February 2011, ERCOT scheduled the winterization checking process to assess the generator operating capacity for 75 to 80 generators annually. ERCOT evaluates the generator winter preparation based on the

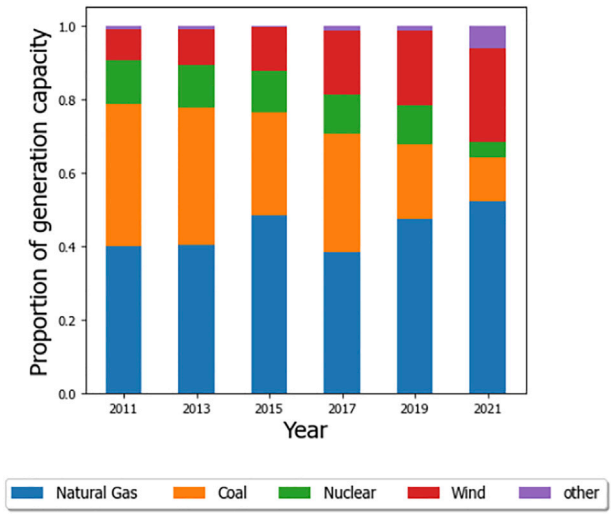

FIGURE 5 | Structure of installed generation capacity in ERCOT from 2011 to 2021.

self-reported questionnaire instead of the on-site visit. In the survey just before the 2021 event, 96% of the investigated generators declared they completed winterization. However, the post-event analysis demonstrated that 82% of the generators that have submitted winter preparation reports experienced at least once or more outages, derates, and start failures.

The overestimation of the winter generation capability can be categorized into two aspects. First, the winter inspection checking list has not been modified since 2011. However, the installed capacity of the power generators has changed over the past years, as shown in **Figure 5**. Based on Electric Reliability Council of Texas (2021d), the generation proportions of wind turbine generators and natural gas-fired generators increased dramatically from 8.5 to 26% and 40 to 52%, while the generation proportion of coal-fired generation decreased from 22 to 6%. Compared to coal-fired generators, wind turbines are more vulnerable under cold weather conditions. Second, most of the winter preparation data are self-reported, including the newly integrated distributed generators. As data validity cannot be ensured, ERCOT could hardly evaluate the winter generation capability accurately.

3.1.2 Lack of Intention to Upgrade the Cold Weather Critical Components

As the central and south US have temperature climates, most power generation facilities do not have the ability to operate in extremely cold winter. Wind turbines, solar panels, and natural gas production facilities are all vulnerable to freezing weather. Therefore, after the rotational load shedding event in 2011, ERCOT once made suggestions to the generators and natural gas production facilities to upgrade the cold weather critical components (Federal Energy Regulatory Commission and the North American Electric Reliability Corporation, 2011). However, regarding the concerns about retrofitting, most generation units lack intention to make substantial upgrades. Because conventionally extreme cold weather was considered a small-probability event, the upgraded generation units with higher operating costs may become less competitive in the market most of the time. Meanwhile, in extreme cold weather, the generators which have not been upgraded could shut down without being punished.

Nonetheless, from the perspective of social welfare, the investment in upgrading the cold weather critical components of the power system could effectively reduce the loss in extreme weather conditions. Using the value of lost load (VOLL) as the measurement, FRBD evaluated the total social loss as over $4.3 billion (Federal Reserve Bank of Dallas, 2021). Meanwhile, the cost of winterizing the piece of equipment for each gas plant is between $50,000 and $500,000, suggesting a total cost of up to $9 million to upgrade the 162 natural gas-fired generation units in Texas; The cost of installing the internal warming equipment for the wind turbines is up to $40,000 per blade, making it costly and infeasible to retrofit for all the 13,000 wind turbines in Texas (Federal Energy Regulatory Commission and the North American Electric Reliability Corporation, 2011). Hence, compared to the loss in social welfare, winterization upgrading investments are cost-effective.

3.2 Deployment of Demand-Side Resources

In Texas, the residential sector generally consumes 37% of the total electricity generation. As 60% of households use electricity as the primary heating fuel (White et al., 2021; US Energy Information Administration, 2019), the residential section takes approximately 51% of total demand during winter peak hours, followed by 26% of the large commercial and industrial and 23% of the small commercial loads. Consequently, with extreme weather conditions, the residential electricity demand increased sharply. In *phase 2* of the 2021 event, driven by the extreme cold weather, the actual load was higher than the forecasted load, especially during peak hours, as shown in **Figure 6** (Energy Information Administration, 2021b; Electric Reliability Council of Texas, 2021c). From February 9th to 14th, the mean absolute percentage error (MAPE) between the actual load and the day ahead forecast was 8.9%, which indicates a significant error in load prediction compared to the yearly average MAPE in 2020 of 1.7%.

In *phase 3* of the 2021 event, EEA showed great importance in utilizing demand resources to stabilize system frequency, relieve transmission congestion, and maintain system operation. However, during this event, the deployment of demand-side resources suffers from two issues that limit their values.

3.2.1 Failure on Identifying Critical Loads Related to Natural Gas Production

As aforementioned, the flexible balancing resources in ERCOT relied on the natural gas-fired generators. Thus, when the system encountered unprecedented demands and the loss of wind generation for consecutive days, the proportion of natural gas generation relative to the total generation increased from an average of 43% in 2021 to 72%, as shown in **Figure 3**. Hence, the need for natural gas fuel increased during the 2021 event.

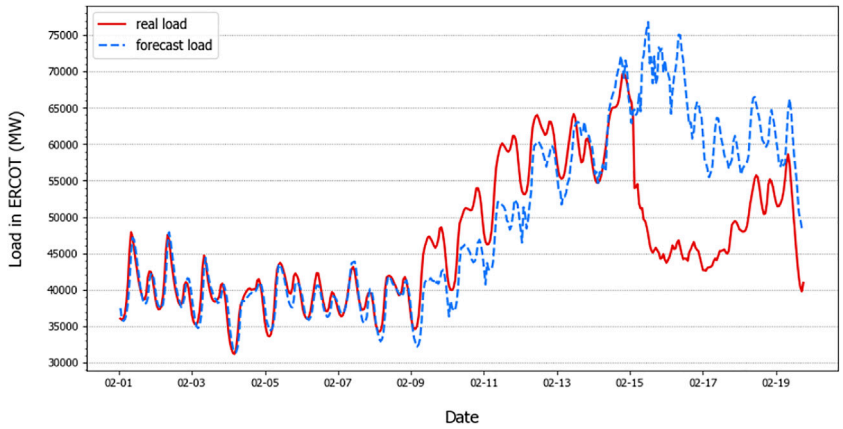

FIGURE 6 | Comparison of real and forecast load from February 1st to February 20th in 2021.

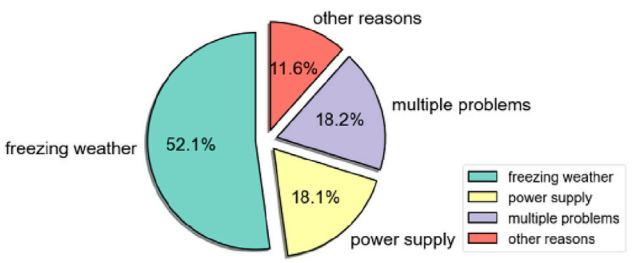

FIGURE 7 | Cause of the natural gas production decline from 2021/2/14 9:00 a.m. to 2021/2/15 9:00 a.m. (measured by the natural gas production volume).

However, all-natural gas production loads were classified as curtailable loads, and some pieces of key equipment involved in the natural gas production were turned off. Consequently, the loss of power supply to natural gas infrastructure caused 23.5 percent of the decline in natural gas production. As shown in **Figure 7**, power supply issues account for an 18.1% loss in natural gas production from February 14th to 15 February 2021.

In practice, the regulations of the PUCT for the Texas state that the load units need to apply for becoming an important load to its transmission operator, and the transmission operator would then collect the self-reported information and report to PUCT every year. Under such a rule, the system operator only has the self-declared loads (Texas Tribune, 2021). For the loads for natural gas production, processing, and transmission which are not self-declared, system operators had classified them as curtailable loads. This phenomenon aggravates the fuel supply shortage for the natural gas-fired generators.

3.2.2 Late Utilization of Demand-Side Resources

The concept of demand-side resources was initially proposed to reduce energy consumption to alleviate the pressure on the supply side of the system to manage the energy. After the large-scale integration of clean energy, the demand side resource management has gradually shifted to a "power-based" approach on a shorter time scale to balance real-time power supply and demand and provide auxiliary services such as frequency regulation and capacity reserve.

In *phase 2* of the 2021 event, although system operators predicted the long-lasting extreme weather with rain and snow, they did not issue early warnings, or power reserve appeals to the users until the wind turbines were interrupted and fuel supply declined. Until *phase 3*, when the load in the affected areas approached the history peak and the generation declined, ERCOT and SPP started to utilize demand-side resources with the power reserve appeal on February 14th (Southwest Power Pool, 2021a). Hence, the system operator did not act early and failed to take advantage of "the energy-based" property of demand-side resources in this event.

Energy not served (ENS) is used to evaluate the amount of insufficiency of generation relative to the forecast demand, calculated by taking the integral of load shedding over the blackout time (Menati and Le, 2021). As shown in **Figure 8**, in the period of EEA in ERCOT, the ENS was estimated as 1170 GWh. With a large amount of demand-side energy consumption in Texas, exploring the potential of demand-side resources to maintain the level of natural gas storage can be valuable.

Long-term energy management is defined as the pre-event energy conservation education or programs to encourage customers to voluntarily reduce electricity consumption during the peak load hours to alleviate system peaking-load operation pressure and avoid system blackouts (Electric Reliability Council of Texas, 2021a). The timely and efficient notifications to the customers could help reduce the peak demand (Darby and McKenna, 2012). In the power system event in California in the summer of 2020, after predicting extremely high demand, CAISO effectively sent flex alerts to users through mobile apps, social media, and press media, making public appeals to users to reduce electricity consumption on August 17th and 18th. Hence, the actual peak electricity usage became 4972 MW and 3488 MW,

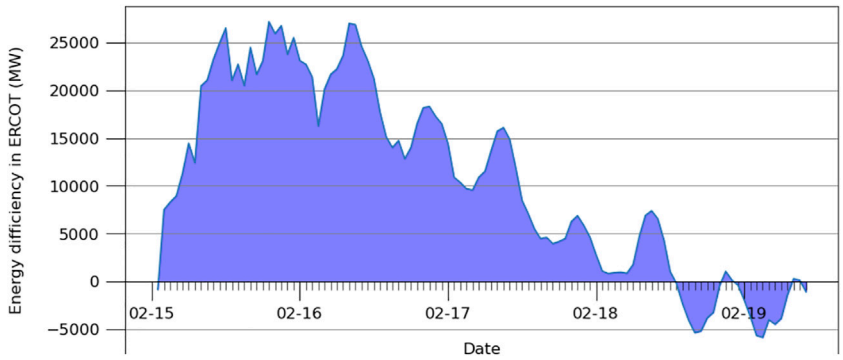

FIGURE 8 | Energy deficiency in ERCOT during EEA.

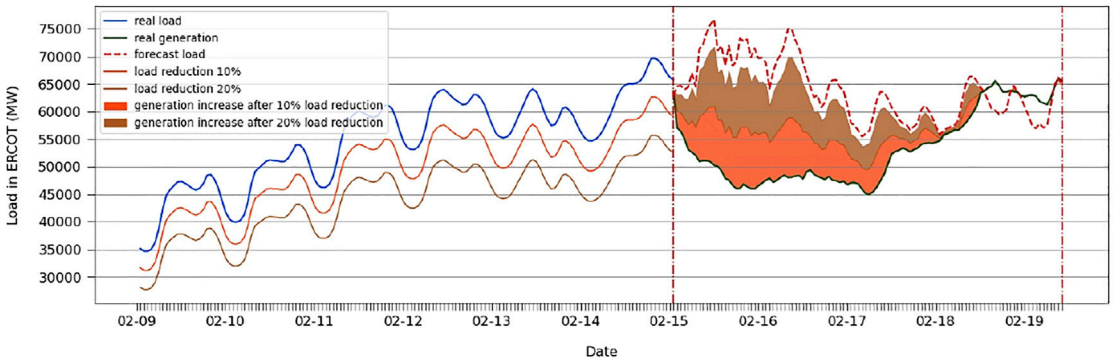

FIGURE 9 | Effect of pre-event load conservation on mitigating energy deficiency.

lower than the day-ahead peak demand forecast, and further avoided the large-scale firm load shedding event (Hu et al., 2020).

In the Texas event, the operators made public energy conservation appeal by the 14th. The system had experienced significant power outages and unexpectedly high demand, which exacerbated the system imbalance. Thus, the public conservation appeals did not have expected effects on load reduction. As the cold temperature was predicted to be long-lasting and the load demand had already exceeded the load forecast, the load demand pattern in the extreme weather event was not fully addressed, and the public was not notified of the possible power system blackouts. Thus, as the coldest temperature arrived, the users lacked intention and adequate preparation to reduce electricity usage, which was reflected by the rising demand after public appeals.

Due to the predicted long-lasting duration of this event, the public should be educated before the coldest temperature arrives on the night of February 14th. Except for the monetary-incentive demand response programs, the effects of the high impact, low-cost information, and education programs should be valued. The electricity conservation target could be achieved by encouraging users' behavioral change by providing information on past energy use, conservation strategies, or peer consumption. The longer-term of such programs would conduct more energy savings (Delmas et al., 2013). Thus, the potential of pre-event load reduction on mitigating ENS is examined. It is assumed that the natural gas storage saved from pre-event load demand conservation could be used to compensate for the primary energy shortage during the coldest weather condition. Based on the publicly available data, the estimation of the saved natural fuel storage can be expressed as follows:

$$\text{natural gas fuel saved (MMBtu)} = r \cdot c \cdot h \sum_{1}^{t} P_t q_t, \qquad (1)$$

where t is the time period from February 9th to February 14th, measured in hours; q is the ratio of the natural gas-fired generation capacity over the total generation at the time t; r is the average load reduction rate; the average amount of natural gas c used to generate a kilowatt-hour (kWh) is assumed to be 7.43 cubic feet; and the average heat content per one thousand cubic feet (Mcf) of natural gas h equals 1.037 MMBtu.

Figure 9 shows the load reduction during the pre-outage time period and the incremental generation capacity during the load shed period. It is estimated that a 25% reduction of daily average electricity consumption between February 9th and 14th could fully compensate for the energy deficiency during the power

TABLE 2 | Effect of average load reduction on natural gas fuel storage.

Average load reduction (%)	Increase in natural gas storage (MMBtu)	Incremental proportion relative to the initial energy storage in Texas (%)
5	1,822,644	7.5
10	3,529,138	15.1
15	5,293,708	22.8
20	7,058,277	30.4
25	9,113,221	38.0

outage. Although it is practically hard for the end-users to reduce the electricity usage by an average daily amount of 25% during such extreme weather, the value of load resources could not be underestimated. **Table 2** demonstrates the incremental proportion relative to the initial energy storage on February 15th under different amounts of average daily reduction.

Because of the abundant natural resources in natural gas and wind energy, ERCOT has been leading in transitioning to the coal-light generation structure that extensively explored the potential of clean energies. The transition has shown significant improvement in energy efficiency and decarbonization. When the frequently occurred power outages could warn the unpredicted system vulnerabilities related to natural gas production under the extreme weather conditions and underscore the importance of primary energy supply during the extremely cold weather conditions. Long-term demand-side management could efficiently alleviate such fuel shortage pressure through effective and efficient programs in a costly manner.

4 CONCLUSION AND DISCUSSION

In the past few decades, extreme weather conditions have been rising due to global climate change. For the power grid operation, the observed outages to the bulk electric system showed a significant increase in the weather-related events, leading to enormous damage to people and the economy.

This study examined the 2021 Texas power crisis caused by the extremely cold weather, mainly from the perspective of DERs' regulation and management. Based on the public data, it is estimated that the natural gas fuel supply saved by a daily average load reduction of 25% in ERCOT before the coldest weather could compensate for the total energy deficiency during the event. Also, the reliable power supply to the critical natural gas production loads could improve another 15% of the natural gas supply. Although it is practically hard to reach the daily average of 25% of load reduction, the value of the long-term demand-side "energy" management should be valued. Also, it is essential to realize the tight coupling relationship between natural gas production and electricity supply to identify the critical loads. Hence, the effective regulations and management of DERs have proven vital for improving the power grid resilience under such extreme weather conditions.

DATA AVAILABILITY STATEMENT

The original contributions presented in the study are included in the article/Supplementary Material; further inquiries can be directed to the corresponding author.

AUTHOR CONTRIBUTIONS

WP and YL conceived and designed the research. WP and YL carried out the data search. WP carried out the simulations and analyses. All authors contributed to the discussions on the method and the writing of this manuscript.

REFERENCES

Busby, J. W., Baker, K., Bazilian, M. D., Gilbert, A. Q., Grubert, E., Rai, V., et al. (2021). Cascading Risks: Understanding the 2021 Winter Blackout in Texas. *Energy Res. Soc. Sci.* 77, 102106. doi:10.1016/j.erss.2021.102106

Climate Central (2014). *Blackout: Extreme Weather, Climate Change and Power Outages*. Princeton, NJ: Climate center. Available at: https://www-ourenergypolicy-org.vpn.seu.edu.cn:8118/wp content/uploads/2014/04/climate-central.pdf (Accessed April 14, 2022).

Darby, S. J., and McKenna, E. (2012). Social Implications of Residential Demand Response in Cool Temperate Climates. *Energy Policy* 49, 759–769. doi:10.1016/j.enpol.2012.07.026

Delmas, M. A., Fischlein, M., and Asensio, O. I. (2013). Information Strategies and Energy Conservation Behavior: A Meta-Analysis of Experimental Studies from 1975 to 2012. *Energy Policy* 61, 729–739. doi:10.1016/j.enpol.2013.05.109

Electric Reliability Council of Texas (2021b). *Data from:* Available Generation and Estimated Load without Load Shed Data. Austin, TX: Electric Reliability Council of Texas. Available at: https://www.ercot.com/files/docs/2021/03/18/Available_Generation_and_Estimated_Load_without_Load_Shed_Data.xlsx.

Electric Reliability Council of Texas (2021d). *Data from:* Generation Fuel Mix Report 2007–2020. Austin, TX: Electric Reliability Council of Texas. Available at: https://www.ercot.com/files/docs/2021/03/10/FuelMixReport_PreviousYears.zip.

Electric Reliability Council of Texas (2021c). *Data from:* Hourly Load Data Archives. Austin, TX: Electric Reliability Council of Texas. Available at: https://www.ercot.com/gridinfo/load/load_hist.

Electric Reliability Council of Texas (2022c). Earn Revenue and Protect Your Equipment in the ERCOT Responsive Reserve Service Program. Austin, TX: Electric Reliability Council of Texas. Available at: https://www.ercot.com/files/docs/2021/12/23/1092NPRR-09%20ERCOT%20Comments%20122321.docx (Accessed April 14, 2022).

Electric Reliability Council of Texas. 2022b Emergency Response Service. Austin, TX: Electric Reliability Council of Texas. Available at: https://www.ercot.com/services/programs/load/eils/ [Accessed April 14, 2022].

Electric Reliability Council of Texas (2020). *ERCOT DC Tie Operations*. Austin, TX: Electric Reliability Council of Texas. Available at: https://www.ercot.com/files/docs/2020/07/30/ERCOT_DC_Tie_Operations_Document.docx.

Electric Reliability Council of Texas (2022a). *ERCOT Fact Sheet*. Austin, TX: Electric Reliability Council of Texas. Available at: https://www.ercot.com/files/docs/2022/02/08/ERCOT_Fact_Sheet.pdf.

Electric Reliability Council of Texas (2021a). Extreme Cold Weather Expected to Result in Record Electric Use in ERCOT Region. Austin, TX: Electric Reliability Council of Texas. Available at: https://www.ercot.com/news/release?id=1f851612-b1c6-3806-ba84-f192b23083c9 (Accessed April 14, 2022).

Electric Reliability Council of Texas Public (2021). *Preliminary Report on Causes of Generator Outages and Derates during the February 2021 Extreme Cold Weather Event*. Austin, TX: Electric Reliability Council of Texas. Available at: https://www.ercot.com/files/docs/2021/04/28/ERCOT_Winter_Storm_Generator_Outages_By_Cause_Updated_Report_4.27.21.pdf.

Energy Information Administration (2021b). *Data from: Day-Ahead Demand Forecast*. Washington, DC: Energy Information Administration. Available at: https://www.eia.gov/opendata/qb.php?category=3389883&sdid=EBA.ERCO-ALL.DF.H.

Energy Information Administration (2021a). *Data from:* Net Generation by Energy Source. Washington, DC: Energy Information Administration. Available at: https://www.eia.gov/opendata/qb.php?category=3390137.

Eskandarpour, R., Khodaei, A., and Arab, A. (2017). "Improving Power Grid Resilience through Predictive Outage Estimation," in *North American Power Symposium (NAPS)*, 1–5. doi:10.1109/naps.2017.8107262

Federal Communications Commission (2021). Winter Storm Uri. Washington, DC: Federal Communications Commission. Available at: https://www.fcc.gov/uri (Accessed April 14, 2022).

Federal Energy Regulatory Commission and the North American Electric Reliability Corporation (2011). *Outages and Curtailments during the Southwest Cold Weather Event of February 1–5, 2011*. Atlanta, GA: Ferc.Gov. Available at: https://www.ferc.gov/sites/default/files/2020-04/08-16-11-report.pdf.

Federal Energy Regulatory Commission (2021). *The February 2021 Cold Weather Outages in Texas and the South-Central united states: FERC, NERC and Regional Entity Staff Report*Washington, DC: Federal Energy Regulatory Commission. Available at: https://www.ferc.gov/media/february-2021-cold-weather-outages-texas-and-south-central-united-states-ferc-nerc-and.

Federal Reserve Bank of Dallas (2021). 2021 Deep Freeze Justifies Weatherization. Available at: https://www.dallasfed.org/research/economics/2021/0415.aspx (Accessed April 2nd, 2018).

Hu, Q., Ding, H., Ding, H., Chen, X., Chen, T., Ding, Y., et al. (2020). Analysis of Texas Blackout in 2021 and its Enlightenment to Power System Planning Management. *Automation Electr. Power Syst.* 24 (44), 11–18. Available at: https://kns.cnki.net/kcms/detail/detail.aspx?

Jufri, F. H., Widiputra, V., and Jung, J. (2019). State-of-the-art Review on Power Grid Resilience to Extreme Weather Events: Definitions, Frameworks, Quantitative Assessment Methodologies, and Enhancement Strategies. *Appl. Energy* 239, 1049–1065. doi:10.1016/j.apenergy.2019.02.017

A. Menati and X. Le (Editors) (2021). *A Preliminary Study on the Role of Energy Storage and Load Rationing in Mitigating the Impact of the 2021 Texas Power Outage*. North American Power Symposium (NAPS). doi:10.48550/arXiv.2111.12908

Midcontinent Independent System Operator (2021a). *Arctic Blast Creating Tight Operating Conditions in the South Region*. Available at: https://cdn.misoenergy.org/2021%20Arctic%20Event%20Report554429.pdf.

Midcontinent Independent System Operator (2021b). MISO Corporate Fact Sheet. Available at: https://www.misoenergy.org/about/media-center/corporate-fact-sheet/ (Accessed April 14, 2022).

Southwest Power Pool (2021b). Fast Facts. An Overview of the SPP System. Available at: https://www.spp.org/about-us/fast-facts/.

Southwest Power Pool (2021a). *Review of Southwest Power Pool's Response to the February 2021 Winter Storm: Analysis and Recommendations*. Available at: https://www.spp.org/Documents/65037/Comprehensive%20Review%20of%20SPP' s%20Response%20to%20the%20Feb.%202021%20Winter%20Storm%202021%2007%2019.pdf.

Sperstad, I. B., Kjølle, G. H., and Gjerde, O. (2020). A Comprehensive Framework for Vulnerability Analysis of Extraordinary Events in Power Systems. *Reliab. Eng. Syst. Saf.* 196, 106788. doi:10.1016/j.ress.2019.106788

Texas Tribune (2021). Paperwork Failures Worsened Texas Blackouts, Sparking Mid-storm Scramble to Restore Critical Fuel Supply. Available at: https://www.texastribune.org/2021/03/18/texas-winter-storm-blackouts-paperwork/ (Accessed April 14, 2022).

University of Texas at Austin, Energy Institute (2021). *The Timeline and Events of the February 2021 Texas Electric Grid Blackouts*. Available at: https://energy.utexas.edu/sites/default/files/UTAustin%20%282021%29%20EventsFebruary2021TexasBlackout%2020210714.pdf.

US Energy Information Administration (EIA) (2019). One in Four US Homes Is All Electric. Available at: https://www.eia.gov/todayinenergy/detail.php?id=39293# (Accessed April 14, 2022).

White, P. R., Rhodes, J. D., Wilson, E. J. H., and Webber, M. E. (2021). Quantifying the Impact of Residential Space Heating Electrification on the Texas Electric Grid. *Appl. Energy* 298, 117113. doi:10.1016/j.apenergy.2021.117113

Wu, D., Zheng, X., Xu, Y., Olsen, D., Xia, B., Singh, C., et al. (2021). An Open-Source Extendable Model and Corrective Measure Assessment of the 2021 texas Power Outage. *Adv. Appl. Energy* 4, 100056. doi:10.1016/j.adapen.2021.100056

Wundergroud (2022). Dallas, TX Weather History. Available at: https://www.wunderground.com/history/daily/us/tx/dallas (Accessed April 14, 2022).

Yan, D. B., Wen, J. Y., Du, Z., Yang, D. J., Yao, W., Zhao, H. S., et al. (2021). Analysis of Texas Blackout in 2021 and its Enlightenment to Power System Planning Management. *Power Syst. Prot. Control* 49 (9), 121–128. doi:10.19783/j.cnki.pspc.210358R

Zhang, G., Zhong, H., Tan, Z., Cheng, T., Xia, Q., and Kang, C. (2022). Texas Electric Power Crisis of 2021 Warns of a New Blackout Mechanism. *CSEE J. Power Energy Syst.* 8 (1), 1–9. doi:10.17775/CSEEJPES.2021.07720

Conflict of Interest: The authors declare that the research was conducted in the absence of any commercial or financial relationships that could be construed as a potential conflict of interest.

frontiers | Frontiers in Energy Research

ORIGINAL RESEARCH
published: 04 July 2022
doi: 10.3389/fenrg.2022.921222

Small-Signal Distributed Frequency Modeling and Analysis for Grid-Forming Inverter-Based Power Systems

Xiaojing Qi[1], *Jianyong Zheng*[1]* *and Fei Mei*[2]

[1]School of Electrical Engineering, Southeast University, Nanjing, China, [2]College of Energy and Electrical Engineering, Hohai University, Nanjing, China

More and more renewable energy sources are integrated into power grids, leading to a power electronic-based low-inertia power system. The grid-forming (GFM) inverter is an effective method for improving the inertia of the system. However, with the increased GFM inverters in the system, how the multiple control parameters affect the frequency response is still not clear. In this study, first, the power-phase model of the power grid is established; then, a small-signal distributed frequency model of the GFM inverter-based power system is established associating with the power-phase model of the power grid and the power-frequency model of the GFM inverter. Based on the proposed model, the influence of the multiple parameters to the frequency response is analyzed. It is concluded that both the inertia and damping coefficient affect the settling time, overshoot, and oscillation of the frequency. Finally, the simulation results verify the proposed model and the conclusion.

Keywords: low-inertia system, grid-forming inverter, small-signal model, distributed frequency response, frequency dynamics

OPEN ACCESS

Edited by:
Qingxin Shi,
North China Electric Power University, China

Reviewed by:
Pudong Ge,
Imperial College London, United Kingdom
Yubin Jia,
Southeast University, China
Qiujie Wang,
China Three Gorges University, China

***Correspondence:**
Jianyong Zheng
jy_zheng@seu.edu.cn

Specialty section:
This article was submitted to Smart Grids, a section of the journal Frontiers in Energy Research

Received: *15 April 2022*
Accepted: *23 May 2022*
Published: *04 July 2022*

Citation:
Qi X, Zheng J and Mei F (2022) Small-Signal Distributed Frequency Modeling and Analysis for Grid-Forming Inverter-Based Power Systems. Front. Energy Res. 10:921222. doi: 10.3389/fenrg.2022.921222

INTRODUCTION

Recently, more and more renewable energy sources (RESs) have been developed to alleviate the increasingly tight power supply of fossil energy (Huang et al., 2011). These RESs adopt the inverter as the interface connected to the power grid. The inverter grid-connected control can be classified into two types: the grid-following (GFL) and grid-forming (GFM) controls. The GFL inverter lacks the inertia and damping compared to the traditional synchronous generator (Liu et al., 2016). Therefore, the increased penetration of RESs has greatly decreased the overall inertia level of the power system, which raises great challenges to the stability of the system, especially for the low-inertia system, such as the microgrid in the islanded mode (Alipoor et al., 2018). To address this problem, the GFM control is considered to be a simple and effective approach for improving the inertia of the system (Quan et al., 2020a) (Quan, 2021) (Wu et al., 2016). The well-known virtual synchronous generator (VSG) control belongs to the GFM control methods (Wu et al., 2016).

The GFM inverter usually adopts power synchronization control which includes the two parameters of inertia and damping (Quan et al., 2020b). These two parameters play critical roles in improving the performance and maintaining the stability of the power system. Compared with the synchronous generator, the virtual inertia and damping coefficient of the GFM inverter are realized in the control software; hence, they are flexible and adjustable. The design of the inertia and damping for a single GFM inverter has been studied well (Wu et al., 2016), (Quan et al., 2020b). However, how

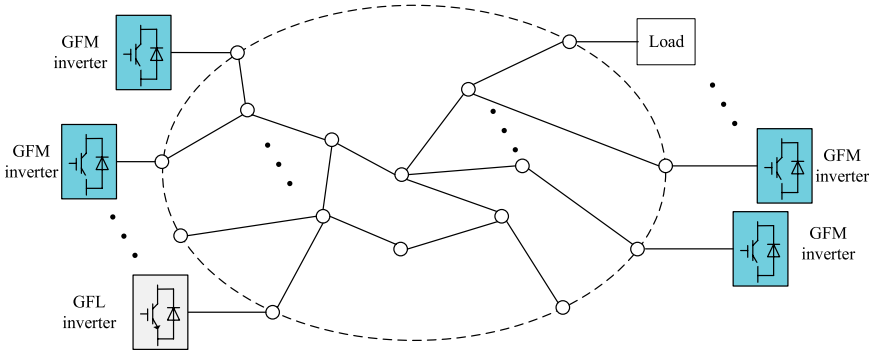

FIGURE 1 | Diagram of the GFM inverter-based power system.

to optimally determine the virtual inertia and damping coefficient for multiple GFMs in a GFM-based power system to get better stability and dynamic performance is still a challenge.

To optimally design the multiple inertias and damping factors, a suitable model should be established first. However, for such a large nonlinear system, the small-signal model is suitable for the optimal design of virtual inertia and damping coefficient. A grid-forming inverter-based power system is comprehensively modeled in (Pogaku et al., 2007), where the small-signal stability issues are analyzed by plotting zero-pole locations. Based on the grid-forming technology, many stability performances in terms of regulating frequency and voltage can be achieved, for example, asymptotical (Bidram et al., 2013) and finite-time (Ge et al., 2021). However, these studies consider the control design from the perspective of a power electronic-based inverter and do not fully consider the interaction between grid-forming inverters and power networks.

Based on the traditional small-signal modeling method, a detailed system model including grid-following inverters and grid-forming inverters is built with the node admittance matrix, and a H_2 norm-based control algorithm is proposed to optimize the virtual inertia in order to improve the stability of the low-inertia power system (Poolla et al., 2019). However, the nodal admittance matrix cannot describe how the load power fluctuation affects the system frequency in an explicit way. Hence, it is not conducive to the parameter optimization. Differently, a model with multiple GFMs was established by using direct current power flow in Ademola-Idowu and Zhang, 2018, and the optimized design of the virtual inertia and damping coefficient was also described as a H_2 norm minimization problem. A more detailed demonstration was proposed in Mešanović et al., 2016 for the system model using DC power flow, based on which a comparison among the H_∞, H_2, and pole optimizations for damping active power oscillations was presented. Nevertheless, the DC power flow algorithm is not applicable for a low-voltage microgrid or low-inertia system where most DGs are connected (Frack et al., 2015) (Kundur, 1994).

Therefore, this study proposes a state space small-signal model for the multi-GFM system. Based on the proposed model, the relationship between the load fluctuation and frequency change is explicitly expressed, which is beneficial to the numerical optimization of the parameters of virtual inertia and damping coefficient. Moreover, the dynamic characteristic of the frequency is also demonstrated by the proposed state space model. Finally, the influence of the parameters on the dynamic response is analyzed and verified.

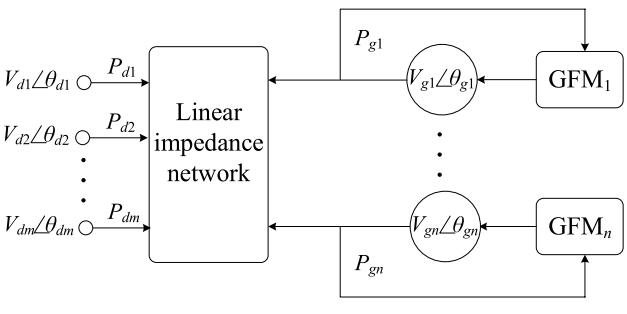

FIGURE 2 | Diagram of the inverter-based power system.

MODELING FOR THE GRID-FORMING-BASED SYSTEM

System Description

As shown in **Figure 1**, in an inverter-based power system, the GFM inverter is necessary to form the AC voltage. Under these conditions, the swing-equation-based power control or power synchronization control will be applied to realize the frequency synchronization and power sharing. Consequently, the control parameters of the power control, for example, the damping factor and virtual inertia, will remarkably affect the system frequency dynamics. Moreover, due to the difference of these power control parameters, the frequency of the system will demonstrate the features of distribution. Hence, it is meaningful to establish a dynamic model to describe the frequency dynamics of the system.

As shown in **Figure 2**, the system nodes are divided into two types. One is the node that is connected with GFM inverters, and it is called the GFM-node. The voltage and frequency of the GFM-

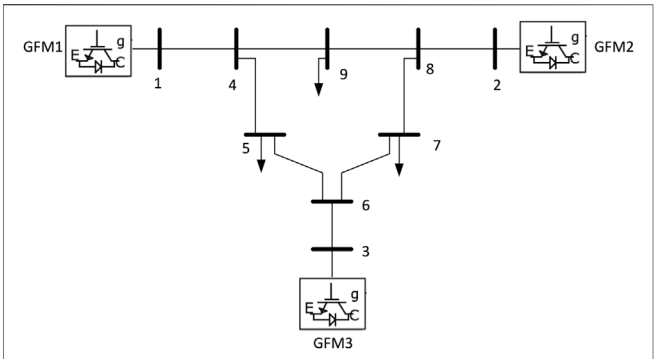

FIGURE 3 | Diagram of in the 9-buses system.

TABLE 1 | | Parameters of the system and the inverters.

Base values			
f_{base} = **50Hz**	$\omega_{base} = 2\pi f_{base}$	U_{base} = **345kV**	S_{base} = **100MVA**
Power network parameters (per-unit values)			
Lines	***R***	***X***	***B***
Line 14	0	0.0576	0
Line 45	0.017	0.092	0.158
Line 56	0.039	0.17	0.358
Line 36	0	0.0586	0
Line 67	0.0119	0.1008	0.209
Line 78	0.0085	0.072	0.149
Line 82	0	0.0625	0
Line 89	0.032	0.161	0.306
Line 94	0.01	0.085	0.176
Loads $S_5 = 0.9 + j0.3, S_7 = 1 + j0.35, S_9 = 1.25 + j0.5$			
Parameters of GFM inverters (per-unit values)			
M and *D* of GFM1: 8,200			
M and *D* of GFM2: 16,300			
M and *D* of GFM3: 24,400			

node are determined by the GFM inverter. The last nodes are classified into one type that injects active and reactive power into the node. In this study, these nodes are treated as the disturbance nodes.

Modeling of the Grid-Forming Inverter

The GFM active power control part simulates the inertia, droop characteristics, and damping action of the synchronous machine. It is assumed that the GFM active power control equation similar to the second-order rotor motion equation of the synchronous machine can be expressed as **Eq. 1**

$$\begin{cases} \dfrac{d\Delta\theta_{gi}}{dt} = \Delta\omega_{gi} \\ M_i \dfrac{\mathrm{d}\Delta\omega_i}{\mathrm{dt}} = \dfrac{P_{\mathrm{set},i} - P_{gi}}{\omega_{\mathrm{n}}} - D_{p,i}\Delta\omega_{gi} \\ \omega_{gi} = \Delta\omega_{gi} + \omega_{\mathrm{n}} \end{cases} \tag{1}$$

where $\Delta\theta_{gi}$ denotes the phase variation of GFM node i at the current operation point, M_i is the virtual inertia of the i-th GFM inverter, $D_{p,i}$ is the damping coefficient, $P_{\mathrm{set},i}$ is the set value of active power, P_{gi} is the output active power, ω_{n} is the rated angular frequency, and ω_{gi} is the angular frequency of the i-th GFM inverter. Considering all the GFM nodes, **Eq. 1** can be written in matrix formation:

$$\begin{cases} \dfrac{d\Delta\boldsymbol{\theta}_g}{dt} = \Delta\omega_g \\ \dfrac{d\Delta\omega_g}{dt} = \dfrac{\boldsymbol{M}^{-1}}{\omega_n}\left(\boldsymbol{P}_{set} - \boldsymbol{P}_g\right) - \boldsymbol{M}^{-1}\boldsymbol{D}_p\Delta\boldsymbol{\omega}_g \end{cases} \tag{2}$$

Modeling of the Power Grid

To establish the model of the GFM inverter-based system, how the phase angles of the GFM inverters and the injected power of disturbance nodes affect the power of the GFM inverter through the impedance network needs to be clarified. To this end, the Jacobian matrix is adopted:

$$\begin{bmatrix} \Delta\boldsymbol{P} \\ \Delta\boldsymbol{Q} \end{bmatrix} = \begin{bmatrix} \boldsymbol{H} & \boldsymbol{N} \\ \boldsymbol{J} & \boldsymbol{L} \end{bmatrix} \begin{bmatrix} \Delta\boldsymbol{\theta} \\ \Delta\boldsymbol{V}/\boldsymbol{V} \end{bmatrix} \tag{3}$$

where matrices $\boldsymbol{H}$, $\boldsymbol{N}$, $\boldsymbol{J}$, and $\boldsymbol{L}$ are derived from the fundamental power flow equations. In the high-voltage power system, it has $\boldsymbol{N} = \boldsymbol{0}$ and $\boldsymbol{J} = \boldsymbol{0}$, which means that the voltage is related with the reactive power, while the frequency is dependent on the active power. Hence, the influence of the reactive power can be ignored when analyzing the frequency dynamics. Then, **Eq. 3** is simplified as

$$\begin{bmatrix} \Delta P_1 \\ \Delta P_2 \\ \vdots \end{bmatrix} = \begin{bmatrix} H_{11} & H_{12} & \cdots \\ H_{21} & H_{22} & \cdots \\ \vdots & \vdots & \ddots \end{bmatrix} \begin{bmatrix} \Delta\theta_1 \\ \Delta\theta_2 \\ \vdots \end{bmatrix} \tag{4}$$

where ΔP_i and $\Delta\theta_i$ denote the power and phase variation of node i at the current operation point, respectively. The elements of the matrix are linearized from the fundamental power equation:

$$\begin{cases} H_{ij} = \dfrac{\partial P_i}{\partial \delta_j} = U_i U_j\left(G_{ij}\sin\delta_{ij} - B_{ij}\cos\delta_{ij}\right), \quad i \neq j \\ H_{ii} = \dfrac{\partial P_i}{\partial \delta_i} = -U_i \sum\limits_{j=1, j\neq i}^{j=n} U_j\left(G_{ij}\sin\delta_{ij} - B_{ij}\cos\delta_{ij}\right), \quad i = j \end{cases} \tag{5}$$

Distinguishing the GFM nodes and disturbance nodes, **Eq. 4** can be rearranged as

$$\begin{bmatrix} \Delta\boldsymbol{P}_g \\ \Delta\boldsymbol{P}_d \end{bmatrix} = \begin{bmatrix} \boldsymbol{H}_{gg} & \boldsymbol{H}_{gd} \\ \boldsymbol{H}_{dg} & \boldsymbol{H}_{dd} \end{bmatrix} \begin{bmatrix} \Delta\boldsymbol{\theta}_g \\ \Delta\boldsymbol{\theta}_d \end{bmatrix} \tag{6}$$

Integrated Model

The phase angle vector of the GFM nodes $\Delta\boldsymbol{\theta}_g$ is the state variable of the system, while $\Delta\boldsymbol{\theta}_d$ is the dependent variable. The power of the disturbance node will be the disturbance that occurs with the phase angle and frequency variations. To extract the disturbance from **Eq. 6**, Kron reduction is applied to **Eq. 6**, obtaining

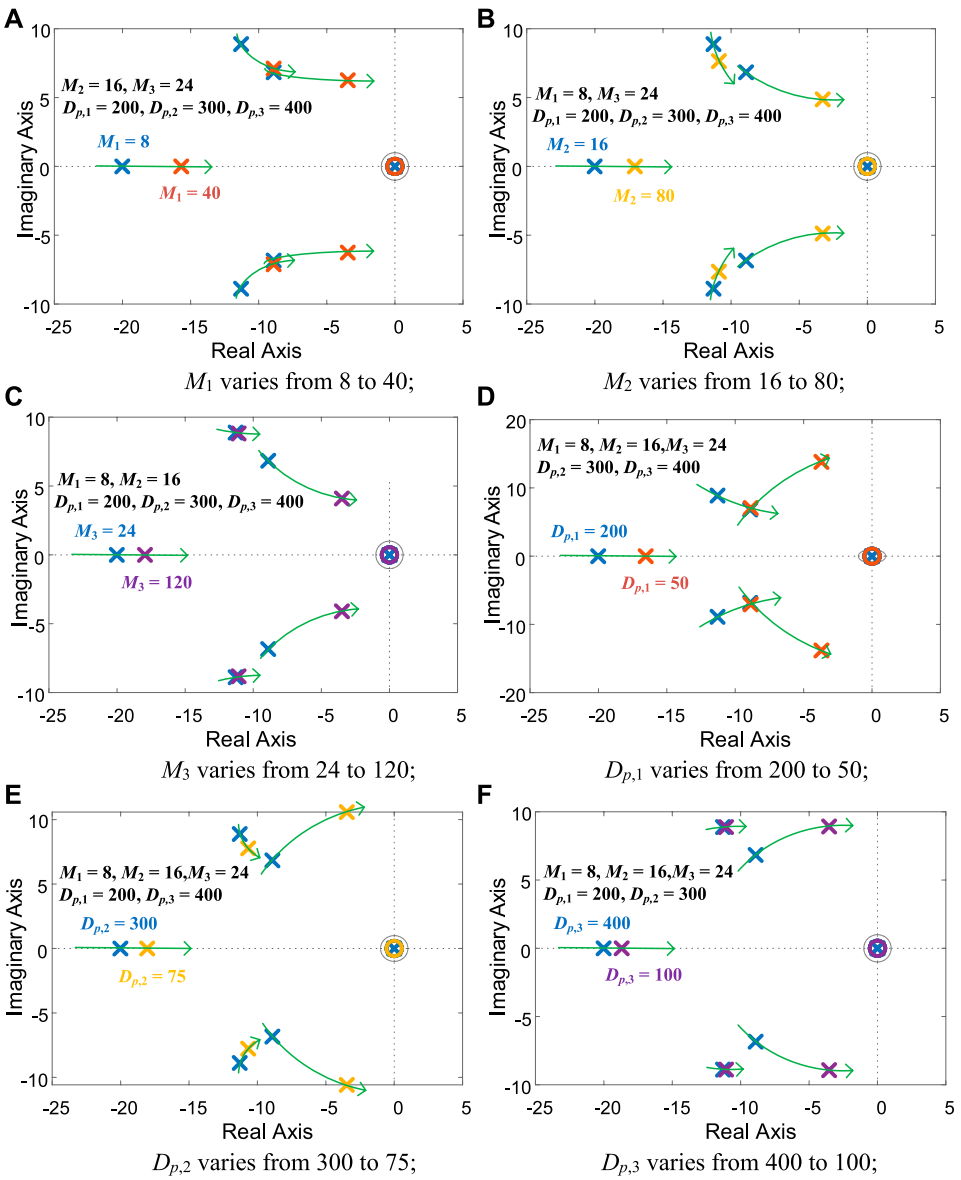

FIGURE 4 | Root locus of the system when the parameters vary.

$$\Delta \boldsymbol{P}_g = \left(\boldsymbol{H}_{gg} - \boldsymbol{H}_{gd}\boldsymbol{H}_{dd}^{-1}\boldsymbol{H}_{dg}\right)\Delta\boldsymbol{\theta}_g + \boldsymbol{H}_{gd}\boldsymbol{H}_{dd}^{-1}\Delta\boldsymbol{P}_d \tag{7}$$

Then, combining **Eqs. 2** and **7**, it has

$$\frac{d}{dt}\begin{bmatrix}\Delta\boldsymbol{\theta}_g \\ \Delta\boldsymbol{\omega}_g\end{bmatrix} = \begin{bmatrix} -(\omega_n\boldsymbol{M})^{-1}\left(\boldsymbol{H}_{gg} - \boldsymbol{H}_{gd}\boldsymbol{H}_{dd}^{-1}\boldsymbol{H}_{dg}\right) & \boldsymbol{I} \\ -\boldsymbol{M}^{-1}\boldsymbol{D}_p \end{bmatrix} \times \begin{bmatrix}\Delta\boldsymbol{\theta}_g \\ \Delta\boldsymbol{\omega}_g\end{bmatrix} + \begin{bmatrix} 0 \\ -(\omega_n\boldsymbol{M})^{-1}\boldsymbol{H}_{gd}\boldsymbol{H}_{dd}^{-1}\end{bmatrix}\Delta\boldsymbol{P}_d + \begin{bmatrix} 0 \\ -(\omega_n\boldsymbol{M})^{-1}\end{bmatrix}\boldsymbol{P}_{set} \tag{8}$$

which is the space state model of the system. The state variables $\Delta\boldsymbol{\theta}_g$ and $\Delta\boldsymbol{\omega}_g$ represent the dynamics of the phase angle and frequency of the GFM nodes. Therefore, we can conveniently evaluate the dynamic response of the frequency for every GFM node during the dynamic process. Thereby, we can optimally design the control parameters of the GFM power controller.

POLE ANALYSIS

In this section, the proposed model is applied to a 9-buses system as shown in **Figure 3**. Three GFM inverters are connected at bus 1, bus 2, and bus 3. Three loads are connected at bus 5, bus 7, and bus 9. The parameters are listed in **Table 1**.

Using the concrete parameters of the 9-buses system shown in **Figure 3**, the model of **Eq. 8** can be obtained. Then, based on the

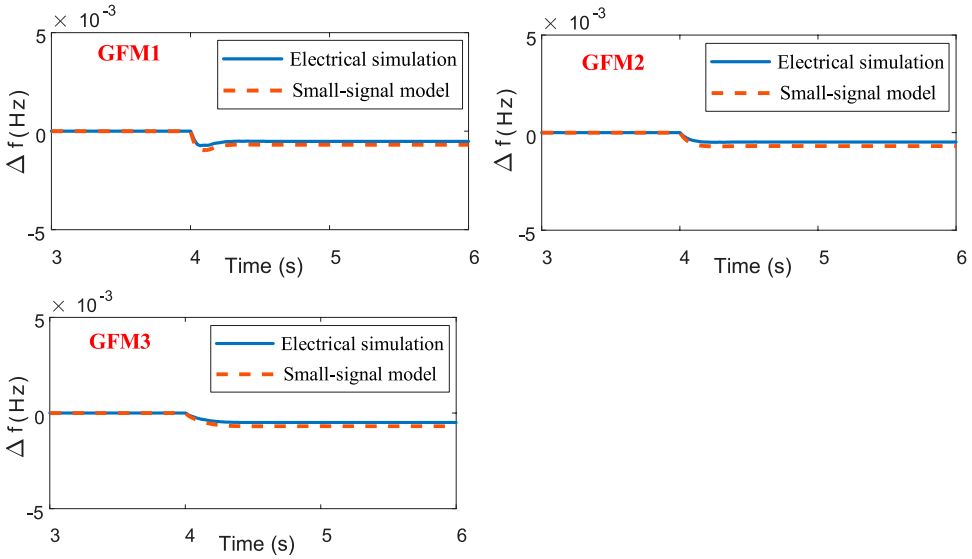

FIGURE 5 | Frequency response of the electrical simulation and the proposed small-signal model.

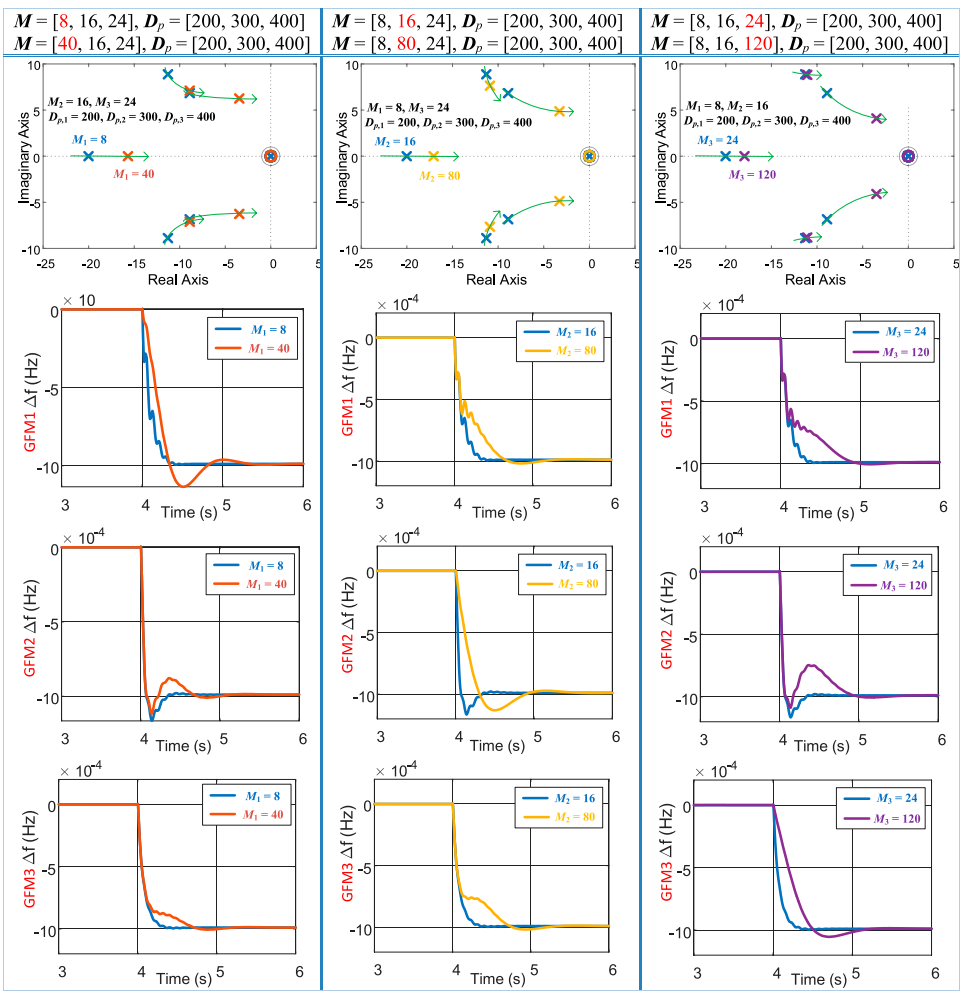

FIGURE 6 | Frequency response when the inertia changes.

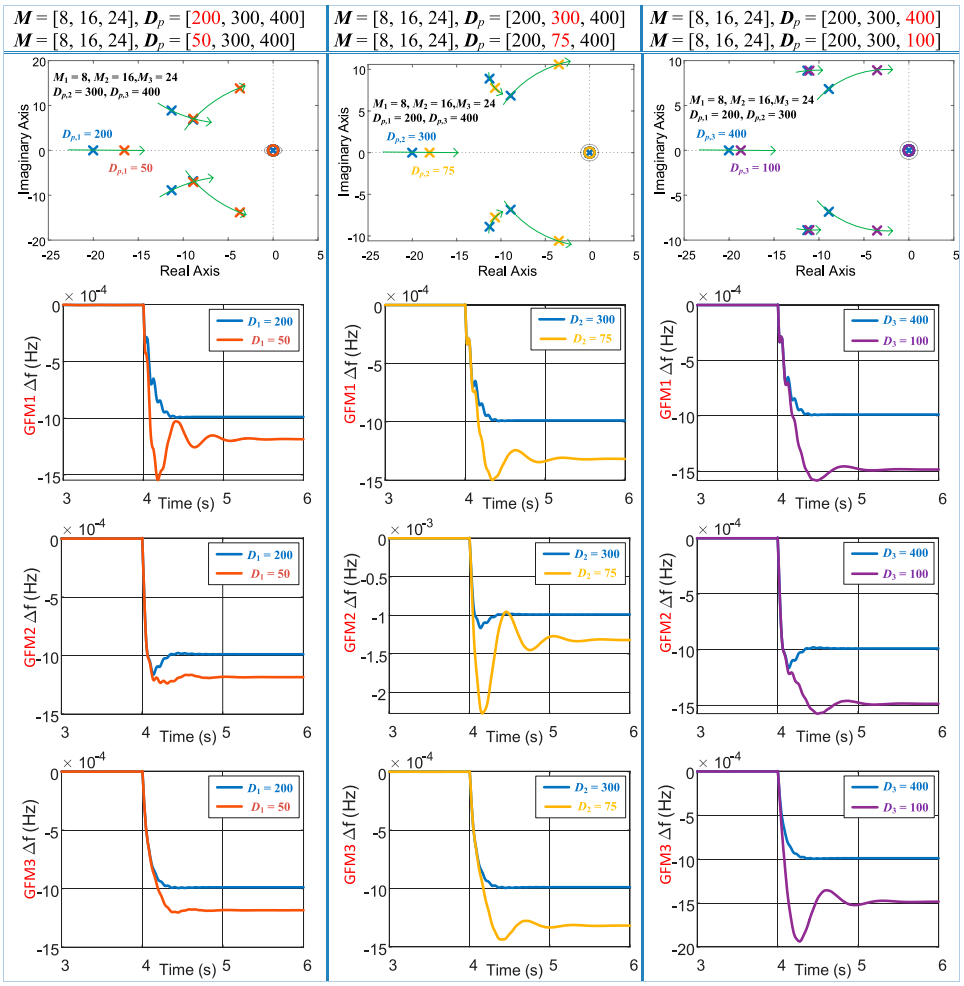

FIGURE 7 | Frequency response when the damping changes.

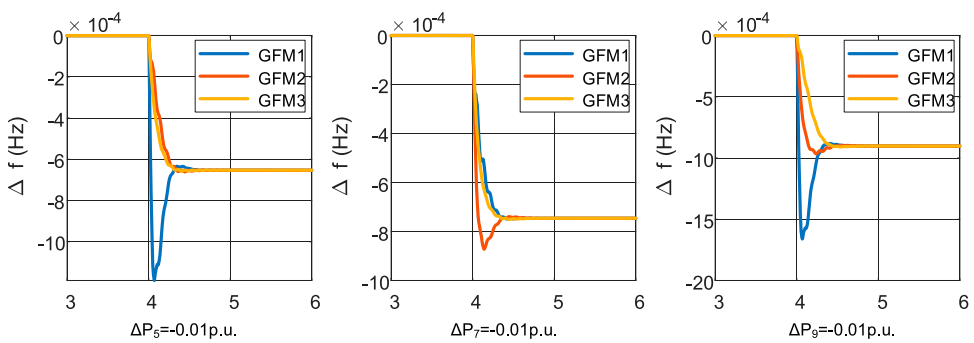

FIGURE 8 | Frequency response with different load variations.

model, the root locus when the inertias vary is investigated. The inertia and damping parameters for the three GFM inverters are denoted as $\boldsymbol{M} = (M_1, M_2, M_3)$ and $\boldsymbol{D}_p = (\boldsymbol{D}_{p,1}, \boldsymbol{D}_{p,2}, \boldsymbol{D}_{p,3})$ for GFM1, GFM2, and GFM3. **Figure 4A–C** shows the pole variation when the inertia parameter of the three GFM inverters changes. Generally, the poles of the system rule the dynamic response of the frequency. Each pair of the conjugate poles has the parameters of damping factor and damping oscillation frequency (the real part of the pole). The high damping factor can reduce the oscillation and overshoot during the dynamic response. The

large damping oscillation frequency reduces the settling time, which means that it increases the response speed. As can be seen in **Figure 4A–C**, with the inertia increasing, all of the poles move toward the imaginary axis, which means that the response will become slow. It is reasonable since the inertia is increased. Moreover, the damping factor is reduced due to the increased inertia. This will enhance the overshoot and oscillation.

Figure 4D–F shows how the damping factor affects the poles. Generally, the damping factors reflect the droop coefficient; hence, they are usually designed by the frequency support capacity. However, from **Figure 4D–F**, it is shown that the damping factors also influence the dynamic response. With the damping factor decreasing (frequency supporting capacity decreasing), the poles move toward the imaginary axis, which means that the response will become slow; meanwhile, the damping becomes worse. It will cause severe overshoot and oscillation on frequency dynamics.

SIMULATION RESULTS

Model Verification

To verify the correctness of the proposed model, the electrical simulation in Simulink is conducted as a comparison. The adopted parameters are $\boldsymbol{M}$ = (8, 16, 24) and $\boldsymbol{D}_p$ = (200, 300, 400). The disturbance appeared on node 7 with 0.01 p.u. active power increase. As shown in **Figure 5**, the frequency responses of the electrical simulation and the proposed small-signal model demonstrate that the dynamic feature of the frequency can be perfectly described by the proposed small-signal model. However, there is a small steady-state error which appears on the proposed small-signal model. This is introduced by the linearization of the Jacobian matrix. Nevertheless, the steady-state value can be obtained by the direct static-state droop computation. Hence, the dynamic feature described by the proposed model can still be adopted optimally to design the control parameters of the GFM inverters.

Performance Verification

Furthermore, to evaluate the effect of the control parameters to the frequency performance, the simulation with different parameters is performed. **Figure 6** shows the different frequency dynamic responses with the inertia variations, and the pole figures are also displayed for a reference. In **Figure 6**, the first column shows that the inertia of GFM1 changes from 8 to 40, while the other parameters stay invariable. The second column shows that the inertia of GFM2 changes from 16 to 80, and the third column shows the inertia of GFM3 changes from 24 to 120. From the results in **Figure 6**, first, it is concluded that the inertia only affects its own rate of change of frequency (RoCoF) but has no effect on the RoCoF of the other node; increasing the inertia of GFM1 only reduces the RoCoF of GFM1 but without the influence of RoCoFs of GFM2 and GFM3. Second, increasing the inertia will move the poles right, which increases the settling time; all the settling times of the frequencies for the three inverters become larger. Third, increasing the inertia also decreases the damping of the system; hence, the oscillation and overshoot of the frequencies of the three inverters are deteriorated.

Figure 7 shows the distributed frequency response of different GFM inverters when the damping coefficients change. The first column shows that the damping coefficient of GFM1 changes from 200 to 50, while the other parameters stay invariable. The second column shows that the damping coefficient of GFM2 changes from 300 to 75, and the third column shows that the damping coefficient of GFM3 changes from 400 to 100. Observing the frequency waveforms in **Figure 7**, first, we can conclude that the damping coefficient still acts as the droop coefficient that denotes the frequency supporting capacity. Hence, reducing the damping coefficients will reduce the frequency steady-state value. Second, the reduced damping coefficient moves the pole toward the imaginary axis; hence, the settling time becomes larger with the reduced damping coefficient. Third, decreasing the damping coefficient decreases the damping of the system; hence, the oscillation and overshoot of the frequencies of the three inverters are deteriorated. Last, the damping coefficient has no effect on the RoCoFs of the frequency.

Moreover, to comprehensively evaluate the effectiveness of the proposed model, the load power disturbance is imposed on different nodes. **Figure 8** shows the frequency response when the load steps 0.01 p.u. active power. The parameters of the inverters are set as M = (8 16 24) and D = (200 300 400). As shown in **Figure 8**, the frequency of GFM2 and GFM3 performs a good dynamic response, while the frequency of GFM1 shows a large overshoot. This because that the inertia of GFM1 is set too small, which occurs as a poor damping factor of the corresponding poles.

CONCLUSION

In this study, a state space small signal model is established for the multiple GFM low-inertia system. The system is modeled in an input–output state space model where the load power is the disturbance input and the frequency of every node is the output. The proposed model can perfectly describe the dynamic feature of the frequency. From the proposed model, it is concluded that increasing the inertia and reducing the damping coefficient will increase the settling times of the frequencies, deteriorate the oscillation, and overshoot of the frequencies. Moreover, increasing the inertia will decrease the RoCoF of its own node frequency, while the damping coefficient has no effect on the RoCoFs of the frequency.

Furthermore, the proposed model is based on the small-signal stability theory; therefore, it is limited to analyze the large-signal stability. In the future work, we will focus on the suitable model for a large-signal stability analysis.

DATA AVAILABILITY STATEMENT

The original contributions presented in the study are included in the article/supplementary material; further inquiries can be directed to the corresponding author.

AUTHOR CONTRIBUTIONS

XQ: Model establishment, running the simulation, and writing the paper. JZ: Advising and revising the paper. FM: Advising and revising the paper.

FUNDING

This study was funded by the Key R&D plan of Jiangsu Province (BE2020027) and in part by the Jiangsu International Science and technology cooperation project (BZ2021012).

REFERENCES

Ademola-Idowu, A., and Zhang, B. (2018). "Optimal Design of Virtual Inertia and Damping Coefficients for Virtual Synchronous Machines," in 2018 IEEE Power & Energy Society General Meeting (PESGM), Portland, OR, USA, 5-10 Aug. 2018 (IEEE), 1–5. doi:10.1109/PESGM.2018.8586187

Alipoor, J., Miura, Y., and Ise, T. (2018). Stability Assessment and Optimization Methods for Microgrid with Multiple VSG Units. *IEEE Trans. Smart Grid* 9 (2), 1462–1471. doi:10.1109/tsg.2016.2592508

Bidram, A., Davoudi, A., Lewis, F. L., and Guerrero, J. M. (2013). Distributed Cooperative Secondary Control of Microgrids Using Feedback Linearization. *IEEE Trans. Power Syst.* 28, 3462–3470. doi:10.1109/tpwrs.2013.2247071

Frack, P. F., Mercado, P. E., Molina, M. G., Watanabe, E. H., De Doncker, R. W., and Stagge, H. (2015). Control Strategy for Frequency Control in Autonomous Microgrids. *IEEE J. Emerg. Sel. Top. Power Electron.* 3 (4), 1046–1055. doi:10.1109/jestpe.2015.2439053

Ge, P., Zhu, Y., Green, T. C., and Teng, F. (2021). Resilient Secondary Voltage Control of Islanded Microgrids: An ESKBF-Based Distributed Fast Terminal Sliding Mode Control Approach. *IEEE Trans. Power Syst.* 36 (2), 1059–1070. doi:10.1109/TPWRS.2020.3012026

Huang, A. Q., Crow, M. L., Heydt, G. T., Zheng, J. P., and Dale, S. J. (2011). The Future Renewable Electric Energy Delivery and Management (FREEDM) System: The Energy Internet. *Proc. IEEE* 99 (1), 133–148. doi:10.1109/jproc.2010.2081330

Kundur, P. (1994). *Power System Stability and Control*. New York: McGraw-Hill.

Liu, J., Miura, Y., and Ise, T. (2016). Comparison of Dynamic Characteristics between Virtual Synchronous Generator and Droop Control in Inverter-Based Distributed Generators. *IEEE Trans. Power Electron.* 31 (5), 3600–3611. doi:10.1109/tpel.2015.2465852

Mešanović, A., Münz, U., and Heyde, C. (2016). Comparison of H_∞, H_2, and Pole Optimization for Power System Oscillation Damping with Remote Renewable Generation. *IFAC Workshop Control Transm. Distribution Smart Grids CTDSG* 49 (27), 103–108. doi:10.1016/j.ifacol.2016.10.727

Pogaku, N., Prodanovic, M., and Green, T. C. (2007). Modeling, Analysis and Testing of Autonomous Operation of an Inverter-Based Microgrid. *IEEE Trans. Power Electron.* 22 (2), 613–625. doi:10.1109/TPEL.2006.890003

Poolla, B. K., Dorfler, D., and Dörfler, F. (2019). Placement and Implementation of Grid-Forming and Grid-Following Virtual Inertia and Fast Frequency Response. *IEEE Trans. Power Syst.* 34 (4), 3035–3046. doi:10.1109/tpwrs.2019.2892290

Quan, X., Huang, A. Q., and Yu, H. (2020). A Novel Order Reduced Synchronous Power Control for Grid-Forming Inverters. *IEEE Trans. Ind. Electron.* 67 (12), 10989–10995. doi:10.1109/tie.2019.2959485

Quan, X. (2021). Improved Dynamic Response Design for Proportional Resonant Control Applied to Three-phase Grid-Forming Inverter. *IEEE Trans. Ind. Electron.* 68 (10), 9919–9930. doi:10.1109/TIE.2020.3021654

Quan, X., Yu, R., Zhao, X., Lei, Y., Chen, T., Li, C., et al. (2020). Photovoltaic Synchronous Generator: Architecture and Control Strategy for a Grid-Forming PV Energy System. *IEEE J. Emerg. Sel. Top. Power Electron.* 8 (2), 936–948. doi:10.1109/JESTPE.2019.2953178

Wu, H., Ruan, X., Yang, D., Chen, X., Zhao, W., Lv, Z., et al. (2016). Small-signal Modeling and Parameters Design for Virtual Synchronous Generators. *IEEE Trans. Ind. Electron.* 63 (7), 4292–4303. doi:10.1109/tie.2016.2543181

Conflict of Interest: The authors declare that the research was conducted in the absence of any commercial or financial relationships that could be construed as a potential conflict of interest.

The reviewer YJ declared a shared affiliation with the authors XQ and JZ to the handling editor at the time of review.

Publisher's Note: All claims expressed in this article are solely those of the authors and do not necessarily represent those of their affiliated organizations or those of the publisher, the editors, and the reviewers. Any product that may be evaluated in this article or claim that may be made by its manufacturer is not guaranteed or endorsed by the publisher.

frontiers | Frontiers in Energy Research

ORIGINAL RESEARCH
published: 13 July 2022
doi: 10.3389/fenrg.2022.935659

Optimization for Transformer District Operation Considering Carbon Emission and Differentiated Demand Response

*Dexiang Jia[1], Yu Zhou[2], Zhongdong Wang[2], Yuhao Ding[3], Hongda Gao[1], Jianye Liu[1] and Ganyun Lv[3]**

[1]State Grid Energy Research Institute Co.,Ltd., Beijing, China, [2]State Grid Jiangsu Electric Power Co.,Ltd., Nanjing, China, [3]School of Electric Power Engineering, Nanjing Institute of Technology, Nanjing, China

With the promotion of the "dual carbon" goal, a large number of distributed photovoltaic power are connected to the distribution network. Since the current operation optimization of the low-voltage transformer district is based on single objectives such as the economy and power reliability, the model is relatively simple and difficult to adapt to the large-scale access of photovoltaics. Therefore, this article comprehensively considers carbon emissions, different load characteristics, and differentiated demand response of the district. An optimization method for low-voltage transformer district operation under the dual-carbon background is proposed. First, the typical structure of a low-voltage transformer district is introduced. Second, the load types and characteristics of the low-voltage transformer district are analyzed, and differentiated demand response models are established for different types of loads. Finally, taking the minimum economic cost and carbon emission as the objective, the low-voltage transformer district operation optimization model considering carbon emission and differentiated demand response is established by considering the voltage overrun of the photovoltaic access point, substation capacity constraint, and carbon emission constraint. The simulation results show that the model can effectively reduce the economic cost and carbon emissions of the low-voltage transformer district, achieve more than 95% reasonable utilization rate of new energy in the low-voltage transformer district, improve the lateral time distribution of load in the low-voltage transformer district, and provide an effective means for low-carbon scheduling of distribution networks.

Keywords: low-voltage transformer district, photovoltaic access, load characteristics, differentiated demand response, carbon emission, optimal scheduling

OPEN ACCESS

Edited by:
Qinran Hu,
Southeast University, China

Reviewed by:
Yonghui Sun,
Hohai University, China
Qian Xiao,
Tianjin University, China

****Correspondence:***
Ganyun Lv
ganyun_lv@njit.edu.cn

Specialty section:
This article was submitted to Smart Grids, a section of the journal Frontiers in Energy Research

Received: *04 May 2022*
Accepted: *01 June 2022*
Published: *13 July 2022*

Citation:
Jia D, Zhou Y, Wang Z, Ding Y, Gao H, Liu J and Lv G (2022) Optimization for Transformer District Operation Considering Carbon Emission and Differentiated Demand Response. Front. Energy Res. 10:935659. doi: 10.3389/fenrg.2022.935659

1 INTRODUCTION

In recent years, with the increasingly prominent global environmental pollution problems and energy crisis, General Secretary Xi Jinping proposed the strategic goal of "carbon peaking and carbon neutrality" at the United Nations General Assembly, demanding to reduce the carbon emission level of the distribution network transformer district (Wei et al., 2021). The new energy power generation represented by photovoltaics has developed rapidly. However, with the increase of photovoltaic penetration rate, the coordination of the source and load in the low-voltage transformer district has become more difficult (Zhao et al., 2019). Demand-side response can be used to absorb new energy

and improve the interaction between the source and load in the district (Huang D. et al., 2022). Therefore, carbon emissions and demand-side response characteristics should be fully considered in the optimal scheduling of the low-voltage transformer district.

At present, the optimal scheduling of the transformer district mainly focuses on distributed power generation. Ma et al., 2021 proposed a robust optimization planning model for a transformer district considering the uncertainty of photovoltaic intensity and considering the ability of the distribution network transformer district to accept distributed photovoltaics and obtained the best access point and optimal installation capacity of photovoltaics. Al-Ismail, 2020 started from the impact of distributed power generation on the transformer district and analyzed three aspects: distribution network reconfiguration technology, distributed power generation location and capacity optimization, and filter selection and location optimization, and summed up the strategy for optimal operation in the transformer district. Chen et al., 2020 proposed a layered control method for source-load-storage control in the transformer district to achieve optimal autonomy of the distribution network based on the multi-time scale complementary characteristics of controllable distributed power generation, energy storage systems, and loads. Cong et al., 2022 aimed at the volatility and intermittent problems brought by the increase in the installed capacity of photovoltaic power generation to the distribution network and proposed a fault recovery self-healing reconfiguration control optimization strategy for the distribution network based on an improved group search algorithm, which improved the efficiency of the distribution network. Zhang X. et al., 2021 analyzed the calculation method of flexibility provided by each component in the distribution network, established a two-layer optimal scheduling model for the distribution network with distributed photovoltaics considering flexibility, and introduced intuitive fuzzy programming to obtain the comprehensive optimal scheduling scheme. The above literature shows that in the optimal scheduling of the transformer district, taking into account the high proportion of the new energy consumption rate and low-carbon emissions at the same time is of great significance to the flexible resource planning of the transformer district, which is helpful to achieve energy saving and emission reduction in the transformer district.

Demand response is an important means to stabilize the output of distributed power generation and improve the consumption rate of new energy. The influence of demand response should be fully considered in the optimal scheduling of the low-voltage transformer district (Shafie-khah et al., 2019). Some scholars have carried out research on the demand response characteristics of low-voltage transformer districts. Shi et al., 2020 constructed a user DR model based on the elasticity coefficient matrix of real-time electricity prices, analyzed the charging load demand of electric vehicles at the same time, and established a robust optimal dispatch model for an active distribution network. Khalid et al., 2018 proposed an active distribution network that considers demand response; the double-layer collaborative configuration model stimulates the charging and discharging of electric vehicles to reduce the peak-to-valley difference of the load and adapt to the various planning requirements of electric vehicle charging stations. Jin et al., 2020 applied the evaluation of the operation status of the distribution network transformer district based on a fuzzy comprehensive evaluation of the incentive demand-side response and realized the comprehensive optimization of the voltage and load of the distribution network transformer district while reducing the peak load. Zhu et al., 2022 considered the user participation in demand response and established an optimal scheduling model of active distribution based on price and incentive demand response; the model has given full play to the flexibility of demand response. Qiu et al., 2021 used triangular fuzzy numbers to describe the uncertainty of demand response and established a distribution system with the goal of minimum users on the load side and maximum wind power consumption. The network master-slave game economic model achieves the game equilibrium by optimizing the real-time electricity price strategy and demand response strategy. However, the existing related studies have not considered the timeliness of demand response and the impact of different loads, which will make the response resources not fully utilized, making it difficult to achieve the expected effect of district scheduling. At the same time, these studies have not considered the difference in response elasticity coefficient and real-time electricity price among different users, without classification of load types, and the amount of electricity change and price change in the considered price-based demand response is linear, which does not conform to the actual situation and cannot reflect the actual demand response features.

To sum up, in order to deal with the current adverse effects of the countys photovoltaics on the optimal dispatch reliability and economic low-carbon operation of the low-voltage transformer district and make full use of demand response resources to increase the consumption of renewable energy and smooth the load curve at the same time, this article comprehensively considers carbon emissions and differentiated demand response. First, the basic structure of the low-voltage transformer district is introduced. Second, the load types and characteristics of the low-voltage transformer district are analyzed, and a differentiated demand response model is established for different types of loads. Under the conditions of photovoltaic access point voltage exceeding the limit and carbon emission constraints, an optimization model of low-voltage transformer district operation was established considering carbon emissions and differentiated demand response. Finally, the effectiveness of the optimal scheduling model was verified through simulation solutions.

2 BASIC STRUCTURE OF THE LOW-VOLTAGE TRANSFORMER DISTRICT

The low-voltage transformer district refers to the 10kV/0.4kV power supply area provided by several distribution transformers. The typical low-voltage transformer district structure constructed in this article is shown in **Figure 1**.

This low-voltage transformer district is divided into the transformer layer, the branch layer, the casing layer, and the user layer from top to bottom, which can play the function of

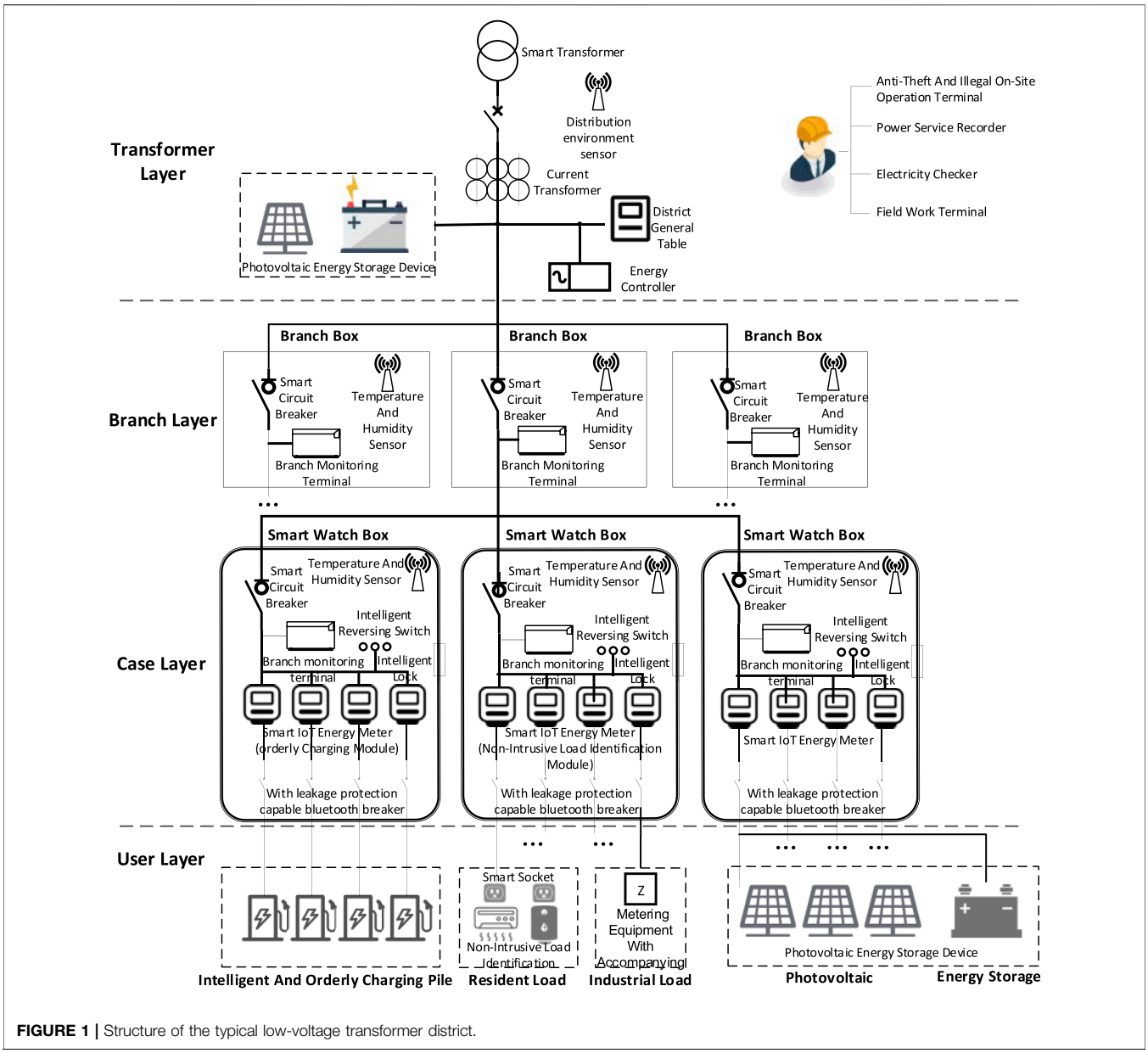

FIGURE 1 | Structure of the typical low-voltage transformer district.

"connecting the previous and the next" in the construction of the energy Internet. The transformer layer is composed of energy controllers, photovoltaic energy storage devices, and smart transformers. The branch layer includes branch monitoring terminals, environmental sensors, and single-phase intelligent miniature circuit breakers. The casing layer mainly includes smart IoT energy meters, intelligent reversing switches, and smart locks. The user layer includes residential load, industrial load, charging pile load, photovoltaics, and energy storage devices. The district can be used for online automated operations, distributed photovoltaic monitoring, reasonable analysis of the operating status of the platform, extraction of the differentiated behavior characteristics of users in the district, orderly charging of electric vehicles, and response to residential industrial energy consumption and take into account the distributed photovoltaic consumption and carbon emissions in the district, which can effectively promote the district. It is an important guarantee for further attracting investment and construction of low-voltage transformer districts in the future.

3 DIFFERENTIATED DEMAND RESPONSE MODEL

The demand-side response mechanism is mainly divided into price-based demand response and incentive-based demand response (Chen et al., 2019). In order to more accurately describe the characteristics of demand response behavior in low-voltage transformer districts, this article considers the classification of loads and adopts differentiated price-based

demand response. There are certain differences in the electricity consumption behavior, real-time electricity price, and elastic coefficient of different loads.

3.1 Load Characteristics of the Low-Voltage Transformer District

This article divides the electricity load of low-voltage transformer districts into three types according to the electricity consumption characteristics of them. They are residential electricity load, industrial electricity load, and electric vehicle charging pile electricity load.

The typical low-voltage transformer district electricity consumption category is mainly residential electricity load. This kind of load is not restricted by grid dispatching. The user's consumption behavior greatly affects the load fluctuation of the low-voltage transformer district. With the popularization of air conditioners, lighting, and other equipment, the impact of climate change and time factors on residential electricity load has become more significant (Meng et al., 2019).

Industrial electricity load is linked to economic factors. The economic situation of the district where the low-voltage transformer district is located directly affects the power consumption level of the industrial load, thereby affecting the growth or decline trend of the load in the entire low-voltage transformer district. In the electricity market, the electricity price is variable. The stepped electricity price and the time-of-use electricity price also show a complex relationship with the industrial load in a low-voltage transformer district (Chau et al., 2018).

The load of electric vehicle charging piles is easily affected by many factors, including the parameters of the electric vehicle itself, the number of charging piles, and many other factors (Zhang Y. et al., 2021). The intraday charging and discharging characteristics of large-scale electric vehicle charging piles will increase the peak-to-valley difference of the load. When the electric vehicle charging piles are connected on a large scale during the peak load period, it is not conducive to the safe and economic operation of the low-voltage transformer district. Therefore, the maximum accessible load of the charging pile is limited by the distribution capacity of the low-voltage transformer district (Tan et al., 2021).

3.2 Differential Price-Based Demand Response

Price-based demand response guides users to actively adjust their electricity consumption habits according to their own electricity consumption through time-of-use electricity prices. In this article, the differential price-based demand response (DPDR) is used to construct a relationship model between the change of load demand and the change of electricity price according to the actual electricity consumption. Introducing power consumption satisfaction can avoid user satisfaction drop due to excessive load response:

$$R_p = 1 - \frac{\sum_{t=1}^{T} |\Delta P_t|}{\sum_{t=1}^{T} P_t}$$

In the formula, R_p is satisfaction with electricity consumption. P_t and ΔP_t are the load amount and the load transfer amount before the demand response in the period of time, respectively. T is the scheduling period. Since different types of loads have different response characteristics of electricity consumption to electricity prices in the dispatch period, the corresponding elastic coefficients are also different. Considering the use of the differentiated electricity price elasticity coefficient matrix to build a demand response model as follows:

$$P_t^{PDR} = P_t + R_p \cdot \Delta P_t,$$

$$\varepsilon_m = \frac{\Delta P_m / P_m}{\Delta D_m / D_m},$$

$$E_m = \begin{bmatrix} \varepsilon_m^{1,1} & \varepsilon_m^{1,2} & \cdots & \varepsilon_m^{1,t} \\ \varepsilon_m^{2,1} & \varepsilon_m^{2,2} & \cdots & \varepsilon_m^{2,t} \\ \vdots & \vdots & \ddots & \vdots \\ \varepsilon_m^{t,1} & \varepsilon_m^{t,2} & \cdots & \varepsilon_m^{t,t} \end{bmatrix},$$

$$\Delta P_{m,t} = \begin{bmatrix} P_{m,1} & \cdots P_{m,t} \end{bmatrix} \cdot E_m \cdot \begin{bmatrix} \frac{\Delta D_{m,1}}{\Delta D_{m,1}} & \cdots \frac{\Delta D_{m,t}}{D_{m,t}} \end{bmatrix}^T,$$

In the formula, m represents the load type, where $m = 1, 2$, and 3 represent the residential, industrial, and charging pile loads, respectively. P_t^{PDR} is the load amount after the demand response in period t. ε_m is the electricity price elasticity coefficient of the m class load. ΔP_m and ΔD_m are the amount of change in m class electricity P_m and electricity price D_m, respectively. E_m is the elastic coefficient matrix of electricity price of the m class load; the diagonal elements of the matrix are the self-elastic coefficients of each corresponding time period, and the off-diagonal elements are the cross elastic coefficients between the corresponding two time periods. $P_{m,t}$, $\Delta P_{m,t}$, $D_{m,t}$, and $\Delta D_{m,t}$ are respectively the load before the demand response, the load change amount, the electricity price, and the electricity price change amount of m class load- in period t.

The three types of loads in this transformer district mentioned in this article have different proportions in the entire station area, and different types of loads have different electricity price demand balance relationships in different time periods, and there are differences in response elasticity. At present, in the study of price-based demand response models, electricity price differentiation or elastic coefficient differentiation response models are mostly used (He et al., 2021), which are obviously insufficient. However, this article comprehensively considers the load power consumption characteristics of the station area and constructs a different type of load response elasticity according to the difference in response elasticity of different types of loads. A new price-type response mechanism is established based on the electricity price elasticity matrix response matrix that

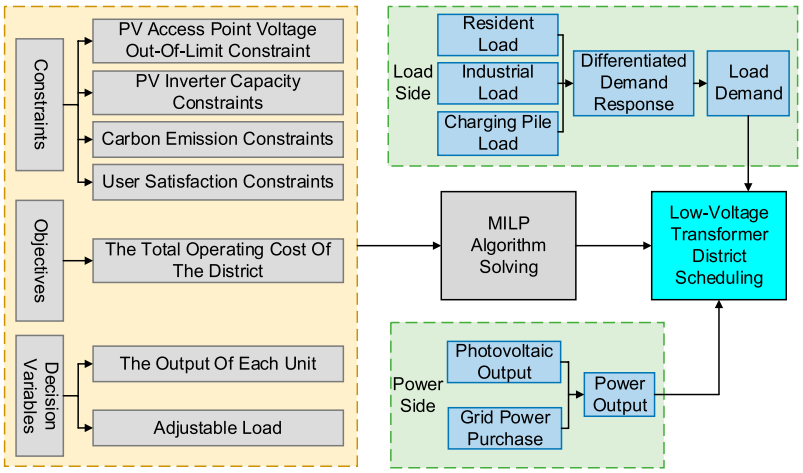

FIGURE 2 | Scheduling framework of the low-voltage transformer district considering carbon emissions and differential demand response.

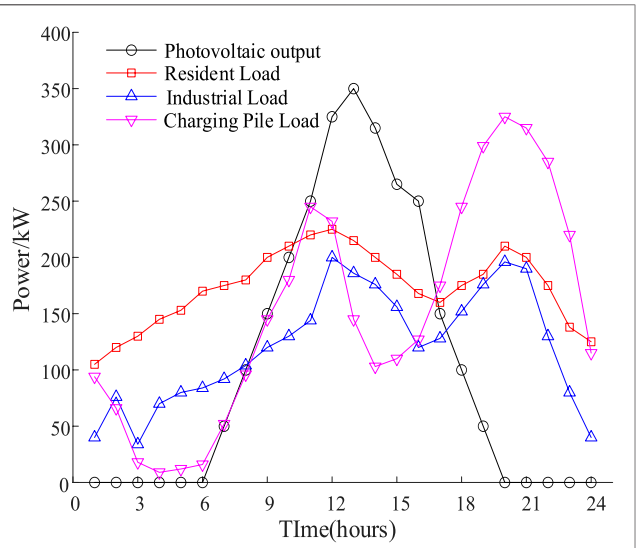

FIGURE 3 | Typical intra-day predicted values of photovoltaic output and load.

takes into account the differences in classified loads and electricity consumption periods.

4 INTRADAY OPTIMAL DISPATCH MODEL OF THE LOW-VOLTAGE TRANSFORMER DISTRICT CONSIDERING CARBON EMISSIONS AND DPDR

This article divides the load side into three types to participate in differentiated price-based demand response when constructing the optimal dispatch framework of a low-voltage transformer district. The power side includes photovoltaic output and grid power purchase. In summary, a low-voltage transformer district scheduling framework considering carbon emissions and DPDR can be constructed as shown in **Figure 2**. On the premise that the output of each unit in the low-voltage transformer district and the battery charge and discharge meet various constraints, different considerations are considered on the power side and the load side. The output of different types of power sources and the power consumption characteristics of different types of loads are aimed at the lowest total operating cost of the low-voltage transformer district, and the MILP algorithm is used to solve the problem to realize the optimal scheduling scheme of the low-voltage transformer district.

4.1 Objective Functions

In the optimal scheduling of the low-voltage transformer district, according to the forecasted values of photovoltaics and load power, taking into account the carbon emission and DPDR and aiming at the lowest total operation cost of the low-voltage transformer district, the objective function of the operation optimization of the low-voltage transformer district is established as follows:

$$\boldsymbol{minF} = \sum_{t=1}^{T}\left(\boldsymbol{F}_{buy,t} + \boldsymbol{F}_{w,t} + \boldsymbol{F}_{CO2,t} + \boldsymbol{F}_{SL,t} - \boldsymbol{F}_{sell,t}\right),$$

In the formula, $\boldsymbol{F}$ is the total operating cost of the low-voltage transformer district. $\boldsymbol{T}$ is the scheduling cycle for the day ahead. $\boldsymbol{F}_{buy,t}$ is the power purchase cost. $\boldsymbol{F}_{w,t}$ is the operation and maintenance cost. $\boldsymbol{F}_{CO2,t}$ is the carbon disposal cost. $\boldsymbol{F}_{SL,t}$ is the satisfaction loss cost. $\boldsymbol{F}_{sell,t}$ is the electricity sales revenue. The specific model of each scheduling cost is as follows:

4.1.1 Power Purchase Costs

$$\boldsymbol{F}_{buy,t} = \boldsymbol{C}_{buy,t} \cdot \boldsymbol{P}_{buy,t} \cdot \Delta \boldsymbol{t},$$

In the formula, $F_{buy,t}$ is the electricity purchase cost in the transformer district in period t. $C_{buy,t}$ is the unit power purchase cost in period t. $P_{buy,t}$ is the power purchased in period t. Δt is the duration of the scheduling period.

4.1.2 Operation and Maintenance Costs

$$F_{w,t} = \sum_{i=1}^{N_w} C_{w,i} \cdot P_{i,t} \cdot \Delta t$$

In the formula, $F_{w,t}$ is the operation and maintenance cost in period t. N_w is the number of units for which the operation and maintenance cost needs to be calculated. $C_{w,i}$ is each operation and maintenance cost of unit i. $P_{i,t}$ is the operating power of unit i in period t.

4.1.3 Carbon Disposal Costs

$$F_{CO2,t} = C_{CO2} \cdot Q_{CO2,t} \cdot \Delta t$$
$$Q_{CO2,t} = \sum_{x=1}^{N_{CO2}} E_{CO2,x} \cdot P_{x,t}$$

In the formula, $F_{CO2,t}$ is the carbon disposal cost in period t. C_{CO2} is the unit carbon disposal cost. $Q_{CO2,t}$ is the total amount of carbon emissions in the transformer district in period t . N_{CO2} is the number of units that need to calculate the carbon treatment cost. External power purchase, photovoltaic power generation, and battery charging and discharging all have carbon emissions. $E_{CO2,x}$ is the carbon emission intensity of unit x, which refers to the carbon emission generated by the unit power growth. $P_{x,t}$ is the output power of unit x in period t.

4.1.4 Satisfaction Loss Costs

The user has the most suitable energy consumption in each period, which calls the users baseline load. When the user deviates from the baseline load, there is a satisfaction loss, which is quantified by the following function:

$$F_{SL,t} = \left(\frac{1}{2}\lambda_{j,m} \cdot P_{j,m,t}^2 - \theta_{j,m} \cdot P_{j,m,t}\right) \cdot \Delta t,$$

In the formula, $F_{SL,t}$ is the satisfaction loss cost in period t. $\lambda_{j,m}$ and $\theta_{j,m}$ are the constant coefficients of energy preference. $P_{j,m,t}$ is the actual load of the m class load in low-voltage transformer district j during period t.

4.1.5 Electricity Sales Revenues

$$F_{sell,t} = C_{sell,t} \cdot P_{sell,t} \cdot \Delta t$$

In the formula, $F_{sell,t}$ is the electricity sales revenue in period t. $C_{sell,t}$ is the benefit of electricity sales per unit in period t. $P_{sell,t}$ denotes the photovoltaic power sales in period t.

4.2 Constraints

4.2.1 Power Balance Constraint

$$P_{buy,t} + P_{PV,t} + P_{dis,t} = P_{cha,t} + P_{sell,t} + P_t^{PDR}$$

In the formula, $P_{PV,t}$ is the photovoltaic power generation in period t. $P_{cha,t}$ and $P_{dis,t}$ are the battery charging and discharging powers in period t, respectively.

4.2.2 Constraint on the Receiving Capacity of the Low-Voltage Transformer District

The penetration capacity of distributed photovoltaics affects the operation state of the transformer district. If the penetration rate of photovoltaics is too high, it will have adverse effects on the district, such as power quality degradation (Ma et al., 2021). Therefore, when the distributed photovoltaics are connected to the low-voltage transformer district, it is necessary to consider the receiving capacity of the distributed photovoltaics in the pressing area. The total capacity of the distributed photovoltaics in the access point should not exceed the receiving capacity of the transformer district for photovoltaics. The constraint formula of the admission capacity of the low-voltage transformer district as follows:

$$\sum_{t=1}^{T} P_{PV,t} \le P_{PV,max}$$

In the formula, $P_{PV,max}$ is the maximum receiving capacity of the low-voltage transformer district for photovoltaics.

4.2.3 Access Point Voltage Violation Constraint

There is a certain error in the forecast value of photovoltaic output, and with the increase of photovoltaic penetration rate, the voltage of the access point has a greater possibility of exceeding the limit (Huang M. et al., 2022). To reduce the probability of voltage overlimit, we set constraints as follows:

$$V_{min} \le \varphi_{buy} \cdot P_{buy,t} + \varphi_{PV} \cdot P_{PV,t} \le V_{max}$$

In the formula, V_{min} and V_{max} are the upper and lower limits of the voltage, respectively; 0.4 and 5.4 are taken in this article. φ_{buy} and φ_{PV} are the power-voltage sensitivity coefficients corresponding to the purchasing power and photovoltaic power, respectively.

4.2.4 PV Inverter Capacity Constraint

During photovoltaic power generation, the photovoltaic inverter provides a certain amount of power to the grid, while maintaining a part of the adjustable ability, and can absorb or emit part of the power to adjust the voltage of the photovoltaic access point (Elkayam and Kuperman, 2019). The total output in the PV inverter must meet the capacity constraints:

$$\sqrt{P_{PV,t}^2 + P_{sell,t}^2} \le P_{INV}$$

In the formula, P_{INV} is the rated capacity of the photovoltaic inverter.

4.2.5 Battery Charge and Discharge Constraints

$$\begin{cases} 0 \le P_{dis,t} \le P_{dis,max} \\ 0 \le P_{cha,t} \le P_{cha,max} \\ P_{dis,max} = (S_{OC,t-1} - S_{OC,min}) \cdot C_{ESS} \cdot \gamma_{dis} \\ P_{cha,max} = (S_{OC,max} - S_{OC,t-1}) \cdot C_{ESS} / \gamma_{cha} \end{cases}$$

$$\begin{cases} S_{OC,min} \le S_{OC,t} \le S_{OC,max} \\ S_{OC,0} = S_{OC,T} \end{cases}$$

In the formula, $P_{cha,max}$ and $P_{dis,max}$ are the maximum charge and discharge powers of the battery, respectively. $S_{OC,t}$ is the state of charge of the battery in period t. $S_{OC,0}$ and $S_{OC,T}$ represent the state of charge in period 0 and T, respectively. $S_{OC,max}$ and $S_{OC,min}$ are the maximum and minimum states of charge of the battery, respectively. C_{ESS} is the rated capacity of the battery. γ_{cha} and γ_{dis} are the charge and discharge rates of the battery, respectively.

4.2.6 Carbon Emission Constraints

$$\sum_{t=1}^{T} Q_{CO2,t} \le Q_{CO2,max}$$

In the formula, $Q_{CO2,t}$ is the carbon emission of the low-voltage transformer district in period t. $Q_{CO2,max}$ is the maximum allowable carbon emission of the low-voltage transformer district.

4.2.7 Grid Interactive Power Constraints

$$\begin{cases} P_{buy,min} \le P_{buy,t} \le P_{buy,max} \\ P_{sell,min} \le P_{sell,t} \le P_{sell,max} \end{cases}$$

In the formula, $P_{buy,max}$ and $P_{buy,min}$ are the maximum and minimum values of the purchased power, respectively. $P_{sell,min}$ and $P_{sell,max}$ are the maximum and minimum values of the sold power, respectively.

4.2.8 User Satisfaction Constraint

$$R_p \le R_{p,min}$$

In the formula, $R_{p,min}$ is the minimum electricity consumption satisfaction.

4.3 Solving the Algorithm

The low-voltage transformer district operation optimization model established in this article, considering carbon emissions and differentiated demand response includes variables such as power purchase and photovoltaics as well as the charging and discharging states of the battery. It is a nonlinear programming problem. Therefore, the mixed integer linear programming (MILP) method is used to convert into a linear model for solving. The method searches the nodes in the solution space tree, discards the nodes that cannot generate feasible solutions, and searches the child nodes of the live nodes until the optimal solution is found (Zhu et al., 2017). The MILP model established is simulated and solved by calling the Yalmip toolbox and Gurobi solver in Matlab.

5 SIMULATION ANALYSIS

In order to verify the correctness of the optimization model of the low-voltage transformer district proposed in this article, a typical low-voltage transformer district demonstration project in a city is taken as an example scenario. The type of users in the transformer district is analyzed according to the information such as the low-voltage transformer district geographic information, the number of users, and the capacity of the power system. The users in the low-voltage transformer district are divided into residential users, industrial users, and charging pile users. The load of this low-voltage transformer district has a trend of upward translation, showing a certain load characteristic.

5.1 Basic Data

The summary of the calculation example is as follows: the total capacity of the photovoltaic power generation system in the low-voltage transformer district is 2800 kW. The rated capacity of the photovoltaic inverter is 250 kW. The total capacity of the battery is 300 kW. The charge and discharge rates are both 30%. The maximum and minimum charge states are 0.8 and 0.2, respectively. The initial energy storage is 30 kW. The parameters of each element in the calculation example are shown in **Table 1**. The calculation example takes 24 h before the day as the scheduling period and 1 h as the length of the scheduling period, and the power is constant during the scheduling period. The power consumption on the load side is divided into three periods: peak periods, usual periods, and valley periods. The peak periods are the 10:00–15:00 period and the 18:00–21:00 period; the usual periods are the 7:00–10:00 period, the 15:00–18:00 period, and the 21:00–23:00 period; the valley periods are the 0:00–7:00 period and the 23:00–24:00 period. The time-of-use electricity prices for residential, industrial, and charging pile loads are shown in **Table 2**. The elastic coefficients of the three types of loads are shown in **Table 3**. The photovoltaic electricity sales prices are 0.68, 0.4, and 0.11 yuan/(kW · h) during the peak-to-valley period. The maximum allowable carbon emission in the low-voltage transformer district is 1500 kg.

In order to verify the effectiveness of the operation optimization model of the low-voltage transformer district proposed in this article, three types of load scenarios in two modes are designed for comparative analysis. Mode 1 is the most basic optimization mode, and carbon emissions and demand response are not considered in the dispatch model. Mode 2 is a comprehensive optimization model on the basis of considering DPDR, and carbon emission factors are further considered. Three types of load scenarios are resident load, industrial load, and charging pile load.

TABLE 1 | Operation parameters of each unit in the low-voltage transformer district.

Transformer district unit	Lower power limit/kW	Upper power limit/kW	Operation and maintenance cost in each period/yuan/(KW·h)	Carbon intensity/Kg/(kW·h)
Photovoltaic	0	350	0.0235	0.015
Electricity Purchase	0	400	–	0.79
Electricity Sales	0	100	–	–
ESS Power Storage	0	300	0.012	0.15
ESS Power Discharge	0	300	0.1	0.15

TABLE 2 | Time-of-use electricity price of three types of load.

Load type	Peak electricity price/Yuan/(KW·h)	Usual electricity price/yuan/(KW·h)	Valley electricity price/yuan/(KW·h)
Resident Load	0.86	0.52	0.13
Industrial Load	0.94	0.6	0.51
Charging Pile Load	1.5	0.8	0.5

TABLE 3 | Differential elastic coefficients of three types of load.

Load type	Self-elastic coefficient	Mutual-elastic coefficient
Resident Load	−0.2	0.03
Industrial Load	−0.05	0.33
Charging Pile Load	−0.12	0.02

5.2 Simulation Results

Figures 4, **5** shows the scheduling results, including the load demand, conventional output, and battery charge and discharge conditions of the three types of load scenarios in different modes.

From **Figure 4** and **Figure 5**, it can be concluded that Mode 1 does not consider DPDR and carbon emissions, and the load of the three types of loads in each period remains unchanged. When the load is in the valley period, the photovoltaic output not only meets the load demand but also charges the battery. When charging to the maximum state of charge, the solar panel may be abandoned in the transformer district. When the load is in the usual period, the state of charge of the battery remains constant, and the load demand is jointly supplied by photovoltaics and power grid purchases. When the load is in the peak period, the photovoltaic output is low. In addition to battery discharge, a large amount of power needs to be purchased from the external power grid to meet the load demand. This model has a relatively high power purchase, a low photovoltaic consumption rate, and a high photovoltaic rejection rate. This operation mode is not conducive to the safe and stable operation of the transformer district and will also increase the economic cost of the transformer district. Mode 2 considers DPDR and carbon emissions. DPDR reduces the load during peak hours and increases the load during valley hours in response to the electricity price. The photovoltaic power generation increases; also, the photovoltaic consumption rate increases, and the economic cost of the transformer district is reduced. In summary, considering demand response and carbon emissions in the optimal scheduling of low-voltage transformer districts can improve the photovoltaic absorption rate and the utilization rate of demand response resources in the transformer district and improve the matching degree of source-load measurements.

The load comparison curve before and after considering the DPDR is shown in **Figure 6**, including the load values of the three

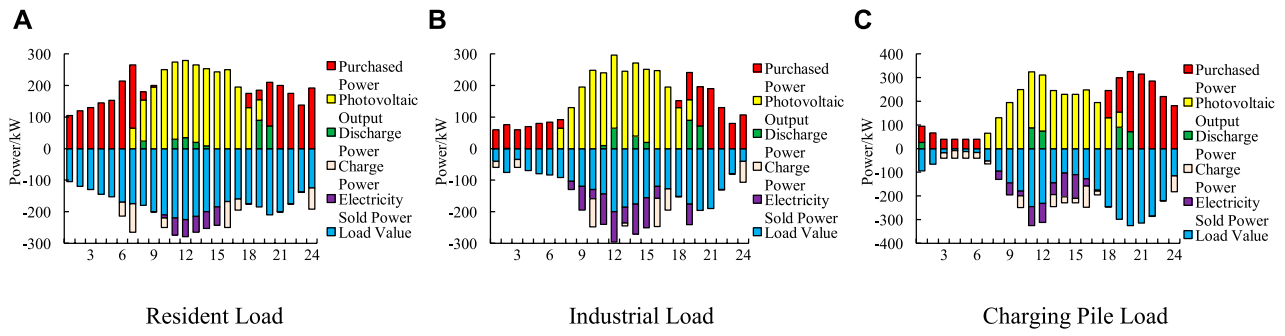

FIGURE 4 | Optimal scheduling outputs of units in Mode 1.

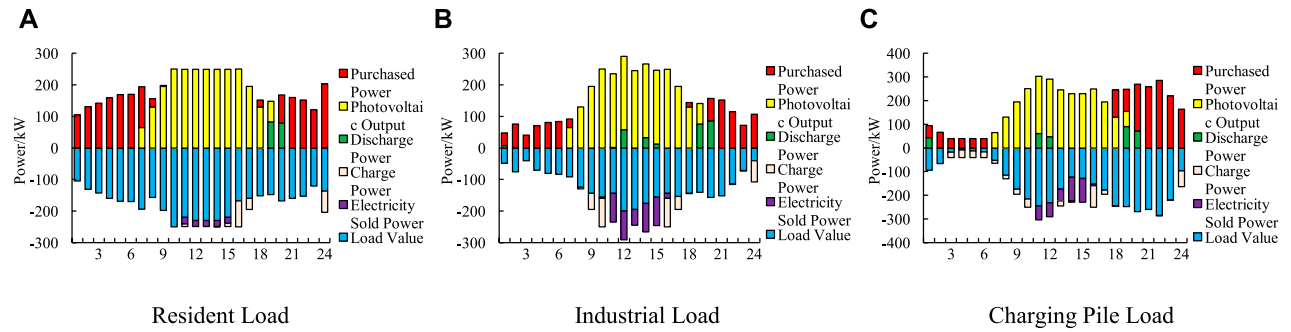

FIGURE 5 | Optimal scheduling outputs of units in Mode 2.

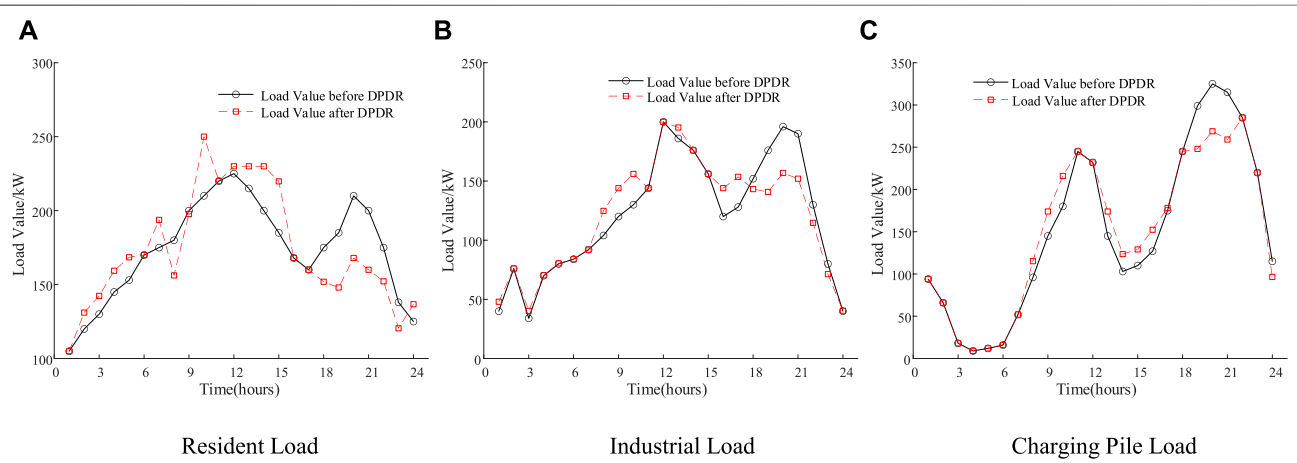

FIGURE 6 | Load comparison curve of three scenarios before and after demand response.

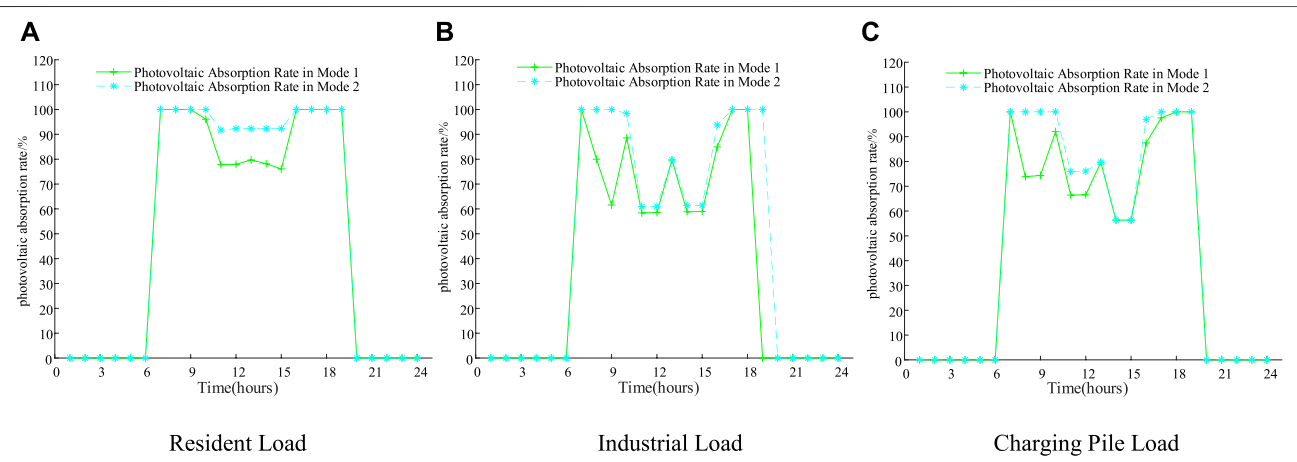

FIGURE 7 | Comparison curves of PV absorption rates in three scenarios under two modes.

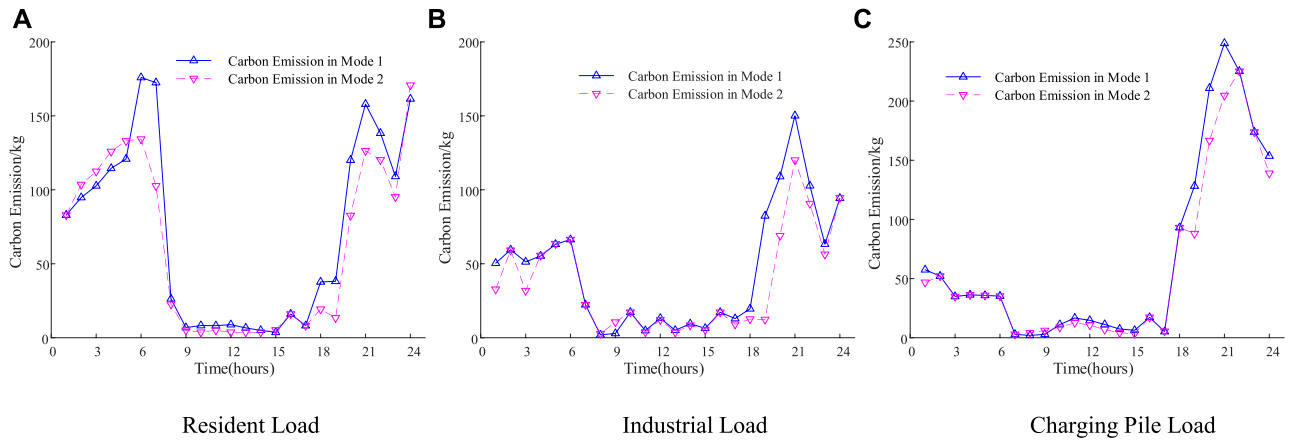

FIGURE 8 | Comparison curves of carbon emission in three scenarios under two modes.

types load scenarios of users in each time period under the two models.

As can be seen from **Figure 6**, compared with Mode 1 and Mode 2, the three types of loads in Mode 2 use the elastic change of electricity price to guide the load to transfer laterally in time during the dispatch cycle under the action of DPDR and perform peak shaving and valley filling to reduce the load. DPDR smooths the load curve, reduces the cost of demand response, and provides a guarantee for the stable operation of the low-voltage transformer district.

Figure 7 shows the comparison curves of photovoltaic consumption in three types of load scenarios under the two modes.

It can be seen from **Figure 7** that the photovoltaic absorption rate of the three types of loads in Mode 1 are only 88.8, 72.8, and 77.7%, the rate is low, and the photovoltaic rejection rate is high. The photovoltaic absorption rate of the three types of loads in Mode 2 compared with that of Mode 1 has improved, reaching 96.1, 82.5, and 84.9%, meeting the requirement of a photovoltaic consumption rate of 80% or more in the low-voltage transformer district. Photovoltaic energy is fully utilized.

Figure 8 shows the comparison curve of carbon emissions before and after comprehensively considering carbon emissions and differentiated demand response, including the carbon emissions of three types of load scenarios in each period under two modes.

It can be seen from **Figure 8** that in Mode 1, the overall carbon emission level of the low-voltage transformer district is relatively high during the dispatch period because the carbon emission factor is not considered. Mode 2 considers carbon emissions in the optimization objective while taking into account carbon constraints. Since the carbon emission of new energy sources such as photovoltaic power generation is very small, the charging and discharging of the battery itself will not produce a lot of carbon emissions, and the carbon emission intensity of external power purchases in the transformer district is relatively high, so it is preferred to use new energy for power generation. The battery will store the excess energy in part of the

TABLE 4 | Optimal scheduling costs in three scenarios under two modes.

Scenarios	Operation costs/yuan	Mode 1	Mode 2
Resident Load	Electricity Purchase Cost	683.13	540.11
	Operation And Maintenance Cost	71.31	66.64
	Satisfaction Loss Cost	69.77	61.34
	Carbon Disposal Cost	434.74	378.00
	Electricity Sales Revenue	186.99	66.42
	Total Operating Cost Of Transformer District	1071.96	979.67
Industrial Load	Electricity Purchase Cost	802.91	596.58
	Operation And Maintenance Cost	70.76	70.15
	Satisfaction Loss Cost	33.91	28.76
	Carbon Disposal Cost	272.44	221.19
	Electricity Sales Revenue	563.21	419.15
	Total Operating Cost Of Transformer District	616.81	497.53
Charging Pile Load	Electricity Purchase Cost	1802.64	1540.67
	Operation And Maintenance Cost	73.38	72.04
	Satisfaction Loss Cost	52.90	46.51
	Carbon Disposal Cost	398.93	356.36
	Electricity Sales Revenue	464.37	369.19
	Total Operating Cost Of Transformer District	1863.48	1646.39

period for use in the photovoltaic valley period. If the photovoltaic and the battery cannot meet the load demand, the electricity will be purchased from the outside. From the optimization results, it can be seen that in the optimization model of the three scenarios, the photovoltaic power generation increased by 1.0, 0.5,, and 0.6%, the power purchase decreased by 11.7, 20.8,, and 11.0%, and the carbon emissions decreased by 13.1, 18.8,, and 10.7%. It is proved that considering carbon emission targets and constraints in the optimal scheduling of a low-voltage transformer district can reduce the total carbon emissions of the district.

From **Table 4**, it can be concluded that due to the good economy of DPDR, it has a significant impact on the operation cost of the transformer district, in addition. The dispatch model takes carbon emissions as the optimization target, which reduces the carbon treatment cost of the transformer district and further reduces the total operating cost of the transformer district. Compared with Mode 1, Mode 2 reduces the total operating costs of the three user types by 8.6, 19.3,, and 11.6%, respectively. The scheduling results show that considering carbon emissions and differentiated demand response in the optimal scheduling of the low-voltage transformer district can reduce the total operating cost and carbon emissions of the transformer district, which proves the correctness of the scheduling model.

6 CONCLUSION

In order to deal with the carbon emission and source-load coordination problems of the low-voltage transformer district under the dual-carbon background, this article takes into account the differences in time-of-use electricity prices and the elasticity of different types of loads and builds a differentiated price-based demand response model. On this basis, considering the carbon emission factor, a low-voltage transformer district optimization model is established with the goal of the lowest total operation cost of the station area, and the MILP method is used to solve the algorithm optimization. The simulation results show that

1) This article proposes a low-voltage transformer district operation optimization method that considers demand response differences and carbon emissions so that demand response resources can be fully utilized, and the output fluctuations of the district are reduced. The optimization method also reduces errors due to PV uncertainty and improves the reliability of the optimal scheduling of the district.
2) The MILP method proposed in this article can efficiently solve the above model, can significantly improve the optimization convergence speed, and has good adaptability to the dynamic environment.
3) The research in this article has important significance for improving the coordination of the source, load, and storage in the low-voltage transformer district. However, this article only considers the differential price demand response and does not consider the incentive demand response. The reliability of optimal dispatch is relatively low. More research is needed in this area in the future.

DATA AVAILABILITY STATEMENT

The original contributions presented in the study are included in the article/Supplementary Material; further inquiries can be directed to the corresponding author.

AUTHOR CONTRIBUTIONS

DJ designed an optimal scheduling method; YZ carried out experiments; HG and JL analyzed experimental results. YD and GL wrote the manuscript.

FUNDING

This work was supported by the State Grid science and technology project (5400-202118485A-0-5-ZN).

REFERENCES

Al-Ismail, F. S. (2020). Discussion on "A New Formulation of Distribution Network Reconfiguration for Reducing the Voltage Volatility Induced by Distributed Generation". *IEEE Trans. Power Syst.* 35 (06), 4974. doi:10.1109/tpwrs.2020.3012366

Chau, T. K., Yu, S. S., Fernando, T., and Iu, H. H.-C. (2018). Demand-Side Regulation Provision from Industrial Loads Integrated with Solar PV Panels and Energy Storage System for Ancillary Services. *IEEE Trans. Ind. Inf.* 14 (11), 5038–5049. doi:10.1109/tii.2017.2782244

Chen, W., Yan, Y., Kang, M., Chen, Z., Ma, W., and Liu, J. (2020). Generation-Load-Storage Layered Coordinated Control of Distribution Network Considering the Influence of Distributed Generation. *Electr. Power Eng. Technol.* 39 (05), 113–119. doi:10.12158/j.2096-3203.2020.05.016

Chen, Z., Zhang, Y., Ma, G., Guo, C., and Zhang, J. (2019). Two-Stage Day-Ahead and Intra-day Robust Reserve Optimization Considering Demand Response. *Automation Electr. Power Syst.* 43 (24), 67–76. doi:10.7500/AEPS20181220001

Cong, Li., Qin, L., and Duan, H. (2022). Research on Reconfiguration of Distribution Network with Photovoltaic Generation Based on Improved Group Search Optimizer. *Acta Energiae Solaris Sin.* 43 (04), 213–218. doi:10.19912/j.0254-0096.tynxb.2020-0834

Elkayam, M., and Kuperman, A. (2019). Optimized Design of Multiresonant AC Current Regulators for Single-phase Grid-Connected Photovoltaic Inverters. *IEEE J. Photovoltaics* 9 (06), 1815–1818. doi:10.1109/jphotov.2019.2937386

He, S., Gao, H., Tian, H., Wang, L., Liu, Y., and Liu, J. (2021). A Two-Stage Robust Optimal Allocation Model of Distributed Generation Considering Capacity Curve and Real-Time Price Based Demand Response. *J. Mod. Power Syst. Clean Energy* 9 (1), 114–127. doi:10.35833/mpce.2019.000174

Huang, D., Wang, X., Yu, N., and Chen, H. (2022). Hybrid Timescale Voltage/Var Control in Distribution Network Considering PV Power Uncertainty[J/OL]. *Trans. China Electrotech. Soc.*, 1–13. doi:10.19595/j.cnki.1000-6753.tces.211188

Huang, M., Zhang, Q., Zhang, S., Yan, Z., Gao, B., and Li, X. (2022). Distribution Network Reconfiguration Considering Demand-Side Response with High Penetration of Clean Energy. *Power Syst. Prot. Control* 50 (01), 116–123. doi:10.19783/j.cnki.pspc.210284

Jin, P., Shen, Q., Wu, H., and Hu, G. (2020). Evaluation and Treatment of Operational State of Distribution Areas Considering Incentive Demand Response. *Electr. Autom.* 42 (06), 76–79. doi:10.3969/j.issn.1000-3886.2020.06.024

Khalid, M., Akram, U., and Shafiq, S. (2018). Optimal Planning of Multiple Distributed Generating Units and Storage in Active Distribution Networks. *IEEE Access* 6, 55234–55244. doi:10.1109/access.2018.2872788

Ma, T., Meng, X., Bai, X., Ge, L., Jia, L., and Zhang, S. (2021). Robust Optimization Planning Method for Distribution Network Considering Large-Scale Distributed PV Access. *Power Capacitor React. Power Compens.* 42 (02), 183–190. doi:10.14044/j.1674-1757.pcrpc.2021.02.029

Meng, K., Dong, Z. Y., Xu, Z., Zheng, Y., and Hill, D. J. (2019). Coordinated Dispatch of Virtual Energy Storage Systems in Smart Distribution Networks for Loading Management. *IEEE Trans. Syst. Man, Cybern. Syst.* 49 (04), 776–786. doi:10.1109/tsmc.2017.2690911

Qiu, G., He, C., Luo, Z., Shen, X., Lou, Y., and Zhang, P. (2021). Economic Dispatch of Stackelberg Game in Distribution Network Considering New Energy Consumption and Uncertainty of Demand Response. *Electr. Power Autom. Equip.* 41 (06), 66–74. doi:10.16081/j.epae.202102021

Shafie-khah, M., Siano, P., Aghaei, J., Masoum, M. A. S., Li, F., and Catalão, J. P. S. (2019). Comprehensive Review of the Recent Advances in Industrial and Commercial DR. *IEEE Trans. Industrial Inf.* 15 (07), 3757–3771. doi:10.1109/tii.2019.2909276

Shi, W., Lv, L., Gao, H., Li, H., Liu, Y., and Liu, J. (2020). Economic Dispatch of Active Distribution Network with Participation of Demand Response and Electric Vehicle. *Automation Electr. Power Syst.* 44 (11), 41–51. doi:10.7500/AEPS20190603006

Tan, J., Wang, Y., Ma, Z., Wang, Z., Xu, G., and Sun, G. (2021). Security-Economy Operational Boundary of Flexible District Considering Large-Scale EV Charging Loads. *Electr. Power Eng. Technol.* 40 (05), 25–33. doi:10.12158/j.2096-3203.2021.05.004

Wei, Z., Pei, L., Chen, S., Zhao, J., and Fu, Q. (2021). Review on Optimal Operation and Safety Analysis of AC/DC Hybrid Distribution Network with High Proportion of Renewable Energy. *Electr. Power Autom. Equip.* 41 (09), 85–94. doi:10.16081/j.epae.202109039

Zhang, X., Guo, M., Lin, Y., Liang, C., Li, Y., Yang, R., et al. (2021). A Bi-layer Optimal Dispatch Approach for Distribution Networks with Distributed Photovoltaic Considering the Flexibility. *J. Electr. Power Sci. Technol.* 36 (03), 56–66. doi:10.19781/j.issn.1673-9140.2021.03.007

Zhang, Y., Wang, Y., Li, F., Wu, B., Chiang, Y.-Y., and Zhang, X. (2021). Efficient Deployment of Electric Vehicle Charging Infrastructure: Simultaneous Optimization of Charging Station Placement and Charging Pile Assignment. *IEEE Trans. Intell. Transp. Syst.* 22 (10), 6654–6659. doi:10.1109/tits.2020.2990694

Zhao, Y., Wu, Z., Qian, Z., Gu, W., Li, D., and Liu, Y. (2019). Distributed Optimal Dispatch of Active Distribution Network Considering Source-Load Temporal and Spatial Correlations. *Automation Electr. Power Syst.* 43 (19), 68–76. doi:10.7500/AEPS20190423003

Zhu, C., Yang, L., Cui, Y., and Wang, S. (2022). Optimal Scheduling of Active Distribution Network Considering User Participation in Demand Response. *Electr. Meas. Instrum.*, 1–9.

Zhu, J., Chen, Y., Zhang, M., Zhao, H., Wan, Q., Sun, J., et al. (2017). Household Micro Grid Energy Optimal Research Based on MILP. *Power Syst. Prot. Control* 45 (22), 96–101. doi:10.7667/PSPC161775

Conflict of Interest: DJ, HG and JL were employed by State Grid Energy Research Institute Co., Ltd., YZ and ZW were employed by State Grid Jiangsu Electric Power. Co., Ltd.

The remaining authors declare that the research was conducted in the absence of any commercial or financial relationships that could be construed as a potential conflict of interest.

Frontiers in
Energy Research

Advances and innovation in sustainable, reliable and affordable energy

Explores sustainable and environmental developments in energy. It focuses on technological advances supporting Sustainable Development Goal 7: access to affordable, reliable, sustainable and modern energy for all.

Discover the latest Research Topics

See more →

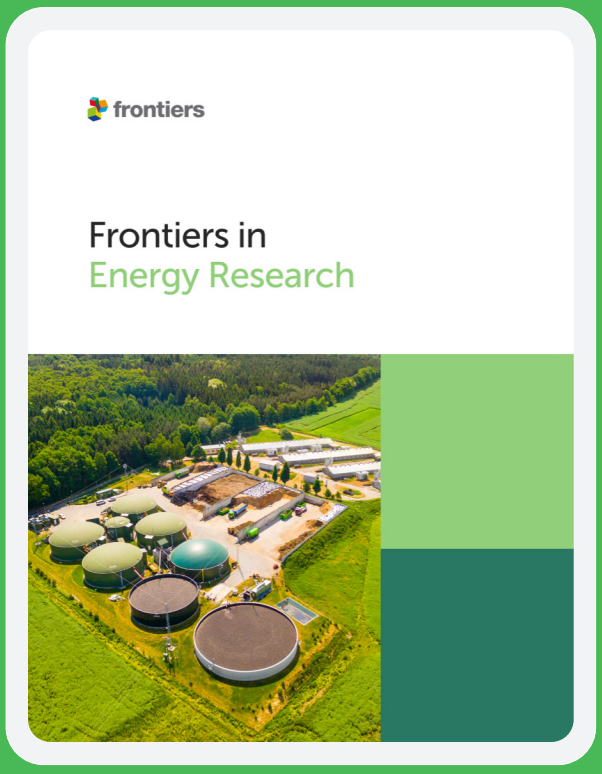

Frontiers

Avenue du Tribunal-Fédéral 34
1005 Lausanne, Switzerland
frontiersin.org

Contact us

+41 (0)21 510 17 00
frontiersin.org/about/contact